Croissance, structure et magnétisme dans les systèmes à décalage d'échange FM/AFM : approche fondamentale par la physique des surfaces

Marcio Soares Medeiros Soares

UNIVERSITÉ DE GRENOBLE

THÈSE

Pour obtenir le grade de

DOCTEUR DE L'UNIVERSITÉ DE GRENOBLE

Spécialité : **Physique de la matière condensée et du rayonnement**

Arrêté ministériel : 7 août 2006

Présentée par

« Márcio M. SOARES »

Thèse dirigée par **« Hélio TOLENTINO »** et
codirigée par **« Maurizio De Santis »**

préparée au sein de **l'Institut Néel, CNRS/UJF**
dans **l'École Doctorale de Physique**

Croissance, structure et magnétisme dans les systèmes à décalage d'échange FM/AFM : approche fondamentale par la physique des surfaces

Thèse soutenue publiquement le **« 9 juin 2011 »**,
devant le jury composé de :

Mme. Michèle SAUVAGE
Directrice de Recherche au Synchrotron Soleil (Présidente)
M. Stéphane ANDRIEU
Professeur à l'Institut Jean Lamour, Nancy (Rapporteur)
M. Yves GARREAU
Professeur à l'Université Paris Diderot, Paris (Rapporteur)
M. Fabrice SCHEURER
Chargé de Recherches à l'Institut de Physique et Chimie des Matériaux de Strasbourg (Membre)
M. Bruno GILLES
Directeur de Recherche CNRS au SIMAP, St. Martin d'Heres (Membre)
M. Robert MOREL
Chercheur au CEA/INAC, Grenoble (Membre)
M. Hélio TOLENTINO
Ingenieur de Recherche au Institut Néel, Grenoble (Membre)

Acknowledgments

First, I thank Hélio Tolentino for his guidance, support and friendship during this three years of thesis. I'm very very grateful to Maurizio De Santis, who taught me a lot about diffraction and surfaces. My large thanks to my french mother Aline Ramos, for all the big help in XAS analysis and for the accueil amical.

I would like to thank the collaborators in Halle, Marek Przybylski, Fikret Yildiz and Rantej Bali and at the ESRF Júlio Cezar.

To all people in the lab, especially to my friends sharing the office, my great thanks.

I acknowledge the financial support by the Fondation Nanosciences.

My acknowledgment to the jury members and rapporteurs, who kindly accepted to evaluate this work.

Finally, I want to thank my family for all their support, and especially to my wife, Maria Isabel, for whom this thesis is dedicated with love.

Nomenclature

AES	Auger electron spectroscopy
AFM	antiferromagnetic
bcc	body-centered cubic
bct	body-centered tetragonal
BL	bilayer
CTR	crystal truncation rod
DFT	density functional theory
DW	Debye-Waller parameter
EB	exchange bias
eV	electron volt
EXAFS	extended X-ray absorption fine structure
fcc	face-centered cubic
FC	field-cooling
fct	face-centered tetragonal
FM	ferromagnetic
GIXRD	Grazing incidence X-ray diffraction
GMR	giant magnetic resistance
H_C	coercive field
H_{EB}	exchange bias field
H_{FC}	Applied magnetic field during field cooling process
IP	in-plane
LEED	low-energy electron diffraction
LRO	long-range order

MAE	magnetic anisotropy energy
MBE	molecular beam epitaxy
ML	monoatomic layer
MOKE	magneto-optic Kerr effect
OP	out-of-plane
PMA	perpendicular magnetic anisotropy
RT	room temperature
S	order parameter
SRO	short-range order
SRT	spin reorientation transition
STM	scanning tunneling microscopy
SUV	Surface Under Vacuum experimental station of BM-32 beamline
T_C	Curie temperature
T_N	Néel temperature
TEY	total electron yield
UHV	ultra-high vacuum
XANES	X-ray absorption near edge structure
XAS	X-ray absorption spectroscopy
XMCD	X-ray magnetic circular dichroism
XRD	X-ray diffraction
XRMS	X-ray resonant magnetic scattering
XRR	X-ray specular reflectivity

Contents

Introduction

"There is Plenty of Room at the Bottom", said the talk's title by the famous physicist Richard Feynman, more than 50 years ago [1]. In this foresight exercise Feynman incites the scientific community to endeavor towards the world of small things:

> "What would the properties of materials be if we could really arrange the atoms the way we want them? They would be very interesting to investigate theoretically. I can't see exactly what would happen, but I can hardly doubt that when we have some control of the arrangement of things on a small scale we will get an enormously greater range of possible properties that substances can have, and of different things that we can do." [1]

He allows himself to imagine a way to storage information on a cube with 5 atoms edge. With a 125 atoms-bit, all the relevant books in world could be stored in a dust grain! Certainly, the scientific and technological evolution have not gone that far for the moment, but many exciting achievements have been done since then. The today widespread field of nanoscience, the science of small objects (1 to 100×10^{-9} m), extends through a vast range of knowledge and technology branches, from fundamental physics, to bio-materials or applications on energy production.

Regarding data storage, of which Feynman was worried about, many developments have been made in the use of magnetic materials for this purpose. The study of static and dynamic magnetic phenomena of matter at the nanometric scale, the nanomagnetism, has brought progress in ultra high density magnetic recording and today's technology is capable to ensemble up to $500\,\mathrm{GB/in^2}$ of information areal density. Many technological developments were necessary to achieve such high density, as the use of perpendicular magnetic anisotropy (PMA) recording media [2] and extremely sensitive reading heads based on giant magnetic resistance (GMR) [3]. The possibilities of nanomagnetism go beyond the data storage and the idea of using the spin of the electron instead of its charge as information career, which is a directly consequence of the discovery of GMR, opens many promising paths to walk through in the new field of spintronics.

The magnetic coupling at the interface of nanoscale artificial structures gives rise to unusual properties when compared to bulk. The size reduction enhances the importance of the magnetic moment distribution at interfaces at the expense of the bulk magnetism. This is particularly true in exchange coupled ferromagnetic-antiferromagnetic (FM/AFM) systems. The magnetic field necessary to switch the magnetization when an AFM material is in contact with a FM one is markedly increased by the interaction at the interface. Such an interaction can lead, in addition, to an unidirectional

anisotropy known as the exchange bias effect [4]. Despite the use of exchange bias effect in common technological devices, as in spin valves and magnetic tunnel junctions [5], a complete picture of its mechanism is not yet evident, since it involves the understanding of the FM/AFM interface not only from the structural point of view but also electronically and magnetically.

The ability of producing magnetic thin films with strong and tunable magnetic anisotropy represents a big challenge. The ordered alloys represent ideal systems in this regard. FePt ferromagnetic alloy, for example, provides a huge PMA ($10\,\mathrm{MJm^{-3}}$) in its $L1_0$ chemically-ordered phase. Antiferromagnetic materials also may show magnetic anisotropy, as MnPt alloy in its $L1_0$ structure. Influenced both by reduced thickness and by epitaxial deposition constraints, even more basic systems present a rich variety of phenomena [6]. One can mention, for instance, the spin reorientation transition for Fe layers grown on Ag(001) [7] or the huge magnetic anisotropy of FeCo on Rh(001)[8].

The availability of synchrotron sources leads to a wealth of well-established tools for structural analysis of surfaces and interfaces, in particular grazing incidence X-ray diffraction (GIXRD) and absorption spectroscopy (XAS) techniques [9]. Element-selective magnetic probes, as X-ray magnetic circular dichroism (XMCD) and X-ray resonant magnetic scattering (XRMS), became available and complement structural and other conventional magnetic probes. Since the AFM/FM interface is buried and changes in the structural and magnetic properties are small, combining all these techniques is of paramount importance to tackle the description of such systems.

In this context, we have been investigating, from a fundamental point of view, ultra-thin films presenting both PMA and implications to GMR technology. The possibility to grow ultra-thin epitaxial films and multilayers by molecular beam epitaxy has been exploited to synthesize samples that are close to ideal models. *In situ* characterization by GIXRD, supported by LEED, STM and AES, assures the control of the structure. Then, a combination of *ex situ* characterizations, using synchrotron techniques (XAS, XMCD) and magneto-optic Kerr effect (MOKE), gives further information on structural, electronic and magnetic properties.

During this thesis, we were especially interested in thin films with out-of-plane anisotropy. The main systems studied were ultra-thin layers of chemically-ordered alloys (FePt and MnPt) and of Fe/Ag(001), eventually coupled to CoO. Our strategy was to find an appropriate surface and, for each coupled bilayer, study the individual growth of each element, alloy or oxide. By controlling a variety of parameters such as surface structure, cleanliness, deposition rate and temperature, we've got a pretty good understanding of the growth process. The systems were not always those we were looking for but, we obtained well-tailored films and were faced with some quite nice surprises.

This manuscript is organized as follows. Chapter 1 states some fundamental concepts of magnetism in thin films and surface physics. It contains also a short review of each system studied. Chapter 2 describes the main experimental techniques. Chapter 3 is dedicated to the study of the metal on metal growth for some (001) surfaces, namely, Mn, Fe and Pt on Pt(001) and Fe and Pt on Ag(001). The synthesis of MnPt ordered alloys on Pt(001), investigated by GIXRD, is presented in chapter 4. The structure

and magnetism of out-of-plane ordered FePt/MnPt heterostructures are the subject of chapter 5. Chapter 6 concerns the study of CoO/Fe/Ag(001) system. A summary of the most relevant results, and some prospects, concludes the manuscript.

Chapter 1

Background

In this chapter, we present some fundamental concepts of thin film magnetism, like exchange interaction, magnetic anisotropy and specially exchange bias. The development given here is based mainly on the textbooks by Stöhr and Siegmann [10], Aharoni [11] and Guimarães [12]. A brief bibliographic review on the specific systems we are concerned with is given as a support for the following discussions. We close this chapter by recalling some concepts in surface physics, valuable to the study of growth and structure of our samples.

1.1 Concepts of thin film magnetism

The ferromagnetic (and antiferromagnetic) ordering of magnetic moments in a material comes from the strongest among the magnetic interactions, the exchange interaction (of the order of eV). This is not, however, a direct interaction between magnetic moments. It arises from the Coulomb interaction between electrons and the symmetrization postulate for Fermions; one manifestation being the Pauli exclusion principle. Being electrons indistinguishable particles with half-integer spin ($s = 1/2$) (i.e. Fermions), the symmetrization postulate asserts that the total wave function (Ψ) of an electron system is antisymmetric ($_{as}$) under the exchange of any electron pair. For a two-electron system this statement can be written as

$$\Psi_{as}(\boldsymbol{r}_1, \sigma_1; \boldsymbol{r}_2, \sigma_2) = -\Psi_{as}(\boldsymbol{r}_2, \sigma_2; \boldsymbol{r}_1, \sigma_1) \tag{1.1}$$

with $\boldsymbol{r}_i$ for spatial and σ_i for spin coordinates. Considering that the Hamiltonian of the system does not depend on the electron spin, we can separate Ψ_{as} in orbital Φ and spin χ components. This way, there are two possibilities to get an antisymmetric total wave function, either the spatial part is symmetric and the spin part is antisymmetric or vice versa. We have either

$$\Psi^{\mathrm{S}}_{as}(\boldsymbol{r}_1, \sigma_1; \boldsymbol{r}_2, \sigma_2) = \Phi_{sym}(\boldsymbol{r}_1; \boldsymbol{r}_2)\chi^{\mathrm{S}}_{as}(\sigma_1; \sigma_2) \tag{1.2}$$

where the antisymmetric two-electron spin function is the singlet state ($^{\mathrm{S}}$) with total spin quantum number $S = 0$ and $M_S = 0$,

$$\chi^{\mathrm{S}}_{as}(\sigma_1;\sigma_2) = \frac{1}{\sqrt{2}}[\uparrow\downarrow - \downarrow\uparrow] \tag{1.3}$$

Or the opposite situation, with

$$\Psi^{\mathrm{T}}_{as}(\boldsymbol{r}_1,\sigma_1;\boldsymbol{r}_2,\sigma_2) = \Phi_{as}(\boldsymbol{r}_1;\boldsymbol{r}_2)\chi^{\mathrm{T}}_{sym}(\sigma_1;\sigma_2) \tag{1.4}$$

and the symmetric two-electron spin function is the triplet state $\left({}^{\mathrm{T}}\right)$ with total spin quantum number $S = 1$ and $M_S = 1,\ 0,\ -1$,

$$\chi^{\mathrm{T}}_{sym}(\sigma_1;\sigma_2) = \begin{cases} \uparrow\uparrow \\ \frac{1}{\sqrt{2}}[\uparrow\downarrow + \downarrow\uparrow] \\ \downarrow\downarrow \end{cases} \tag{1.5}$$

The spatial function is written as

$$\Phi^{sym}_{as}(\boldsymbol{r}_1;\boldsymbol{r}_2) = \frac{1}{\sqrt{2}}[\phi_a(\boldsymbol{r}_1)\phi_b(\boldsymbol{r}_2) \pm \phi_b(\boldsymbol{r}_1)\phi_a(\boldsymbol{r}_2)] \tag{1.6}$$

where ϕ_a and ϕ_b are spatial wave functions that solve the Schrödinger equation for the two-electron system described by some Hamiltonian $\mathcal{H}$. We are not going to suppose any particular form for $\mathcal{H}$, but only assume that the electrons interact through the Coulomb repulsion potential[1] $\left(\frac{e^2}{4\pi\varepsilon_0|\boldsymbol{r}_1-\boldsymbol{r}_2|^2}\right)$. The energy difference between the singlet state (S) and the triplet state (T) will be given by[2]

$$E^{\mathrm{S}}_{\mathrm{e-e}} - E^{\mathrm{T}}_{\mathrm{e-e}} = 2J = 2\int\int \phi_a(\boldsymbol{r}_1)\phi_b(\boldsymbol{r}_2)\frac{e^2}{4\pi\varepsilon_0\left|\boldsymbol{r}_1-\boldsymbol{r}_2\right|^2}\phi^*_a(\boldsymbol{r}_2)\phi^*_b(\boldsymbol{r}_1)\,d\boldsymbol{r}_1 d\boldsymbol{r}_2 \tag{1.7}$$

J is called the exchange integral because it reflects the energy associated with a change of quantum states between the two electrons. The sign of J determines which spin state has lower energy. If J is positive the triplet state ($S = 1$) is favored, and the spins point to the same direction and are aligned parallel (ferromagnetism). For negative J, the singlet state has lower energy, and the spins are antiparallel (antiferromagnetism). In the singlet state the space function is symmetric and the electrons tend to be close to each other. In the triplet state the space function is antisymmetric and the electrons tend to avoid each other. Note that, by assumption, the Hamiltonian does not depend on the spin, so that it is the antisymmetry requirement, expressed in equations 1.2 and 1.4, the responsible for linking the spatial and spin wave functions. The exchange interaction is of fundamental importance not only for magnetism but also for many basic phenomena like the chemical covalent bond or spectral splitting on atomic energy levels.

[1] The two electrons may be, for example, bounded to two atoms like in a H_2 molecule. Their spatial wave functions will depend on the particular Hamiltonian of the system. The correlation between them, however, is assumed to be only of Coulombian nature.

[2] All energy terms that do not depend on the electron-electron interaction are equal for both singlet and triplet states and cancel out in the subtraction. The same is valid to the ordinary electrostatic Coulomb repulsion between the electron densities $I = \int\int |\phi_a(\boldsymbol{r}_1)|^2 \frac{e^2}{4\pi\varepsilon_0|\boldsymbol{r}_1-\boldsymbol{r}_2|^2} |\phi_b(\boldsymbol{r}_2)|^2 \, d\boldsymbol{r}_1 d\boldsymbol{r}_2$.

This simplified treatment aims only to set the basis for the understanding of the exchange interaction. For a real problem, of a $3d$ metal crystal for example, the picture is much more complex and it is very difficult to establish a first-principle theory, like the molecular orbital theory or the density functional theory, that can handle the problem. It is common to explore the magnetic properties of materials by means of model Hamiltonian's, like the Heisenberg and Hubbard models. The Heisenberg model describes the exchange interaction by explicitly introducing a spin-spin interaction in the Hamiltonian $\left(\mathcal{H}_{exch} = -\sum_{\substack{i,j \\ (i\neq j)}}^{N} J_{ij}\boldsymbol{s}_i \cdot \boldsymbol{s}_j\right)$. The Hubbard model explores the interplay between two competing energies in the formation of the electronic states in a multi-atom and multi-electron system, the electrostatic Coulomb energy between electrons, and the hopping energy of electrons from one atom to the next. The spin enters by imposing restrictions in accordance with the Pauli principle. The problem of exchange coupling at FM/AFM interfaces is even more complex, and phenomenological models are generally the alternative to handle it, as will be addressed in next section.

The above described exchange interaction, that strongly couples neighbor spins parallel or antiparallel, is isotropic. It is well known, however, that magnetic materials generally present preferential directions to align magnetic moments, as is the obvious case of permanent magnets. The magnetic anisotropy is a key parameter in the design of all magnetic materials, ranging from transformer and electromagnet cores to magnetic recording media. It may have various origins, like the shape of the sample, its crystalline structure, the presence of interfaces or constraints, etc. To these preferential directions one gives the name of easy-axes or easy-directions, while hard-axes designates directions avoided by the magnetic moments. The effective anisotropy energy is the energy necessary to rotate the magnetization from easy to hard directions. When a sample is broken into magnetic domains, the moments are also preferentially oriented along easy-directions.

The magnetocrystalline anisotropy is determined by the spin-orbit interaction, that is one or two orders of magnitude weaker than the exchange interaction. The lattice crystal field has a direct effect on the electron orbital moments. The contribution to the magnetism of the electron orbital moments is generally small. However, the electron spin and orbital moments are coupled through the spin-orbit interaction $\mathcal{H}_{\mathrm{SO}} = \zeta \boldsymbol{s} \cdot \boldsymbol{l}$ (where ζ is the *spin-orbit coupling constant* with [energy] dimension) and an alignment of the orbital moment implies an alignment of the spin moment. This magnetocrystalline anisotropy is responsible for the strong perpendicular anisotropy observed in the ordered alloys. Stress at thin films interfaces, caused by lattice mismatch in epitaxial growth, also play a role in the coupling of the electronic orbitals with the lattice crystal field, and equivalently influence the magnetocrystalline anisotropy through the spin-orbit interaction. To this kind of interface anisotropy one give the name of magnetoelastic anisotropy. Magnetostriction, the expansion (or contraction) of a material as a consequence of being magnetized, also can give rise to magnetoelastic anisotropy in domain boundaries or in constrained layers.

The exchange bias is also an interface anisotropy, but of exchange nature, not spin-orbit. It is all but trivial to develop a reliable calculation of the magnetocrystalline

(including magnetoelastic) anisotropy energy and to predict the easy magnetization axis. The most common approach is to make simple phenomenological models, that satisfactorily reproduce the experimental results and have support on the system symmetry.

The long range dipolar interaction is at the origin of the shape anisotropy, that for thin films tends to make the magnetization to lie in the film's plane. The demagnetizing field[3] $\boldsymbol{H}_{\mathrm{d}}$ for a homogeneously magnetized thin film is nearly zero for in-plane magnetization, while it is $\boldsymbol{H}_{\mathrm{d}} = -\boldsymbol{M}$ for out-of-plane magnetization $\boldsymbol{M}$. The shape anisotropy energy density for a thin film is then $K_{\mathrm{d}} = -\frac{\mu_0 M_{\mathrm{S}}^2}{2}$, where μ_0 is the vacuum permeability and M_{S} is the magnetization at saturation. This long range interaction is also responsible for the creation of magnetic domains.

1.2 Exchange bias

The exchange bias (EB) effect was discovered by Meiklejohn and Bean in 1956 [4] during the study of fine Co particles covered by a thin oxide layer. Since about fifteen years ago, this phenomenon has become an integral part of modern magnetism, with implications in basic research and in numerous device applications (see some reviews [13, 14, 15]). The EB effect manifests itself by a shift of the hysteresis loop (H_{EB}) towards the negative or the positive direction with respect to the applied field during a field cooling process (H_{FC}). Its origin is related to the magnetic coupling across the common interface shared by a FM and an AFM layer. The coercive field (H_{C}), the field necessary to switch the magnetization, is markedly increased by the exchange interaction at the FM/AFM interface. One says that the AFM is a pinning layer for the FM layer because it induces an extra anisotropy term through the interfacial exchange coupling. AFM materials that present strong anisotropy exchange coupling have found important technological application as pinning layers in spin-valve based devices, where the AFM layer keeps the magnetization of a FM layer in a fixed direction in space, while another FM layer switches under an applied magnetic field or spin-polarized current.

The basic description of the EB phenomenon was given since the pioneering work of Meiklejohn and Bean. A qualitative picture of the EB effect is sketched in figure 1.1. For a given temperature T above the AFM ordering Néel temperature (T_N) and below the FM layer Curie temperature (T_C), the AFM spins are disordered while the FM are ordered (fig. 1.1-a). A magnetic field H_{FC} is applied in order to saturate the FM layer in a direction parallel (or perpendicular) to the film surface. After field-cooling (FC) the AFM/FM bilayer below T_N, the AFM spins at the interface couple with the FM spins (fig. 1.1-b), yielding the energetically stable situation for the coupling at the interface. If some portion of the AFM spins at the interface are uncompensated or if there is some canting, a unidirectional anisotropy is created in the process. When the applied magnetic field H is reversed, the AFM spins at the interface exert a microscopic torque on the FM spins, tending to keep them in their original direction (fig. 1.1-c). The field needed to reverse the magnetization will be larger ($|H_{C1}| > |H_{C2}|$) and the magnetic hysteresis loop will be shifted by an amount $H_{EB} = (H_{C1} + H_{C2})/2$, due to

[3] For a magnet, the demagnetizing field is the magnetic field generated by its own magnetization.

this additional interfacial magnetic energy, $\Delta\sigma$, that has to be overcome (fig. 1.1-d). The same FM layer, without being coupled to an AFM one, would have smaller coercive field and no EB (dashed hysteresis loop in fig. 1.1).

The phenomenological expression of the exchange field is simply given by

$$H_{EB} = \Delta\sigma/(M_S^{FM} \times t^{FM}) \tag{1.8}$$

where M_S^{FM} and t^{FM} are the magnetic moment density and the thickness of the FM layer, respectively. While this basic description of the exchange bias is generally accepted, the microscopic interfacial interactions that contributes to the interfacial energy are more controversial. Nevertheless, it is known that the coupling is correlated to the magnetic anisotropy energy (MAE) of the AFM layer. The expression that relates the bias field H_{EB} to the AFM is

$$H_{EB} \propto \sqrt{A_{AFM} \times K_{AFM}} \tag{1.9}$$

where A_{AFM} and K_{AFM} are, respectively, the exchange stiffness and the magnetocrystalline anisotropy of the AFM layer [16].

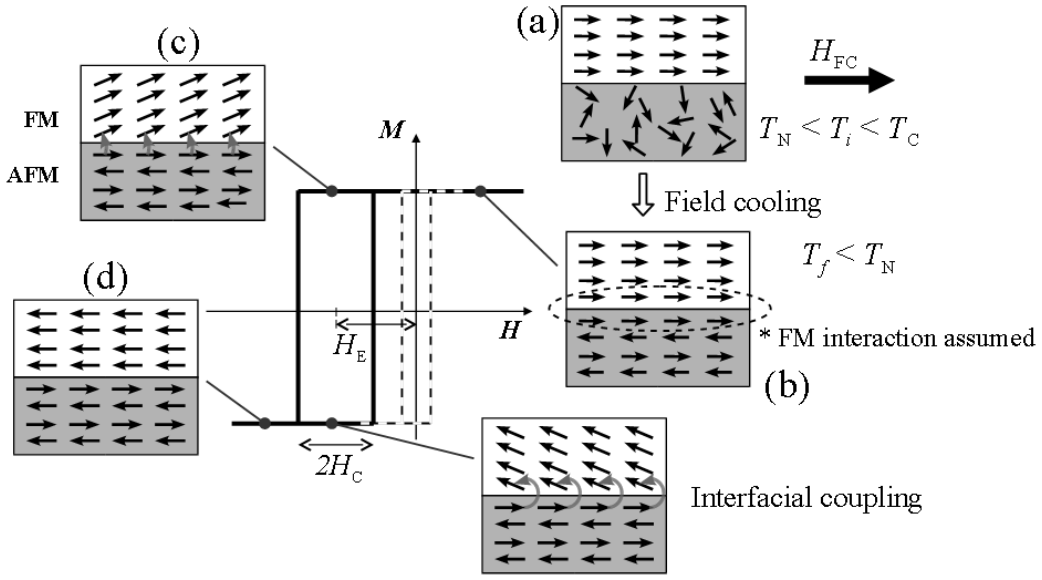

Figure 1.1: Sketch of exchange bias mechanism for an in-plane anisotropy FM/AFM system with perfectly uncompensated AFM spins at the interface. The exchange bias field (H_{EB}) and the enhanced coercive field (H_C) are indicated at the hysteresis loop. The dotted line, with smaller H_C and no EB, corresponds to the hysteresis for the FM layer alone, without being coupled to an AFM layer.

Many microscopic models have been proposed for the expression of the total magnetic energy and, in particular, for the interface exchange energy [17, 16, 18, 19, 20, 21]. Among the complex phenomena taking place close to the interface, domain-wall formation in the AFM layer, random interface roughness, contribution of compensated AFM/FM interfaces, extension of the coupling beyond interfacial layers [22] and non-collinear interface spin configuration are to be considered.

We recall that - contrary to the schema of figure 1.1 - the AFM interface layer is not always completely uncompensated (with all AFM spins coupled parallel). Indeed, in many situations, as for along the c-axis of $L1_0$ MnPt discussed later, the spins are coupled antiferromagnetically, giving a compensated interface. Moreover, the role of pinned (frozen) and unpinned (rotatable) interfacial uncompensated AFM spins in the exchange bias has been recently revealed by X-ray photoemission microscopy and X-ray magnetic linear and circular dichroism [23, 24]. It has been demonstrated that only the fraction of the AFM spins that are pinned contributes to the EB shift. Furthermore, a gradual degradation of the EB shift may be observed upon cycling the applied field. This aging phenomenon is known as training effect [25].

The major part of exchange bias studies have been performed with the magnetization parallel to the FM/AFM interface. Studies on systems with perpendicular (out-of-plane) magnetic anisotropy are rather recent [26, 27, 28] and only few address the role of spin configuration at the interface [29, 30]. Thin ferromagnetic films with PMA is a recognized way for increasing magnetic storage density. In addition, magneto optical effects are enhanced at polar (sensitive to perpendicular magnetization component) geometry compared to in-plane one [31, 32]. Atomic scale control and characterization of the interface structure and morphology is thus essential for the fundamental understanding of the magnetic interaction at real FM/AFM interfaces.

1.3 Systems of interest

All along this thesis work we were interested in a variety of systems related to PMA and EB effect. Indeed, many attention was paid to chemically-ordered alloy systems, as they represent a more direct way towards perpendicular coupling, when one is capable of tuning their magnetic anisotropy to be out-of-plane. Other materials of interest included ultra-thin Fe on Ag(001), that shows PMA at room temperature for thickness around 4 to 6 monoatomic layers (ML). Owing to its matching parameters, CoO is a well-suited antiferromagnetic material for coupling with Fe. Some additional systems were investigated. This is the case of FeCo alloy grown on Rh(001) and Ir(001) single crystal substrates, that presents an extremely large PMA [8] whose relation to the structural anisotropy and pseudomorphism has not yet been clarified. For these systems the data analysis is still preliminary and they are not presented in this manuscript.

We address below some general background on the chemically-ordered alloys and give a brief review on the main issues of each system.

1.3.1 Chemically-ordered magnetic alloys

The interest in ferromagnetic chemically-ordered alloys, such as FePt, FePd, CoPt, CoPd, FeNi [33, 34, 35, 36], arises from their high magnetocrystalline anisotropy. Antiferromagnetic chemically-ordered alloys, such as MnPt, IrMn and NiMn [37], are among the most used as pinning layers for spin-valves applications. All these chemically-ordered alloys present different equilibrium structures, depending on the stoichiometry

and preparation conditions. Generally the magnetic properties of an ordered alloy are intrinsically related to its degree of order.

Figure 1.2 shows the unit cells[4] of the chemically-ordered $L1_0$ and $L1_2$ structures[5], as well as that of the disordered $A1$ structure. The different chemical species appear as dark and light spheres. The $L1_2$ phase is face-centered cubic (*fcc*) structure with stoichiometry $A_{0.75}B_{0.25}$ where the minority atoms occupy the cube corners while the majority ones occupy the face-centered positions. The most relevant structure in our studies is the equiatomic $L1_0$ one, that presents the best magnetic properties for our systems, as described in the following sections. This structure is face-centered tetragonal (*fct*), where the cubic symmetry is broken due to the stacking of alternate planes of each chemical species along the tetragonal axis (c-axis). We call tetragonality the difference from unit of the c/a ratio. The $A1$ phase has a *fcc* chemically-disordered structure in which the hatched circles indicate a random occupation of the lattice sites.

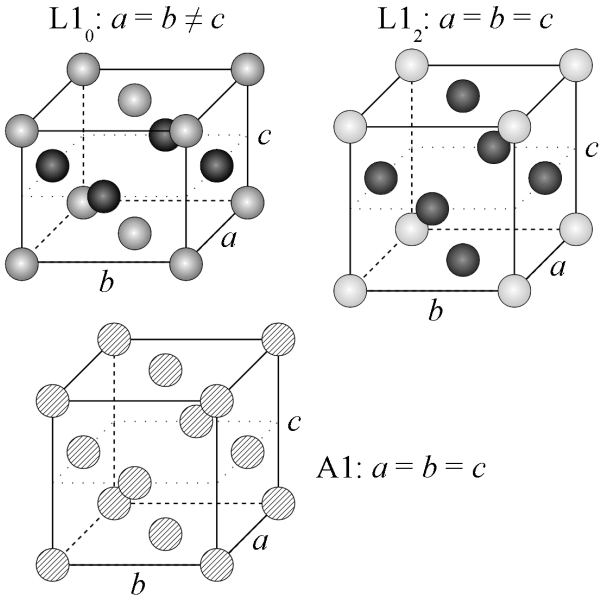

Figure 1.2: Unit cell representation for the *fct* $L1_0$, the cubic $L1_2$ and the *fcc* $A1$ structures. The dark and light spheres represent atoms of different nature, while the hatched circles in the $A1$ structure indicate that it is equally probable to have one or the other atom species in each position of the *fcc* lattice.

1.3.2 FePt

FePt alloy in the $L1_0$ chemically ordered phase has drawn much attention as a candidate for ultrahigh density magnetic storage media [38, 33]. Coercive fields up to 10 T have been already reported [33] in $L1_0$ FePt single domain particles grown on a heated MgO(001) substrate. According to its bulk phase diagram, presented in figure 1.3, a *fcc* solid solution is observed at high temperatures. Around the $FePt_3$ and Fe_3Pt stoichiometries, ordered alloys are formed in the $L1_2$ phase. The alloy close to

[4]The conventional unit cells, not the primitive ones.

[5]This notation is known as Strukturbericht notation. They are also called AuCu and $AuCu_3$ structures, respectively.

the equiatomic concentration exhibits at 1573 K a disorder-order transformation from the disordered *fcc* $A1$ (high temperature phase) to the $L1_0$ phase (low temperature phase). The lattice parameters[6] are $a_{FePt}^{\text{powder}} = 3.852\,\text{Å}$ and $c_{FePt}^{\text{powder}} = 3.720\,\text{Å}$ giving $c/a_{FePt}^{\text{powder}} = 0.966$ for powder diffraction data [39]. For a nanocrystalline system [42] where $L1_0$ ordered grains are submitted to stress at their boundaries, the values are slightly different, $a_{FePt}^{\text{nanocryst.}} = 3.860\,\text{Å}$ and $c_{FePt}^{\text{nanocryst.}} = 3.713\,\text{Å}$ with $c/a^{\text{nanocryst.}} = 0.962$. This last case is likely to be more comparable to the kind of sample we obtain by epitaxial growth. The $L1_0$ FePt is ferromagnetic below 673 K (see the Curie temperature, T_C, indication in the phase diagram, fig. 1.3) and is one of the hardest magnetic materials. The uniaxial magnetic anisotropy along the c-axis is predicted to have an energy density of [43] $K_u \sim 16 \times 10^7\,\text{erg/cm}^3$. Reported experimental values reach $K_u \sim 6.6$ to $10 \times 10^7\,\text{erg/cm}^3$ [44, 45, 34]. The high uniaxial anisotropy of FePt results from the large spin-orbit coupling of Pt atoms and the strong hybridization of Pt $5d$ band with highly polarized Fe $3d$ band [43].

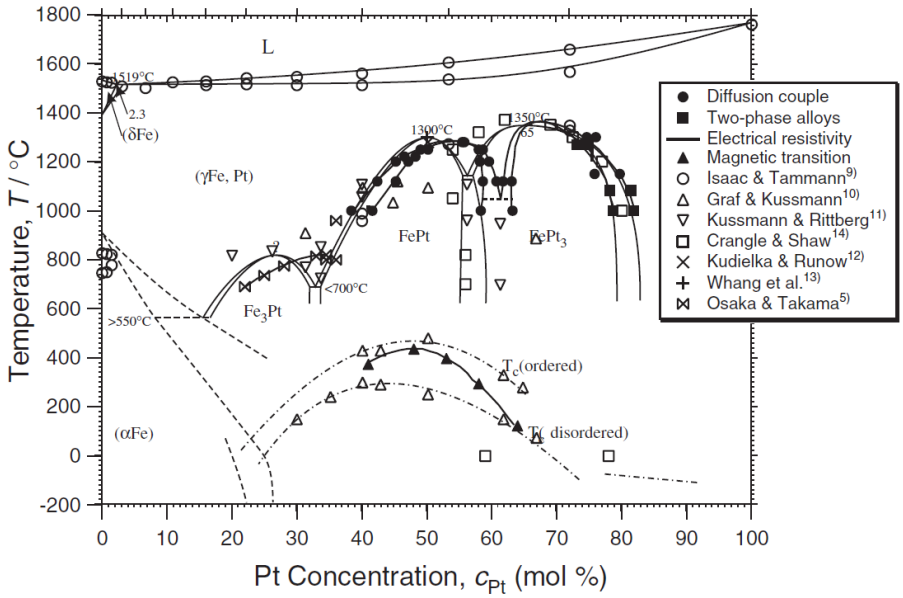

Figure 1.3: Fe-Pt binary alloy phase diagram taken from ref. [40].

The magnetic anisotropy depends on the order [46], and therefore it is essential to establish a preparation procedure that leads to high degree of chemical order. Molecular beam epitaxy (MBE) coevaporation of Fe and Pt on a Pt(15 nm)/MgO(001) substrate held at about 820 K is reported to give an order parameter[7] of $S = 0.9 \pm 0.1$ [47]. The alternate Fe and Pt monoatomic layer deposition [48] reduces the required temperature to achieve order ($S = 0.8 \pm 0.1$ for $T_{\text{growth}} = 503\,\text{K}$). The lattice mismatch also influences the chemical ordering of this alloy. As reported by Ding et al. [49] a maximum order is obtained for FePt(20 nm)/$Cr_{95}Mo_5$(30 nm)/MgO(001), with 6.33% mismatch

[6]The primitive in-plane lattice parameter is reported in [39] as $a = 2.7235 \pm 0.0010\,\text{Å}$ and is multiplied by $\sqrt{2}$ to give the *fct* parameter (error bars are omitted), which is easier to compare with other data and coherent with our c/a definition. It is worth noting that the crystal structure of $L1_0$ FePt, in Pearson Symbol Code, is $tP2$ [40] rather than $tP4$ reported by [41]. All the lattice parameters given here are at room temperature.

[7]See equations 2.21 and 2.22 to a definition of the order parameter.

and $c/a = 0.9466$. Beyond the influence of chemical order on the anisotropy of FePt, it has been recently proposed [50] that a variation of the tetragonal c/a ratio can change the magnetic properties of this alloy. After this density functional theory (DFT) study, even an antiferromagnetic arrangement could exist for a $c/a < 0.948$.

In this thesis we study the epitaxial growth of FePt on monocrystalline Pt(001) (sections 3.1.5 and 5.2). Besides the study of order, directly related to the anisotropy strength, we are also interested in the influence of the tetragonality on the FePt magnetic properties. We investigate the structural aspects of films obtained by two distinct methods. The first is based on He et al. [51] approach, where these authors have reported that for low Fe coverages on Pt(100), atomic exchange takes place and Fe is buried under a Pt top layer, even at room temperature (RT). For thickness between 2 to 5 MLs, annealing up to 600 K results in the formation of ordered FePt alloys presenting perpendicular magnetic anisotropy. The second one is the alternate monoatomic layer deposition [48].

1.3.3 MnPt

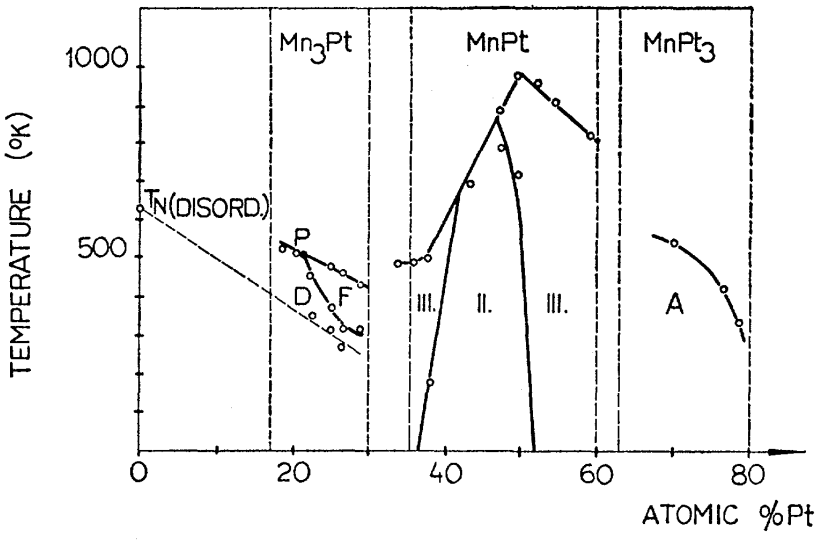

Figure 1.4: Magnetic phase diagram of the Mn-Pt binary alloy taken from reference [52]. Region II corresponds to the $L1_0$ structure with Mn magnetic moments along the c-axis while region III presents the same structure but with the Mn moments perpendicular to the c-axis.

We emphasize here some key aspects to understand the exchange coupling in systems based on the MnPt alloy. Bulk MnPt in the tetragonal $L1_0$ chemically ordered phase is an antiferromagnet with a high ordering temperature ($T_N = 975$ K). Its bulk lattice parameters are [41] $a_{MnPt} = 4.002\,\text{Å}$ *and* $c_{MnPt} = 3.665\,\text{Å}$. Along the plane perpendicular to the c-axis (the c-plane) Mn nearest-neighbors are antiferromagnetically coupled (fig. 1.5). Two configurations are possible depending on the stoichiometry and temperature, as shown in the magnetic phase diagram [52] in figure 1.4. At RT it is generally accepted that the equiatomic alloy has the Mn magnetic moments aligned with the c-axis (region II in fig. 1.4), as described by the schema of figure 1.5-a (type-A). Along the c-axis, the spins are ferromagnetically aligned. For off-stoichiometric

alloys the Mn spins may lie in the c-plane (region III in fig. 1.4), with a configuration as sketched in figure 1.5-b (type-B). In this case, however, it is not determined what is the preferential direction of the spins within this plane. It has been shown by Hama et al. [53] for a bulk crystal, that a spin-flip transition takes place from the type-A to the type-B between 580 and 770 K. This thermal induced transition goes along with an increase in the tetragonality, when the c/a ratio drops from 0.914 at RT to 0.896 after the spin-flip transition. This result suggests that lower c/a favors type-B and higher c/a favors type-A. A recent DFT study [50] has indicated the same dependence on the tetragonality, however, according to these calculations, the minimum energy is attained for type-B, while type-A only is set up for $c/a \sim 0.95$. It is important to stress that, in the disordered *fcc* $A1$-phase, this alloy is mostly considered to be non-magnetic [54], although some calculations suggest that a 3Q or 2Q antiferromagnetic structure with T_N below RT could take place [55].

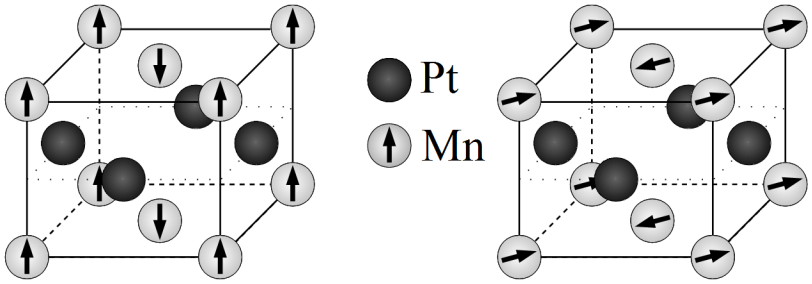

(a) type-A (b) type-B

Figure 1.5: Sketch of two possible magnetic configurations of the antiferromagnetic MnPt $L1_0$ alloy, with (a) spins aligned parallel to the c-axis and (b) spins along the c-plane.

For the preparation of exchange biased systems the robustness of the pinning depends on a large exchange coupling in the AFM/FM interface, a high T_N of the AFM and on a good resistance to corrosion. MnPt alloy in the $L1_0$ phase is one of the best AFM materials in this sense [37]. It has been used in the production of devices based on spin valves and tunnel junctions with in-plane anisotropy [56]. In future sensors, the total spin valve thickness must significantly decrease and the AFM layer would be by far the thickest one in the device. However, high exchange bias and thermal stability are difficult to maintain when reducing the thickness. The exchange coupling in MnPt/FM bilayers is strongly reduced below 20 to 30 nm and vanishes, at RT, when the MnPt layer is thinner than 6 to 10 nm [57, 58, 59, 60]. Among the possible factors that can influence this critical thickness (thermal instability [57, 58, 61], finite-size scaling of T_N [62], proximity effect [63]) the degree of chemical order seems to be the key issue for MnPt films [59, 60]. In the ultra-thin regime (< 10 nm) it is hard to produce well ordered films by the procedures followed so far. Without order, the film is not AFM at RT and so, there is no exchange bias. With few exceptions, all experimental studies were performed on films grown by sputtering and with different degrees of texture and chemical order.

Two studies of MBE growth of MnPt alloys on a Pt buffer deposited on MgO(001) have been reported for films thicker than 10-15 nm [64, 65]. In both cases, the MnPt layer is composed of two types of partially ordered structural domains whose c-axis are perpendicular to each other in the surface plane. A MBE MnPt layer grown on a Si(001) substrate covered by a thick Ag/Pt buffer was shown to give some degree of $L1_0$ order with the c-axis perpendicular to the surface plane [66]. Although this film presents huge roughness (>100 nm !) and small exchange bias field when coupled with NiFe (planar magnetic anisotropy) for thickness $\geqq$ 10 nm, the increase in H_C persists down to thickness of 3 nm. The use of MnPt alloy on perpendicular exchange bias systems [27] has not yet been reported, however it seems a promising candidate if one is capable to produce high quality $L1_0$ films with perpendicular c-axis and couple them with a FM layer with out-of-plane anisotropy. This is one of the main issues of this thesis. We will come back to the study of MnPt in the ultra-thin limit in section 4.1.2.

1.3.4 CoO/Fe/Ag(001) bilayer

The CoO/Fe bilayer is a widely studied exchange bias system. Bulk CoO has the prototypical rock-salt structure above T_N: pure Co and O planes alternate along the [111] direction of the *fcc* lattice. Below the Néel temperature ($T_N \approx 289\,K$), CoO becomes a type-II AFM. Following the [100] direction of the *fcc* lattice, the Co spins (separated by oxygen) are coupled antiparallel. Furthermore, the Co spins are coupled ferromagnetically within the {111} planes; neighboring planes are then coupled antiferromagnetically. Accompanying the paramagnetic-antiferromagnetic transition, CoO also undergoes a crystallographic phase change from cubic to monoclinic lattice.

Strain-induced spin orientation has been shown to be a critical issue: the magnitude and orientation of the magnetic moments strongly depend on the strain induced by the substrate [67, 68]. The coupling between Fe and Co spins at the interface is a warm subject [68, 69]. The direction of the anisotropy, either in the FM or in the AFM layers, and the morphology at the interface are among the fundamental parameters determining the exchange coupling. Moreover, the role of the Fe oxide layer formed at the interface is rarely characterized or even mentioned, but is not always negligible.

As concerns the FM Fe layer, ultra-thin Fe/Ag(001) films exhibit a strongly enhanced magneto-crystalline anisotropy with an easy axis perpendicular to the surface plane. This perpendicular anisotropy persists up to about 6 monolayers at room temperature, then a spin reorientation transition (SRT) takes place with the easy axis in the film plane [70, 7]. Epitaxial Fe/Ag(001) films have been extensively studied, but accurate determinations of the structural parameters in the ultra-thin regime (< 6 ML) are scarce. Only a few authors have properly addressed the epitaxy and highlighted the importance of the substrate quality, deposition rate and temperature and annealing procedures for ultra-thin films. The influence of these parameters might explain many contradictory results reported in literature.

Within the scope of this thesis, we intended to shed some light on the interaction between the AFM and FM layers at an Fe/CoO interface of a well-characterized sample grown under well-controlled UHV conditions. We coupled several advanced experimen-

tal techniques (*in situ* and *ex situ* MOKE, *in situ* GIXRD, reflectivity and polarized XAS) probing structural organization, morphology and magnetism.

1.4 Surface physics concepts

From the above exposed, we see that there is an intrinsic dependence of the magnetic properties on the specific structure of the systems studied. When coming into the thin film regime, parameters like roughness, inter-diffusion and mixing of ordered and disordered phases add new degrees of complexity. The elaboration of well characterized samples with sharp surface/interfaces is a required stage for the understanding of the exchange coupling mechanism [71]. A fundamental study of the growth mechanisms of the various metal on metal systems is an important step toward the control of the structure, especially in the case of ordered alloys. Growth on atomically flat monocrystalline surfaces is foreseen to produce such model-systems.

Preparing high quality, atomically controlled ultra-thin films requires special experimental environments. Ultra-high vacuum (UHV) conditions, i.e. pressures in the range of 10^{-9} to 10^{-11} mbar, is one of the most restrictive. The influence of the residual gas in the vacuum chamber and the impurities on the substrate can alter the structure of an ultra-thin film: physical defects at the surface can act as nucleation sites for adsorbates and perturb homogeneous growth. A substrate cleaned in UHV can maintain its cleanliness for a longer time without contamination from impurities. Another aspect is that even under vacuum, evaporated atoms may meet other species at a given distance (known as the mean free path) while traveling from the evaporator to the substrate. Because the mean free path is inversely proportional to the pressure, UHV is needed to maintain a slow and stable deposition rate for building up a structure with atomic scale control. The use of UHV conditions, together with a collection of techniques and methods used in surface physics laboratories to achieve an atomic scale control of surfaces, interfaces and films structures, makes up what is called here the "surface physics approach" to study magnetic ultra-thin films. Indeed, in a more general picture the techniques of surface science, going from UHV to electrochemical environments, go far beyond this. The surface science is a vast branch of knowledge, that gets renewed importance with the emphasis given today to miniaturization of devices and to new physical phenomena unrevealed in the nanometric scale. The fundamental concepts of the physics of surfaces and interfaces are subject of a vast literature, of which we refer mainly to two recent textbooks, one in English by Ibach [72] and the other in French by Andrieu and Muller [73]. Here we address briefly a few important notions on surface physics that are valuable to the problem we are facing.

In a simplified picture, the surface of a crystal can be seen as a truncation of the bulk infinitely periodic structure along a defined direction, perpendicular to the surface. The energy necessary to create such a surface, by cleaving of the bulk for example, corresponds roughly to the energy of the bonds between atomic planes that are broken in the process. The surface energy density[8] γ, expressed in Jm^{-2}, is particular for each

[8] To be precise, γ defines the work necessary to create a surface. In the system we are dealing with, this corresponds to the surface free energy density (f^{Surf}), so that we call it simply surface energy

material and is anisotropic, depending on the crystallographic orientation of the surface. Surface atoms have a lower coordination than their counterparts in the bulk and in many cases the bare surface keeps the same in-plane bulk symmetry but relax the atomic distances perpendicular to surface, so as to minimize energy towards thermodynamic equilibrium. However, in a few metals the positions of the atoms in the surface layer rearrange dramatically to compensate this lower coordination and minimize energy. The surfaces where the atomic arrangement is different from that which would result from a simple truncation of the bulk structure are said to be reconstructed. Generally, the rearrangement involved in such reconstructions tend to produce a more densely packed surface layer. That is the case of some $5d$-transition metals surfaces [74], like the quasi-hexagonal reconstruction of Pt(001), the first experimentally observed reconstruction on a clean metallic surface [75]. This reconstruction is explored in details in section 3.1.1.

The study of metal-on-metal growth on single crystal surfaces, although close to an idealized situation, is far from being straightforward [76]. At the temperatures where growth experiments are typically carried out, the rates for many atomic scale processes on the surface, such as adsorption, surface diffusion, chemical bonding, atom exchange, among others, are too low for global thermodynamic equilibrium to be established. The film production usually proceeds through nucleation and growth stages and the resulting morphology is dominated by the effects of kinetic limitations and does not represent thermodynamic equilibrium. The richness of attainable structures is therefore immense. Depending on temperature or deposition rate different processes are allowed, in a complex hierarchy of (quasi-)equilibria. There are three basic modes of crystal growth in the absence of surface defects and inter-diffusion: the island, the layer-by-layer and the layer plus island modes. However, more complex growth modes, such as one-dimensional monoatomic wire growth [77] or self organized clusters [78], can be achieved by using anisotropic or patterned substrates. In the island, or Volmer-Weber mode, small clusters are nucleated directly on the substrate surface and then grow into 3D-islands. The layer-by-layer, or Frank-van der Merwe mode, displays the opposite characteristics and, ideally, one monolayer[9] is completed before the next one begins to grow. The layer plus island, or Stranski-Krastanov, growth mode is an intermediate case. After forming the first ML, or a few MLs, subsequent layer-by-layer growth is unfavorable and islands are formed on top of this "intermediate" layer.

Heteroepitaxial growth can be pseudomorphic, also called coherent epitaxy, which means that the layer grows with an in-plane lattice constant that matches the substrate one. The misfit between the natural lattice constants of the deposited film a_f and the substrate a_s gives rise to a surface strain of magnitude

$$\varepsilon_{\mathrm{mf}} = \frac{a_f - a_s}{a_s}. \tag{1.10}$$

density. This is not always the case and generally one has, $\gamma = f^{Surf} - \sum_i \mu_i \Gamma_i^{Surf}$, where μ_i is the chemical potential of component i and Γ_i^{Surf} is the excess density of the component i at the surface. For a single crystal in vacuum ($i = 1$), we can choose the Gibbs surface so that $\Gamma^{Surf} = 0$.

[9] One monolayer is defined as the number of atoms in a substrate atomic plane parallel to the surface, which means 1.3×10^{15} atoms/cm^2 and 1.2×10^{15} atoms/cm^2 for Pt(100) and Ag(100) surfaces, respectively.

Assuming isotropic strain and deposited film elastic properties, the elastic energy per area carried by the film is given by [72]

$$\widetilde{s} = \frac{t}{2}\frac{Y}{1-\nu}\varepsilon_{\mathrm{mf}}^2 + \Delta s^{(s)}\varepsilon_{\mathrm{mf}} \tag{1.11}$$

where Y is the *Young modulus* of the film, ν the *Poisson ratio* (generally close to 0.3) and t its thickness. The change in the surface stress $\Delta s^{(s)}$ is the total change in the surface stress due to film deposition. Note that the elastic energy scales linearly with the film thickness, so that relaxation is expected after some critical thickness t_c. The film can relax for instance by the formation of dislocations or by growth of 3D-clusters giving a layer-plus-island mode.

Chapter 2

Experimental techniques

Surface preparation and characterization techniques are intrinsically based on the interaction of photons, electrons and ions with matter. When these particles interact with matter many different processes are observed. As a general rule, these processes are largely dependent on the energy scale involved in the interaction.

The very limited penetration depth of electrons into the material makes the Auger electron spectroscopy (AES) and the low-energy electron diffraction (LEED) techniques very sensitive to surfaces. Charged ions, usually Ar accelerated at quite large energies, are employed to clean surfaces by sputtering. High energy X-ray photons interact weakly with matter and may penetrate a few hundreds of micrometers into the material. The surface sensitivity with X-rays comes from a particular geometry where the angle of incidence is close to the so called critical angle for total reflectivity (θ_c). At this particular geometry the penetration depth is reduced to some dozens of nanometer, improving the surface sensitivity in X-ray diffraction measurements. Many processes may occur after the photon-matter interaction and we are particularly interested in the elastic scattering and in the absorption followed by inelastic emission. In this chapter, we discuss the main techniques used.

2.1 Surface preparation and analysis

To prepare clean and flat single crystal surfaces, noble gas ion sputtering followed by annealing is the standard procedure used. Bombardment with low energy Ar+ ions removes superficial atom layers through a knock-off process, where collisions of the ions with surface atoms remove surface atoms by linear momentum transfer. In our experiments standard ion guns were used with typical working conditions of: energy = 800 eV, current = 10 μA and $P_{Ar} = 10^{-6}$ mbar. The ion sputtering is routinely used to remove deposited films from the surface. A side effect of the sputtering is that it disorders the substrate surface. An annealing step is required to flatten the surface. The details of surface preparation, like the annealing temperature, vary with the substrate and will be presented for each case studied.

Our films are prepared by the molecular beam epitaxy technique, also called thermal deposition, where thermally evaporated atoms are deposited onto the substrate from an effusion cell. A standard resistive effusion cell (Knudsen cell) is used for Mn depo-

sition. Fe, Co and Pt are deposited from electron-beam heating sources. In our case the growth rate was typically a few minutes per ML. In UHV pressures (10^{-10} mbar), metals usually evaporates directly from the solid phase (sublimation). A special case is Pt, which evaporates very close to the melting point (2040 K). At a temperature of 2020 K the vapor pressure is of 10^{-4} mbar. The typical evaporation rate from a Pt rod is of 30 min/ ML. This slow deposition rate should favor the growth in thermodynamical equilibrium conditions, resulting in one of the three typical situations described previously: Frank-van der Merve (layer-by-layer), Volmer-Weber and Stransky-Kranstanov, but indeed the growth at room temperature can be controlled by the kinetics. In the case of Pt on Pt(111) homoepitaxy, it is well known that room temperature growth results in quite a rough surface, while almost ideal layer-by-layer growth is obtained at high temperature [79].

To control the thickness in the ML level two methods are employed. In the first, the evaporation rate is calibrated with a quartz crystal micro-balance positioned at the place of the sample, where the amount of material deposited is quantified from the corresponding shift on the quartz oscillation frequency. In the case of layer-by-layer growth, periodic oscillations of the scattered X-ray intensity are observed at a well defined reciprocal space position [80], which are directly related to the growth rate.

Auger electron spectroscopy, is routinely used for surface chemical analysis, with 3 keV primary electron beam. In this technique the secondary electrons emitted after the interaction of the primary beam with the sample surface are collected and analyzed in energy, so as to distinguish the Auger electrons. The primary beam ejects electrons from core energy levels of the atoms close to the surface. In the Auger process after the core hole is filled by an outer shell electron, the transition energy is transferred to a second electron, the Auger electron, which is emitted from the atom with a kinetic energy dependent on the particular electronic transition that originates it (and on its own binding energy). Since energy levels (and transition energies) are specific to each atomic element, an analysis of the kinetic energy of emitted electrons can yield information on the chemical composition of the surface. The surface sensitivity is a consequence of the small electron mean free path ($\sim$ 1 nm) for the typical Auger electron energies. AES is used both to check the substrate cleanliness and to compare the relative composition of the different deposits.

In preliminary experiments of the growth process investigations (chapter 3) we use low energy electron diffraction and scanning tunneling microscopy (STM) to obtain the size and symmetry of the surface unit cell and to have clues on the degree of order and surface morphology. The electron diffraction is a direct consequence of the wave nature of electrons. In LEED a normal incidence electron beam with energies on the 20 to 500 eV range is elastically backscattered by the crystal surface atoms and generates a diffraction pattern corresponding to the surface reciprocal lattice. As in AES, the surface sensitivity comes from the small electron mean free path. The STM is an instrument for imaging surfaces at an atomic level, based on the quantum tunnel effect. The tunneling current between an atomically sharp conducting tip and the surface of a (metallic) sample is a function of the tip position, the applied voltage and local density of states of the sample. Scanning the tip on the sample surface with subatomic precision

(obtained by piezoelectric motion stages) makes it possible to attain atomic resolution, since the tunnel current depends exponentially on the sample-to-tip distance. We have used the constant current mode for the STM studies presented here, where the tip is scanned over the surface at a fixed bias voltage while a feedback circuit regulates the vertical position of the tip in relation to features of the surface in such a way that the tunnel current is kept constant at some fixed (nA) value. During this procedure the vertical position of the tip is stored as a function of the lateral coordinates of the tip, yielding a STM image. Indeed, the STM image represents a complicated convolution of the electronic states of the tip and the sample, and is not a direct topographical image.

A more complete description of the above techniques may be found in surface physics books [72, 73] and references therein.

2.2 X-ray scattering and diffraction

When an electromagnetic wave interacts with matter many processes can be observed. For the materials studied here, we are mainly interested in the photon absorption and scattering in the X-ray range. The scattering process can be elastic or inelastic, coherent or incoherent. After a photon absorption we can observe emission of photons (fluorescence) or electrons (Auger effect) at specific energies. In this section we are mainly concerned with the elastic scattering and interference of monochromatic beams with wavelength λ comparable to the inter-atomic spacing, the X-ray diffraction (XRD). After an introduction about XRD, the surface sensitive technique of XRD in the grazing incidence geometry is discussed, followed by a brief description of the specular reflectivity technique (XRR). The objective is to provide the reader with some essential concepts needed to follow the arguments made in this thesis. First we recall a few concepts and definitions of kinematic diffraction theory that will set the basis for the understanding of GIXRD and XRR. All concepts collected here have been subject of detailed description in numerous textbooks, reviews and PhD thesis [81, 9, 82, 83, 84, 85].

2.2.1 Introduction to X-ray diffraction

To begin, we will briefly explain some basic terminology. Crystal structures are a repetitive arrangement of atoms along all three direction in space. These directions are defined by three lattice vectors $\mathbf{a}_1$, $\mathbf{a}_2$ and $\mathbf{a}_3$, whose modules give the lattice parameters along the three crystal axes. Reciprocal lattice base vectors $\mathbf{b}_1$, $\mathbf{b}_2$ and $\mathbf{b}_3$ are defined for the reciprocal space in such a way that

$$\mathbf{a}_j.\mathbf{b}_g = 2\pi\delta_{jg} \tag{2.1}$$

The vectors $\mathbf{k}_i$ and $\mathbf{k}_f$ denote respectively the incident and scattered beam wave vectors, and present the same modulus $\mathrm{k} = \frac{2\pi}{\lambda}$ (elastic scattering). The vector $\mathbf{q} = \mathbf{k}_f - \mathbf{k}_i$, called momentum transfer, may be written in terms of the reciprocal space vectors as

$$\mathbf{q} = h_1\mathbf{b}_1 + h_2\mathbf{b}_2 + h_3\mathbf{b}_3 \tag{2.2}$$

where the coefficients h_1, h_2 and h_3 are continuous. The angle formed between $\mathbf{k}_i$ and $\mathbf{k}_f$ is the scattering angle 2θ, so that we have $q = \frac{4\pi \sin\theta}{\lambda}$. The incident beam is considered as an unpolarized plane wave with electric field amplitude E_0 and intensity $I_0 = \frac{E_0^2 c}{8\pi}$. The scattered beam is evaluated at a distance R, far from the crystal.

To calculate the X-ray scattered intensity by a crystal, one simply add coherently all independent contributions coming from each individual electrons of all atoms in the crystal. For a given atom containing several electrons, the instantaneous value of the electric field of the scattered beam is given by

$$\epsilon_{atom} = \left(\frac{E_0 e^2}{mc^2 R}\right) e^{2\pi i\left[\nu t - \left(\frac{R}{\lambda}\right)\right]} f \tag{2.3}$$

where the atomic scattering factor f is the sum of the scattering of each individual electron. The pre-factor $r_e = \frac{e^2}{mc^2} \approx 3 \times 10^{-13}\,\text{cm}$ (cgs units) comes directly from the electromagnetic wave scattering by one electron in the dipole approximation (calculated in appendix B of reference [9]) and is known as the classic electron radius or Thomson scattering length. e and m are the electron charge and mass and c the speed of light. Such a small value of r_e evidences the weakness of the interaction between X-ray and crystal, which allows the use of the kinematic approximation[1]. In the treatment given here, we assume that the X-ray energy[2] (of wavelength λ and frequency ν) is always much larger than any of the absorption edges that can be excited in our material, so that only elastic scattering is taken into account. The electron distribution is considered to have spherical symmetry. With this assumptions, the atomic scattering factor of each atom n with Z electrons can be simply written as:

$$f_n = \sum_{j=1}^{Z} \int_0^\infty 4\pi r^2 \rho_j(r) \frac{\sin(qr)}{qr} dr \tag{2.4}$$

where r is the distance from the atom center and $\rho_j(r)$ is the charge density of electron j (supposed isotropic).

The atomic scattering factor is the amplitude of the unmodified[3] scattering per atom expressed in electron units (amplitude of a single electron scattering according to classical theory). For small values of q it approaches Z, the number of electrons in the atom.

To discuss the X-ray intensity diffracted by a crystal, we suppose that the crystal is small enough, so that one can neglect absorption and extinction effects. The amount of scattered intensity is a negligible fraction of the incident beam intensity so that each crystal atom is subjected to the same incident amplitude. For simplicity we consider a small crystal with a parallelepiped shape and edges equal to $N_1 a_1$, $N_2 a_2$, $N_3 a_3$ parallel to the crystal axes $\mathbf{a}_1$, $\mathbf{a}_2$ and $\mathbf{a}_3$. This restriction imposes in fact a finite scattering

[1] The kinematic approximation assumes that the scattered beam is not scattered a second or third time before leaving the crystal.

[2] The numerical relation between wavelength λ in Å and photon energy $\mathcal{E}$ in keV is $\lambda[\text{Å}] = \frac{hc}{\mathcal{E}} = \frac{12.398}{\mathcal{E}[\text{keV}]}$.

[3] No absorption or anisotropy effects.

volume δV, the shape not being crucial. The position of the atom of type n in the unit cell with coordinates (m_1, m_2, m_3) is expressed by $R_m^n = m_1\mathbf{a}_1 + m_2\mathbf{a}_2 + m_3\mathbf{a}_3 + \mathbf{r}_n$.

The instantaneous value of the electric field of the scattered beam far from the small crystal can be expressed by (chap. 3 of [81]) :

$$\epsilon_{crystal} = \left(\frac{E_0 e^2}{mc^2 R}\right) e^{(2\pi i)[\nu t - (R/\lambda)]} \sum_n f_n e^{i\mathbf{q}.\mathbf{r}_n} \prod_{j=0}^{3} \left(\sum_{m_j=0}^{N_j-1} e^{i\mathbf{q}.m_j\mathbf{a}_j}\right) \tag{2.5}$$

where the product on j accounts for the three directions in space. The summation over n involves the atomic positions $\mathbf{r}_n$ of the different atoms in the unit cell and depends not only on the atomic scattering of each atom but also on the particular structural arrangement. This term denoted by F_u is called the unit cell structure factor:

$$F_u = \sum_n f_n e^{i\mathbf{q}.\mathbf{r}_n} \tag{2.6}$$

The structure factor plays an important role in X-ray scattering because it contains all information concerning atomic positions. It represents nothing else than the Fourier transform of the electron density inside the unit cell.

Each of the sum over m_j, that accounts for all unit cells of the crystal with edges $N_j a_j$, may be expressed by :

$$s_j(\mathbf{q}.\mathbf{a}_j) = \sum_{m_j=0}^{N_j-1} e^{i\mathbf{q}.m_j\mathbf{a}_j} = \frac{e^{i\mathbf{q}.N_j\mathbf{a}_j} - 1}{e^{i\mathbf{q}.\mathbf{a}_j} - 1} \tag{2.7}$$

The intensity of the scattered beam, given by $I = \frac{c}{8\pi}\epsilon.\epsilon^*$, can be written, observing equations 2.1 and 2.2, as

$$I = I_e F F^* \prod_{j=0}^{3} \left(\frac{\sin^2(\pi h_j.N_j)}{\sin^2(\pi h_j)}\right) \tag{2.8}$$

with

$$I_e = I_0 \frac{e^4}{m^2 c^4 R^2} \left(\frac{1 + \cos^2 2\theta}{2}\right)$$

The term in brackets is the polarization factor for the unpolarized plane wave considered.

One can see that for reasonably large values of N_j the intensity I is negligible for all values of the continuous variables $h_1,\ h_2$ and h_3, except when they are very close to integers. When one has $h_1 = h,\ h_2 = k,\ h_3 = l$, with integer $h,\ k$ and l, the many atoms in the crystal scatter in phase, and we have a maximum of intensity. The function

$$|s(x)|^2 = \frac{\sin^2(N_j x)}{\sin^2 x} \tag{2.9}$$

has as maximum values N_j^2, so that the intensity maximum is given by

$$I = I_e F_u F_u^* N_1^2 N_2^2 N_3^2 \tag{2.10}$$

The resulting intensity distribution is then a series of δ-functions at each $\mathbf{H}_{hkl} = h\mathbf{b}_1 + k\mathbf{b}_2 + l\mathbf{b}_3$ position of the reciprocal space, with maximum value I. This conditions are know as Laue conditions and are equivalent to the Bragg's law, $\lambda = 2d_{hkl}\sin\theta$, where d_{hkl} is the distance between the particular scattering atomic planes. In a similar statement one can say that when the momentum transfer $\mathbf{q}$ (eq. 2.2) is equal to a reciprocal lattice vector $\mathbf{H}_{hkl} = h\mathbf{b}_1 + k\mathbf{b}_2 + l\mathbf{b}_3$, a Bragg peak is observed. The modulus of the reciprocal lattice vector is related to the atomic planes distance by $|\mathbf{H}_{hkl}| = \frac{2\pi}{d_{hkl}}$ and the integers hkl are known as the Miller index.

The unit cell structure factor for a given hkl reflection can be expressed as :

$$F_u^{hkl} = \sum_n f_n e^{2\pi i(hx_n + ky_n + lz_n)} \tag{2.11}$$

where x_n, y_n and z_n are numbers between 0 and 1 representing the coordinates of each unit cell atom n in lattice parameter units, i.e.

$$\mathbf{r}_n = x_n\mathbf{a}_1 + y_n\mathbf{a}_2 + z_n\mathbf{a}_3. \tag{2.12}$$

The atom positions R_m^n given above represent only average positions about which atoms may deviate from or oscillate due to thermal effects or disorder. It can be shown that the deviations from the ideal positions introduce a decrease in the scattered intensity that may be taken into account by replacing F_u by :

$$F_u^{'} = \sum_n f_n e^{-M_n} e^{2\pi i(hx_n + ky_n + lz_n)} \tag{2.13}$$

where $M_n = B_n(\sin\theta/\lambda)^2 = B_n\frac{q^2}{(4\pi)^2}$ may be different for different atoms. B_n, called Debye-Waller parameter, does not depend on q, while e^{-M_n}, the Debye-Waller factor, decreases for higher momentum transfer.

The peaks represented by the function $s(x) = \frac{\sin^2(Nx)}{\sin^2 x}$ in eq. 2.8 have a finite width proportional to $1/N$, so that there is an appreciable intensity in the diffracted beam at values of $\mathbf{q}$ which differ slightly from $\mathbf{H}_{hkl}$. The maximum intensity measured, proportional to N^2, would depend on the precise alignment of the primary beam, on its divergence and on small deviations of the angle of incidence due to some mosaicity in the crystal. A better suited measurable quantity is the integrated intensity.

In order to measure integrated intensities, the crystal is rotated continuously around the Bragg angle θ at a constant angular velocity ω about an axis parallel to the planes hkl and normal to the primary beam. The rotation is such that it covers the whole angular range that gives any contribution to the reflection. The detector slit is set so wide that all the diffracted radiation from the reflection hkl is recorded. With such an experimental procedure, one measures the total diffracted energy rather than intensities, and due to the rotation of the crystal, all small crystallites with some degree of misorientation will participate to the total diffracted energy at some time of the rotation.

The total diffracted energy when a small single crystal is rotated at velocity ω through a Bragg angle turns out to be :

$$E = \frac{I_0}{\omega}\left(\frac{e^4}{m^2c^4}\right)\frac{\lambda^3 \delta V F_u' F_u'^*}{v_a^2}\left(\frac{1+\cos^2 2\theta}{2\,\sin 2\theta}\right) \tag{2.14}$$

where the factor $\left(\frac{1+\cos^2 2\theta}{2\,\sin 2\theta}\right)$ is the Lorentz-polarization factor for a single crystal and an unpolarized primary beam, and $v_a = \mathbf{a}_1 \cdot (\mathbf{a}_2 \times \mathbf{a}_3)$ is the unit cell volume. Notice that the total diffracted energy E scales with the volume δV of the small crystal.

2.3 Grazing incidence X-ray diffraction

The potential of X-rays to provide valuable information about surfaces was first demonstrated by pioneering experiment by Eisenberger and Marra in 1980 [86]. Since then, with the increasing accessibility of third-generation synchrotron facilities, a new branch of X-ray crystallography was developed: the surface X-ray diffraction or grazing incidence X-ray diffraction. Unlike electron diffraction, where multiple scattering has to be taken into account, the low X-ray scattering cross section allows the diffracted intensity to be interpreted within the kinematic theory.

In a qualitative manner, we can use Fourier transforms to develop some ideas about the diffraction by a crystal surface. The diffraction pattern of a given crystal structure is proportional to the square modulus of the Fourier transform of its electron density distribution. The convolution theorem states that the Fourier transform of the product of two functions g and h is equal to the convolution of the Fourier transforms of the individual functions ($\mathcal{F}(g \cdot h) = \mathcal{F}(g) \otimes \mathcal{F}(h)$). For an infinite crystal, modeled by an infinite lattice of δ-functions (the real space Bravais lattice) multiplied by the atomic electron density $\rho(r)$ (or the unit cell electron density), the Fourier transform corresponds to another infinite lattice of δ-functions (the reciprocal space Bravais lattice) convoluted with the atomic scattering factor f (or structure factor F for a lattice with a basis). In the case of a crystal with a surface, we can imagine a similar construction, but this time with a truncation in a direction z perpendicular to the surface, that we take into account by multiplying our crystal by a Heaviside step function $H(z)$. The structure of the crystal is no longer infinitely periodic, as the surface breaks the symmetry in the z direction. The Fourier transform along this direction cannot be discrete any longer, and hence its diffraction pattern must be continuous. Through the convolution theorem we have the result shown in figure 2.1.

The Fourier transform of $H(z)$ is $\frac{1}{q_3}$, which gives a $\frac{1}{(\Delta q_3)^2}$ dependence for the intensity near each of the Bragg points. This smearing of the scattering intensity perpendicular to the surface, that overlaps between Bragg peaks to form continuous rods[4], gives rise to the so-called crystal truncation rods (CTRs)[88].

The origin of the CTR can also be seen by introducing a small damping or absorption term e^{γ} for each unit cell layer and calculating the diffraction coming from the semi-infinite crystal inside $z \leq 0$. In the z-direction, equation 2.7 gives rise to

[4]For low index surfaces, at least. If the surface have a large miscut the rods do not connect Bragg peak, as they are always perpendicular to the surface [87].

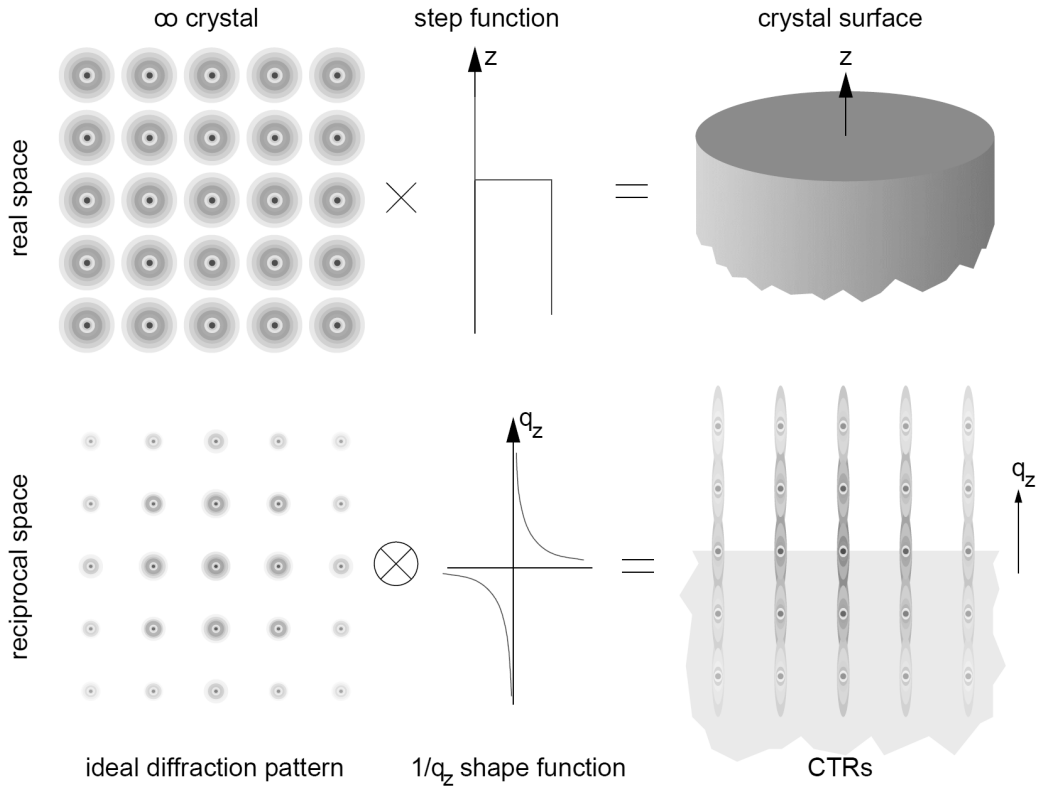

Figure 2.1: Origin of crystal truncation rods, explained qualitatively by the convolution theorem (taken from ref. [85]).

$$F_{\mathrm{CTR}}(\mathbf{q}.\mathbf{a}_3) = \sum_{m_3=-\infty}^{0} e^{(i\mathbf{q}.\mathbf{a}_3-\gamma)m_3} = \frac{1}{1-e^{i\mathbf{q}.\mathbf{a}_3-\gamma}} \tag{2.15}$$

In the limit of γ tending to zero, the square modulus of F_{CTR} gives

$$|F_{\mathrm{CTR}}(q_3a_3)|^2 = \frac{1}{4\,\sin^2\left(\frac{1}{2}q_3a_3\right)}$$

and the CTR intensity dependence on the out-of-plane momentum transfer $\mathbf{q}_3$ is then,

$$I_{\mathrm{CTR}} = I_e F_u^{'} F_u^{'*} N_1^2 N_2^2 \frac{1}{4\,\sin^2\left(\frac{1}{2}q_3a_3\right)} \tag{2.16}$$

Nothing has changed about the intensity distribution along the $\mathbf{q}_1$ and $\mathbf{q}_2$ directions. It is still strongly peaked around the reciprocal lattice points with negligible intensity in between for reasonably large values of N_1 and N_2. In real surfaces, the presence of steps, for example, have the effect of broaden the in-plane CTR profile. The in-plane breadth $\Delta q_{\|}$ of the CTR is related to the correlation length L of the surface by [89]

$$L = \frac{1}{\Delta q_{\|}} \tag{2.17}$$

where $\Delta q_{\parallel}$ is estimated to be the full width at half maximum (FWHM) of a Lorentzian or a Gaussian or a pseudo-Voigt[5] line shape that best fits the measured profile.

The Fourier transform reasoning above gives the correct Δq_3 dependence close to the Bragg peaks. In the same way, if instead of an absolutely perfect and infinitely sharp truncation ($H(z)$) we consider a broader transition due to surface roughness, the CTR dependence will be steeper than $\frac{1}{(\Delta q_3)^2}$. For the simple β-model of statistical roughness proposed by Robinson [88], where the occupancy of the kind β^n, with $0 < \beta < 1$ and n the surface layer index, we have

$$I_{rough} = I_{\mathrm{CTR}} \frac{(1-\beta)^2}{1+\beta^2-2\beta\cos(q_3 a_3)} \tag{2.18}$$

Up to this point, our crystal surface is just a truncation of a bulk crystal. Now, if we allow atoms to relax in response to the low coordination number on the surface (section 1.4) or we consider an adlayer on top of the bulk crystal, the result would be very different from the idealized bold surface. Indeed, the purpose of GIXRD is exactly to determine these changes with regard to the known crystal structure of the substrate. This is done by comparing the experimental value of the integrated intensity at each hkl reflection with a calculated value. The essential quantity that can be obtained from the experiment and compared to simulations is the surface structure factor amplitude, called simply$|F_{hkl}|$. Here on, it is convenient to change the nomenclature from momentum transfer $\mathbf{q}$ to reciprocal lattice units, where the continuous coefficients are now labeled as h, k and l, following eq. 2.2.

In this thesis, all the $|F_{hkl}|$ calculations are done with the help of the ROD program[90, 91]. F_{hkl} is obtained by the interference of the bulk contribution, and a contribution of the surface unit cell where all atoms close to the surface whose position or chemical nature differ from that one of the bulk unit cell are included.

$$F_{hkl} = F_{Bulk} + F_{Surf}$$

$$F_{Bulk} = F_u^{hkl} \frac{1}{1-e^{2\pi i l-\gamma}} \tag{2.19}$$

$$F_{Surf} = \sum_{n}^{surf.cell} f_n e^{-M_n} e^{2\pi i(hx_n+ky_n+lz_n)}$$

The surface unit cell may contain an arbitrary number of atoms with variable interatomic distances and Debye-Waller factors, that are used as fitting parameters to reproduce a particular set of experimental data.

2.3.1 Integrated intensity in GIXRD

As discussed previously (eq. 2.14) the integrated intensity from an hkl reflection of a crystal is measured by setting the Bragg conditions and rocking the sample until

[5] A pseudo-Voigt function is a mixture of a Gaussian function and a Lorentzian function, with a fitted weight $0 < \eta < 1$ so that, $PV = \eta L + (1-\eta)G$.

the intensity falls down to the background level. In surface X-ray diffraction we are interested, for a given (hk) CTR, to collect the integrated intensity as function of the continuous variable l. The rocking scans are then performed to integrate the in-plane profile of the CTR at a particular value of l. In the integration procedure, a broad background coming from thermal diffuse scattering is subtracted and only the sharp contribution coming from the CTR is considered in the numerical integration procedure used[6]. Structure factor amplitudes $|F_{hkl}|$ are then extracted[7] by applying standard correction factors [92] for the z-axis diffractometer geometry of SUV station.

$$|F_{hkl}|^2 \propto \frac{I_{rocking}}{PL_{rocking}C_{area}C_{det}C_{beam}C_{rod}} \tag{2.20}$$

The polarization correction P takes into account the attenuation factor due to the angle between the incident and the scattered electric field. The Lorentz correction $L_{rocking}$ depends on the way the rod crosses the Ewald sphere during the rocking scan. The C_{area} normalize for the area of the surface participating to the diffracted signal. The CTR is integrated along l, and the measured intensity needs to be normalized by the integration interval, which depends on the width of the slits. This is the role of C_{rod}. Finally an important factor for the present work is C_{det}, which corrects for the in-plane acceptance of the detector. Rod shape can be so wide that only a portion is integrated by the detector either during a rocking scan or a scan in reciprocal space. This happens for example along rods which include short range order peaks. In this case the intensity across the rod is measured with a rocking scan and is fitted with a pseudo-Voigt line shape, which allows an evaluation of the overall scattered intensity at this l value of the rod.

2.3.2 GIXRD applied to ordered alloys

A quantitative study of the degree of order is of special importance for determining fundamental properties like the strength and orientation of the magnetic anisotropy. GIXRD allows the study of the growth and of the chemical order in a few nm-thick surface alloys. However, for such experiments a high brilliance synchrotron source is required, that is why the number of studies devoted to this subject is quite limited. Most order studies by GIXRD performed up to now are focused on the surface layers of bulk ordered binary alloys, especially with regards to the order-disorder phase transition [93, 94] and to segregation induced short-range order (SRO) [95, 96].

The study of ordered binary alloys by XRD is active since the first half of XX^{th} century. A good description of the basic concepts can be found in Warren's book [81]. Long-range order (LRO) occurs for several binary alloys (as CuAu, Cu_3Au, MnPt, FePt etc.) below a critical temperature. Above this temperature (or in quenched samples) one can still find some short-range order, which means that one atom can only locally influence the occupancy of its close-neighbors. We work below the ordering temperature of the alloys studied, so we are always concerned with LRO. A basic concept that is

[6]The measured intensity is always normalized by a monitor to take into account variations in the primary beam intensity.

[7]The ANA program [91] is used to integrate rocking scans and derive $|F_{hkl}|$ values.

worth defining here is the long-range order parameter (p. 209 of [81]). We will call the two kinds of atoms A and B and represent the two sites by α and β. For the ideal stoichiometry composition and perfect long-range order, the α-sites are all occupied by A-atoms and the β-sites are all occupied by B-atoms. We define $r_\alpha\,(r_\beta)$ as the fraction of $\alpha\,(\beta)$-sites occupied by the right atom type and $w_\alpha\,(w_\beta)$ as the fraction of $\alpha\,(\beta)$-sites occupied by the wrong atom. The long-range order parameter S is defined to be linearly proportional to $(r_\alpha + r_\beta)$, with $S = 0$ for a completely random arrangement and $S = 1$ if the composition is stoichiometry and $(r_\alpha = r_\beta = 1)$. Using these two conditions, one finds that :

$$S = r_\alpha + r_\beta - 1 = r_\alpha - w_\beta = r_\beta - w_\alpha \tag{2.21}$$

Let y_α and y_β be the fraction of α and β sites in the ordered structure $(y_\alpha + y_\beta = 1)$, and x_A and x_B the atom fraction in the sample $(x_A + x_B = 1)$. Then $y_\alpha r_\alpha + y_\beta w_\beta = x_A$ and $y_\alpha w_\alpha + y_\beta r_\beta = x_B$ and order parameter can be rewritten as:

$$S = (r_\alpha - x_A)\,/y_\beta = (r_\beta - x_B)\,/y_\alpha \tag{2.22}$$

Chemical order in alloys increases the primitive cell size and gives rise to superstructure reflections. For each Bravais lattice one can derive the conditions for allowed reflections based on the structure factor. We are particularly interested in the *fcc* lattice of Pt and Ag that will be discussed throughout this manuscript. We will also discuss the $L1_0$ chemically ordered *fct* structure.

In a *fcc* (or *fct*) lattice, for every atom with coordinates (x_n, y_n, z_n) (eq. 2.12), there are three identical atoms with coordinates $(x_n + \frac{1}{2},\, y_n + \frac{1}{2},\, z_n)$, $(x_n + \frac{1}{2},\, y_n,\, z_n + \frac{1}{2})$, $(x_n,\, y_n + \frac{1}{2},\, z_n + \frac{1}{2})$. The unit cell structure factor (eq. 2.11) can be expressed by a sum over these 4 identical atoms with atomic scattering factor *f*. Choosing (x_n, y_n, z_n) to be (0,0,0) in the unit cell reference frame:

$$F_u^{hkl} = f\left[1 + e^{\pi i(h+k)} + e^{\pi i(h+l)} + e^{\pi i(k+l)}\right] \tag{2.23}$$

One can readily see that the sum takes the value 4 if *hkl* are unmixed (all odd or all even) and the value zero if *hkl* are mixed:

hkl unmixed : $F_{hkl} = 4f$

hkl mixed : $F_{hkl} = 0$

So, the *fcc* structure is recognized by the fact that all mixed reflections are missing.

We will consider now the specific case of the $L1_0$ structure, which is the prototypical case for the MnPt and FePt discussed in this work. In this case we have two α and two β sites for unit cell: $\beta = 000,\ \frac{1}{2}\frac{1}{2}0,;\ \alpha = \frac{1}{2}0\frac{1}{2}, 0\frac{1}{2}\frac{1}{2}$. The structure factor becomes:

$$F_{\mathrm{L1_0}}^{hkl} = (r_\alpha f_A + w_\alpha f_B)\left[e^{\pi i(h+l)} + e^{\pi i(k+l)}\right] + (r_\beta f_B + w_\beta f_A)\left[1 + e^{\pi i(h+k)}\right] \tag{2.24}$$

We have three kinds of reflections:

hkl unmixed, $F_{\mathrm{L1_0}}^{hkl} = 4\,(x_B f_B + x_A f_A)$, Fundamental;

$h + k = even$ and $k + l = odd$, $F_{\mathrm{L1_0}}^{hkl} = 2\,S\,(f_B - f_A)$, Superstructure;

$h + k = odd$, $F^{hkl}_{\mathrm{L1_0}} = 0$.

In this manuscript, unless otherwise noted, the fcc (001) substrate structure is represented by the *surface unit cell* instead of the conventional cubic one. For a (001) surface these two unit cells are rotated one from the other by 45° about the surface normal (see fig. 2.2). The relations between the surface and cubic lattices are: $\mathbf{a}^1_S = \frac{\mathbf{a}^1_{fcc}+\mathbf{a}^2_{fcc}}{2}$; $\mathbf{a}^2_S = \frac{-\mathbf{a}^1_{fcc}+\mathbf{a}^2_{fcc}}{2}$; and $\mathbf{a}^3_S = \mathbf{a}^3_{fcc}$. In the reciprocal space, the relationship between the Miller indexes is given by:

$$h_{fcc} = h_S + k_S$$

$$k_{fcc} = -h_S + k_S \tag{2.25}$$

$$l_{fcc} = l_S$$

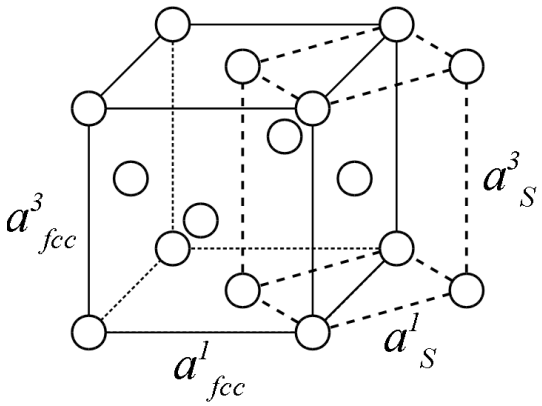

Figure 2.2: Surface and *fcc* unit cells.

Then, considering a pseudomorphic $\mathrm{L1_0}$ surface alloy with $\mathbf{c}$ parallel to $\mathbf{a}^3_{fcc}$, superstructure (order) peaks are observed along the (10) CTR at $l_S = 2n\frac{a_{fcc}}{c}$ (horizontal hatch-fig. 2.3), between bulk Bragg reflections, while the fundamental (structure) alloy peaks are close to the substrate Bragg reflections at $l_S = 2n + 1$ (solid circles-fig. 2.3), with n integer). The inverse situation in encountered along the (11) CTR, with LRO peaks at $l_S = (2n+1)\frac{a_{fcc}}{c}$ and substrate Bragg peaks at $l_S = 2n$. Pseudomorphic growth of the alloy with the c-axis parallel to $\mathbf{a}^1_{fcc}$ double the surface unit cell size and additional $(\frac{2n+1}{2}\,\frac{2m+1}{2})$ rods are observed. These are not CTR, once the diffracted intensity comes from the surface alloy only. On the (1/2 1/2) rod, peaks will be observed at $l_S = 2n\frac{a_{fcc}}{a_{fct}}$, while on the ($\bar{1}$/2 1/2) rod peaks will be observed at $l_S = (2n+1)\frac{a_{fcc}}{a_{fct}}$ (╱hatch-fig. 2.3). However, a symmetry equivalent domain rotated by 90° in-plane, i.e. with the c-axis parallel to $\mathbf{a}^2_{fcc}$, will be also observed (╲hatch-fig. 2.3). In the case of a non pseudomorphic alloy with in-plane c-axis, rods are observed at $(\frac{(2n+1)a_{fcc}}{2c}\ \frac{(2m+1)a_{fcc}}{2a_{fct}})$

When considering ultra-thin films, an important issue is the effect on the diffraction of anti-phase domains. Nucleation of ordered domains during the growth, which do not match each other, can occur resulting in anti-phase domain boundaries. Unlike bulk alloys, the domain size cannot be increased by long high temperature annealing to avoid

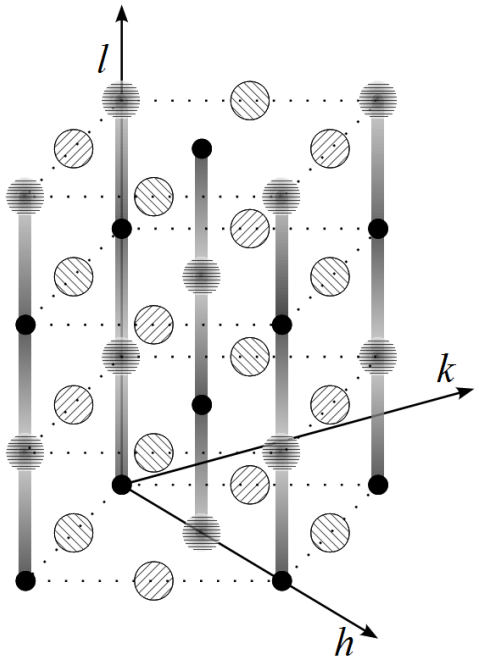

Figure 2.3: Reciprocal space representation of the structure (solid circles) and order (hatched circles) peaks from an $L1_0$ alloy. The hatch pattern indicates the orientation of the c-axis of the domain generating each peak, following the correspondence: $[1/2\,1/2\,0] \rightarrow (/)$; $[1/2\,\overline{1/2}\,0] \rightarrow (\backslash)$ and $[0\,0\,1] \rightarrow (—)$.

inter-diffusion with the substrate. It can be shown that anti-phase domains influence the peak intensity and shape, but not the integrated intensity [81]. For bulk materials and powders the order parameter can be obtained by comparing the integrated intensity of fundamental and superstructure peaks (with appropriate geometrical corrections) [97]. This approach is useful also for thin films where one can well distinguish the alloy diffraction peaks (order and structure) from the substrate ones [47, 98]. This is the case of many studies of ordered alloy thin films for high magnetic anisotropy purposes, where usual substrates are for instance, amorphous SiO_2, or metallic buffers on top of a single crystals like MgO or Saphire. The films are usually grown by sputtering and in some cases by MBE and frequently present an orientation texture with some degree of epitaxy with the underlying buffer. The approach we have chosen, growth on top of single crystalline clean metallic surfaces with lattice constants chosen to induce not only epitaxy, but also pseudomorphic growth, makes it impossible to follow this same method to obtain the order parameter S (an exception will be in this work PtMn/Ag(001)). Both the order and the structure peaks are superposed (and interfere) to the bulk CTR, and we cannot separate them to calculate the alloy structure factor and derive S in the same way. The elaboration of a method to evaluate properly the order parameter is a relevant part in this work and will be discussed in detail in chapters 4 and 5.

2.3.3 Experimental aspects

The *in situ* GIXRD experiments were performed at the European Synchrotron Radiation Facility (ESRF) BM32 beam line which belong to the french Collaborative Research Group on InterFaces (CRG-IF). The X-ray source is a bending magnet and the monochromator is a Si(111) double crystal, with the second crystal bent to give sagittal focusing on the sample. The vertical focusing is provided by a mirror positioned after the monochromator, resulting in a spot size of about $0.3 \times 0.3\,\mathrm{mm}^2$. The measurements were performed at photon energies between of 19 and 25 keV, with an energy resolution of about 2 eV. The Surface Under Vacuum (SUV) experimental station consists of an UHV chamber, mounted on a z-axis type diffractometer, which provides large angular ranges both for the incident and the emergent beams. Further degrees of freedom are available to align the sample normal parallel to the azimuthal rotation axis. The UHV chamber is equipped with several kind of pumps (ion pump, turbo pump, liquid nitrogen cooled titanium sublimation pump), a grazing reflection high energy electron diffraction (RHEED) gun, an Auger analyzer, and several evaporation sources which can be operated during RHEED, Auger and X-ray analysis. The sample is also prepared *in situ* by ion bombardment and annealing with an infrared pyrometer control. A full description is given in ref. [99]. The figure 2.4 shows a schema of the z-axis diffractometer (a) and a picture of the experimental setup (b).

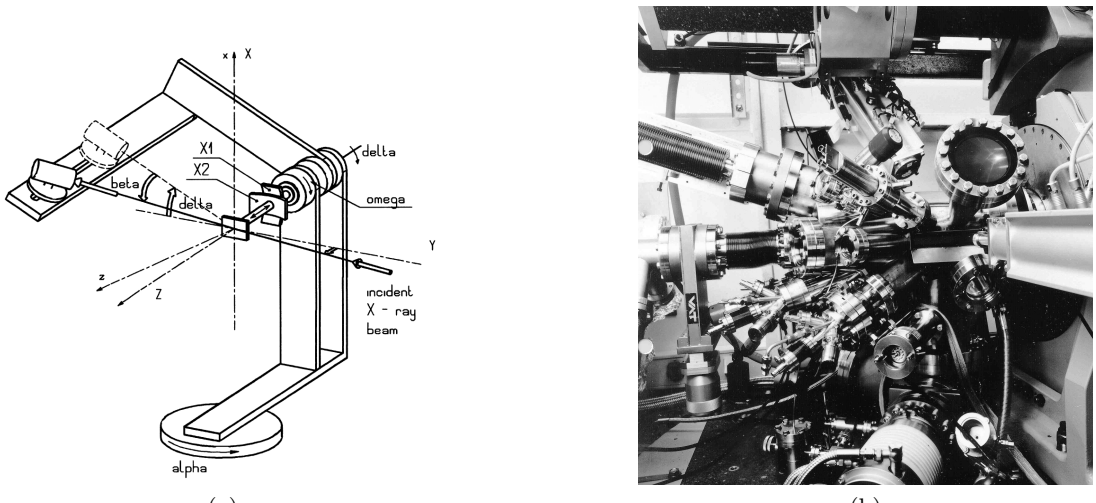

(a) (b)

Figure 2.4: (a) Schema of the z-axis diffractometer [99]. (b) Picture of the SUV experimental setup.

2.4 X-ray specular reflectivity

X-ray specular reflectivity [100, 9] is a technique widely employed to determine electron density, thickness and roughness of single layers and multilayers on flat substrates. This non-destructive technique can be applied to the study of surfaces and interfaces of thin layers at atomic resolution without any condition on the level of crystallinity. The XRR technique is based on the coplanar scattering of X-ray radiation around

reciprocal-lattice point (000). The scattered intensities are measured as a function of the scattering angle by keeping equal the incident and scattered angles of X-rays with respect to the sample surface normal (this is the specular condition) (fig.2.5-a). The XRR profile is the plot of the scattered X-ray intensity against the incidence angle or against the reciprocal-lattice vector **q**.

The refractive index in the X-ray energy range for a homogeneous medium can be written as

$$n = 1 - \delta - i\beta \quad , \tag{2.26}$$

with

$$\delta = (r_e\lambda^2/2\pi)\sum \rho_i(Z_i + f_i')/A_i \tag{2.27}$$

and

$$\beta = (r_e\lambda^2/2\pi)N_A\sum \rho_i f"_i/A_i \tag{2.28}$$

recalling that $r_e = \frac{e^2}{mc^2}$. ρ_i is the mass density of the i$^{\text{th}}$ element with atomic weight A_i and atomic number Z_i, f' and f" are the real and imaginary anomalous dispersion factors, respectively and summation is made on all atoms of the unit cell. At the interface air/surface the direction of the refractive beam can be obtained from Snell's Law as $cos\alpha_i = ncos\alpha'$. The grazing angle of incidence for which the angle of refraction α' becomes zero, known as the critical angle, can be written as $cos\theta_c = n_0$. In the small angle approximation the critical angle can be written as $\theta_c = (2\delta)^{1/2}$. The specular reflectivity, defined as ratio of scattered intensity over the incident intensity is equal to unity below θ_c.

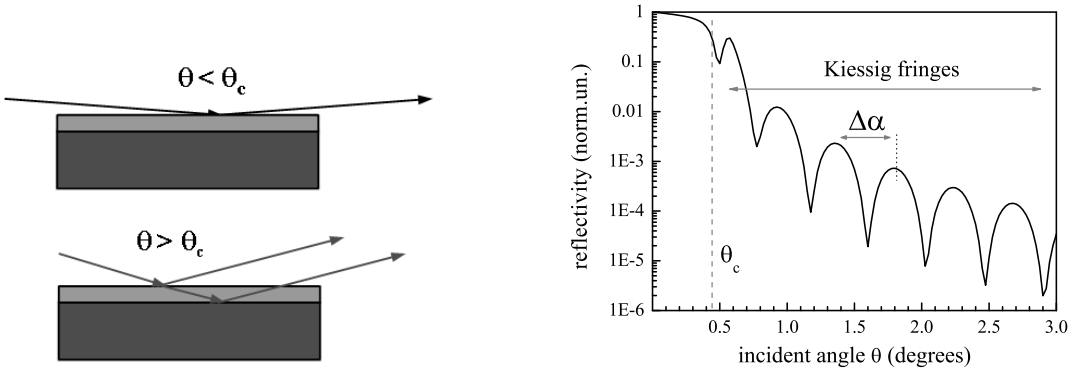

(a) (b)

Figure 2.5: (a) Scheme of X-ray reflectivity. (b) X-ray reflectivity profile as function of the incidence angle. The thickness oscillations are known as Kiessig fringes.

The full reflectivity profile can be calculated using the classical laws of optics for refraction and reflection at the interfaces. The amplitude of the reflected and transmitted waves are derived imposing boundary conditions to the waves and their derivatives (Fresnel formalism).

The interference of X-rays reflected from the interfaces, layers and multilayers on flat substrates, gives rise to oscillations or diffraction effects in the X-ray intensity as function of the angle of incidence (see fig. 2.5-b). These thickness oscillations are named

Kiessig fringes. Fringe amplitude depends on surface and interface roughness and the relative electron densities of the materials [101, 102]. Thicknesses of a single layer, bilayer or periodic multilayer can be evaluated through the so-called modified Bragg equation

$$m\lambda = 2t(n^2 - cos^2\theta_m)^{1/2} \tag{2.29}$$

where m is the diffraction order, t is the layer thickness (or multilayer period), n is the (mean) refractive index of the (multi)layer and m is the incidence angle for which the interference maximum of the order m occurs. Therefore, for simple systems, direct procedures allow extraction of the required information from the XRR profile without modeling and fitting. In particular, the film thickness, t, of a single layer sample can be directly evaluated by the angular positions of the m^{th} fringe maxima by the following equation, which holds in the small-angle regime:

$$t = \frac{\lambda}{2(\theta_m^2 - \theta_c^2)^{1/2}} m \tag{2.30}$$

with θ_c, critical angle of the layer material [100].When the layered structure is complex, these methods are not suitable and it is necessary to proceed through a modeling and fitting procedure. The simulations widely used are usually based on the Parratt recursive formalism of the Fresnel equations [103].

2.4.1 Experimental aspects

All XRR experiments presented in this thesis work were carried out with a Bruker D8 Discover diffractometer using a line focus from a Cu target X-ray tube. Göbel multilayer optics was used to select Cu wavelength (1.5418 Å) and to make the beam quasi-parallel (divergence $\leqq 0.03^{o}$). The beam size at sample position was 50μm in the incidence plane. Data were collected using a scintillation detector for $2\,\theta$ up to 12°, with an increment of 0.05° and an acquisition time around 30 sec/step. The interpretation of XRR measurements is carried out by fitting the experimental scans with theoretical curves using Bruker LEPTOS® software[104].

2.5 X-ray Absorption Spectroscopy

2.5.1 Basic principles

The X-ray absorption spectroscopy (XAS) consists in the excitation of a core electron via the absorption of a photon of energy $\hbar\omega$, where $\hbar$ is the Planck constant and ω the photon frequency. The variation of the absorption coefficient is measured as a function of the incident photon energy. The so-called Beer-Lambert rule expresses the linear absorption coefficient μ of the sample as a function of sample thickness and the measured intensities of the incident (I_0) and the transmitted beam (I_T):

$$\mu(E) = \frac{1}{t} \ln\left(\frac{I_0}{I_T}\right) \tag{2.31}$$

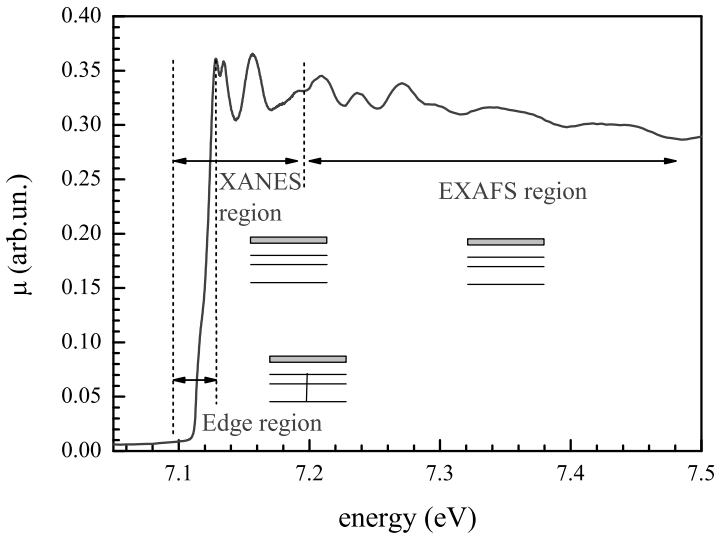

Figure 2.6: X-ray absorption spectrum at the Fe K edge.

μdepends on the photon energy, the atomic density and the atomic species in the sample.

In the case of ultra-thin supported films, the absorption of the substrate does not allow the direct measure of μ from this equation. In this case the absorption coefficient is obtained from the fluorescence yield and is proportional to $\left(\frac{I_0}{I_F}\right)$, with I_F intensity of the emitted fluorescence.

Depending on the photon energy different physical processes give rise to the structures observed in an absorption spectrum. Figure 2.6 shows a spectrum collected at the Fe K edge ($1s$ excitation) for an Fe metal foil. In the region before the edge, the energy of the incident photons is lower than the ionization energy E_0 (around 7112 eV for the Fe K edge). In transmission measurements the absorption coefficient is due to all other elements and core states that can be excited and decreases monotonically. In a fluorescence measurement only the decay channel of interest is selected and the absorption coefficient of the element at the edge is close to zero. This continuous background is considered as the base line μ_0.

The XANES (X-ray absorption near edge structure) [105, 106] range is normally defined from a few eV before to around 60 eV above the edge. The XANES region contains information on the electronic structure of the investigated samples and on the symmetry of the absorbing site. For energies lower but close to E_0 the energy may be sufficient to promote the photo-electron towards its first empty or partially occupied levels, that are localized levels. This phenomenon yield to the emergence of pre-edge structures, whose shape and position with respect to the main absorption edge inform on the oxidation state of the absorbing, its coordination geometry, site symmetry, and orbital hybridization.

For energies higher than E_0 up to around 60 eV above the edge, the photo-electron is ejected towards states with a low kinetic energy, the excess energy above the binding threshold. Its mean free path - average distance covered by the electron without energy losses - is high. In this energy range the structures are dominated by multiple scattering

processes suffered by photo-electron from its atomic neighbors.The comparison between the XANES spectrum of a sample and those collected for reference compounds ("finger-print" analysis) directly gives information on the structural and electronic environments of the absorbing atoms. However, the full exploration of the richness of the XANES spectrum needs to resort to *ab initio* simulations using advanced codes. During this study we performed some preliminary simulations using FDMNES code[107].

In the energy region, starting from about 60 eV above the edge the core electron is ejected towards delocalized states of the continuum. Its kinetic energy being large, its mean free path is short and the structure in this range are mainly due to single scattering events. The absorption spectrum is composed of a slowly varying function μ_1 and an oscillatory part around μ_1. The photo-electron wave is backscattered by the neighbors of the absorbing element. The absorption cross section is modulated by the interference between the outgoing and the back-scattered photo-electron waves. As the X-ray energy increases, the kinetic energy of the photo-electron increases. This results in a decreasing photo-electron wavelength, and thus, in alternating destructive interference and giving rise to an interference phenomenon between emerging and backscattering waves. The absorption spectrum is composed of a slowly varying function μ_1 and an oscillatory part around μ_1 that is called the EXAFS function (extended X-ray absorption fine structure) and contains information on the atomic local structure around the absorber atom.

2.5.2 EXAFS formalism

The basic theory of XAS has been addressed by many authors ([108, 106, 105]). The contribution to the X-ray-absorption coefficient $\mu(E)$ from a given core-state i at X-ray energy $\hbar\omega$ can be calculated in terms of initial and final states of the Hamiltonian for the system using the golden rule,

$$\mu(E) \propto |\langle f\,|H_I|\,i\rangle|^2\,\delta(E_f - E_i - \hbar\omega)\rho(E_f) \tag{2.32}$$

where $|i>$ and $|f>$ are the wave functions for the initial and final states, $E_i + \hbar\omega$ is the photo-electron energy, H_I is the coupling to the X-ray field, E_i is the (large negative) energy of the core level, the sum is over unoccupied, final states of energy E_f. The differences in various theoretical approaches reflect different approximations for the calculation of these ingredients. In particular, the question of precisely which one-electron states to use is not unambiguous, and depends on the energy range of interest. Most practical calculations are based on the reduction of the many-body golden rule to an one-electron approximation. In addition, the basic theory routinely used in the quantitative analysis of EXAFS experiment implies the reduction of a dipole coupling to the X-ray field, that allows writing the absorption cross section as:

$$\mu(E) \propto |\langle f\,|\hat{\epsilon}\cdot\vec{r}|\,i\rangle|^2\,\delta(E_f - E_i - \hbar\omega)\rho(E_f) \tag{2.33}$$

Using single electron and dipole approximation, assuming a Gaussian radial distribution function around the absorbing atoms and limited structure, the EXAFS function in the formalism of single scattering of spherical waves can be reduced to a summation over all i atomic shells (standard EXAFS formula):

$$\chi(k) = \sum_i N_i S_0^2 F_i(k) e^{-2R_i/\lambda(k)} e^{-2k^2\sigma_i^2} \frac{\sin(2kR_i + \Phi_i(k))}{kR_i^2} \tag{2.34}$$

with

k: wave vector modulus for the photo-electron, defined as : $k = \sqrt{\frac{2m}{\hbar^2}(\hbar\omega - E_0)}$, with m as the electron mass

$\chi(k) = \frac{\mu(k)-\mu_1(k)}{\mu(k)-\mu_0(k)}$

R_i : distance to the atoms of the i^{th} atomic shell,

σ_i^2: relative mean square deviation of the R_i distance. The term $e^{-2k^2\sigma_i^2}$ takes into account distance fluctuations due to a structural and/or thermal disorder, under the assumption of small displacements and Gaussian distributions of distances. Includes thermal (dynamic) and structural (static) disorder

$F_i(k)$, backscattering amplitude function characteristic of the i^{th} neighbors

$\Phi(k)$, is a phase function that takes account of the varying potential field along which the photo-electron moves; it can be expressed as the sum of two potential terms, $\Phi i(k) = 2\delta(k) + ji(k)$, the former given by the absorber, the latter given by the scatterer

$\lambda(k)$ mean free path associated to the ejected photo-electron

S_0^2 amplitude factor, taking into account the contributions of the inelastic losses and overall many-body phenomena. It is an average amplitude reduction factor. Its value is the percent weight of the main excitation channel with respect to all possible excitation channels, usually 0.8–0.9

In the case of isotropic samples, N_i is simply the number of atoms in the atomic shell i.

For a non-isotropic structure, the product $\vec{\epsilon} \cdot \vec{r}$ results in an angular dependence of the EXAFS signal and N_i is an effective multiplicity number given by: $N_i = 3\sum_j cos^2\theta_{ij}$ where θ_{ij} is the angle between the absorber-scatterer axis and the polarization direction.

The linear polarization of synchrotron radiation, coupled with this directional dependence of the photo-absorption process, allows probing the structural features along specific directions of the crystalline samples (Polarized XAS). In the case of oriented films, when the polarization vector $\vec{\epsilon}$ lies in the film's plane (in-plane geometry) $cos\theta_{ij} = 0$ for the bonds perpendicular to this plane and their contributions are zero. On the other hand when $\vec{\epsilon}$ is aligned with the normal to the film's plane (out-of-plane geometry), the contribution of the bonds in this plane are zero ($cos\theta_{ij} = 0$).

2.5.3 Experimental aspects of XAS

Metal K edge (Fe: 7112 eV, Mn 6539 eV, Co 7709 eV) XAS spectra were collected in fluorescence mode at the French CRG BM30b-FAME beamline [109] of the ESRF. The storage ring is operated at 6 GeV with a 200 mA current. Energy was selected using a

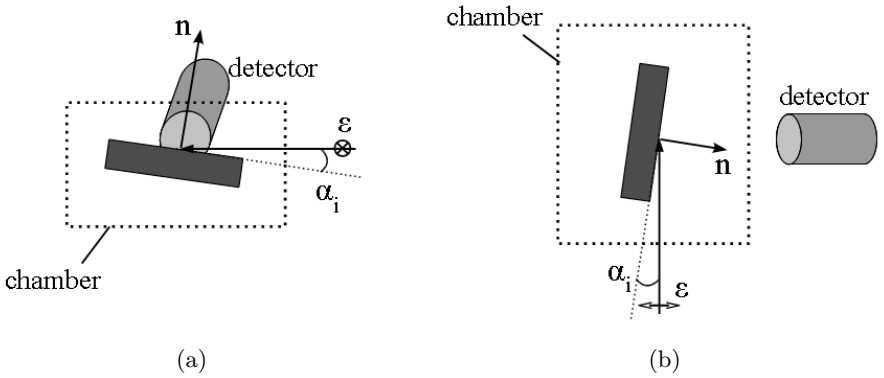

(a) (b)

Figure 2.7: Schema of linear polarized XAS detection for (a) in-plane and (b) out-of-plane geometries.

Si(111) double-crystal monochromator with dynamic sagittal focusing, yielding a beam spot on the sample of 300 μm horizontal 200 μm vertical and an X-ray photon flux of 10^{12} photons/s, allowing acquisition of good quality XANES/EXAFS spectra. Silicon diodes collecting scattered radiation from a Kapton foil were employed for measuring the intensities of incident and transmitted X-rays. Fluorescence spectra were collected in the right-angle geometry using a Canberra 30-element solid state germanium detector. Energy was frequently calibrated using a metal foil. Its K edge energy was set at 7112 eV (Fe), 6539 eV (Mn) or 7709 eV (Co) as the maximum of the first derivative of the main edge spectrum. Details about the beamline and X-ray setup may be found in [110, 109]. Measurements were performed with X-ray polarization vector oriented nearly parallel (in-plane geometry) and nearly perpendicular (out-of-plane geometry) to the film plane (fig. 2.7). In both geometries the incident angle on the film α_i is chosen to be small (5° to 10°) to maximize the signal coming from the deposited film and is optimized in order to eliminate the Bragg peaks due to the substrate.

2.5.4 EXAFS Data analysis.

The purpose of EXAFS analysis is to obtain the parameters of the local structure of the absorbing atom from its experimental cross-section. The experimental EXAFS spectra were treated following standard methods using the ATHENA-ARTEMIS analysis package[111].

ATHENA code is used for all steps in data processing including conversion of raw data to spectra, background subtraction, Fourier transforming and plotting. The background subtraction algorithm determines an empirical background spline based on a distinction between data and background in terms of Fourier components. Edge-step normalization of the data is determined by a linear pre-edge subtraction and regression of a quadratic polynomial beyond the edge. The difference between these two polynomials extrapolated to the edge energy E_0 is used as the normalization constant. E_0 is chosen by finding the first large peak in the first derivative of the spectrum.

ARTEMIS is a program for analysis of EXAFS data using theoretical standards computed by the FEFF program ([112]), using an equation similar to (2.34) to model

the observed oscillations. The fitting is done either in k space or in R (Fourier transform) space, with essentially equivalent results. The data are described as a summation of one or more scattering paths. The parameters that define the scattering ($F_i(k)$, $\Phi(k)$, and $\lambda(k)l(k)$) are determined from *ab initio* calculations included in the code. S_0^2 is determined from the analysis of a reference metal foil. Once these parameters have been specified, the structurally related parameters (N_i, σ_i, and R_i) are refined, via a non-linear least-square fitting procedure. Distance estimates are within 0.02 Å and errors in coordination numbers are less than 10%. Simultaneous refinement can be performed for multiple data sets.

2.6 X-ray Magnetic Circular Dichroism

Since the first report in 1987 [113], X-ray magnetic circular dichroism (XMCD) using synchrotron light has become one of the most important techniques to study localized magnetic moments in thin and multilayer films. XMCD is the difference in X-ray absorption measured using light with helicity parallel and antiparallel to the magnetization direction of the sample. It couples a magnetic probe with all advantages of XAS, i.e., the atomic and symmetry of electronic states selectivity, localized information, sub-monolayer detectability. Sum rules correlate the integrated signals of the dichroism spectrum to the experimental values of the spin and orbital magnetic moments. This provides fundamental insights into the microscopic origin of magnetic properties, such as anisotropy, magneto-crystalline effects, coupling among different elements.

2.6.1 XMCD sum rules

The X-ray magnetic circular dichroism XMCD sum rules have been introduced by Thole et al. in 1992 [114] and Carra et al. in 1993 [115]. Thole et al. showed that the integral over the XMCD signal of a given edge allows the determination of the ground state expectation values of the orbital moment $\langle L_Z \rangle$ and Carra et al. introduced a second sum rule for the effective spin moment $\left\langle S_Z^{eff} \right\rangle$. The sum rules apply to a transition between two well-defined shells.

We are interested in the transition from a 2p core state to 3d valence states in our 3d transition-metal systems. As a result of spin-orbit coupling in the 2p state, the spectrum displays two prominent features, corresponding to the L_3 ($2p_{3/2} \rightarrow 3d$) and L_2 ($2p_{1/2} \rightarrow 3d$) absorption edges. These 3d valence states are assumed to be separable from other final states. This implies that the $L_{3,2}$ absorption edges must be separated from the 2p-4s and other 2p-continuum transitions. In general, it is assumed that continuum transitions can be described as an edge step followed by a constant cross section.

We briefly introduce here the main aspects of the XMCD sum rules. The integrated $L_{3,2} - edges$ XAS spectrum is proportional to the number of empty 3d states n_h, or $(10 - n_{3d})$, where n_{3d} is the number of 3d electrons in the shell. The absorption cross section $\mu(E)$ is integrated over a certain energy range that covers the complete $L_{3,2} - edges$:

$$\int \mu(E) \equiv \int_{L_3+L_2} (\mu_{+1} + \mu_0 + \mu_{-1}) = \frac{C}{5} \langle (10 - n_{3d}) \rangle \tag{2.35}$$

C is a constant factor including the radial matrix element of the dipole transition. The integrated circular dichroism spectrum is defined as the absorption of left circular polarized X-rays μ_{+1} minus the absorption of right circular polarized, X-rays μ_{-1}. In case of a 2p-3d transition this yields

$$\int_{L_3+L_2} (\mu_{+1} - \mu_{-1}) = -\frac{C}{10} \langle L_Z \rangle = -\frac{C}{10} \frac{3}{2} m_{orb} \tag{2.36}$$

This XMCD sum rule implies that one can directly determine the orbital moment m_{orb} from the difference of positive (μ_{+1}) and negative (μ_{-1}) helicity X-rays. In most soft X-ray experiments, the absolute absorption cross section is not measured, only a relative signal is obtained by normalizing the XMCD signal by the absorption edge. This defines the orbital moment sum rule as

$$m_{orb} = -\frac{\int_{L_3+L_2} (\mu_{+1} - \mu_{-1})\, d\omega}{\int \mu(E)} \frac{4}{3} \langle (10 - n_{3d}) \rangle \tag{2.37}$$

The determination of the effective spin moment is also possible with an additional sum rule :

$$m_{spin}^{eff} = -\frac{6 \int_{L_3} (\mu_{+1} - \mu_{-1})\, d\omega - 4 \int_{L_3+L_2} (\mu_{+1} - \mu_{-1})\, d\omega}{\int \mu(E)} \langle (10 - n_{3d}) \rangle \tag{2.38}$$

However, this effective spin sum rule has some additional complications.

The effective spin moment m_{spin}^{eff} is given as

$$m_{spin}^{eff} = m_{spin} \left(1 + \frac{7 \langle T_Z \rangle}{2 \langle S_Z \rangle} \right) \tag{2.39}$$

where $\langle T_z \rangle$ is the magnetic-dipole coupling, which accounts for the asphericity of the spin moment distribution. If this sum rule is used to determine the spin moment m_{spin} one has to assume that $\langle T_z \rangle$ is zero or that $\langle T_z \rangle$ must be known from other experiments or theoretically approximated. The effective spin sum rule makes an additional approximation that theL_3 and the L_2 edges are not mixed and well-separated. Large errors in the effective spin moment are caused by the mixing of theL_3 and the L_2 edges. In our case, we could apply these sum rules to have the effective spin moment at the Fe L edge but not at the Mn L edge.

The experimental validation of the XMCD sum rules was made by Chen et al., using simple 3d transition metals [116]. They found that spin moments need to be corrected by only a few percents in pure Fe and Co elements, and that no correction is needed for orbital moments. However, it was shown that in the case of the Ni(001) surface, discrepancies up to 50% may occur [117]. On the other hand, on the same paper it is shown that in cubic symmetries the magnetic dipole term may be safely neglected. For

a recent critical analysis on the validity and limitations of the XMCD sum rules see Piamonteze et al. [118] and references therein.

Anyway, when the spin-orbit coupling is large, as in systems like FePt and MnPt, the $\langle T_Z \rangle$ term has to be considered, at least as a possible source of errors [119, 120, 121]. A huge number of researchers applies the sum rules to get information on the orbital and spin contribution to the total magnetic moments. The point is that the same systematics must be followed in their application and much care has to be taken concerning background subtraction and normalization, in order to compare similar systems among them. This has been done in this thesis to study Fe and FePt systems at the Fe $L_{3,2}$ edges (chapter 5).

2.6.2 Experimental aspects of XMCD

Soft X-ray absorption XAS and XMCD experiments at the $L_{2,3}$ Fe and Mn absorption edges were performed at the ID08 beamline of the European Synchrotron Radiation Facility (ESRF, Grenoble, France). The XMCD experiments were carried out under varying temperature and applied field with total electron yield detection and a 100% polarization rate. Electron yield mode was employed by measuring the current flowing from the sample through an electrometer. The left and right circular polarized light were produced by phasing an APPLE II type undulator. The samples were installed in a UHV chamber of a cryogenic holder whose temperature can vary from RT down to about 10 K. Superconducting coils produced a magnetic field up to 6 Tesla along the direction of the incoming beam. The applied magnetic field orientation on the sample was changed by rotating the sample about a perpendicular axial rotation inside the cryostat. To apply a perpendicular magnetic field the sample was normal to the incident beam; to apply a field in the plane, the beam was aligned at a grazing incidence of about 5 to 10 degrees to the sample surface.

2.7 MOKE

Many different techniques may be applied to probe the magnetic properties of ultra-thin magnetic films. Among them, the magneto-optic Kerr effect (MOKE) is a well-established technique [122, 31] that has been widely used to study continuous layers or nanostructures with sub-monolayer sensitivity [70, 123, 8, 124]. The MOKE is characterized by a complex rotation of the plane of polarization of the linearly polarized incident light upon reflection from the surface of a ferromagnetic material. Maybe the most important advantage of the MOKE technique compared to other techniques, like SQUID or VSM, is the simplicity of implementation and flexibility of the sample environment. Such an apparatus may be easily coupled to a Surface Science set-up in order to follow, in an UHV environment, the magnetic properties at the different stages of growth [70, 123, 8, 124, 125, 126].

Magneto-optic effects are usually described in the context of macroscopic dielectric theory [122, 127]. They arise from the antisymmetric, off-diagonal elements in the dielectric tensor. A microscopic description of the magneto-optic effect concerns the

different response of the electrons to left- and right-circularly polarized light. The coupling between the electromagnetic field and the electron spin within a magnetic medium occurs through the change of the wave functions due to the spin-orbit interaction [128].

The MOKE macroscopic description is based on the analysis of the dielectric properties of a magnetized medium. Linearly polarized light may be expressed as a linear combination of left- and right-circularly polarized components. When light propagates in a magnetized medium, there are in general two main processes taking place : first, the two circularly polarized components are phase-shifted due to their different propagation velocities, yielding a rotation of the polarization plane - this is the conventional Faraday rotation; second, the different absorption rates of the two modes affect the ellipticity. A quite general macroscopic formalism has been developed for magnetic multilayer by Zak et al. [127]. Since most magnetic materials of interest are metals, which strongly absorb light, it is more convenient from the experimental point of view to measure the reflected light. Hence, the formalism has been developed for magneto-optic Kerr effect, even if it can be extended to the Faraday effect. The general method is to apply Maxwell's equations to the multilayer structure and to satisfy the boundary conditions at each interface. The Kerr rotation ϕ' and ellipticity ϕ" for $s-$ and $p-$polarized light are then connected to the reflection coefficients by :

$$\phi_s = \phi_s^{'} + i\,\phi_s^{"} = \frac{r_{ps}}{r_{ss}} \; and \; \phi_p = \phi_p^{'} + i\,\phi_p^{"} = \frac{r_{sp}}{r_{pp}} \tag{2.40}$$

where s and p correspond to the electric field vector perpendicular to or in the plane of reflection, respectively. The crossed reflection coefficients are linear functions of the magnetization.

Amongst several ways of measuring a MOKE signal, we will introduce here one of the simplest one, which is the one we used to measure the main part of the data presented in this manuscript. Consider a linear $p-$polarized light reflected from a sample surface. If the sample is ferromagnetic then the reflection beam should consist of an s component (E_s) in addition to the dominant $p-$component (E_p), with $E_s/E_p = \phi_p^{'} + i\,\phi_p^{"}$ being the Kerr rotation. Experimentally, the measurements can be realized by placing in front of the photo-detector a linear polarizer at a small angle δ from the $p-$axis. The intensity measured by the photo-detector after the polarizer is

$$I = |E_p \sin\delta + E_s \cos\delta|^2 \approx |E_p\,\delta + E_s| \tag{2.41}$$

and then becomes

$$I = |E_p|^2 \left|\delta + \phi^{'} + i\,\phi^{"}\right|^2 \approx I_0 \left(1 + \frac{2\phi^{'}}{\delta}\right) \tag{2.42}$$

with $I_0 = |E_p|^2\,\delta^2$ representing the intensity at zero Kerr rotation.

Since both ϕ' and ϕ" are linearly proportional to the magnetization, the measured intensity as a function of the applied magnetic field yields the magnetic hysteresis loop. One can easily see that saturation Kerr rotation can be expressed by $\phi_{max}^{'} = \frac{\delta}{4}\frac{\Delta I}{I_0}$, where ΔI is obtained by reversing the magnetization from saturation.

The rotation is directly related to the magnetization of the material within the probed region of the light. If the total optical thickness is much less than the wavelength of the incident beam, the total Kerr signal is simply the summation over all magnetic layers in a multilayered film. This summation rule has been verified for many systems and one can state that up to about 10 nm it works. Light penetrates much more than that into metals, so, the MOKE technique derives its surface sensitivity, in fact, from the limited thickness of the deposited magnetic nanostructures.

2.7.1 Experimental aspects of MOKE

A laser, followed by a polarizer, is usually used as a source of polarized light. The detector is a photo-diode. For *in situ* measurements, the UHV windows usually produce a birefringence. In such a situation, a quarter-wave plate can be placed before the analyzing polarizer to compensate for the window birefringence. The counterpart is that the quarter-wave plate introduces a $\frac{\pi}{2}$- phase difference between the $s-$ and $p-$components, and the Kerr intensity gives the ellipticity rather than the rotation because $\phi^{"}$ replaces $\phi^{'}$. To measure the rotation, a half-wave plate replacing the quarter-wave, might be used. This is, in fact, the configuration of the apparatus used for most of the data collected during this work.

The MOKE setup is installed in the ultra-high vacuum (UHV) multi-chamber system at the Max Plank Institut of Halle, Germany. This is a collaboration with the group of Dr. Marek Przybylski, through a LEA - Laboratoire European Associé - program. The multi-chamber system is equipped with many instruments for synthesis under UHV conditions. The MOKE apparatus is connected to the synthesis chambers through an UHV transfer line. The maximum applied field is limited to 5.5 kOe. Two different MOKE geometries are possible, with an incidence angle of 21° for longitudinal MOKE (L-MOKE) and with an incidence angle of 69° to the sample normal for polar MOKE (P-MOKE). The sample can be cooled down close to 5 K.

Chapter 3

Growth on (001) surfaces

This chapter is dedicated to the metal on metal growth for some (001) surfaces. A fundamental comprehension of the growth process is an important step towards the preparation of multilayers and ordered alloys with specific orientation requirements, as is the case for the PMA systems we are interested. Especial attention is dedicated to the Pt(001) surface, on which the majority of our samples were prepared. Structural aspects of the Mn, Fe and Pt growth on Pt(001) are investigated by GIXRD, with the help of LEED and AES. The growth of Pt, MnPt and Fe on Ag(001) are also investigated by GIXRD.

3.1 Growth on Pt(001)

The Pt(001) surface is well-suited to the coherent epitaxial growth of MnPt and FePt. Pt lattice parameter ($a_{Pt} = 3.924$ Å) lies in between the MnPt a and c parameters, which are, for bulk stoichiometric $L1_0$ alloy [41], $a_{MnPt} = 4.002$ Å ($2.0\% > a_{Pt}$), $c_{MnPt} = 3.665$ Å ($6.6\% < a_{Pt}$). The smaller in-plane mismatch is expected to favor a perpendicular orientation of the c-axis. In the case of FePt, the values are [42] $a_{FePt} = 3.860$ Å ($1.6\% < a_{Pt}$), $c_{FePt} = 3.713$ Å ($5.4\% < a_{Pt}$) and the same tendency is expected.

The Pt(001) surface displays a quasi-hexagonal reconstruction on its topmost layer that has many consequences on the growth of adlayers. In the following, we start by an overview of this reconstruction and then we present a study on the growth process of Mn, Pt and Fe on the clean Pt(001) surface.

3.1.1 Pt(001) surface reconstruction

It is well known that some 5d-transition metal surfaces present surface reconstructions [74], as is the case of the Pt(001) surface. The topmost layer of Pt reconstructs to a quasi-hexagonal arrangement while the layer just below keeps the bulk square symmetry [129]. A high resolution STM image taken from Borg et al. [130] (fig. 3.1-a) illustrates the quasi-hexagonal packing (highlighted by dashed lines). In this picture, one can observe the characteristic corrugation along the [1 0] substrate direction[1] and

[1] [1 1 0] direction in *fcc* notation

the close-packed rows of atoms running parallel to [0 1], as indicated in the figure. This corrugation comes from a mismatch between the substrate and the reconstruction along [1 0], where one have roughly 6 hexagonal rows to each 5 substrate rows, with a periodicity of $\approx 14\,\text{Å}$. The typical height difference between 4-fold hollow-sites and on-top sites gives a corrugation amplitude reported to be in the range of 0.4 to 1.2 Å [129, 131, 132]. From our LEED measurement shown in figure 3.1-b one can recognize the superimposition of two nearly (5x1) patterns, coming from reconstructed domains rotated by 90° among each other.

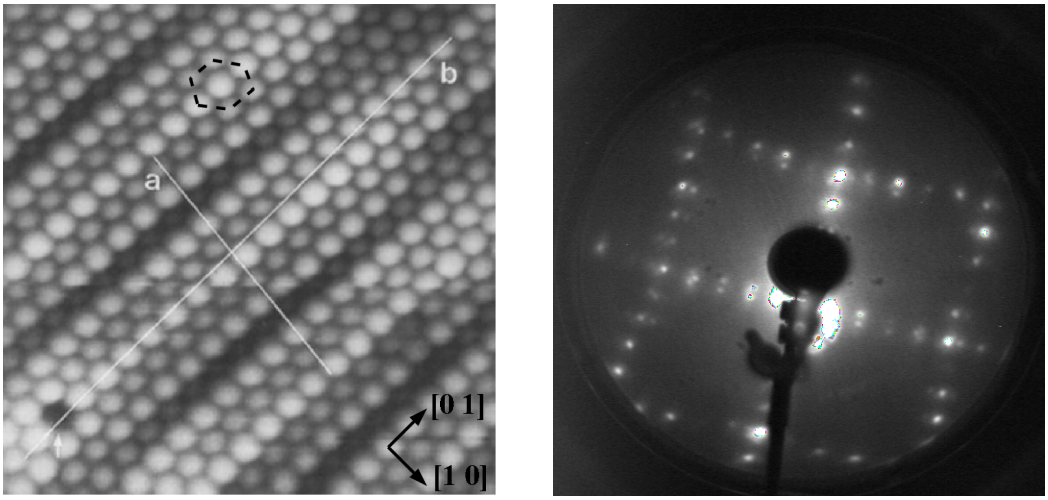

(a) (b)

Figure 3.1: a) Atomic resolution STM image of reconstruction taken from ref. [130] appended with indication of quasi-hexagonal packing (dashed line) and surface orientation convention (arrows); b) (5x1) LEED pattern of a clean, reconstructed Pt(001) substrate without miscut, with beam energy of 60 eV.

The hexagonal reconstruction is stable and its surface energy was measured and theoretically evaluated to be lower than the unreconstructed surface energy by about 0.12 eV per (1×1) unit cell [133]. The phase transition from (1×1) to hexagonal has been theoretically described by a intriguing atomic process that includes the formation of an intermediary phase with vacancies in the (1×1) sublayer [134].

A phase diagram of the reconstruction was given by Abernathy et al. [135]. They showed that between 1820 and 1685 K the hexagonal overlayer has a high-symmetry direction aligned with a high-symmetry direction of the bulk (direction [0 1] in figs. 3.1-a and 3.3). We abbreviate this aligned-hexagonal phase by *Pt-hex*. At 1810 K the surface is very flat and the *Pt-hex* domains extends over more than 1500 nm. Above 1820 K the surface is disordered and rough. When slowly lowering the temperature below 1685 K, two slightly rotated phases appears while the *Pt-hex* phase vanishes. At RT these two phases are rotated by $\theta = 0.75°$ and $\theta = 0.9°$ relative to the aligned direction: we call them *Pt-hex-0.7°* and *Pt-hex-0.9°*, respectively. According to these authors, at RT the domains are smaller than at high temperature, the larger ones being those of the *Pt-hex-0.7°* phase with a translational order of about 200 nm (fig. 3.3 presents a sketch of this phase).

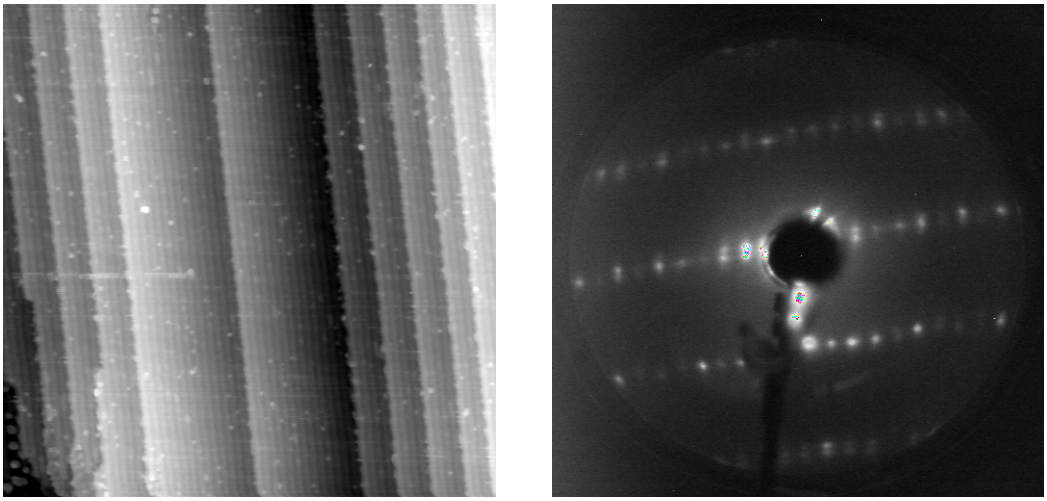

(a) (b)

Figure 3.2: a) 100 nm × 100 nm STM image of a 1°-miscut surface, showing the reconstruction rows aligned with the step edges; b) (5x1) LEED pattern of the same surface, evidencing that only one family of domains are present (beam energy of 169 eV).

The kind of reconstruction one obtain at RT depends strongly on the substrate preparation and thermal history. For instance, if the sample is heated up to 1000 K during 5 min and then cooled down to RT, small domains of the unrotated *Pt-hex* phase cover the surface with no traces of rotated domains [135]. A miscut of the surface also affects the reconstruction [136]. In our experiments, we used substrates with different miscut angles along the [1 0] direction, namely: no miscut, 0.34° and 1°. We observed that the reconstruction rows have a tendency to align with the step edges along [0 1], avoiding 90° rotated domains. This can be clearly seen in our STM and LEED pictures shown in figure 3.2 for the substrate with a 1°-miscut (in the *fcc* notation, it corresponds to a (1 1 80) vicinal substrate): only the domains aligned to the steps are observable. The GIXRD measurements in this surface revealed that these domains are mostly of the *Pt-hex-0.7°* phase, while a negligible amount of 90°-rotated domains are also present but with $\theta = 1.02^{o}$. Indeed, for all miscut angles used the *Pt-hex-0.7°* domains turn out to be the largest and most stable ones.

Our sample preparation procedure consisted in cleaning the Pt(001) surface by several cycles of Ar+ sputtering (typically: $P_{Ar} = 4 \times 10^{-6}$ mbar, 800 V, 10 μA, 40 min at RT) and annealing (at 1170 K for 5 to 10 min), followed by annealing under oxygen (at 2×10^{-7} mbar O_2 and 970 K for 5 min) to get rid of carbon impurities segregated from the bulk, then a flash-annealing at 1170 K - for CO desorption - before slowly cooling down. The cleanness of the surface was checked by AES. After this procedure the surface used to be flat and covered predominantly by *Pt-hex-0.7°* domains as large as about 200 nm. We should say that the hexagonal reconstruction was not always rotated because this depends also on the thermal history and number of cleaning cycles.

Figure 3.3 resumes the detailed structure of *Pt-hex-0.7°* in the real and reciprocal space, with all dimensions taken from ref. [135]. In this scheme one can distinguish a hexagonal domain (circles) on top of bulk atoms (crosses). In the bottom, the first and second layers are partially removed to evidence the picture construction. One

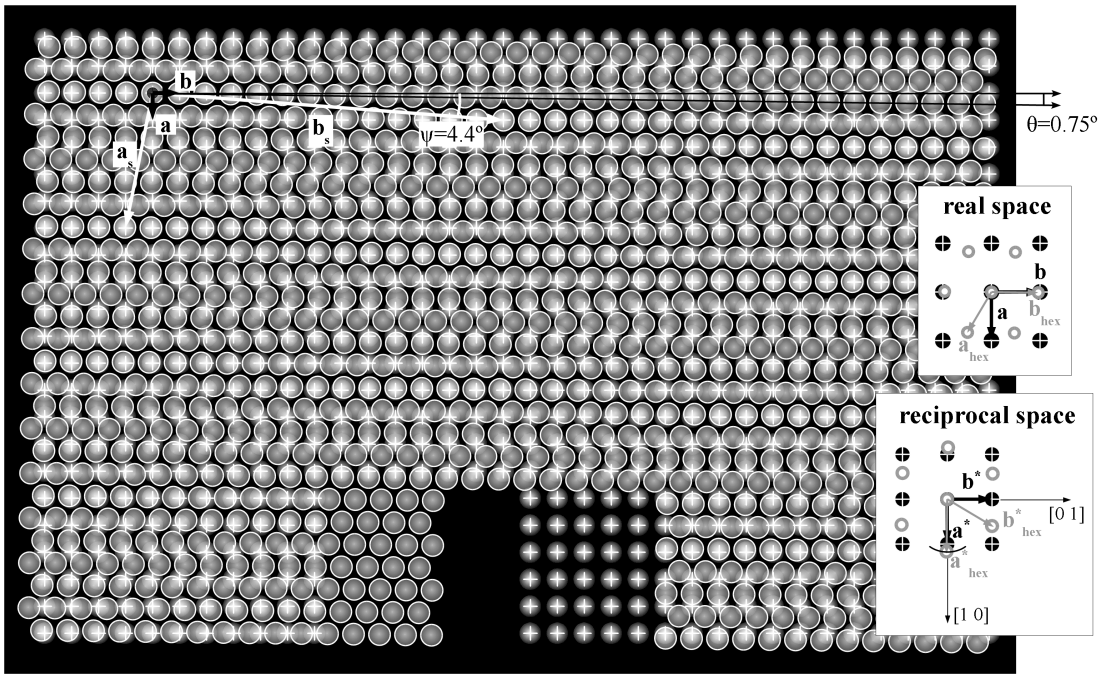

Figure 3.3: Schematic view of the *Pt-hex-0.7°* phase putting in evidence the the $\theta = 0.75^{o}$ rotation angle. White circles represent the top hexagonal layer, while crosses represent the underling bulk with square symmetry. A possible surface unit cell is given by vectors $\mathbf{a_s}$ and $\mathbf{b_s}$. In the insets the real and reciprocal spaces surface unit cell vectors are represented for both hexagonal and square layers.

must remember that there are other three symmetry-equivalent *Pt-hex-0.7°* domains besides the one represented. The angle between hexagonal and square rows $\theta = 0.75^{o}$ is shown. It corresponds to the angle between $(1\,0)_{hex}$ (around $(1.21\,0)$ in the reciprocal space) and the $[1\,0]$ directions. One can observe in this picture the nearly on-top position for the atoms in each end of the white arrows. This corresponds almost to a $\begin{pmatrix} 5 & -1 \\ 1 & 13 \end{pmatrix}$ reconstruction with a superstructure unit cell represented by a_s and b_s as indicated. Some STM, LEED and Helium diffraction studies have proposed this kind of commensurate superstructure unit cell to describe the different reconstruction phases. However, strictly speaking, the precise GIXRD measurements cited above [135] showed that the reconstruction is incommensurate in both directions for all its phases. One can say generally that the Pt hexagonal reconstruction has an orientational epitaxy, but is incommensurate.

Anyway, this superstructure unit cell is useful to help the comprehension. The angle between $\boldsymbol{b_s}$ and $[0\,1]$, $\psi = 4.4^{o}$, is effectively the angle between the reconstruction lines and underlying substrate rows. In the reciprocal space inset, the black arc represents the region of reciprocal space probed during an angular scan of the sample about its surface normal (rocking scan). Figure 3.4-a shows a rocking scan about the $(1\,0)_{hex}$ rod of the clean reconstructed surface, revealing two symmetric domains rotated by an angle $\theta = 0.74^{o}$ from the $[1\,0]$ direction. Taking the inverse of the full width at half maximum (FWHM) in reciprocal lattice units for two Lorentzian peaks fitting this rocking curve (not shown), we estimate the correlation length of *Pt-hex-0.7°* domains at RT to be about 150 ± 50 nm, while the crystal presents terraces of about 900 ± 100 nm.

From the position of the $(1\,0)_{hex}$ and $(-1\,2)_{hex}$ rods one can calculate that the surface reconstruction is 25% denser than the underlying square plane or 8% denser compared to the Pt(111) bulk close-packed plane [135]. When the reconstructed surface is exposed to a reacting gas like CO, NO or C_2H_4 [131] or when a metal, like Ag [137], Fe [51], Mn [138], Co [139] or Cu [132] is deposited on it, the reconstruction is lifted to the (1×1) bulk-like structure. In this process, also referred to as "restructuring" or "deconstruction", the 25% excess surface atoms are forced up to become adatoms, which may interfere with the growth process by forming islands and steps or alloying with the deposited material, or even acting as a surfactant.

3.1.2 Mn growth on Pt(001)

The very first steps of Mn growth on a *Pt-hex-0.7°* was studied *in situ* by GIXRD using the SUV station of the French CRG BM32 beamline at ESRF with a beam energy of 24 keV. During the growth, the reconstruction rod was followed in real time around the (1.21 0 0.15) to obtain an estimation of the amount of reconstruction left on the surface at each step of deposition (fig. 3.4). Complete sets of crystal truncation rods (CTRs - section 2.3) were measured for some particular coverages. The integrated intensity at each *hkl* node was get from rocking scans, from where the broad background coming from thermal diffuse scattering is subtracted in the numerical integration procedure used[2]. Structure factor amplitudes $|F_{hkl}|$ were then extracted by applying standard correction factors [92] for the z-axis diffractometer of SUV station (section 2.3.1 gives more details about the correction factors used). Equivalent rods were measured and symmetry averaged, the error bars were based on their agreement factor (about 5% for the CTRs presented in figs. 3.6 and 3.9). Both $|F_{hkl}|$ derivation and modeling/fitting of surface parameters were performed using the ANA-ROD package [90, 91]. High purity Mn was deposited from an effusion cell with an alumina crucible heated at about 1000 K, the pressure rising up to 5×10^{-10} mbar while operating the source. The evaporation rate was calibrated with a quartz crystal micro-balance, and cross-checked measuring the oscillation period of the X-ray scattering intensity in anti-phase (1 1 1) during a calibration deposition. The X-ray calibration was corrected by a factor 1.05 to take into account the difference in lattice parameter of Pt and Mn [80]. An average deposition rate of 0.02 ML/min was established with an error estimated to be smaller than 10% and used for the sub-monolayer study. For higher coverages, a rate of 0.18 ML/min was employed. The substrate used in this study had a not-on-purpose 0.34° miscut, checked afterward in our laboratory diffractometer, almost aligned with the [10] direction. Such a miscut error causes an asymmetry in the amount of reconstruction along the main axes, but has no consequences on the growth process. We also performed some auxiliary STM and LEED measurements, using the facilities at the Institut Néel, to obtain a qualitative picture of the growth process and of possible ordered alloying formed during deposition.

The *Pt-hex-0.7°* reconstruction was followed in different steps of the Mn deposition by rocking scans around the reciprocal space position (1.21 0 0.15) (fig. 3.4). The

[2]The measured intensity is always normalized by a monitor to take into account variations in the primary beam intensity.

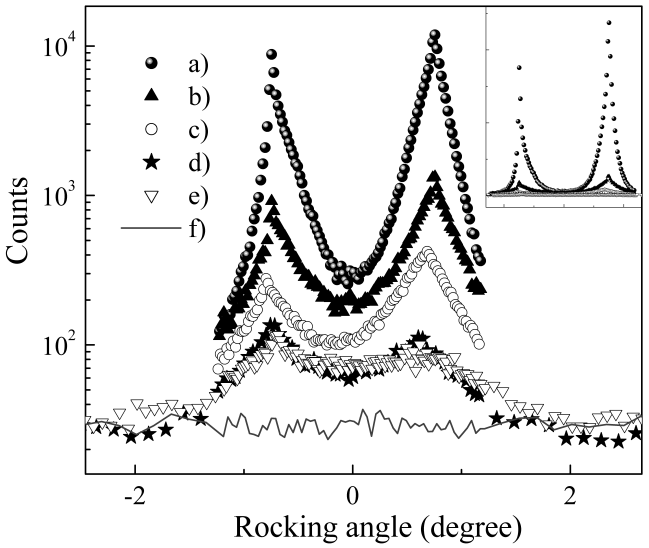

Figure 3.4: Rocking curves around the reconstruction rod (1.21 0 0.15) for the following surfaces (remaining *Pt-hex-0.7°* in brackets): a) freshly clean surface (100%); b) just after 0.35 ML Mn deposition; c) 10 hours after; d) previous layer annealed up to 250°C for 30 min; e) 1.2 ML Mn deposition on a freshly cleaned substrate; f) 1 ML of Pt on top of the previous layer. Inset: Same plot in linear scale.

integrated intensity of the clean reconstruction surface, just after the cleaning process, has been considered as meaning 100% of the surface being reconstructed. However, we only follow the peak around (1.21 0 0.15), favored by the small miscut, and assume that the corresponding 90° turned domains behave in the same way. The amount of reconstruction left after Mn deposition is calculated as the ratio between the integrated intensity of the rocking scan after and before Mn deposition. This reasoning is analogous to the integrated intensity for a small crystal (chapter 4 of Warren's book [81]) that is proportional to the volume of the crystal, but here applied to a surface.

After RT deposition of a fraction of Mn monolayer (0.35 ML), the intensity of the reconstruction peaks is significantly attenuated. Indeed, in the freshly deposited submonolayer, Mn atoms deconstructs about 80% of the *Pt-hex-0.7°* (fig. 3.4-b) and stabilize the (1×1) surface. This drastic decrease is better seen in the linear scale inset. Simultaneously, faint $c(2 \times 2)$ peaks at half-integer indexes show up. LEED measurements (figure 3.5) for similar Mn coverage and conditions confirm this result. The presence of $c(2 \times 2)$ peaks - from both LEED and GIXRD - indicates that the 25% excess of Pt atoms comes to the surface and reacts with the Mn adatoms to form a partially $c(2 \times 2)$ ordered MnPt surface alloy from the very first steps of growth. Similar features have been seen by LEED for annealed films of 0.6 up to 3 ML of Mn on *Pt-hex* [138] and correspond to a $MnPt_3$-like surface alloy.

Ten hours after the 0.35 ML deposition, only 8% of the surface remains reconstructed (fig. 3.4-c). This further deconstruction may be a consequence of a kinetic process of the Mn adatoms taking place or of the residual gases, especially with the high density of surface defects [130] after deposition. A complete set of reflection intensities along integer CTRs were measured, during an interval between 4 to 10 hours after the deposition.

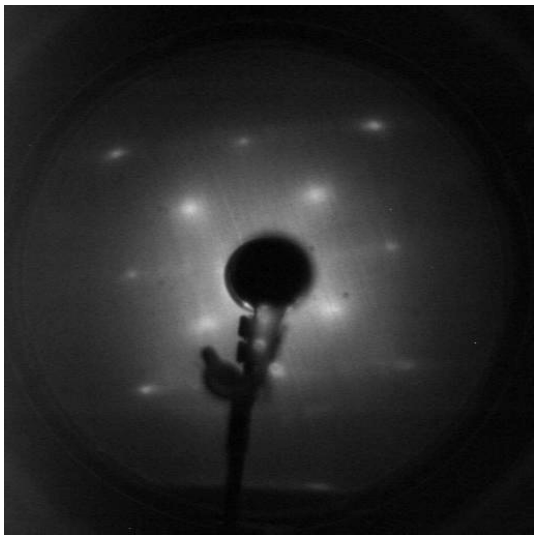

Figure 3.5: LEED pattern (beam energy of 105 eV) after 0.4 ML Mn deposition, giving the $c(2 \times 2)$ symmetry.

The deconstruction process is faster just after the growth, as the chamber pressure is higher while the source is turned on, so the CTRs measured should correspond to the situation of figure 3.4-c, with only about 8% of reconstruction left.

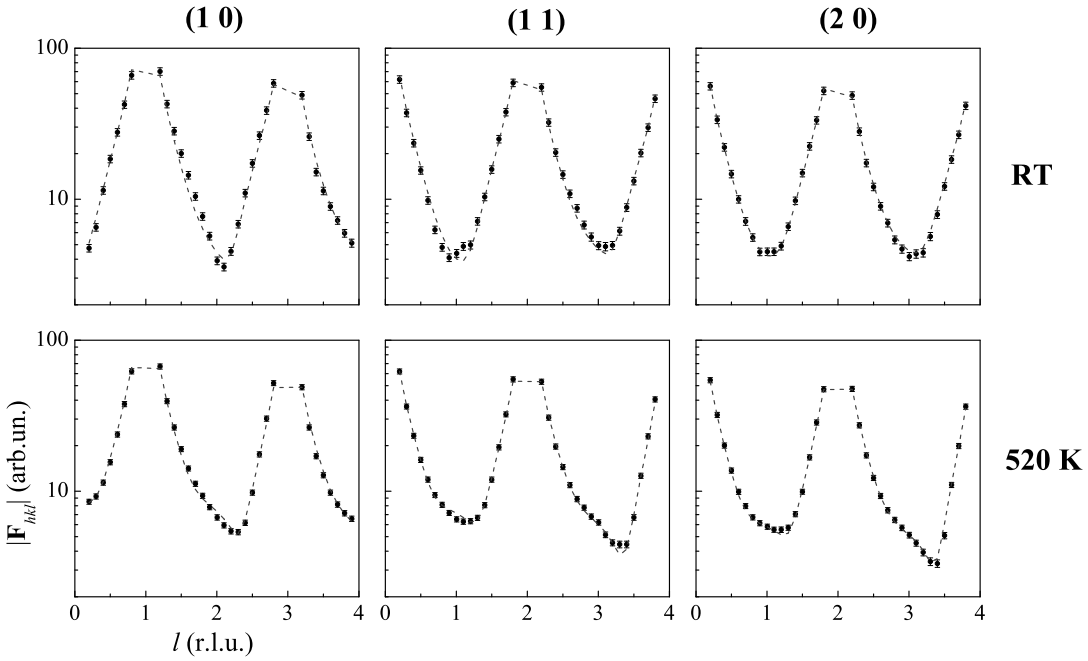

Figure 3.6: Experimental data with error bars and fitting curves (dashed gray) of CTRs for 0.35 ML of Mn at RT (top panels) and after annealing at 520 K (bottom panels).

A fitting model composed by three atomic layers with the bulk plane group symmetry (P4mm) was used to simulate the structure factors derived from measurement. We give the index 0 to the layer initially covered by the reconstruction, indicating that it comes from the substrate itself. Other two more adlayers are considered, layer 1 and 2. The main fitting parameters are the occupancy (θ) of Mn and Pt atoms in each layer,

varying from 0 to 1, and the distance d between layers. Two distinct Debye-Waller factors (DW) are also fitted, one for layer 0 and the other for both layers 1 and 2. To the substrate DW is given the bulk value of 0.31 [140]. In general, the DW is strongly correlated to the occupancy parameters, as will be discussed below. The quality of the fit is evaluated by the normalized χ^2-value (the smaller the better) and by comparing the shape of the simulated and experimental structure factors of the CTRs.

We find a strong correlation between the Mn and Pt concentration in the different layers. In the fitting, there is a tendency to overestimate the Mn content without, however, any significant improvement on the fitting quality (χ^2 slightly decreases in spent of a drastic change in θ_{Mn}). We decided then, to rely on the nominal value of 0.35 ML, calibrated by the quartz-balance and by the anti-Bragg scattering oscillations, and fix the total Mn occupancy. A comparison of the best fit with the experimental structure factors is displayed in figure 3.6 and a scheme of the corresponding model in figure 3.7. The fitting details are summarized in table 3.1.

The fit results show just small variations of the inter-layer distance, within reasonable values. Layer 0 presents no Mn atoms, indicating a negligible inter-diffusion, consistent with the low surface energy of Mn ($1.6\,\mathrm{Jm^{-2}}$) [141] compared to Pt one ($2.7\,\mathrm{Jm^{-2}}$) [51]. However, this layer is not completely filled, the Pt occupancy ($\theta^0_{\mathrm{Pt}} = 0.92$) indicates that the remaining 8% of the surface is composed by *Pt-hex-0.7°*, as the hexagonal domains do not contribute to the diffraction intensity in the integer rods. This result is in excellent agreement with the value expected from the (1.21 0 0.15) rocking scan integration (fig. 3.4-c). All Mn atoms are in layer 1 and formation of Mn islands is avoided.

The total Pt occupancy of layers 1 and 2 ($\theta^{1,2}_{\mathrm{Pt}} = 0.4$) is higher than the expected value (0.23) from a deconstruction of 92% of the *Pt-hex-0.7°* layer with 25% excess atoms. This Pt excess is however, within the fitting error, once there is a correlation between Pt occupancy and DW. Indeed, the fitted ($\chi^2 = 2.1$) DW for layers 1 and 2 (DW = 1.62) seems to be over-estimated,[3] as a value of DW = 0.7 gives the expected value for the Pt occupancy with $\chi^2 = 2.2$, only. Many different models were tried: among others, the most relevant involved 2, 3 or 4 layers, allowing buckling of Mn and Pt atoms in layer 1 and fixing DW with bulk values. The model described above is the simplest one found that gives the best fit, based only on physically reasonable assumptions.

In summary, we obtain both qualitative and quantitatively that the first surface layer contains an ordered MnPt alloy and that the *Pt-hex-0.7°* is almost completely lifted after the 0.35 ML of Mn deposition at room temperature.

The previously described layer was then annealed up to 520 K for 30 min and the same measurements were performed. According to the rocking scan integration (fig. 3.4-d) only a residual part, 3%, of the original reconstruction remains; this is as also observed in the CTRs fitting, where $\theta^0_{\mathrm{Pt}} = 0.96$ (table 3.1). The faint $c(2 \times 2)$ peaks are still present with roughly the same intensity as before. The same model as before was assumed and the CTRs fitting (fig. 3.6 and table 3.1) gives results very similar to the as-deposited sample, with an even better agreement factor (χ^2=1.5). An important

[3] Bulk values are $\mathrm{DW_{Mn}} = 0.44$ and $\mathrm{DW_{Pt}} = 0.31$, taken from ref. [140].

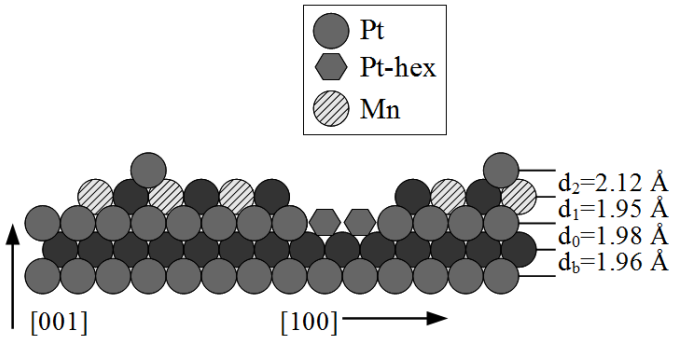

Figure 3.7: Sketch of RT model with indication of fitted inter-layer distances.

outcome from the quantitative analysis is that the Mn diffusion, although existing, is negligible after annealing at 520 K. The DW values are reasonably small, so that the Pt occupancy in layer 2 ($\theta^2_{\mathrm{Pt}} = 0.11$) and the total amount of Pt in the surface ($\theta^{1,2}_{\mathrm{Pt}} = 0.4$) indicate that some additional Pt atoms migrate to the surface.

sample:	0.35 ML Mn			+ annealing at 520 K		
layers	θ(Pt/Mn)	d(Å)	DW	θ(Pt/Mn)	d(Å)	DW
2	0.07/0.00	2.12	1.62	0.11/0.00	2.08	0.44
1	0.33/0.35	1.95	1.62	0.29/0.34	1.91	0.44
0	0.92/0.00	1.98	0.50	0.96/0.01	1.96	0.64
Bulk	1/0	1.96	0.31	1/0	1.96	0.31
χ^2	2.1			1.5		

Table 3.1: Fitting results for 0.35 ML of Mn at RT and annealed at 520 K

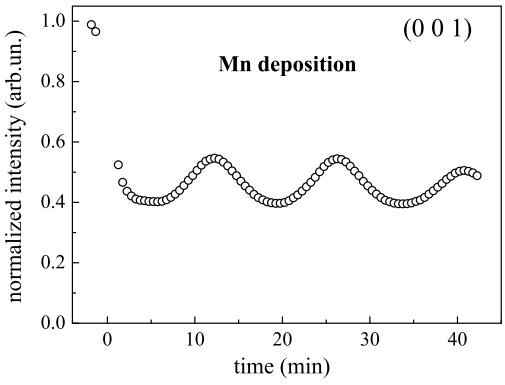

Figure 3.8: Growth-oscillations for Mn RT deposition at specular (0 0 1) position, evidencing a layer-by-layer growth mode up to at least 6 ML.

The deposition of 1.2 ML of Mn in a freshly cleaned substrate yields a surface structure that is a quite natural evolution compared to the sub-monolayer case. The hexagonal peaks are reduced to 2% but are still present (fig. 3.4-e) and similar traces of MnPt-c(2x2) peaks are observed. The quantitative analysis of the CTRs (fig. 3.9 and table 3.2) yields a first surface layer with $\theta^1_{\mathrm{Mn}} = 0.58$ and $\theta^1_{\mathrm{Pt}} = 0.39$, which is an almost complete layer containing non-stoichiometric ordered and/or disordered MnPt alloy. A second surface layer with essentially the remaining Mn atoms ($\theta^2_{\mathrm{Mn}} = 0.60$)

and negligible inter-diffusion completes the model (table 3.2). In this fit the Debye-Waller factors were kept constant with the bulk values, as they have a tendency to even smaller values, what is not reasonable. As a matter of fact, it has been verified up to six monolayers that, after the initial alloying process, Mn on Pt(001) grows layer-by-layer at RT, as can be seen by the oscillations at the anti-Bragg specular position (fig. 3.8). The same behavior was observed at non-specular (111) position, confirming an epitaxial growth. This observation agrees with the CTR analysis that gives an almost complete layer 1 and no third surface layer. This result is consistent with LEED observation by Kim et al. [138] that the hexagonal reconstruction spots turns to bright $p(1\times1)$ for RT Mn deposition up to 3.0 ML.

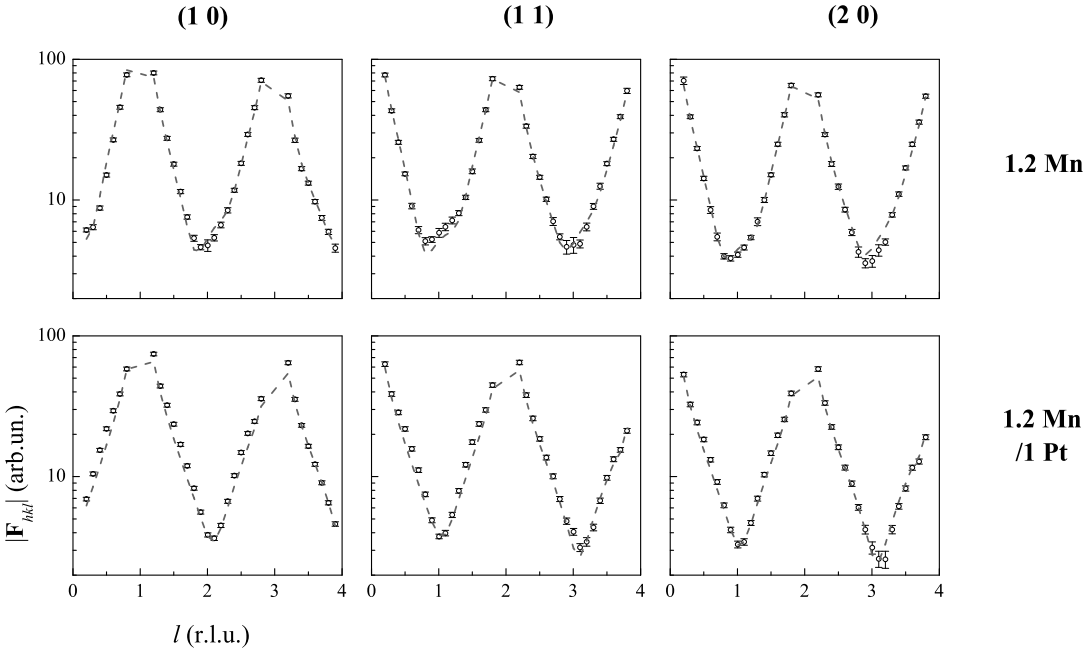

Figure 3.9: Experimental data with error bars and fitting curves (dashed gray) of CTRs for 1.2 ML of Mn (top panels) and 1 Pt/1.2 Mn bi-layer (bottom panels) at RT.

sample:	1.2 ML Mn		+ 1 ML Pt	
layers	θ(Pt/Mn)	d(Å)	θ(Pt/Mn)	d(Å)
more	-	-	*Pt islands*	2.04
2	0.00/0.60	1.91	0.08/0.60	2.00
1	0.39/0.58	1.95	0.39/0.58	1.94
0	0.97/0.03	2.00	0.97/0.03	1.95
Bulk	1/0	1.96	1/0	1.96
DW	0.31/0.44		0.31/0.44	
χ^2	4.4		11	

Table 3.2: Fitting results for 1.2 ML of Mn and for 1.2 ML Mn/1ML Pt at RT

3.1.3 Pt growth on Mn/Pt(001)

Always at RT, one monolayer of Pt was deposited on the Mn(1.2)/Pt(001) surface, described just above, and the surface was studied again. Six non-equivalent CTRs ((1 0), (1 1), (2 0), (2 1), (2 2) and (3 0)) were measured, and the fit curves for the first three CTRs can be compared to the 1.2 ML-Mn ones in figure 3.9 (bottom panels). After trying different models, the simplest and most consistent one was found to be similar to the previous model, only with the addition of Pt islands above layer 2. During the fit, the occupancies for Mn and Pt in layers 0, 1 and for the Mn in layer 2 were fixed to the values obtained for the 1.2 ML-Mn surface (table 3.2).

The CTR intensity half-way between Bragg peaks, is considerably reduced (fig. 3.9, bottom panels), as for example at the deep around $l = 2$ for the (1 0) rod, indicating an increased roughness (3D Pt growth). The Pt islands are simulated with a beta-like model [88], where each island layer (with label n=0,1,2,etc.) have an occupancy given by $\theta_n = \theta_0 \beta^n$. From the fitting results we obtain a quite rough surface, with $\theta_0 = 0.17$ and $\beta = 0.8$. The amount of Pt in the second surface layer is also small ($\theta^2_{Pt} = 0.08$). A sketch of the final model, where small Pt islands cover the Mn (MnPt) layer, is shown in figure 3.10, with inter-layer distances indicated (see also table 3.2). The high roughness of the surface affects the data quality, in a measure that it makes difficult the background subtraction in anti-phase region. As consequence, quantitative analysis are compromised ($\chi^2 = 11$) and the high value of β or the inter-layer distances within the islands (2.04 Å, while one could expect to be smaller than the bulk value) cannot be trusted. The possibility of structural disorder in these islands cannot be neglected, as the non-specular CTRs are sensitive only to the atoms with the same symmetry as the substrate. Anyway, this model clearly gives us the important general information that, at RT, Pt grows in 3D-mode on the Mn(1.2)/Pt(001). Moreover, the hexagonal reconstruction is washed out (fig. 3.4-f) and no traces of $c(2 \times 2)$ are found after Pt deposition. One has to consider, however, that the large roughness may simply hinder these features.

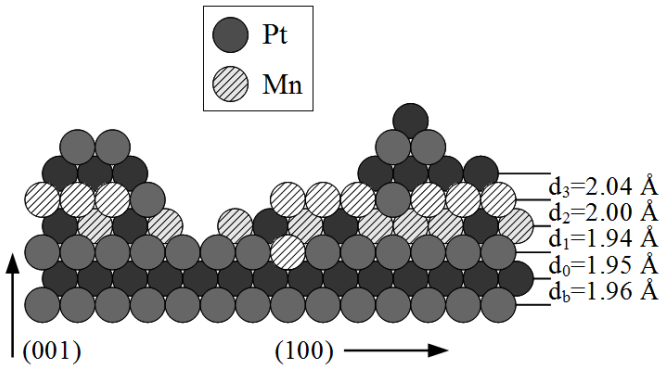

Figure 3.10: Sketch of model for 1 Pt/1.2 Mn bi-layer with indication of fitted inter-layer distances.

3.1.4 Homoepitaxial Pt growth on Pt(001)

Growth oscillations are barely observable for Pt deposited at RT on *Pt-hex-0.7°* (open triangles in figure 3.11), pointing to a rough surface, as in the growth on Mn/Pt(001) described above. As reported by Linderoth et al. [142], Pt deposition contributes to lift the reconstruction for coverages higher than 0.07 ML of Pt; below this coverage Pt nucleates as anisotropic reconstructed islands. We determined, by the same procedure of integrating the reconstruction peak (see figure 3.4), that 0.65 ML of Pt deconstructs up to 50% of the surface and 0.8 ML deconstruct about 80%. This property was used as a first step before starting alternate depositions of Mn and Pt; the aim was to get rid of the reconstruction and reduce the alloying in the first steps of growth (section 5.1.1). The effect of temperature in the homo-epitaxial Pt growth can be observed in figure 3.11 (full circles), where clear growth-oscillations show up at 610 K. A systematic study of temperature dependence of Pt homo-epitaxial growth on the Pt(001) face is still lacking, but a tendency of layer-by-layer growth with higher temperatures can be expected. The formation of Pt-islands on the surface (3D growth) at RT is not surprising and can be directly related to the behavior of homo-epitaxial growth of Pt on Pt(111) at temperatures near to RT [79]: in this case, a reflection barrier to jump down step edges is proposed as the responsible for the 3D growth. For higher temperatures, above 500 K, the thermal energy is large enough so that island adatoms can jump easily onto the layer below and there is no nucleation until layer completion (2D growth). A similar reflection barrier was proposed at the island edges of the Pt(001) plane [143]. Moreover, for Pt(001)-(1 × 1) surface obtained by lifting *Pt-hex-0.7°* using CO/NO [144], a maximum island size is obtained at 495 K, indicating a higher mobility of Pt atoms in the surface, not being trapped by the presence of kinks or steps at this temperature [144].

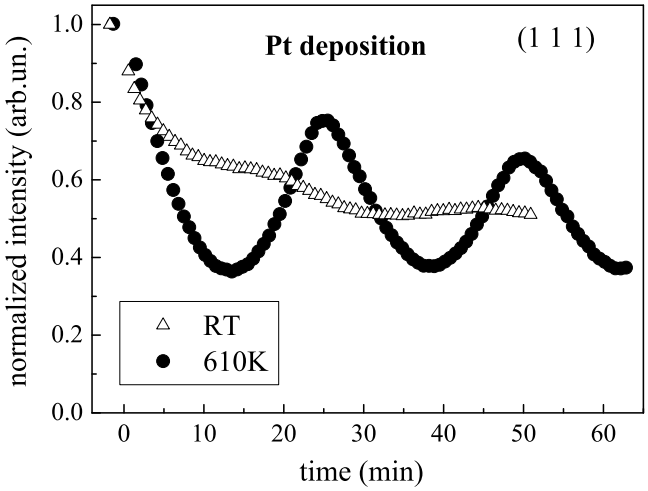

Figure 3.11: Growth-oscillations for Pt on Pt(001) at RT (open triangles) and at 610 K (full circles), around (1 1 1).

From these considerations, we learn that the better path towards a Pt and Mn alternate stacking is a deposition at elevated temperatures, where Mn presents negligible inter-diffusion into the bulk and Pt grows in a nearly layer-by-layer mode. From

fig. 3.11, $T \approx 610\,K$ seems a good compromise. The initial growth steps presented here clearly points to the inherent difficulties in obtaining long-range $L1_0$ chemically ordered MnPt structures. Our results indicate that it is not possible to grow a $L1_0$ MnPt alloy on Pt(001) at RT. The fundamental limitation are basically the 3D Pt growth mode that leads to a rough surface and the formation of an ordered two dimensional MnPt alloy. This result represents basically the interface that comes out when thicker films are deposited. The growth of thicker films, presented in the next chapter, will use favorably these pieces of information.

3.1.5 Fe deposition on Pt(001)

The RT growth of Fe on Pt(001) single crystal have been studied by STM, LEED and MOKE for coverages up 7 MLs [51]. These authors report that an atomic exchange process occurs at RT, so that after Fe deposition of 1.2 ML the surface is nearly covered with one monolayer of Pt (one Fe atom replaces one Pt atom on average), where *Pt-hex* reconstructed and unreconstructed regions coexists. For higher coverages the film grows in a quasi layer-by-layer mode. The magnetic anisotropy of as-deposited films is always in-plane. Annealing at 600 K switches the easy magnetization axis from in-plane to out-of-plane for thickness smaller than 5.2 ML. Moreover, a change from higher to lower PMA was observed at about 3.3 ML and was attributed to a phase transformation from tetragonal $L1_0$ (< 3.3 ML) FePt to $L1_2$ (> 3.3 ML) Fe_3Pt phases [51]. This structural aspect was indicated by appearance of a $c(2 \times 2)$ LEED pattern for higher thickness, however, it requires further confirmation.

We have studied qualitatively both Fe RT deposition followed by annealing and the thermally assisted deposition with the substrate held at different temperatures. The RT deposition gives no traces of order: there is no $c(2 \times 2)$ peak and no increase of the anti-phase intensity in the CTRs either. The annealing of a 5 MLs film at 650 K during 10 h gives rise to $L1_2$ domains of about 4 MLs thick and lateral correlation of 30 nm. These domains are pseudomorphic within 0.3% and have a tetragonality of $c/a = 0.96$. The unit cell volume is estimated to be of $V = 58\,\text{Å}^3$, in close agreement with the unit cell volume of $FePt_3$ alloy, that is paramagnetic at RT and antiferromagnetic below 160 K [145]. This result indicates that the Fe diffusion into the Pt is more favored than the Pt diffusion into the Fe layer. A similar result has been observed by TEM in Fe/Pt multilayer systems [146]. He et al. [51] make the supposition that the $c(2 \times 2)$ pattern observed comes from a ferromagnetic Fe_3Pt phase, what explains their magnetic behavior. Our finding puts in doubt this conclusion, although we cannot wash out the presence of Fe_3Pt by our measurements. An *in situ* MOKE study of the magnetic behavior just after GIXRD characterization would be a perfect tool to shed light into this question.

The thermally assisted deposition shows up to be a better strategy to induce the $L1_0$ ordering and no traces of $c(2\times2)$ was found to any temperature or coverage investigated. Different substrate temperatures were tried and in general the higher the temperature, the better the $L1_0$ order. Figure 3.12 shows an l-scan along the (1 1) CTR of a 3 ML Fe layer deposited with a substrate temperature of 600 K (the highest used), featuring an

order peak close to the anti-phase position. The peak width permits to estimate that 2 ordered bilayers are formed. No relaxation is observed, and the layer is pseudomorph. The peak center position ($l \approx 1.13$) gives a tetragonality of $c/a = 0.89$, suggesting that the ordered layer is Fe rich, as the bulk equiatomic $L1_0$ alloy would give a tetragonality of 0.92 for constant volume pseudomorphism.

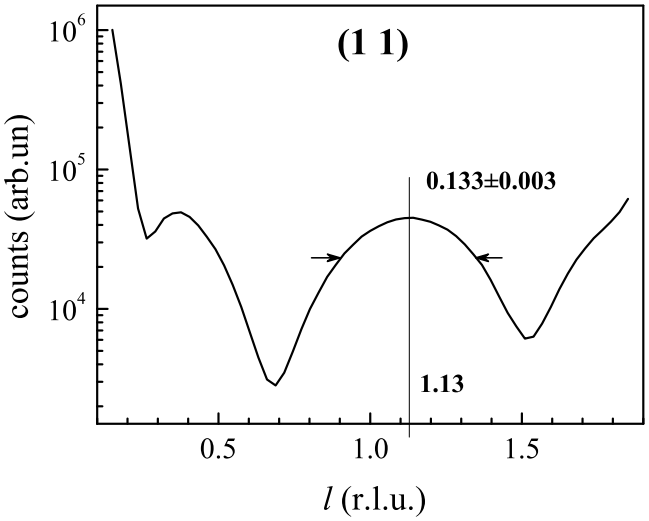

Figure 3.12: l-scan along the (1 1) CTR for 3 MLs of Fe deposited at 600 K on Pt(001). The order peak is center and width are indicated.

3.2 Growth on Ag (001)

Ag(001) has a lattice constant $a_{Ag} = 4.085$ Å, which is 2.1% and 10% larger than a_{MnPt} and c_{MnPt}, respectively. The deposition of MnPt on such a surface is therefore expected to yield the epitaxial growth of $L1_0$ MnPt with the c-axis perpendicular to the surface plane. Contrary to what happens for the deposition on Pt(001), the pseudomorphic growth of MnPt on Ag(001) would lead to a more tetragonally-distorted lattice, i.e. smaller c/a, which could have interesting consequences on the (antiferro)magnetic properties [50]. A drawback of using silver as substrate is its low surface energy. Atomic exchange processes were observed for room temperature deposition of rhodium on Ag(001): the Rh/Ag(001) system evolves toward the energetically favored Ag/Rh/Ag(001) structure [147] showing the surfactant effect of Ag atoms. Intermixing is also observed for room temperature deposition of Fe on Ag(001), where an almost pure Fe surface is obtained only after deposition of more than 3 ML [148]. The Mn/Ag(001) system also shows to be highly unstable at room temperature for thickness up to 1 ML. Such a 1 ML Mn deposition yields, at room temperature, a two-layer thick MnAg-$c(2 \times 2)$ ordered alloy [149]. Moreover, a Ag enrichment and a Mn depletion of the surface plane was observed on a time scale of about 60 min, leading to unalloyed Ag islands [150].

We are interested on basically two different systems: the possibility of growing MnPt ordered alloy with a slightly larger anisotropy and the growth of pure Fe, which shows perpendicular magnetic anisotropy up to 6 MLs. Up to this thickness, the growth

aspects and the structure are rather unclear. We have initiated a study of such systems, but quantitative analysis has not been performed, yet. For the Fe/Ag(001) we will give only a brief qualitative description. As far as the MnPt system is concerned, it seems quite clear that starting by Mn deposition is not a well-suited route due to the tendency of Mn to form the MnAg-$c(2\times2)$ alloy. Hence, before growing MnPt, we were led to the study of a thin buffer layer of Pt on Ag(001). We describe below some results obtained until now on both systems.

3.2.1 Pt/Ag(001)

To our knowledge, a study of the growth of Pt deposited on Ag(001) has never been reported. Besides the film structure is not known, surface segregation is expected due to the low Ag surface energy. The bulk phase diagram of Ag-Pt binary alloy shows a large degree of immiscibility.

We report here the study by GIXRD of the growth of 1 and 2 Pt ML on Ag(001) at room temperature. Pt is evaporated from a 2 mm ultra-pure rod using electron beam heating. The evaporation rate was about 1 ML each 20 min, calibrated measuring the oscillation in anti-phase position on the specular reflectivity, cross-checked with the quartz balance rate. The misfit between Ag and Pt is about 4%, however, deposition at room temperature of about 5 Pt ML result in an almost pseudomorphic film, evidenced by the Kiessig fringes along the Ag CTRs.

sample:	1 ML Pt/Ag(001)		2 ML Pt/Ag(001)	
layers	θ(Pt/Ag)	d(Å)	θ(Pt/Ag)	d(Å)
4			0/0.81	1.85±0.04
3	0/0.60	1.82±0.02	0.40/0.60	1.88±0.04
2	0.60/0.40	1.93±0.01	0.90/0.10	1.90±0.03
1	0.40/0.60	2.002±0.005	0.45/0.55	2.01±0.02
Bulk		2.0425		2.0425
DW	0.9±0.1/2.2±0.3		1.1±0.1/1.9±0.3	
χ^2	1.3		2.3	

Table 3.3: Fitting results for 1 ML and 2 ML Pt on Ag(001) at RT

A quantitative structural analysis was performed after 1 ML deposition. A set of 114 (hkl) non-equivalent reflections were measured along the (1 0), (1 1), (2 0), and (2 $\bar{1}$) CTR, plus 25 equivalent ones in the P4mm plane group ((0 $\bar{1}$), (1 $\bar{1}$) and (0 $\bar{2}$) CTR, the agreement factor being 0.054). The intensity of each reflection was measured quantitatively through a rocking scan and the amplitudes of the structure factors were extracted applying the standard corrections (eq. 2.20). Then, we started to model the surface considering the two border situations, 1 ML of Pt pseudomorphic on Ag(001) and a Ag/Pt/Ag(001) sandwich. The χ^2 factor for the two models are equal to 55 and 22, respectively. Despite the low agreement, the sandwich fits much better the data. Then a model was tried, with impinging Pt atoms exchanging only partially with substrate atoms. This resulted in a two-mixed layer, with an incomplete top one which was assumed to be formed by silver (see fig. 3.13, where Pt is represented by dark spheres). Besides the Ag occupancy in the top layer and the Pt concentration in

the next two ones, the first three average inter-layer distances were optimized, as well as the Debye-Waller of Pt and of Ag in the last two layers, that one of the underlying layer being kept to the bulk value. The experimental structure factors together with the best fits are shown in figure 3.14, while the optimized parameter values are reported in the table 3.3. Note the reduced χ^2 value of 1.3. The distance d_n represents the spacing between the n and the $n-1$ layer, layer 0 being the last substrate one with bulk characteristics.

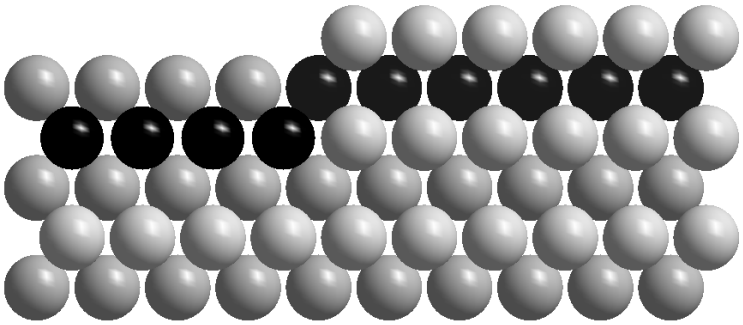

Figure 3.13: Sketch of one Pt ML on Ag(001)

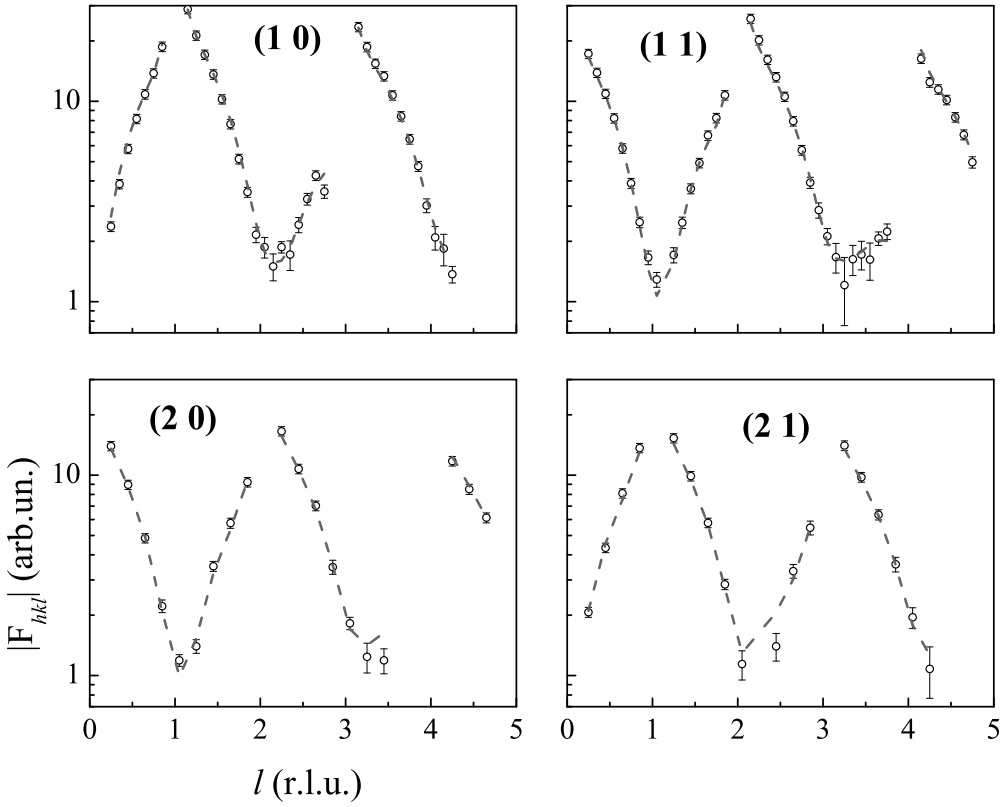

Figure 3.14: Experimental and fitted structure factors for 1 ML Pt/Ag(001) deposited at room temperature

As a next step, a second Pt monolayer was added on the previous surface. A set of structure factor amplitudes were measured on the (1 0) and (1 1) CTRs. Equivalent reflections were not measured in this case, but the same agreement factor obtained for

the 1 ML data, measured in the same experimental conditions, was used for the error bar. The fit was performed considering that only Ag atoms at the surface can exchange with freshly deposited Pt, and fitting parameters of layer 1 at the interface were then kept fixed within the error bar. A comparison of the experimental and simulated structure factors is given in figure 3.15, while the values of the best fit are summarized in table 3.3. The error bar on the atom occupancy is 0.1 or better. The incomplete top layer is supposed to be pure silver, but it is quite difficult to find separately occupancy and composition by GIXRD. It could exist some amount of Pt in the surface, what would increase the total amount of Pt found in the fit (1 ML and 1.75 ML instead of the nominal thickness of 1 and 2 ML, respectively).

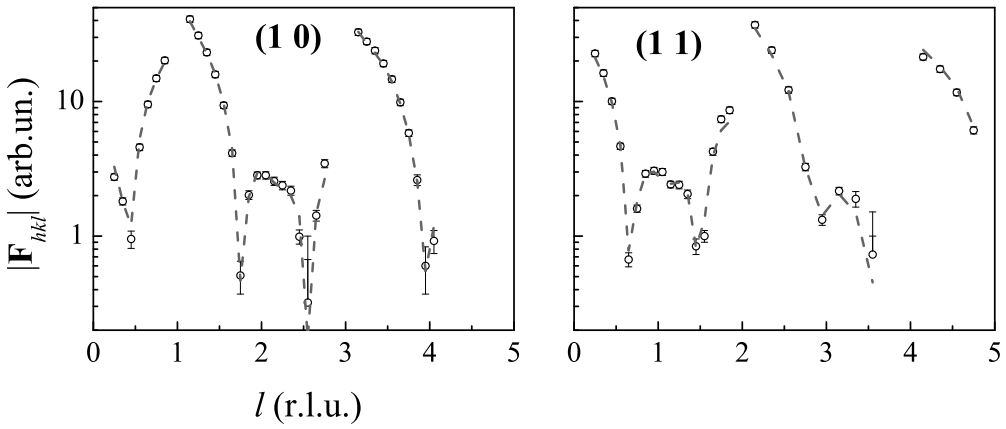

Figure 3.15: Experimental and fitted structure factors for 2 ML Pt/Ag(001) deposited at RT.

It is clear from table 3.3 that Pt deposition on Ag(001) results in a Pt enrichment in buried layers close to the surface. This is likely the result of atomic exchange where impinging Pt atoms replace Ag atoms which segregates on top. This Pt enrichment is also evidenced by the contraction of the inter-layer distances, which decrease below the Pt d_{001} one.

3.2.2 MnPt/Pt/Ag(001)

A PtMn film was grown on the Ag substrate. It was shown in the last paragraph that silver segregate on top of Pt even at room temperature. Looking at the bulk phase diagrams, it is known that above 1235 K the equilibrium phases of the Ag-Pt system are a liquid, and an *fcc* solid solution, with a large degree of immiscibility. The existence of inter-metallic phases at lower temperatures is controversial. For Ag-Mn, contradictory results exist in the literature, too. However, substantial Mn solubility in solid Ag has generally been reported [145].

In this work a temperature of 570 K was chosen for growing PtMn, despite the fact that Ag segregation is expected. The idea is that silver could act as a surfactant layer favoring a layer-by-layer growth, possibly without intermixing with the PtMn alloy. After deposition of a 2 ML Pt buffer layer at room temperature, a nominal 8 PtMn bilayer thick alloy was grown at 570 K by alternated monolayer deposition of

each element, to mimic the $L1_0$ order. An extra Pt layer was deposited on the last Mn one. The Auger spectroscopy shows large values for the Auger peaks signal ratios Ag(351 eV)/Pt(235 eV) and Ag(351 eV)/Mn(589 eV), confirming the silver surface segregation.

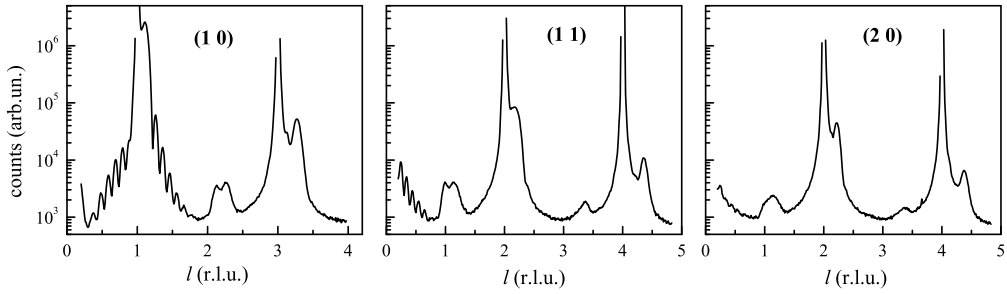

Figure 3.16: $(PtMn)_8Pt_3/Ag(001)$. Intensity measured by l-scans along the (1 0), (1 1) and (2 0) CTRs.

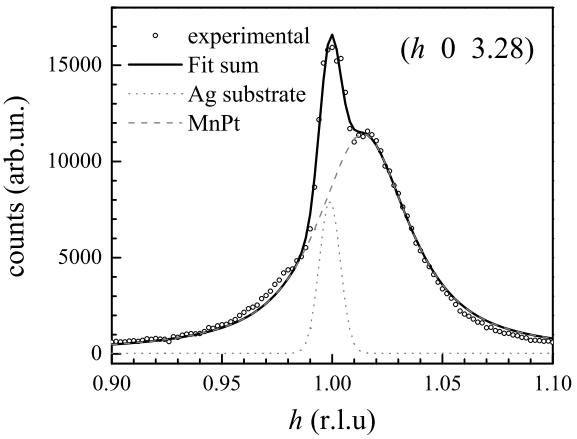

Figure 3.17: $(PtMn)_8Pt_3/Ag(001)$. Intensity measured scanning the momentum transfer modulus parallel to the plane, close to the (1 0) Ag CTR.

Figure 3.16 shows the intensity measured along the (1 0), (1 1) and (2 0) CTRs. This raw data allows already several considerations. The Kiessig fringes give the film thickness, as described in chapter 2. A value of 4.0 ± 0.1 nm is obtained, which is a little bit larger than the nominal thickness of 3.5 nm obtained considering 8 PtMn bilayers plus 3 Pt MLs at the interface, but the difference is within the typical error bar of the sources calibration. The very nice Kiessig fringes observed at low l prove that there is neither inter-diffusion into the silver at the interface nor intermixing over a few layers at the surface, despite the Ag segregation. The strong decreasing of the fringes amplitude with increasing momentum transfer is an indication of a loss of pseudomorphism. This is particularly clear in the comparison between the (1 1) and the (2 0) CTRs. Indeed, a high resolution scan of the momentum transfer modulus parallel to the surface (radial scan) is shown in fig. 3.17. A rod characteristic of the deposited film is observed, which is convoluted with the Ag CTR. It corresponds to a smaller in plane lattice parameter of the film with respect to the substrate. Fitting the position of the PtMn rods measured

close to several CTRs, a value $a_{MnPt}^{film} = 4.03 \pm 0.01$ Å is found. Due to the correlation length of the domains parallel to the surface, which determine the rod broadening, and to the epitaxial relationship with the substrate, a film contribution is observed along the silver CTRs. However the structure factors cannot be fitted in an easy way, and only a qualitative analysis was performed. Peak characteristic of the film are observed at higher l values compared to Bragg peaks. Fitting this peak with a Gaussian, a value $c_{MnPt}^{film} = 3.75 \pm 0.02$ Å is found. Both a_{MnPt}^{film} and c_{MnPt}^{film} are slightly larger than the corresponding ones for the stoichiometric MnPt bulk alloy, which can be due to a richer Pt composition originating either by the inter-diffusion with the 3 Pt MLs at the interface or/and by the incertitude in the source calibration.

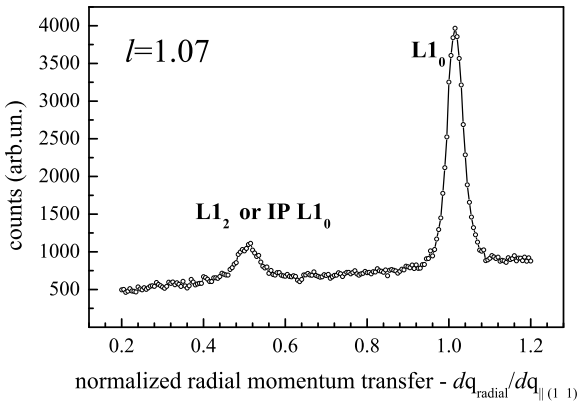

Figure 3.18: $(PtMn)_8Pt_3$/Ag(001). Radial scan across the (1.015 1.015 1.07) LRO peak.

The peaks almost in the middle between Bragg peaks are a signature of the ordered $L1_0$ phase. Neglecting the Debye-Waller term, a rough estimation of the order parameter S is given by $S = \sqrt{\frac{I_{sup}}{I_{fun}}} \cdot \frac{f_{Pt}(q_{fun})+f_{Mn}(q_{fun})}{f_{Pt}(q_{sup})-f_{Mn}(q_{sup})}$ (see chap. 2). Measuring along the (10) rod, we have $S = \sqrt{\frac{I(1\ 0\ 2.18)}{I(1\ 0\ 3.7)}} \cdot \frac{f_{Pt}(1\ 0\ 3.7)+f_{Mn}(1\ 0\ 3.7)}{f_{Pt}(1\ 0\ 2.18)-f_{Mn}(1\ 0\ 2.18)} = 0.37$. This is a relatively high value. A better long range order can be surely achieved by a more accurate calibration of the evaporation rates, considering that a deviation from the PtMn stoichiometry results in a smaller order parameter. Parallel to the plane, the correlation length of ordered domains is about 6 nm, which is the same of the PtMn film itself. Figure 3.18 shows a radial scan across the (1.015 1.015 1.07) long range order peak. A second peak appear at (0.508 0.508 1.07) which is the signature of an ordered minority phase. This can be explained either with the presence of a $L1_2$ phase region or with a $L1_0$ domain with in plane c-axis.

In conclusion, deposition on Ag(001) surface at 570 K favors the growth of a PtMn $L1_0$ phase with the c axis perpendicular to the surface, with silver segregation, and a relatively high order parameter.

3.2.3 Fe/Ag(001)

The first steps of Fe growth on Ag(001) was studied *in situ* by GIXRD. A beam energy of 22 keV was used. The films were grown at room temperature, to minimize intermixing, then moderate annealing, up to 470 K, was done to improve the quality of the surface

and modify morphological aspects. The growth was followed in real time along the (1 $\bar{1}$) CTR - to track the perpendicular lattice parameter c, or tetragonal distortion (c/a) - and in the plane (h, k) at the (1 $\bar{1}$ 2.7) and (1 $\bar{1}$ 2.83) positions in reciprocal space - to confirm (or infirm) the pseudomorphic behavior. Complete sets of CTRs were measured for some particular coverages. This allows to solve the structure and get accurate lattice parameters. However, these data have been quite recently acquired and a complete quantitative analysis has not been done, yet. We present here some remarkable outcomes that deserve a brief comment.

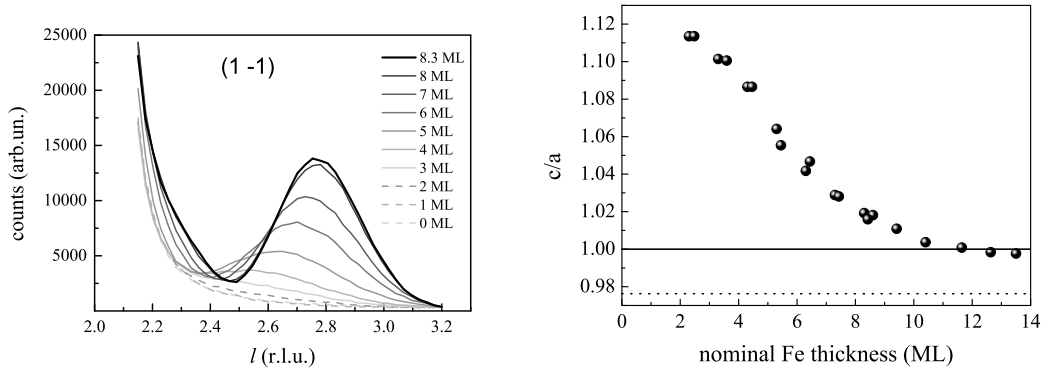

(a) (b)

Figure 3.19: (a) Real time evolution of the (1 $\bar{1}$) CTR during the Fe deposition. (b) Tetragonal distortion as function of coverage for two different depositions. Solid line gives the limit of no distortion; dotted line gives the situation where the volume of the unit cell is the same as bulk *bcc* Fe.

Probably, the most interesting property of the Fe/Ag(001) system is the spin reorientation transition as function of the thickness and temperature [70]. At room temperature, the easy axis changes from out-of-plane to in-plane around 6 MLs. By tracking the in-plane lattice parameter of the deposited layer up to 8, 11 and 14 MLs, in three different depositions and even after annealing at 470 K, we could eliminate a possible relaxation of the Fe film as an explanation for the SRT. The Fe films grow pseudomorphically taking the in-plane lattice parameter of Ag, $a_{Ag} = 4.0853$ Å, or, in the body-centered cubic lattice of Fe, $a = 2.889$ Å, larger than the bulk *bcc* Fe ($a_{Fe} = 2.8665$ Å) by 0.8%. Interestingly, however, c/a does not become smaller than one, as it would be expected after pseudomorphic growth at constant volume.

The real time evolution of the (1 $\bar{1}$) CTR during Fe on Ag(001) deposition for a up-to-8.3 MLs film is presented in figure 3.19-a. Tracking the position of the peak, running from about 2.6 to 2.8 in reciprocal lattice units, yields a good average estimation of the c value. A more accurate quantitative analysis based on a model layer has not been performed, yet. In figure 3.19-b, we present the estimation of the tetragonal distortion for two different experiments, namely for the up-to-8 and up-to-14 MLs depositions. One clearly see that the distortion is larger than unit up to about 10 MLs. Nevertheless, we must emphasize that the in-plane parameter is that of Ag(001) and, even above 10 MLs where c/a is close to one, the volume of the unit cell is still larger than for bulk Fe. In figure 3.20 one can observe the evolution of the cell volume at different coverages,

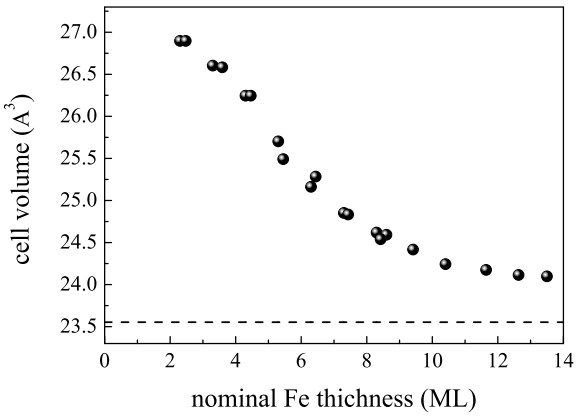

Figure 3.20: Evolution of the volume of the unit cell for the Fe film as function of the coverage. The dash lines gives the volume of the bulk Fe *bcc*.

compared with the *bcc* Fe bulk cell volume of 23.55 Å^3. For very low coverages, the average cell volume of Fe films is larger by about 14%. It is evident that a more accurate analysis must be done, in particular in this low-coverage regime, to take into account the contribution of the first layer spacing and a possible influence of a surfactant Ag layer.

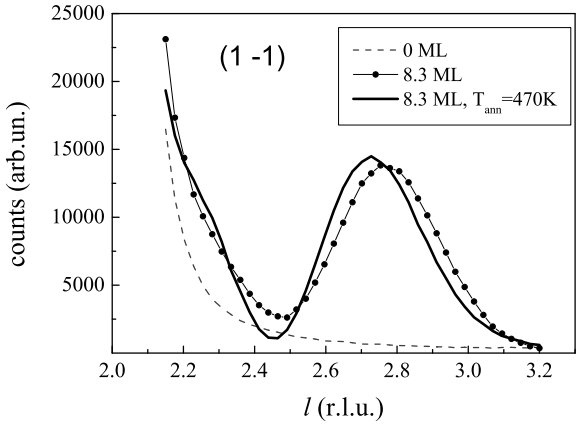

Figure 3.21: (1 $\bar{1}$) CTR before and after annealing the 8.3 MLs Fe film on Ag(001).

One additional comment concerns the annealing at 470 K that is often mentioned in the literature. This is normally done to improve the morphology by reducing the surface roughness. Fe and Ag have a high degree of immiscibility and this would also help to separate a possible presence of Ag on the Fe layer. Schaller et al. [151] used STM to demonstrate that an initial 4.5 MLs rough surface ($\sigma_{RT} \simeq 0.105$ nm) is transformed into islands with single atomic steps after annealing at 470 K ($\sigma_{470K} \simeq 0.079$ nm). In addition, they observed that, concomitant with the improvement in morphology, the in-plane anisotropy turns into out-of-plane.

In figure 3.21 we show the effect of the annealing on the (1 $\bar{1}$) CTR for the 8.3 MLs film. The annealing reduce the roughness, as seen from Kiessig oscillations (not shown), and has the effect of increasing the c lattice parameter, while keeping the pseudomorphism (no changes in a lattice parameter). In addition, from Kiessig oscillations (not

shown) we observe that the initial rough surface is thicker than the nominal value but goes back close to it after annealing. This is compatible with the idea that the surface is much flatter and some scattered Ag atoms within the layer goes to the surface. Auger electron spectroscopy showed a increased amount of Ag compared to Fe after the annealing.

The epitaxial conditions and inter-layer spacing will be precisely determined in a wide range of coverage, in particular within the SRT region. This will teach us which parameters are the more relevant for the perpendicular magnetic anisotropy.

To summarize this section, we verified the limit of the pseudomorphic growth and demonstrated that there is no relaxation of the Fe films up to coverages of 14 MLs, and even after mild annealing at 470 K. It is known that for constant thickness (4 to 6 ML) the SRT takes place by moderate heating above room temperature. We have shown that the structural counterpart is an increasing of the tetragonal distortion and the appearance of a surfactant layer of Ag.

3.3 Summary

The first steps of metal growth on *Pt-hex* are strongly affected by the reconstruction. The substrate reconstruction is lifted locally by metal deposition. We show that for Mn deposition this lifting leads to an incorporation of platinum excess atoms into the first layer of the growing film, resulting in a local $c(2 \times 2)$ arrangement. Alloying in the first layer is a drawback of deposition on *Pt-hex* surface. Such phenomena could perhaps be reduced by suppressing the reconstruction with exposure to hydrogen, as happens for Ir(001)-(5×1) [152].

Homoepitaxial growth of Pt on Pt(001) results in quite a rough surface, as evidenced by the behavior of the intensity measured in anti-phase condition for the scattering from next (001) planes. Such an intensity measured versus time during deposition at RT do not show any oscillations, at the opposite of what is expected for layer-by-layer growth. An equivalent behavior has been observed for Pt on Pt(111) growth, and is the result of a potential barrier for adatoms at the steps, which have no enough thermal energy to jump on a lower terrace. A detailed GIXRD analysis shows that 3D growth also happens for Pt deposited on the Mn/Pt(001) surface. It was found that almost layer-by-layer growth is achieved by deposition at about 610 K, temperature at which no significant Mn diffusion into the Pt bulk is observed. Deposition of Fe on *Pt-hex* at 600 K results directly in an ordered $L1_0$ phase. These findings will be exploited in growing the alloys described in the next chapter.

At room temperature Fe grows pseudomorphic on Ag(001), up to 14 ML at least. We show here that the the spin reorientation transition observed at about 6 ML is probably related at a change in the volume of the unit cell and not to a relaxation of the lattice parameter parallel to the surface plane.

Finally, an ordered alloy is obtained by alternated Pt and Mn deposition at about 570 K on Ag(001). Silver segregates at the surface, and seems to act as a surfactant for the layer-by-layer growth. The large substrate lattice constant favors the growth of a $L1_0$ phase with the *c*-axis perpendicular to the surface.

Chapter 4

GIXRD approach to the study of order on $L1_0$ MnPt films

We present here *in situ* GIXRD investigations of the synthesis of MnPt alloy with the purpose of obtaining out-of-plane $L1_0$ films in a controlled manner. As described previously, the $L1_0$ structure corresponds to an *fct* binary alloy with alternate stacking of atomic planes (of different nature) along the *c*-axis. To mimic this order, we perform an alternate deposition of Mn and Pt MLs, as done by Shima et al. [48] for growing ultra-thin FePt. We often refer to the deposition of two alternate monolayers as a bilayer (BL). The substrate temperature has shown to play an important role inducing out-of-plane $L1_0$ order [48, 54]. This technique has advantages, from an applied point of view, in relation of the RT deposition plus annealing. Generally, the required temperatures to attain order are lower and the process is faster, once the time consuming step of annealing is eliminated.

The study of the growth and ordering of MnPt alloy on Pt(001) follows two preparation methods: the alternate deposition at RT with subsequent annealing, and the thermal alternate deposition. The misfit between substrate and deposited layer is expected to influence the ordering, the orientation and the lattice distortion of the alloy. The study of the first steps of growth gives the necessary basis to understand the growth of thicker films. There is a delicate temperature threshold that one has to play with to obtain an almost flat surface during growth (layer-by-layer growth) and induce the desired order, without however destroy the interfaces by diffusion.

The final thickness of our samples attains up to 6 nm, or 30 MLs, what can be classified as ultra-thin film from a magnetic point of view, but for the GIXRD analysis this represents thick films. For such a thick film, a greater number of reflections have to be measured in order to make possible the layer modeling and fitting. The conventional measurement mode turns out to be too time-consuming and we used a faster data acquisition mode. Corresponding analysis procedures were implemented and are described.

4.1 GIXRD to "thick" films

For the first steps of growth presented in chapter 3 the total thickness of the layers studied quantitatively was limited at most to 4 MLs, less than 1 nm. The CTRs show smooth variations (fig. 3.6 and 3.9) and the experimental structure-factor amplitudes ($|F_{hkl}|$) are derived from the integrated intensities of the rocking scans at each ($h\,k\,l$) position (arcs indicated in figure 4.1). The modeling takes into account each surface layer independently, permitting occupancy and inter-layer spacing to vary without severe constraints. This same approach, however, is not suitable to thicker films (up to 6 nm). When film thickness increases, the complexity to the CTRs also increases. The first feature is the presence of thickness oscillations (or Kiessig fringes), giving a fast varying CTR profile (as seen in fig. 4.2, close to Bragg peaks). Then, inter-diffusion, segregation, roughening and ordering add more degrees of complexity to the layers.

A proper study of these layers demands the acquisition of large number of reflections. For example, we measure about 10 CTRs with up to 700 reflections per CTR for the final samples, what gives 7000 reflections. With the usual rocking scan procedure, each reflection corresponds typically to a 40-points scan (1 second per point), giving a total time (just for data acquisition) of more than three days. The picture is even worse if we want to prepare hetero-structures composed by two layers (anti-ferromagnetic and ferromagnetic) and we intend to study the first one separately, before depositing the other one. Not only we would spend the double of the time for acquisition, but mainly the interface would be contaminated by residual gases during this time[1]. Specially the FM/AFM interface should be as free from contamination as possible.

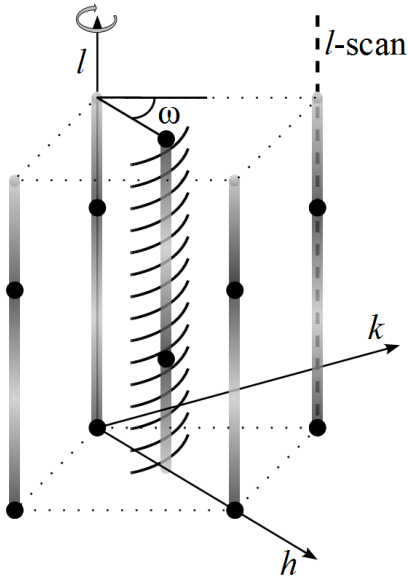

Figure 4.1: Reciprocal space sketch showing rocking scans (solid arcs) and stationary l-scans (dashed line) along a CTR. The scattered intensity is represented by cylinders and the Bragg peaks by solid spheres.

[1] In a pressure of 10^{-10} mbar, we have 1 Langmuir in less than 4 hours

An alternative data acquisition strategy based on stationary l-scans, which allows the reduction by approximately one order of magnitude of the time needed to measure a complete data set, was then used [153, 154]. In this procedure, one stays always on the crest of the CTR, without rocking the sample, while changing the value of l in reciprocal space (all sample and detector movements are computer controlled to follow the desired trajectory in reciprocal space). Instead of taking a full scan, only one point is measured at each l, which implies a huge time saving. We often use this fast scans during sample growth or while annealing a sample, to have a quick qualitative picture of the sample evolution. It was recently shown [154] that l-scans could also reliably be used to derive $|F_{hkl}|$, once some care was taken in the data acquisition. This requires good quality single crystals. We have developed a systematical measurement and data treatment procedure based on this approach to study the structure of our films. An evident drawback of the l-scan is that it is very sensitive to sample misalignment, as one can easily deviate from the maximum intensity of the CTR. To minimize misalignment effects, for each CTR, the $(h\,k)$ positions are carefully optimized at two points (low l and high l) by repeated sample rocking and detector in-plane scans (respectively, ω and δ circles in SUV z-axis diffractometer, fig. 2.4-a). The l-scan trajectory is then determined by the straight line passing through these two optimized points. Indeed, this kind of alignment is also done for the standard rocking scan procedure, but in that case it is not so crucial.

The background coming from thermal diffuse scattering, that for rocking scans is subtracted in the integration procedure, has also to be taken into account in the fast scans. To estimate the background, we measure an additional l-scan shifted from the CTR maximum (integer h and k) [154] by rotating the sample by an angle $\sim 3 \times \Delta\omega$ from the aligned position to avoid any CTR contribution ($\Delta\omega$ is the angular width of the CTR measured in a rocking scan). After subtracting the measured background from the l-scan to obtain the intensity I_{lscan}, a set of correction factors, similar to eq. 2.20 are applied to derive the final corrected $|F_{hkl}|$ values. The geometrical Lorentz factor that applies to stationary l-scans, given by $L_{lscan} = 1/\sin\beta$,[2] is different from $L_{rocking}$. The rod interception correction C_{rod} is not applicable in this geometry [154]. A procedure to automatically apply correction factors for l-scans and extracting $|F_{hkl}|$ was developed. We checked the validity of this procedure by comparing with the $|F_{hkl}|$ values obtained by the ANA program [91] for rocking scans.

As shown in figure 4.2, with the inclusion of a multiplicative scale factor, these two methods have a quite good agreement. To determine the multiplicative factor, we have included in the general procedure developed the measurement of some rocking scans along all the CTRs (with typically 0.5 r.l.u. between points) that are integrated and corrected with ANA program and compared to the corrected l-scans. The corrected $|F_{hkl}|$ obtained by this procedure allow us to compare consistently data collected by both methods, as will be necessary in the following when treating ordered alloys. In figure 4.2, one can remark that for the (2 1) CTR there is a disagreement between the l-scan and rocking scan $|F_{hkl}|$ at low l. This is due to misalignment, once in this region the detector acceptance is very small and consequently, very sensitive to misalignment.

[2] The β angle is the polar exit angle, commonly called γ in z-axis diffractometer (see fig. 2.4-a).

The differences observed around anti-phase regions, are intrinsic of the film measured and will be recalled in next section.

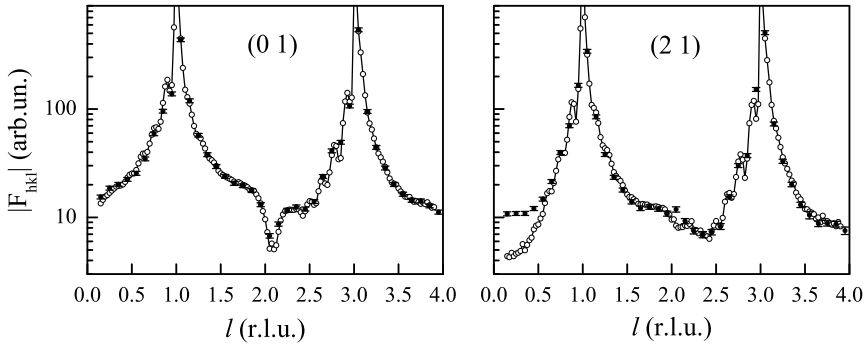

Figure 4.2: Comparison between $|F_{hkl}|$ profiles obtained from rocking scans (filled circles with error bars) and from stationary l-scans (open circles with guideline).

4.1.1 Procedure for quantifying order

The procedure developed for calculating the order parameter for pseudomorphic $L1_0$ alloy films with c-axis perpendicular to the surface (S_{OP}) follows three distinct steps: structure modeling and fitting; determination of order peak structure factor $\left|F_{hkl}^{order}\right|$; and simulation of $\left|F_{hkl}^{order}\right|$ from the fitted model. The first step is the structural determination, that consists in using the $|F_{hkl}|$ derived from stationary l-scans, as input to the modeling and fitting with the ROD program. In this quantitative analysis we get important information on the composition, thickness, inter-layer distances, roughness and inter-diffusion of the layer. All these structural parameters are independent, at least directly, from the degree of order. Indeed, this first step plays the same role as the structure peak measurement in the standard order determination for bulk or relaxed films (like MnPt on Ag(001) described previously). Generally, the order peaks we obtain are broader than the CTRs or than the fundamental alloy peaks (as will be shown in the following sections), and sometimes the order peaks are so wide that they are not even visible in l-scans or a short rocking curve about the CTR. The reason for these wide order peaks is the small size of the ordered domains. The structural correlation length, that depends only on the quality of pseudomorphic growth, is found to be larger than the order correlation length, that depends both on the pseudomorphism and on the chemical ordering. The strategy used to derive $\left|F_{hkl}^{order}\right|$ from this broad order peaks is similar to the rocking-scan procedure described in section 2.3.1. A quite large rocking scan is needed to reach the background and makes possible a proper integration of the peak intensity. The measured intensity profile in this rocking scan, however, represents only a slice of the smeared projection of the broad peak in a plane perpendicular to the [001]-axis. For taking into account all the intensity of the peak for a particular l value (integration along h and k), the correction for in-plane detector slits acceptance is of crucial importance. The obtained $\left|F_{hkl}^{order}\right|$ is then simulated using the model fitted in the first step.

At this point, we make the assumption that, if the chemical order was uniformly distributed along the layer, with the same correlation length as the surface itself (instead of divided in small domains), all the intensity scattered along the broad peak would be concentrated in the CTR. Based in this reasonable assumption, we model with ROD an ordered surface unit cell that permits us to vary the degree of order. Keeping fixed all the structural parameters obtained from the fit, only the degree of order is then adjusted so as to reach $\left|F_{hkl}^{order}\right|$, with the simulation. The order parameter S is calculated using equation 2.21, from the occupancies of each layer in the simulated model. This original procedure will be applied in next sections.

4.1.2 MnPt ordered alloy in the ultra-thin limit

The equiatomic $L1_0$ ordered phase is shown to present 1Q antiferromagnetic order, with optimal characteristics towards application as pinning layer in devices. If disordered, it is not antiferromagnetic at RT. It is difficult to keep anti-ferromagnetic character as the thickness is reduced so, in general, reasonably thick layers are studied ($> 10\,$nm). The reason for this thickness limit is believed to be intrinsically related to the degree of order [59, 60]. In the ultra-thin regime ($< 10\,$nm) it is hard to produce well ordered films by the procedures followed so far, as surface/interface effects becomes crucial. Our fundamental investigation of the epitaxial growth, structure and ordering for ultra-thin layers ($< 3\,$nm), following different preparation methods, aims to shed light into this issue.

For thicker films (30 nm) it has been shown that even a RT co-deposition leads to well ordered alloy (S=0.65) [65, 54]. Films are deposited epitaxially by MBE on a Pt(45 nm)/Cr(3 nm)/MgO(001) substrate and result on a twinned $L1_0$ domain structure, with in-plane c-axis. Mn and Pt co-deposition with higher substrate temperature gives rise to the same kind of structure but with better degree of order (S=0.76 at 620 K [54], or S=0.75 to Pt(5 nm)/MnPt(100 nm)/Pt(10 nm)/MgO(001) deposition at 570 K [64]). In this thickness range, the films are almost fully relaxed and the lattice parameters tends to the bulk ones for well ordered samples.

Only a few works have been reported in the way to produce $L1_0$ MnPt with out-of-plane (OP) c-axis. Fujii at al. [155, 156] have claimed to produce 6 and 8 ML MnPt film with OP c-axis on Fe(001) substrate by RT coevaporation followed by 500 K annealing, however, the lack of a structural characterization do not permit to confirm that the layer is effectively ordered. Co-deposition onto a rough multilayered substrate at 570 K is reported to lead to OP c-axis orientation with the final configuration Pt(5 nm)/NiFe(6 nm)/MnPt(20 nm)/Pt(5 nm)/Ag(130 nm)/Si(001), and a total peak to peak roughness of $\sim 300\,$nm [66]. No attempt to quantify the order parameter is reported, however, this OP ordering is extrapolated to be valid to thinner MnPt films (3 nm) to explain an increase in the NiFe coercive field at RT (50 Oe) compared to its usual value.

Alternate mono-atomic layer deposition has been successful used by Borme [54] to epitaxially grow 30 nm-thick MnPt with OP orientation, on Pt(45 nm)/Cr(3 nm)/MgO(001). This author found that at RT the alternate deposition leads to a poorly ordered film

($S_{OP} = 0.04$ and $S_{IP} = 0.13$), but subsequent annealing at 720 K for 2h favor the OP order ($S_{OP} = 0.55$), while the in-plane order stays small. Even better result are observed for thermal deposition, where up to $S_{OP} = 0.97$ is claimed when the substrate is held at 720 K during the alternate growth. Also here the layers are thick enough to relax towards bulk lattice parameters through the emergence of interface defects. One should note that the error bars in the order parameters determination for the works cited above, although not often given, tends to be quite high once the MnPt and Pt buffer peaks are hardly distinguishable in the majority of the cases. We could not find in literature any work that reports a perpendicular exchange coupling with a MnPt layer. However, this would be the case if one is able to grow MnPt with OP c-axis coupled to a film with perpendicular magnetic anisotropy. The compensated interface, should not be a problem if one considers that surface steps, defects or spin canting, can lead to exchange coupling in compensated surfaces[71].

Our aim in this study is the understanding of the many parameters governing the ordering process in the MnPt ultra-thin regime. Special attention is paid to the layer constraints. A pseudomorphic growth can lead to substantial changes in lattice parameters, compared to the bulk values. This turns out to be of fundamental importance, once it can determine the easy-axis of the $L1_0$ MnPt, as was theoretically predicted by Lu at al. [50]. These authors predict that an increase in the c/a ratio, as should be the case for OP MnPt on Pt(001) at constant volume, goes in the sense of favoring the spin orientation along the c-axis.

The ground basis of this study is given in chapter 3, where the first steps of Mn and Pt growth on Pt(001) are investigated. Here we will focus on the RT alternate deposition followed by annealing at 770 K and the thermal deposition. The temperature is kept moderate to avoid inter-diffusion. There are two main structural parameters that strongly influence the magnetic behavior of the film: the degree of order and the correlation length of the ordered domains. A major portion of the subsequent discussion will turn around these parameters, that are carefully derived in the next sections.

4.2 Room temperature deposition and annealing of MnPt on Pt(001)

4.2.1 Room temperature alternate deposition

We start the study of ordered layers by the preparation of a MnPt alloy at RT on a Pt(001) substrate with a small (not on purpose) miscut of 0.34° along the (10) direction. We have grown by alternating deposition of Mn and Pt monolayers a film composed by 6 BL. After each ML deposited, a fast l-scan along the (1 1) CTR was measured to give a qualitative idea of the growth mode. Figure 4.3 shows these l-scans for some intermediary stages (Mn, $(PtMn)_1$, $Mn(PtMn)_1$, $(PtMn)_2$, $Mn(PtMn)_2$) and for the complete $(PtMn)_6$ layer. The Clean *Pt-hex-0.7°* surface and the background, measured along (1.03 1.03), are also represented (gray dash and dot lines, respectively). Looking at the intensity in the anti-phase region ($l \sim 1$), very sensitive to roughness [88], one observe that after each Mn deposition the surface tends to be smoother but after each

Pt deposition the surface is rougher. This qualitative observation is in accordance with the results presented in section 3.1.3 showing the 3D growth mode of Pt on Mn/Pt(001) at RT.

The final film of 6 PtMn BL is indeed quite rough, as is evident from figure 4.3 (black solid line) once the CTR intensity reaches the same level as the background scan (gray dots) in the anti-phase region. A rocking scan in the (1 1 1) position, where one would expect an OP order peak, gives no peak at all. Likewise, no traces of IP order were found in the (1/2 1/2 0.15) position (not shown). This means that, if there is some degree of order, it is weak enough to be hidden by the high roughness. One can observe just below $l = 2$ well-defined Kiessig oscillations of the complete film. Taking the inverse of the period of these oscillations, marked with vertical bars, we estimate the total thickness of the film to be around 15 ML, or 2.9 nm. The small discrepancy from the nominal value (12 ML) should come from the initial diffusion and alloying of Mn with the Pt excess atoms from the hexagonal reconstruction and from some source calibration error within our 10% of precision.

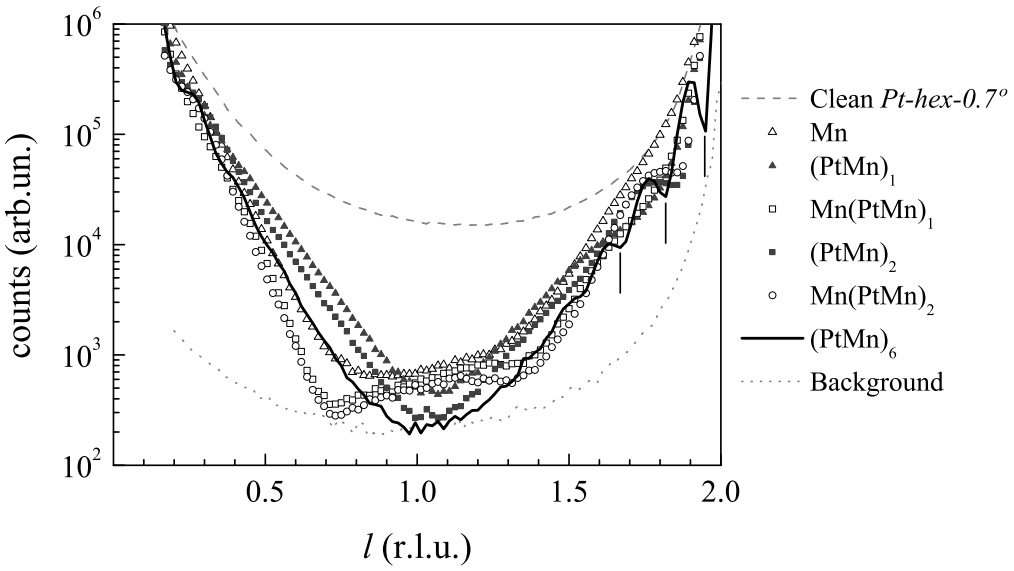

Figure 4.3: Stationary l-scans intensity along (1 1) CTR during Mn and Pt alternate growth at RT on a clean *Pt-hex-0.7°*. The legend indicates each corresponding layer. Note that, hollow symbols represent Mn terminated and filled symbols Pt terminated layers. The final $(PtMn)_6$ film is plotted in a black solid line, where vertical bars highlight the thickness oscillations period. Yet, we added the measured clean surface and the background along (1.03 1.03), dash and dot gray lines, respectively, to make clear that the RT deposition yields a rough surface (the intensity in the anti-phase region comes only from the background in the final film).

4.2.2 Annealing at 770 K

The rough sample was then annealed (following a few steps) from RT up to 770 K, with temperature calibrated using a pyrometer. During this process, we systematically measured the (1 1) CTR below $l = 2$ and we verified the presence of IP order peaks by rocking scans at (1/2 1/2 0.15). No change was visible up to 570 K, when the intensity

close (1 1 1) starts to slightly increase (fig. 4.4). About this same temperature, wide peaks appear in the half-integer position, indicating the presence of small domains with IP order. Above 670 K we can note a more significant evolution in the (1 1) l-scan, with a general increase of the CTR intensity, but with the appearance of a deep around a small region close to $l = 1.03$ (upper curve in figure 4.4). The sample was finally kept at 770 K for about 30 min before turning the heater off. Apart from this localized deep (that will be discussed later), the scattered intensity in the anti-phase region is recovered, which is a clear indication that roughness has decreased. Indeed, the surface presents quite large terraces after annealing, about 700 nm along miscut terraces (0 1) ant 100 nm along miscut steps (10). We remark that the Kiessig oscillations (see vertical bars in fig. 4.4) are preserved, what signifies that the layer has kept the same thickness (2.9 nm) and there is no additional Mn diffusion into the substrate.

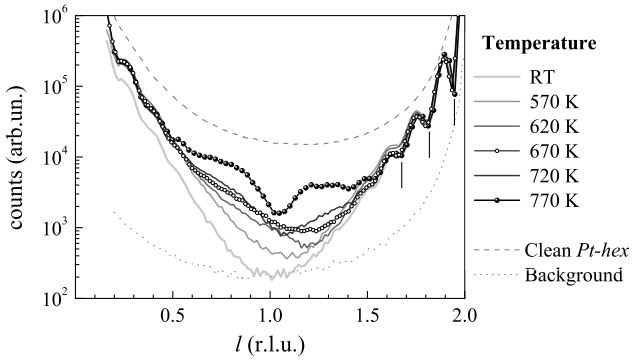

Figure 4.4: l-scans along the (1 1) CTR below $l = 2$. The corresponding annealing temperatures are indicated in the legend.

For this annealed sample, a whole set of l-scans (including background) and rocking-scans was measured, making a total of 9 CTRs (6 nonequivalents). No peak related to the long-range chemical order of OP oriented domains, expected close to the (1 1 1) position, shows up in the l-scan along the crest of the CTR. However, as shown in figure 4.5, the (offset) l-scan along (1.03 1.03) yields a broad peak in the anti-phase region corresponding to small $L1_0$ ordered domains with the c-axis oriented perpendicular to the surface. We determine the l-position and width of these order peaks for each measured shifted CTR (18 peaks in total) by means of a pseudo-Voigt fit. With this piece of information we thus obtain the average tetragonal distortion[3] of out-of-plane domains, $c/a^{OP} = 0.971 \pm 0.004$, and its average correlation length[4] perpendicular to the surface, $L_{\perp}^{OP} = 1.67 \pm 0.32$ nm (approximately 9 ML). The measured c/a is larger than the bulk $L1_0$ MnPt value ($c/a^{bulk} = 0.916$) but is in remarkable agreement with the expected value for a pseudomorphic layer with constant unit cell volume ($c/a^{V=const.} = 0.971$). This result suggests that the layer is pseudomorphic and has the right stoichiometry.

[3]For a pseudomorphic layer, the in-plane lattice parameter is the Pt one. The OP lattice parameter is taken from the inverse of the peak position. For an order peak centered at (1 1 3.3) (instead of (1 1 3)) the tetragonal distortion is of $c/a = 0.91$.

[4]The calculation of correlation length is taken from the inverse of the peak width. See section 2.2.1 for details.

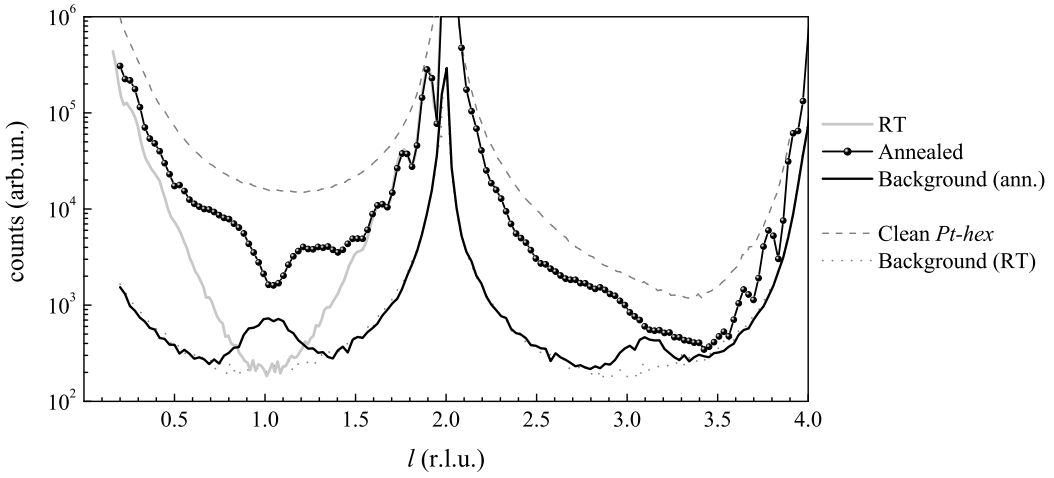

Figure 4.5: X-ray scattering along the (1 1) CTR for the $(MnPt)_6$ layer as deposited (gray solid line) and after annealing at 770 K (spheres). The offset scans, along (1.03 1.03 l), evidence a large peak in the background after annealing.

A large rocking scan along the (1 1 1) position reveals a broad peak (fig. 4.6) coming from the small OP ordered domains with a CTR sharp peak superposed to it. The lateral correlation length estimated from this broad peak is $L_{\parallel}^{OP} = 2.5 \pm 0.2\,\text{nm}$. At this point, we are able to comment on the "deep" observed in the CTRs around the order peak positions (fig. 4.5). In a l-scan (or a short rocking-scan) mainly the sharp part of the peak is taken into account. However, as illustrated in figure 4.6, the large rocking-scan can be fitted with a double pseudo-Voigt function, where most of the integrated intensity comes from the broad order peak of quite small domains. The deep around the broad peak position in l (fig. 4.5) means that the scattering from the small domains does not add coherently. They act like a sort of chemical roughness to the sharp CTR profile. Nevertheless, if one integrates all the scattered intensity (sharp and broad part), applying the appropriate corrections for each part,[5] the resulting $\left|F_{hkl}^{order}\right|$ value corresponds to an order peak, instead of a deep (see highlighted cross in fig. 4.8).

Gathering a reliable data set is the first step before modeling and fitting with ROD program. We have shown in figure 4.2 that some discrepancies may exist between $|F_{hkl}|$ obtained from rocking scans and from l-scans due to misalignment at low l. The discordant region of the (2 1) rod was removed from the data-set before fitting. Moreover, the deep region cannot be modeled in ROD, since they come from a peak broadening effect due to the presence of small domains. Hence, we also remove from the data-set, points within deeps at anti-phase regions. By this way, we can model and fit the structural part (not the ordered one) of the layer. However, the model is constructed in a way that order can be included later on.

A total number of 16 MLs (numbered n = [1 to 16]) composes the best model achieved: 5 MLs take into account mixing and inter-diffusion, 9 MLs represent the main part of the film, and 2 MLs at the top allow roughness or segregation. $|F_{hkl}|$ values with

[5] The detector acceptance correction take into account the width of the broad an sharp contributions separately.

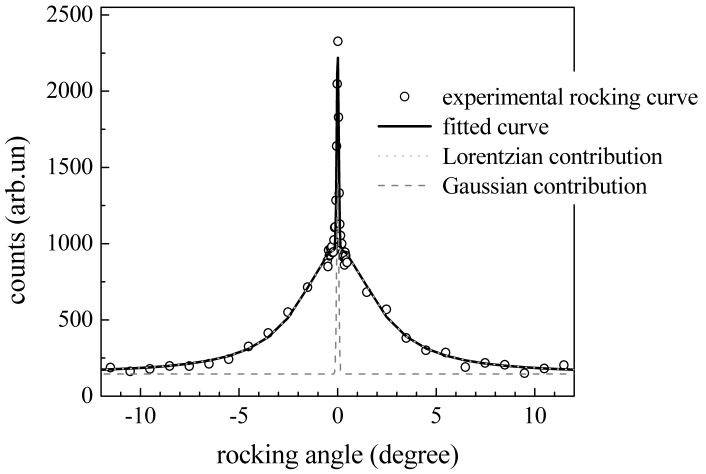

Figure 4.6: Fitting of large rocking scan around (1 1 1) with a double pseudo-Voigt function. In this particular case, the broad part has a Lorentzian line shape, while the sharp one is Gaussian.

error bars and the corresponding fitted curves are shown in figure 4.7 for all measured CTRs. An agreement factor better than 10% was found in the averaging of equivalent CTRs measured.

In the 5 first MLs, Mn and Pt occupancies are free, only constrained to fill complete layers ($\theta^n_{\mathrm{Mn}} + \theta^n_{\mathrm{Pt}} = 1$). To reduce the number of fitting parameters, the interlayer distances are imposed to to vary linearly like, $d_n = d_b + n\Delta d$, where the fitted value $\Delta d = -0.005\,\text{Å}$ is the slope with which the interlayer distance decreases. As seen in table 4.1 the fit gives a gradient of increasing Mn content within the interval $n = [1\text{to}5]$, compatible with an interdiffusion picture. The intermediary part (n = [6 to 14]) is supposed to be stoichiometric and homogeneous ($\theta^n_{\mathrm{Mn}} = \theta^n_{\mathrm{Pt}} = 0.5$) to the fitting, but it is constructed following the rules: $\theta^n_{\mathrm{Mn}} = \theta^{n+1}_{\mathrm{Pt}}$ and $\theta^n_{\mathrm{Mn}} + \theta^n_{\mathrm{Pt}} = 1$, so that order can be included later on with only one additional parameter (θ^6_{Mn}). Only one interlayer distance is considered in the fit, giving the value $d_n = 1.93\,\text{Å}$, not far from the expected value from the order peak positions ($d^{OP,IP} = {}^{c^{OP,IP}}/_2 = 1.90 \pm 0.01\,\text{Å}$). In the 2 last MLs the occupancies and interlayer distances are let completely free. The fitted values are summarized in table 4.1. Layer 15 is complete and slightly Mn-rich, while the last one is almost half-filled only with Pt. The last distance is 3% shorter compared to the bulk value, what is not surprising to a surface layer, once the presence of dangling bonds is commonly observed to cause a shrink in the OP lattice parameter [72]. This surface composition is coherent with a Pt-finished deposition and the small roughness is expected after a 770 K annealing. To limit the number of parameters, bulk values are imposed to all DW factors.

Many other models were tried, changing the total number of MLs, considering a beta-like roughness model, with distinct number of MLs of each part of the film, and letting free all distances and DW parameters. The model described is the simplest one (with less free parameters) that reasonably fits the data (fig. 4.7, $\chi^2 = 8$) and gives a proper picture of the layer structure.

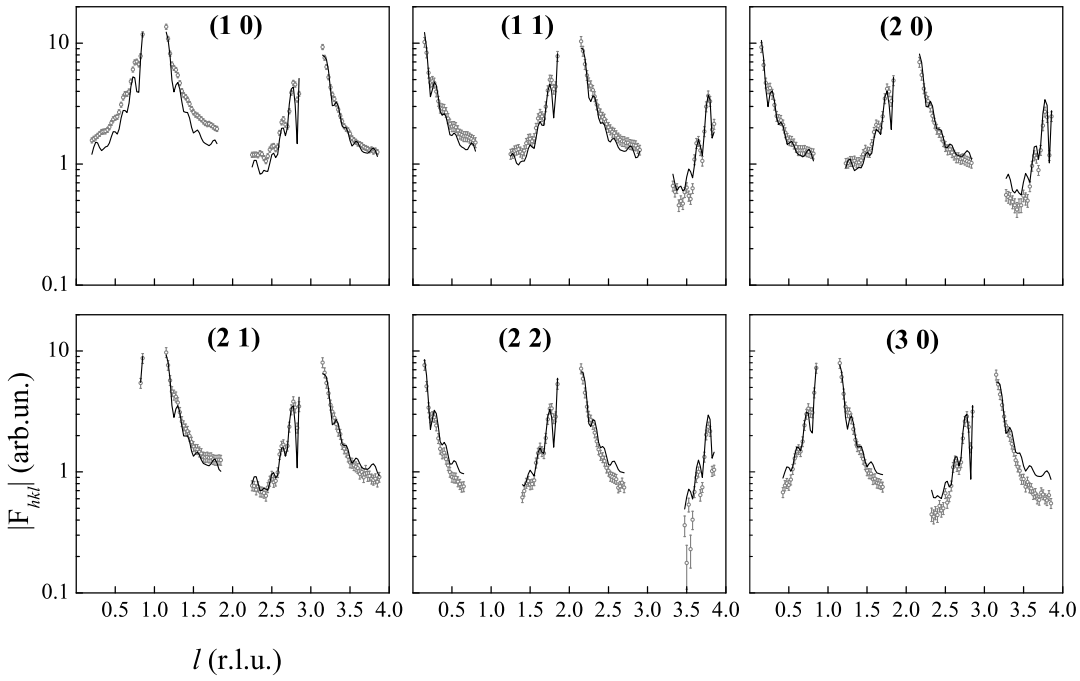

Figure 4.7: Fitting with ROD of $|F_{hkl}|$ for sample $(PtMn)_6/Pt(001)$ annealed at 770 K. The continuous black lines represents the fit, while the gray symbols with error bars represent the $|F_{hkl}|$ obtained with the l-scans procedure. Only the structural contribution is fitted, once the anti-phase regions are not fitted (gaps in the bottom of CTRs).

As described previously, the fitted model achieved is the first step for estimating S_{OP}. In the second step, the integration of the large rocking curve at (1 1 1), shown in figure 4.6, is done both numerically and by the area of the fitted double pseudo-Voigt. We apply the appropriate corrections (eq. 2.20) to the mean value of the two integrals, using the fitted FWHM of the large peak to calculate C_{det} and derive $\left|F_{1\,1\,1}^{order}\right|$. The difference between the integration methods is included in the error bars. Another source of error taken into account is the uncertainty, from the fitting procedure, on the width of the large peak. The obtained value is then $\left|F_{1\,1\,1}^{order}\right| = 8.5 \pm 0.9$, represented in figure 4.8 by a cross with error bar. In the model, chemical order can be added within 9 MLs (or ~ 1.7 nm). This thickness corresponds to the $L_{\perp}^{OP}$ value obtained from the peak width along l. To simulate the chemical order, we fix all parameters of the structural fitting and adjust the occupancy parameter θ_{Mn}^{6} within the layer to obtain the value $\left|F_{1\,1\,1}^{order}\right| = 8.5 \pm 0.9$ in the (1 1 1) position.

Figure 4.8 shows the simulated curve passing through the experimental value marked with a cross, obtained with $\theta_{\mathrm{Mn}}^{6} = 0.74 \pm 0.03$[6]. The order parameter within this 9 MLs is then calculated using equation 2.21 as, $S_{OP}^{9\,MLs} = \theta_{\mathrm{Mn}}^{6} - \theta_{Pt}^{6} = 0.48 \pm 0.06$. Then, we normalize this value by the nominal number of monolayers deposited (12) to give the general OP parameter $S_{OP} = 0.36 \pm 0.5$. We should recall that this quite large order parameter comes from a large amount of very small chemically ordered domains with OP c-axis.

[6]Recall that $\theta_{\mathrm{Mn}}^{6} = 0.74$ is sufficient to determine the other occupancies: $\theta_{Pt}^{6} = 0.26$,$\theta_{Pt}^{7} = 0.74$,$\theta_{\mathrm{Mn}}^{7} = 0.26$, etc.

layers	θ(Pt/Mn)	d(Å)
16	0.44/0	1.90
15	0.39/0.61	1.95
[6..14]	0.5/0.5	1.93
5	0.55/0.45	1.93
4	0.61/0.39	1.94
3	0.71/0.29	1.94
2	0.83/0.17	1.95
1	0.93/0.07	1.96
Bulk	1/0	1.96
DW	bulk: 0.31/0.44	
χ^2	8	

Table 4.1: Fitting results for $(PtMn)_6$/Pt(001) annealed at 770 K.

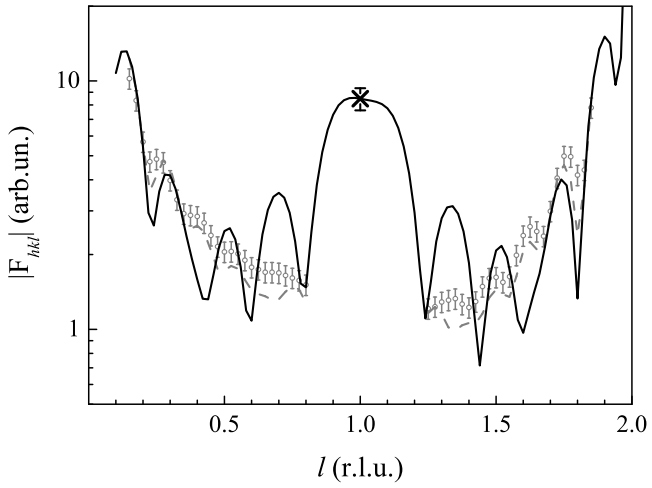

Figure 4.8: Simulated CTR to fit $\left|F^{order}_{1\,1\,1}\right| = 8.5 \pm 0.9$.

The diffracted intensity along the half-integer rods (1/2 1/2) and (3/2 3/2) originates from $L1_0$ domains with IP c-axis.[7] As can be seen in figure 4.9-a, the scattering along the (1/2 1/2) rod yields broad peaks near each integer l value, corresponding alternately to domains oriented along [1 1] and [1 $\bar{1}$] (see fig. 2.3 to recall which peak corresponds to each orientation). From the average position and width of the measured peaks, assessed with pseudo-Voigt fits (4 peaks in total), we determine the tetragonal distortion[8] and the perpendicular correlation length of the IP oriented domains to be $b/a^{IP} = 0.968 \pm 0.006$ and $L^{IP}_{\perp} = 1.34 \pm 0.14$nm. The calculated volume of the unit cell, considering pseudomorphism, is also constant within 0.3% compared to the bulk MnPt, as is the case for OP domains. As compared to the OP domains, the in-plane ones are 2.5 times wider, as seen by the narrower rocking curves (fig. 4.9-b), with $L^{IP}_{\parallel} = 6.3 \pm 0.7$nm.

[7]Here, the c-axis denotes the direction of chemical order (Mn/Pt stacking), even if the IP domains are pseudomorphic with the c-lattice parameter equal to a_{Pt}.

[8]The tetragonal lattice parameter, perpendicular to the surface, is called b, and not c (reserved to the order direction).

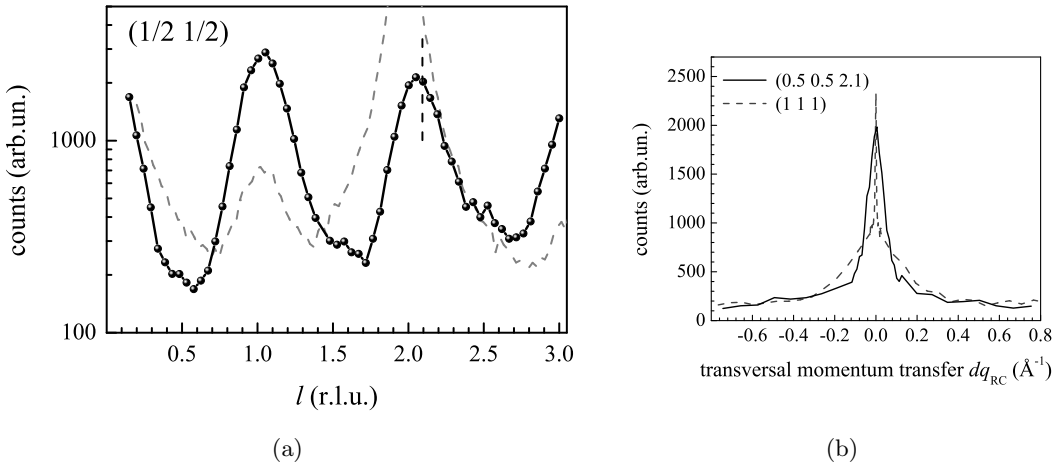

Figure 4.9: a) X-ray scattering along the (1/2 1/2) CTR (black spheres with connecting line). The shifted l-scan, along the (1.03 1.03), is shown to compare intensities (gray dotted line). b) Rocking curve about the (1/2 1/2 2.1) reciprocal space point (indicated in by a dashed bar in (a)), compared to the (1 1 1) rocking scan, that has the same momentum transfer modulus$|\vec{q}|$. The abscissa is converted from degrees to transverse momentum transfer dq_{RC}.

The in-plane order parameter can be indirectly estimated by comparing the structure factors obtained for the IP and the OP peaks. We apply the appropriate corrections to the integrated intensity of the (1/2 1/2 2) IP order peak, chosen because it have the same momentum transfer[9] of the (111) reflection, integrated above. Additionally to the usual corrections for a large rocking curve, a correction to take into account the peak width in l is considered, giving the final value $\left|F^{order}_{1/2\ 1/2\ 2}\right| = 6.7 \pm 0.3$. The ratio $\frac{\left|F^{order}_{1\,1\,1}\right|}{\left|F^{order}_{1/2\ 1/2\ 2}\right|}$ gives directly $\frac{S_{OP}}{S_{IP}^{1/2\ 1/2}}$, from where we calculate $S_{IP}^{1/2\ 1/2} = 0.28 \pm 0.05$, the order parameter of the domains with c-axis aligned along [1/2 1/2]. Here we make the assumption, by symmetry reasons, that both IP variants have the same population. The in-plane order parameter is then twice that for the one domain type, $S_{IP} = 0.57 \pm 0.1$, and the total order parameter, summing IP and OP contributions is finally $S = 0.93 \pm 0.15$.

The final picture of this layer, obtained by deposition at RT of 6 (MnPt) BLs on clean reconstructed Pt(001) and annealed up to 770 K for 30 minutes, is a multi-domain $L1_0$ structure with c-axis orientation in the three possible directions, filling almost all the layer volume. Indeed, from the definition of order parameter given above, it is not possible to say if $S < 1$ means that a random disorder is distributed within the ordered domains (that occupy then all the volume) or if we have perfectly ordered domains with disordered regions in between them (with volume ratio of $1 - S$), for example in domain boundaries. Transmission electron microscopy studies reported in literature for thicker films [65, 64] and [54, p.41], show that MnPt alloys may form columnar structures with disordered regions between ordered grains. This gives an indication that the second picture is most likely valid, but we have no elements to conclude on that. The in-plane domains are found to be rather small in the direction perpendicular to the surface

[9]The equivalence of both $|\vec{q}|$ values becomes obvious if we write these reflections in cubic notation: $(1\,0\,2)_{FCC}$ and $(2\,0\,1)_{FCC}$.

(about half the layer thickness) but with a larger lateral correlation length. From the investigation of the initial steps of growth presented in last chapter, we saw that in-plane order is present in the very beginning of Mn growth on *Pt-hex-0.7°*, once Mn atoms reacts with the Pt 25% excess atoms of the reconstruction to form a partially ordered surface alloy. This initial alloying is likely to work as a seed to the growth of IP ordered domains. It is a typical interface effect that influence the kind of order obtained when one explores a thickness range < 3 nm. For thicker layers (30 nm) J. Borme found that alternate RT deposition and annealing at 720 K leads to a majority of OP order ($S_{OP} = 0.55$), with small IP contribution (not quantified in [54]). This suggests that the volume contribution, induced by the alternate deposition, favors the OP order. In a constrained layer, as is our case, we expect that the OP domains to be even more favored, once the elastic energy is smaller for these domains due to the smaller lattice mismatch with the Pt substrate. The OP domains were shown to be slightly thicker than the IP ones, however its lateral correlation length is 2.5 times smaller. This result, is intrinsically related to the high roughness of RT deposited MnPt described above, mostly influenced by the three-dimensional Pt growth mode. In a rough surface, many nucleation points can be formed from the local order induced by the alternate deposition. In the annealing process a great number of nucleation points gives rise to small ordered domains.

4.2.3 Covering with Fe

This MnPt layer was then covered at RT with 15 Fe MLs (in-plane magnetic anisotropy) for exchange coupling studies and protected against oxidation with 10 Pt MLs. *Ex situ* XRR was performed to check the final thickness and interface roughness of the sample (figure 4.10). The fit results have a good agreement with the nominal values, as summarized in table 4.2. It is worth noting the rather small roughness in the MnPt/Fe interface (<1 Å), configuring a sort of "model interface" to the study of the exchange coupling.

layer	Nominal	Fitting results	
	Thickness (nm)	Thickness (nm)	Roughness (nm)
Pt	1.96	1.81	0.145
Fe	2.3	2.44	1.095
MnPt	2.28	2.85	0.085
Pt(001) substrate	-	-	0.335

Table 4.2: Fitting results of XRR measurements compared to nominal values for sample S0.

4.3 Alternate Mn and Pt deposition at 500 K and annealing 670 K

We show here the results for a MnPt layer grown by alternate deposition with the substrate held at a moderate temperature of 500 K then annealed at 670 K. 500 K was

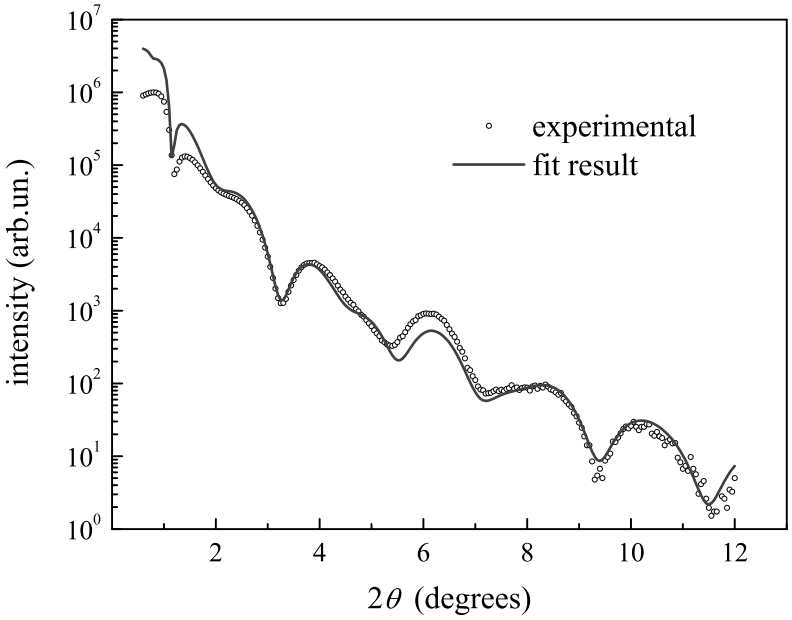

Figure 4.10: XRR fitting

not sufficient to give a high degree of order, what required an annealing at 670 K. A quantitative analysis of the order parameter, is not given for this layer, since it presents an intermediary behavior between the RT deposition plus annealing and the deposition at 570 K, presented in next chapter.

As a first step of deposition, 2 MLs of Mn are grown on *Pt-hex-0.7*º already at 500 K, in order to lift the reconstruction and produce a flat surface. The initial alloying process, as described in chapter 3, gives rise to faint $c(2 \times 2)$ peaks. On this 2 Mn MLs, we perform the alternate deposition of 6 PtMn BLs, finishing with Pt, with the substrate always held at 500 K. The final thickness, estimated from the period of Kiessig fringes, corresponds to roughly 8-9 MnPt BLs, or about 3.2 nm. A qualitative picture can be deduced directly from the l-scans presented in figure 4.11 and from the many in-plane scans[10] measured.

The 500 K deposited film (gray line in fig. 4.11) shows a small roughness, as evidenced by the thickness oscillations that persists even in the anti-phase region of the (1 1) CTR. Only a faint intensity is observable in a large rocking curve along the (1 1 1) reciprocal space position (not shown). This comes from quite small OP partially ordered domains (lateral correlation length of about 1.5 nm). An annealing procedure is required to improve the ordering, as was the case for the RT deposited sample. The annealing at 670 K for 7 hours gives rise to a large peak in the anti-phase region, visible in the shifted l-scan along (1.02 1.02) (solid black line in fig. 4.11), due the improvement of OP order. Additionally, the intensity of the whole CTR increases, indicating a decrease of the layer roughness. From the shifted l-scans we fit the anti-phase large peaks with pseudo-Voigt functions, to estimate the OP domain height and tetragonal distortion to

[10]The refereed in-plane scans are rocking curves, already described, and radial scans, where one fix l and change the modulus of the in-plane momentum transfer.

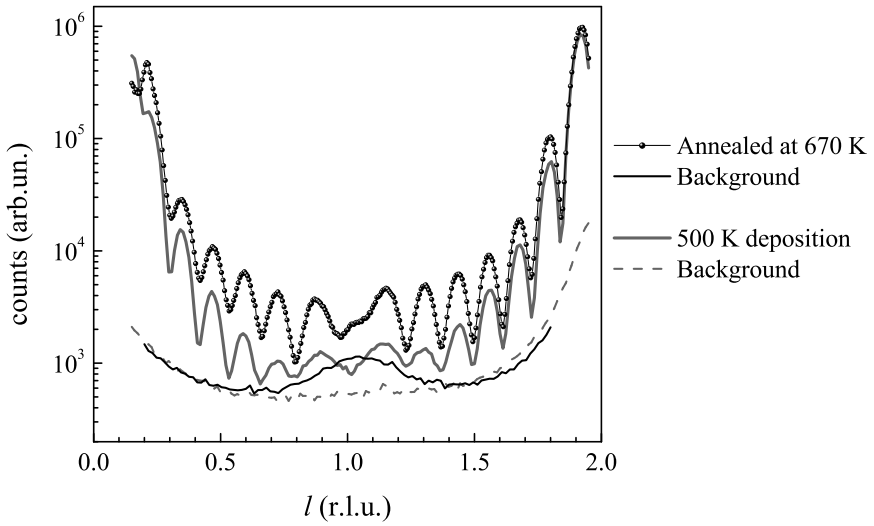

Figure 4.11: Comparison of $(MnPt)_8$ layer just after deposition at 500 K (gray line) and after annealing at 670 K (black circles with guide line). A large peak at the anti-phase region also shows up in the shifted l-scan (black solid line).

be[11], $L_{\perp}^{OP} = 1.37 \pm 0.11$ nm and $c/a^{OP} = 0.960 \pm 0.005$, respectively. In-plane scans about the (1 1 1) peak, both rocking and radial (fig. 4.12), give a lateral correlation length of $L_{\parallel}^{OP} = 3.7 \pm 0.2$ nm. This is only 1.5 times the average width obtained with the previous RT deposition plus annealing procedure. The peak position in the radial scan (fig. 4.12) evidences the pseudomorphism of the OP domains with the substrate (within 0.03%). Taking the c/a^{OP} value and assuming a perfect pseudomorphism, we calculate a unit cell volume slightly smaller than the bulk value for these domains. This contraction (of 1% in volume), in the limit of error bars, could be due to an excess of Mn within the calibration precision.

IP domains are also present, and from the l-scans we obtain $L_{\perp}^{IP} = 1.67 \pm 0.19$ nm and $b/a^{IP} = 0.983 \pm 0.006$ (from 8 peaks fitted by a pseudo-Voigt function). They have a smaller lateral correlation length compared to the OP domains, $L_{\parallel}^{IP} = 2.6 \pm 0.4$ nm, obtained from the average of 4 measured half-integer peaks, taking the inverse of the FWHM of both rocking scans and radial scans. Figure 4.13 shows a radial scan along the (1/2 1/2 2.027) position fitted by a pseudo-Voigt function that includes a linear background. The plot abscissa is normalized by the in-plane momentum transfer of (1/2 1/2), $\frac{|\vec{q}_{\parallel}|}{|\vec{q}_{\parallel}^{(1/2\ 1/2)}|}$, so that the position of the peak center gives a direct estimation of the relaxation of the c lattice parameter. The values of FWHM and peak center in the plot, correspond to the mean value of two measured peaks, (1/2 1/2 2) and (1/2 $\overline{1/2}$ 2). The error bars are given by the standard deviation of the the fit, bigger than the difference between independently fitted values. We observe that the c-lattice parameter (along the stacking direction), presents some relaxation, being about 1.5% contracted in relation to the Pt substrate ($c/a^{IP} = 0.985 \pm 0.002$), but still 5.4% larger than the bulk value ($c_{MnPt}^{bulk} = 3.665\,\mathring{A}$). This relaxation is possibly related to the initial

[11] The calculated values and error bars are obtained from the average and standard deviation for 3 non-equivalent peaks measured.

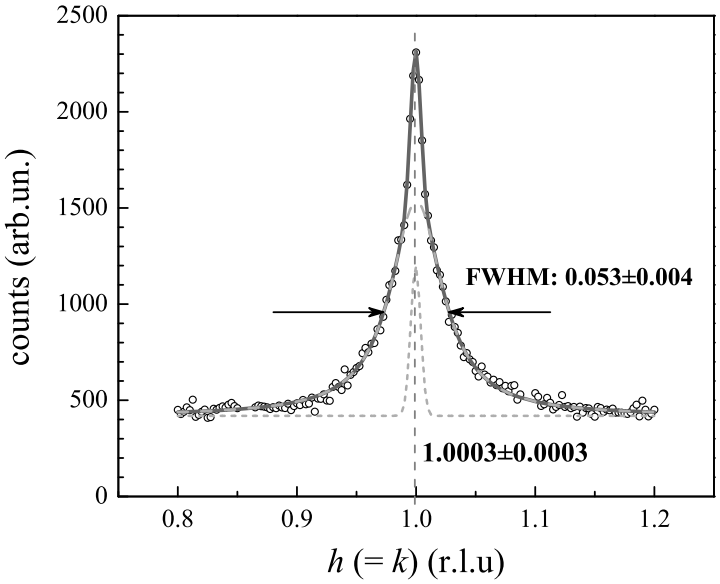

Figure 4.12: Fit of a radial scan along the (1 1 1) peak with two pseudo-Voigt lines. The large peak, coming from the small ordered domains gives $\eta = 1$ in the fit, meaning a Lorentzian line-shape. The narrow part corresponds to the CTR interception, and is fitted with a Gaussian line-shape ($\eta = 0$). The center position of the large peak, shown in the figure, attests the pseudomorphism of the OP domains ($a^{OP}_{MnPt} \cong a_{Pt}$). From the FWHM obtained from the fit (also shown), one can derive the in-plane correlation length, recalling that $h = k$ so that a $\sqrt{2}$ factor is included, $L^{OP}_{\parallel} = (\text{FWHM} \times \sqrt{2})^{-1} \times a_s$, where $a_s = 2.775\,\mathring{A}$ is the surface lattice parameter.

deposition of two Mn MLs, that could help to relief the substrate constraint. The radial scans along the (1/2 1/2 1) and (1/2 $\overline{1/2}$ 1) peaks gives, applying the same fitting procedure (not plotted), that the a lattice parameter is pseudomorphic within the error bars, ${a_{MnPt}/a_{Pt}}^{IP} = 1.002 \pm 0.002$. The unit cell volume, calculated with the above a, b and c lattice parameters, is the same as for the bulk alloy.

Without the modeling and fitting of the CTRs we cannot calculate the absolute order parameter, but we are still able to estimate the ratio between OP and IP ordered domain volumes from the structure factor amplitudes of the respective order peaks. The same reasoning applied for the previous layer (section 4.2) is used here to calculate $\left|F^{order}_{hkl}\right|$ from the large rocking scan along (1 1 1) and along half-integer reflections with the same momentum transfer, (1/2 1/2 2) and (1/2 $\overline{1/2}$ 2). The calculated ratio is $\frac{S_{OP}}{S_{IP}} = 0.61 \pm 0.12$, evidencing that the total volume and correlation length for the IP and OP domains are not significantly different.

4.4 Summary

We have verified the validity of the stationary l-scan mode for the measurement of thick layers. Then, a procedure for quantifying by GIXRD measurements the order parameter of pseudomorphic alloys, was developed. Following this procedure, we have studied the growth of MnPt alloy on Pt(001) by alternate deposition at two different substrate temperatures. At RT a rough and disordered layer is obtained, influenced by

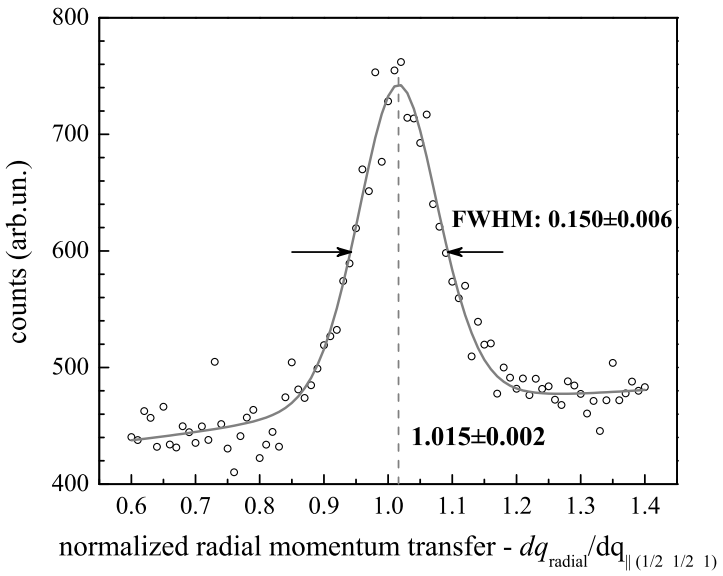

Figure 4.13: Radial scan along the (1/2 1/2 2) position, giving the relaxation of the c parameter of IP domains. The abscissa is normalized by the in-plane momentum transfer corresponding to (1/2 1/2), $\frac{|\vec{q}_{\parallel}|}{|\vec{q}_{\parallel}^{(1/2\ 1/2)}|}$, in order to give a direct estimation of the relaxation.

the Pt 3D growth mode. Annealing this layer at 770 K smoothens the surface and gives rise to small $L1_0$ ordered domains, without visible Mn diffusion into the bulk. Three possible c-axis orientation of the $L1_0$ domains are observed. The twinned in-plane c-axis domains are majority ($S_{IP} = 0.57 \pm 0.1$) and wider ($L_{\parallel}^{IP} = 6.3 \pm 0.7$nm) than the OP ones ($S_{OP} = 0.36 \pm 0.5$ and $L_{\parallel}^{OP} = 2.5 \pm 0.2$ nm), giving a ratio $\frac{S_{OP}}{S_{IP}} \sim 0.6$.

For a 500 K deposition, the layer roughness is appreciably decreased. However, this temperature has not yet been sufficient to give a high degree of order. Annealing at 670 K improves the order, with the OP domains slightly wider. It will be shown in next chapter that further increase in deposition temperature can improve the OP order.

Chapter 5

Perpendicularly exchange coupled MnPt/FePt alloys

We turn now to the growth, structure and magnetism of coupled FM/AFM layers with perpendicular anisotropy. We start by presenting the *in situ* GIXRD investigations of the synthesis of out-of-plane $L1_0$ MnPt and FePt alloys. As described in section 1.3.1 the $L1_0$ structure corresponds to an *fct* binary alloy with alternate stacking of atomic planes of different nature along the *c*-axis. To mimic this order, we perform an alternate growth of Mn(Fe) and Pt MLs. There is a delicate temperature threshold to obtain an almost flat surface during growth (layer-by-layer growth) and induce the desired order.

The preparation of MnPt/FePt heterostructures is exposed, with the *in situ* characterization by GIXRD, and compared to the *ex situ* characterization by XAS. The magnetic properties, measured by MOKE and/or XMCD, are discussed and interpreted in the light of the structural characterizations.

5.1 $Pt_8/(PtFe)_4/(PtMn)_8/Pt(001)$ (Sample S4)

In this first sample, named S4, the AFM layer is composed by 8 MnPt BLs alternately deposited on a Pt(001) substrate with a 1° miscut along the $[1\ 1\ 0]_{fcc}$ axis held at 570 K. This layer was characterized *in situ* by GIXRD, keeping the same substrate temperature, before the deposition of 4 FePt BLs (FM layer). After fully *in situ* GIXRD characterization at RT, the sample was covered with 8 Pt MLs at 540 K to protect against oxidation. Further *ex situ* GIXRD, XRR and XAS completed the structural characterization. The magnetic properties were studied by MOKE and XMCD.

5.1.1 Alternate Mn and Pt growth at 570 K

The substrate temperature is an important parameter to establish the growth of chemically ordered alloys with the c-axis perpendicular to the surface (see section 4.3). In the MnPt system, we show (section 3.1.4) that a leading issue is the temperature at which Pt grows in a layer-by-layer mode on Pt(001) and of Mn/Pt(001) surfaces. From the anti-phase growth oscillations (fig. 3.11) we see that at for a substrate temperature

of 570 K the Pt grows layer-by-layer, at a deposition rate of 0.04 ML/min (or 25 min for 1 ML). Higher substrate temperatures are expected to improve the Pt deposition mode, however, it would lead to diffusion of Mn atoms into the bulk. This compromise is specially critical for the low Mn growth rate (0.17 ML/min) that favors atoms diffusion into the bulk. To prevent as much as possible this diffusion, the Mn monolayer was covered immediately by a Pt monolayer, in the deposition procedure. Much higher temperature, 720 K, was used by Borme [54] to grow a 30 nm film with a rate of 1ML in 3.8 s (15 ML/min).

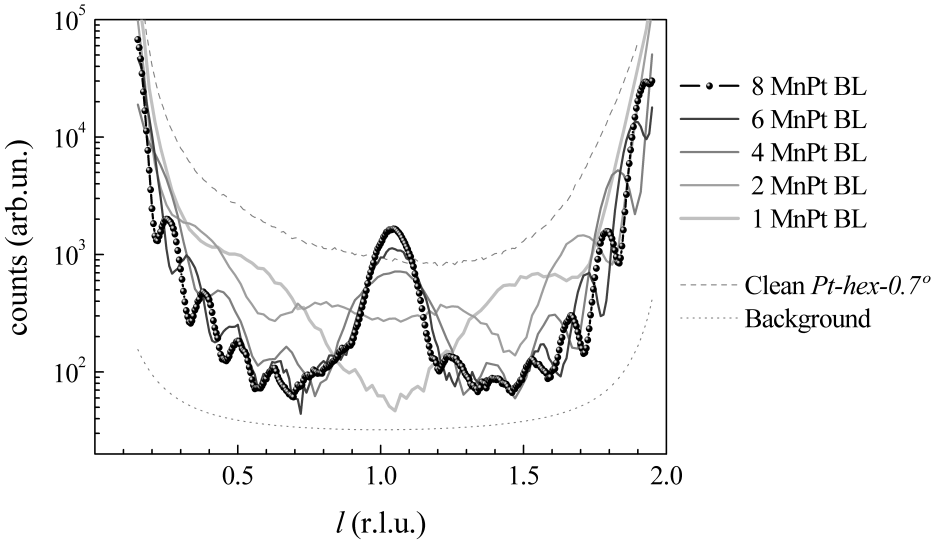

Figure 5.1: l-scans along the (1 1) CTR during 573 K alternate deposition. There are represented the clean surface, 1, 2, 4, 6, and 8 (closed circles) BLs and the background.

At 570 K, about 1 ML of Pt was deposited on the clean reconstructed Pt(001) surface before the first Mn deposition. Our intention was to minimize the interface alloying process among Mn and Pt in the earliest process and reduce the formation of IP domains. Then, the alternate Mn and Pt mono-atomic deposition, emulating the OP $L1_0$ stacking, was repeated 8 times, giving a nominal thickness of 3.05 nm.

Scans were performed during the Pt deposition. From the beginning, weak traces of $c(2 \times 2)$ MnPt alloying, seen by rocking scans at (1/2 1/2 0.15), were observed. After each complete Pt monolayer deposition l-scans along the (1 1) CTR were measured (fig. 5.1).

The CTR of the first MnPt bi-layer (light gray in fig. 5.1) presents a deep in the anti-phase region and a general shape that suggests an alloying process (sections 3.1.3) instead of an ideal MnPt BL. For two BLs, the anti-phase intensity increases, although still being a local minimum. From 3 BL on, an order peak clearly shows up, and gets more intense and sharp after each bi-layer growth, as clearly observable in figure 5.2, that is a linear scale zoom of the order peak region. This behavior is remarkably distinct from the two previous cases, of RT deposition plus annealing at 770 K and of 500 K deposition followed by 670 K annealing. Here, the order peak is visible in the CTR itself, what suggests a higher degree of OP order (to be quantified later) and some

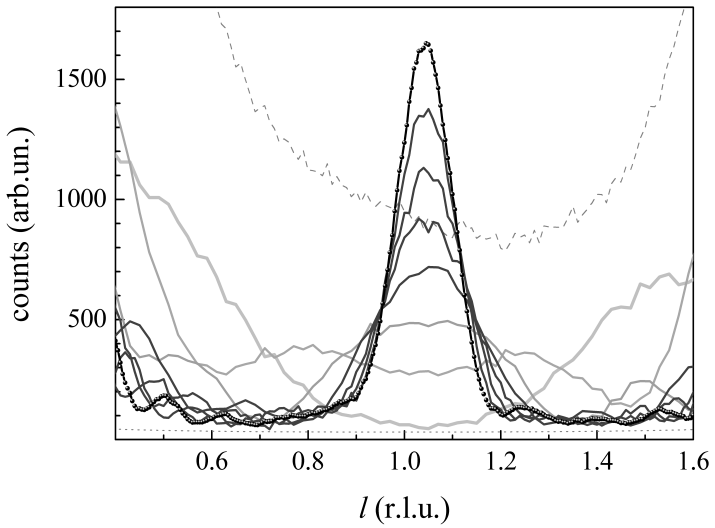

Figure 5.2: Order peak growth (linear scale) followed after the deposition of each bilayer.

coherence between ordered domains. Note that above 6 BLs the order peak intensity is higher than for the clean surface.

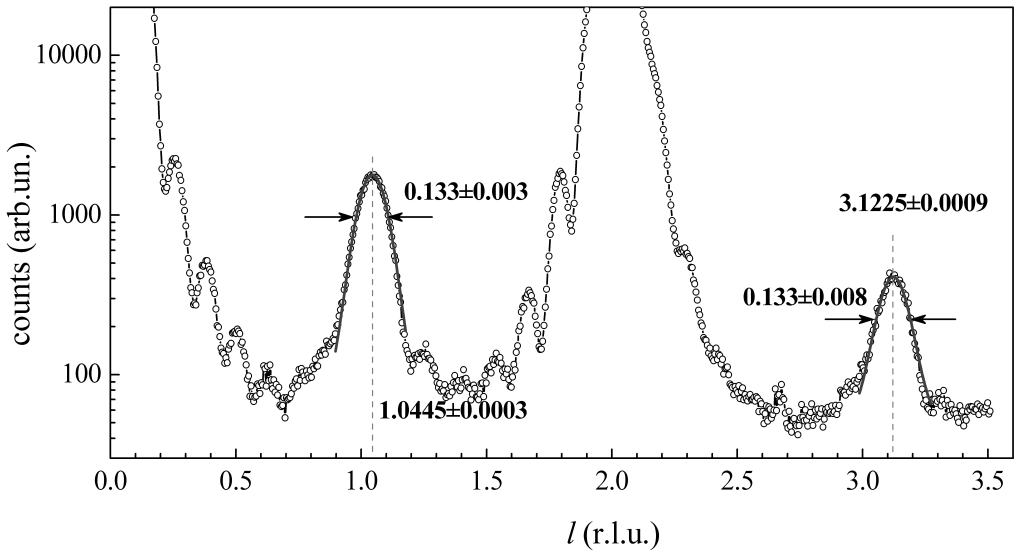

Figure 5.3: Fitting procedure of order peaks along the (1 1) CTR, illustrating how the center and width of peaks are determined. On average, the peak shape is closer to a Gaussian function.

Order peaks of different CTRs are fitted with pseudo-Voigt line shapes, as shown in figure 5.3. The peak center position and width, averaged among 11 peaks of 8 distinct CTRs[1], gives the characteristic values for the OP domains, $c/a^{OP} = 0.960 \pm 0.001$, or $c^{OP} = 3.768 \pm 0.005\,\AA$, and $L_{\perp}^{OP} = 2.92 \pm 0.06\,\text{nm}$. The lateral correlation length of these domains, taken from the fitting of the rocking curves following the procedure described in section 4.3, is of $L_{\parallel}^{OP} = 6.6 \pm 0.6\,\text{nm}$ (4 peak average). Figure 5.4 gives the

[1]Namely: (1 0), (0 1), ($\bar{1}$ 0), (0 $\bar{1}$), (1 1), ($\bar{1}$ 1), (0 2) and (2 1).

fit for the (111) peak as an example. A radial scan at this position gives a value of 0.997 for the large peak center and we can consider that these domains are pseudomorphic, within our accuracy. All measurements of the MnPt layer were performed with the substrate held at 570 K, however, the lattice parameter are those calculated to RT, taking into account the Pt thermal expansion coefficient ($8.8 \times 10^{-6}\mathrm{K}^{-1}$).

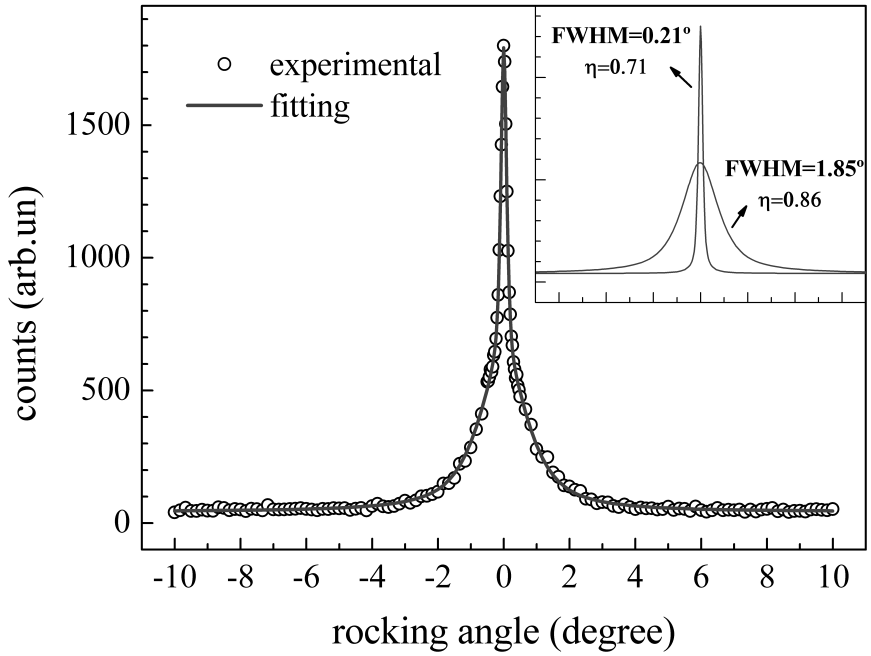

Figure 5.4: Rocking scan along the (1 1 1.04) position with double pseudo-Voigt fitting. In the inset the sharp and broad components are distinguished with the respective FWHM and η values displayed.

In-plane domains are also observed, but with lower intensity. A similar analysis of the peak position and width for l-scans of half integer rods was performed. Figure 5.5 shows the peak fitting with a pseudo-Voigt line-shape (with linear background) for two peaks along the (1/2 1/2) rod. In the total four peaks are averaged, from the (1/2 1/2) and (1/2 3/2) l-scans, from where we derive $b/a^{IP} = 0.979 \pm 0.003$ and $L_{\perp}^{IP} = 2.68 \pm 0.12$ nm. One can remark that in this sample both the IP and OP domains have a perpendicular correlation length close to the nominal film thickness (3.0 nm). The FWHM of rocking scans evidences that this IP domains are on average 1.6 times smaller than the OP ones, $L_{\parallel}^{IP} = 4.1 \pm 0.3$ nm. This represents an opposite situation in relation to the first sample analyzed, RT deposition plus annealing (sample S0), where the IP domains were larger than the OP ones by 2.5 times. This observation have implications in the magnetic properties, discussed later.

In figure 5.6 a radial scan along (1/2 1/2 1.019) gives information on the pseudomorphism along the a-axis. Once we have only one measured scan, the fitted value, $\frac{a_{MnPt}^{IP}}{a_{Pt}} = (1.0047)^{-1} = 0.995 \pm 0.005$, or about 0.5% of contraction, just allows us to say that this layer is not relaxed beyond the experimental error bars. Indeed, we expect an expansion of a_{MnPt} rather than a contraction, once its bulk value is larger than a_{Pt}. We will then consider that these domains are pseudomorphic in this direction. No

measurements were done concerning c-axis relaxation of the IP domains, and we treat it as pseudomorphic in the simulations below.

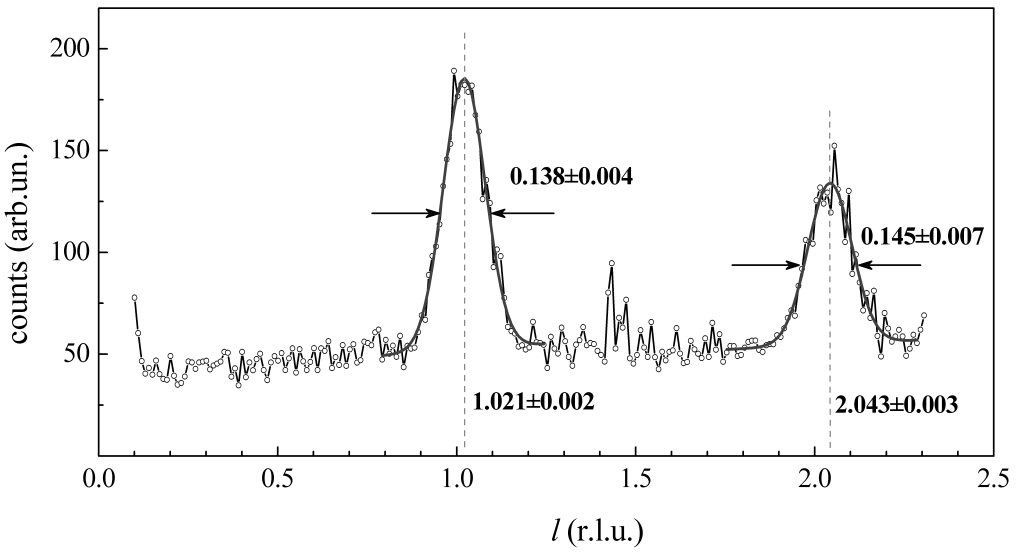

Figure 5.5: Pseudo-Voigt fit of l-scan peaks along (1/2 1/2), showing the peaks position and FWHM.

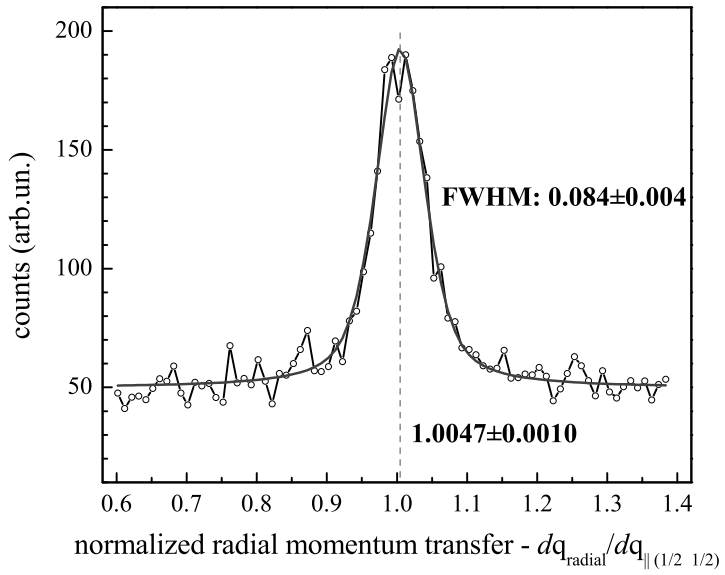

Figure 5.6: Pseudo-Voigt fit of radial scan along (1/2 1/2 1.019). The abscissa is normalized by the in-plane momentum transfer corresponding to (1/2 1/2), $\frac{|\vec{q}_\parallel|}{|\vec{q}_\parallel^{(1/2\ 1/2)}|}$, in order to give a direct estimation of the relaxation of a lattice parameter in the IP domains.

5.1.2 Modeling the $(MnPt)_8/Pt(001)$ structure

A similar reasoning as applied to modeling and fitting the CTRs in section 4.2 is used for this MnPt layer. First of all, the $|F_{hkl}|$ data set, to be fitted with ROD, is obtained by the fast stationary l-scan procedure, always comparing with a few $|F_{hkl}|$ values

derived from rocking scans integration to avoid misalignment errors (section 4.1). A set of 8 CTRs is averaged, with 4 non-equivalents, so that the agreement factor gives the experimental error bars. The use of fast scans are exceptionally important in this case, once the measurements are performed in an intermediary step of the deposition, with the substrate kept at 570 K and with the surface exposed to residual gases (recalling that this is the interface where FM/AFM magnetic coupling takes place). In contrast with the previous fitting (section 4.2) we use all measured points in the l-scans, including the anti-phase region, once the OP ordered domains also contribute to the CTR (order peaks in fig. 5.1 to 5.3).

Intermediary models revealed useful to give insights onto the film properties, before converge to the final model used to calculate chemical order. In a model where the number of layers is a fitting parameter, we get the thickness of the film that matches the Kiessig fringes. The total layer thickness is fitted to be of 3.26 nm, in agreement with the nominal thickness (with one inter-mixing layer at the interface with the substrate). In a similar model, we fix the number of layers, but allows the presence of two distinct domains with different inter-layer distances. In this way, the χ^2 value is consistently reduced when these domains, of equal weight, have inter-layer distances close to ${}^{c^{OP}}/_{2}$ and close to ${}^{b^{IP}}/_{2}$. These values were obtained from the above l-scan peak fit procedure (figs. 5.3 and 5.5).

From these indications, the final model is composed by two parts, where we fix the different inter-layer distances to the above values, thus reducing the number of free variables. One part, corresponding to IP domains ($d^{IP} = {}^{b^{IP}}/_{2} = 1.92\,\text{Å}$) does not contribute to the intensity at the anti-phase region for the integer CTRs. The average Mn and Pt occupancy is homogeneously distributed within this domain, so that they do not contribute to the order peak. The other part, with $d^{OP} = {}^{c^{OP}}/_{2} = 1.884\,\text{Å}$, is allowed to be ordered, and gives rise to the anti-phase intensity in the fitted curve, as shown in figure 5.7. These two parts have both 13 ML thickness, and interfere coherently. At the interface with Pt(001) substrate three inter-diffusion layers are considered with an imposed linear increase of the inter-layer distance and free occupancy parameters. The layer 0 have only 11% of Mn, that represents Mn mixing with the substrate. The other two layers present already some degree of order from the fit, as the first one is Mn richer ($\theta^1_{Mn} = 0.43$) than the second one ($\theta^1_{Mn} = 0.31$). At the surface, only Pt atoms are present, with a total occupancy close to unit, but spread along 2 or 3 atomic planes (roughness with $\beta \sim 0.5$). The surface presents small steps of about one quarter of ML, coming from the height difference between IP and OP domains. The Debye-Waller parameters are fixed to bulk values calculated for measurement temperature (570 K), $\text{DW}^{570\text{K}}_{Pt} = 0.61$ and $\text{DW}^{570\text{K}}_{Mn} = 0.85$, using equation 3.3.5.1.1-(7) and tables 5.2.2B and 3.3.5.1A of the International Tables of Crystallography [140]. The final fitting results ($\chi^2 = 7.3$) of the layer structure, before treating the chemical order issue, are summarized in table 5.1.

To properly give a quantitative description of the order parameter of this layer, large rocking curves along the order peaks have to be taken into account. These peaks are composed by a broad contribution, coming from the ordered domains, superposed to the narrow CTR contribution. Besides the (1 1 1.04) peak, already shown in figure

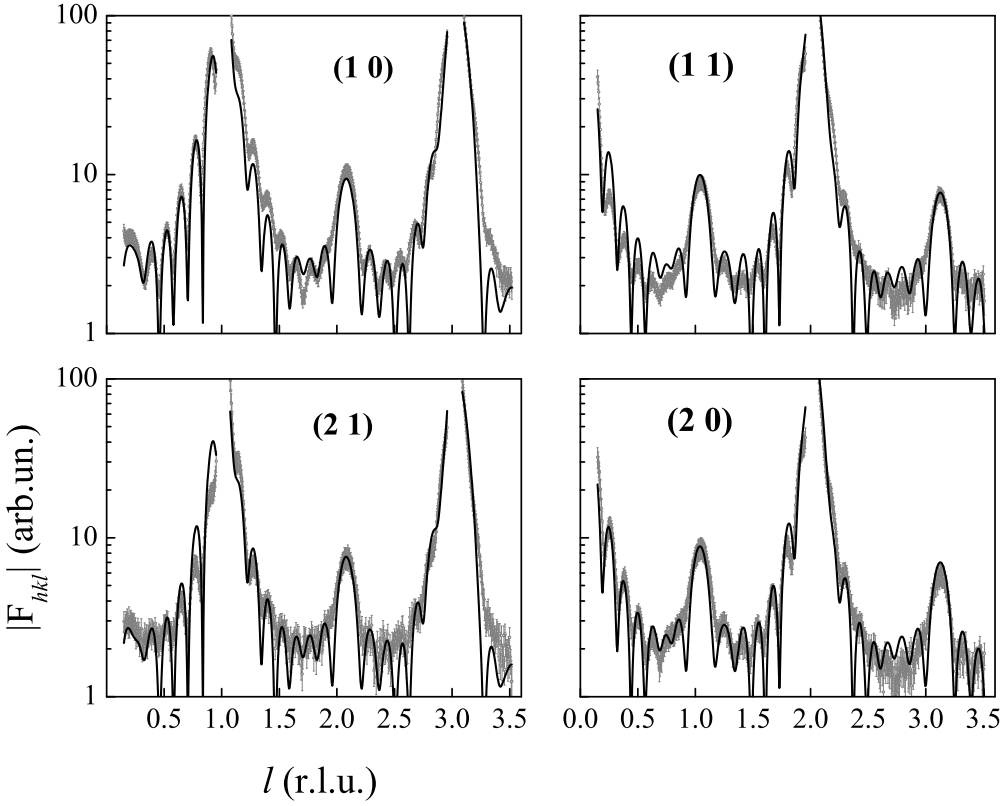

Figure 5.7: Experimental and fitting of $(MnPt)_8$ layer CTRs.

	structure fit		order simulation	
layers	θ(Pt/Mn)	d(Å) (IP/OP)	θ(Pt/Mn)	d(Å) (IP/OP)
18	0.12/0	1.84	fix	fix
17	0.23/0	1.84	fix	fix
16	0.46/0	1.90	fix	fix
[4, 6, ..., 14]	0.55/0.45	1.92/1.88	0.78/0.22	fix
[3, 5, ..., 15]	0.45/0.55	1.92/1.88	0.22/0.78	fix
2	0.69/0.31	1.93	fix	fix
1	0.57/0.43	1.94	fix	fix
0	0.89/0.11	1.95	fix	fix
Bulk	1/0	1.96	fix	fix
DW	bulk (570 K): 0.61/0.85		fix	
χ^2	7.3		-	

Table 5.1: Result of the fitting for the $(MnPt)_8$

5.4, the (0 1 2.08) peak is also measured (solid black line in figure 5.9). In both cases, the numerical integration or the area of a fitted two-peaks pseudo-Voigt function give similar values. We take the mean of the two integrals as the value for each (hkl) position. The values $\left|F^{order}_{0\,1\,2}\right| = 42 \pm 3$ and $\left|F^{order}_{1\,1\,1}\right| = 46 \pm 2$ are derived by applying the appropriate corrections (section 4.3). The error bars are obtained by adding to the integration method difference, the error in the detector acceptance correction coming from the fit uncertainty of the large peak width. In the simulation, we keep fixed all structural parameters and change only the Mn and Pt occupancies (table 5.1) in order

to be as close as possible to the structure factors above, leading to chemical order. The black solid line in figure 5.8 gives the simulation that gets closer to both peak values. It gives a general OP order parameter of $S_{OP} = 0.50 \pm 0.05$, averaged to 16 MLs, where we consider also the layers 1, 2 and 16 in the calculation. To get the error bars of the order parameter, we simulate the two limiting situations where the curve crosses the extremities of the $\left|F_{hkl}^{order}\right|$ error bars.

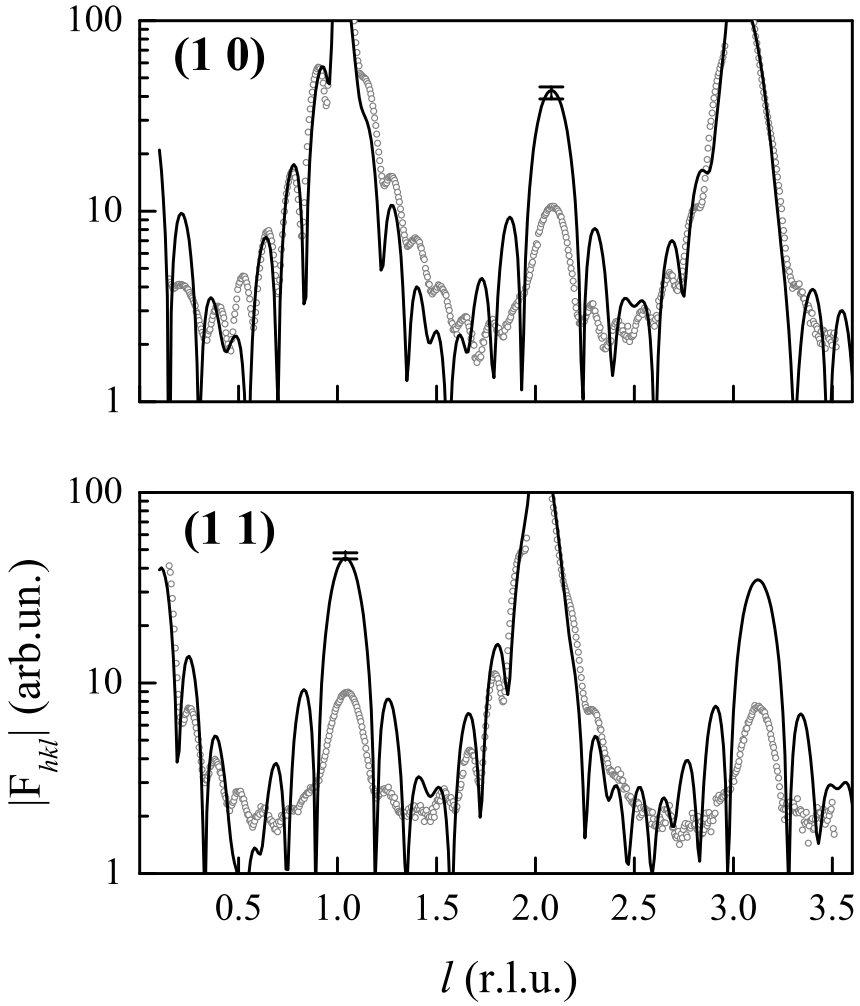

Figure 5.8: Simulation of order parameter for the two CTRs where we have measured the large rocking scans.

An indirect quantification of the order parameter for in-plane domains is performed by comparing the $|F_{hkl}|$ in the (0 1 2.08) and (1/2 3/2 1.02). This reciprocal space positions have the same momentum transfer, as can be easily seen if we write them in the *fcc* basis, giving $(1\,1\,2)_{fcc}$ and $(2\,1\,1)_{fcc}$, respectively. Rocking scans at these positions are compared in figure 5.9, where the abscissa is in transverse momentum transfer units. Applying the appropriate corrections to the integrated intensity and extracting the square root we get, $\frac{\left|F_{\text{ø}}^{order}\right|}{\left|F_{1/2\ 3/2\ 1}^{order}\right|} = 2.2$. Considering that the 90º turned symmetric IP domains have the same structure factor, we have to multiply by two the IP order parameter, to finally obtain, $S_{IP} = 0.45 \pm 0.05$. The order parameter of the layer is, finally, close to unit: $S = S_{IP} + S_{OP} = 0.95 \pm 0.1$.

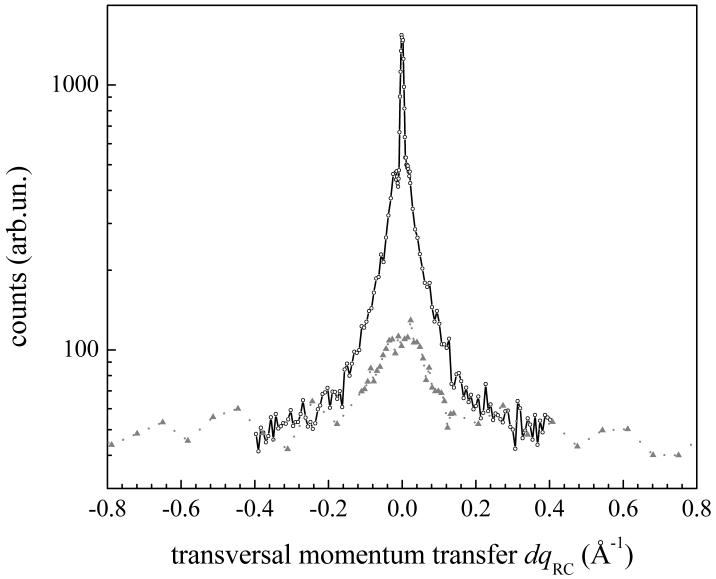

Figure 5.9: Rocking curve at (0 1 2.08) and (1/2 3/2 1) in transverse momentum transfer units, comparing equivalent scans

We note that the order parameter for this sample is similar to the one presented in chapter 4. However, the main difference among these samples is that the volume of the OP ordered domains is much larger for the present situation (more than 10 times) than for the RT deposition plus annealing sample.

5.1.3 FePt deposition at 570 K on $(MnPt)_8$/Pt(001)

The alternate FePt growth (4 BLs) on the previous $(MnPt)_8$ layer was performed keeping the substrate temperature at 570 K. The frequency of Kiessig oscillations increase, but no further attenuation in the CTR is observed (see fig. 5.11), suggesting that pseudomorphism persists. Figure 5.10 presents the evolution of the order peak near the (1 1 1) position after deposition of each FePt BL, as indicated in the label. We observe both an increase of the order peak and a shift toward higher l values. This additional contribution, coming from the FePt layer, evidences that this layer also present OP $L1_0$ order. Moreover, rocking curves and l-scans along the half-integer positions are unchanged in relation to the previous layer, what mean that the FePt layer do not have IP domains, neither $L1_2$ phase is present. This result is expected, once the lattice mismatch between FePt and Pt (and consequently the pseudomorphic MnPt) favors the out-of-plane orientation of the c-axis (see section 3.1). No in-plane relaxation was observed.

After the 4 FePt BLs, 2 Pt ML were immediately grown to protect the surface during the *in situ* measurements, done at RT. A complete set of l-scans, as well as rocking curves around the (0 1 2) order peak, were measured. Figure 5.11 compares the (01) CTR of this layer with the $(MnPt)_8$ one (a vertical shift is applied for clarity). The most prominent feature observed is the structure peak around $l \sim 3.3$ (indicated by an arrow), corresponding to the FePt structure peak $(0\,1\,3)_{FePt}$. It is not straightforward

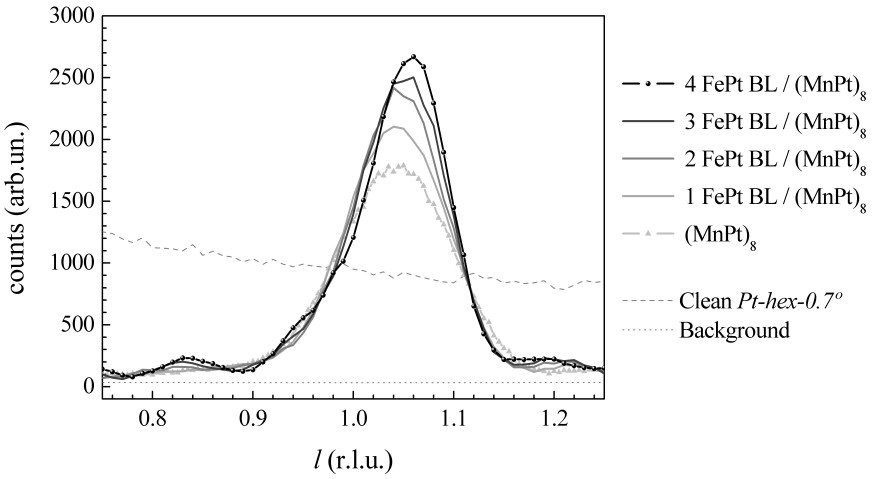

Figure 5.10: l-scans along the (1 1) CTR, for intermediary steps of FePt deposition.

to obtain a precise value of the FePt lattice parameter from this data because of the superposition with bulk contribution.

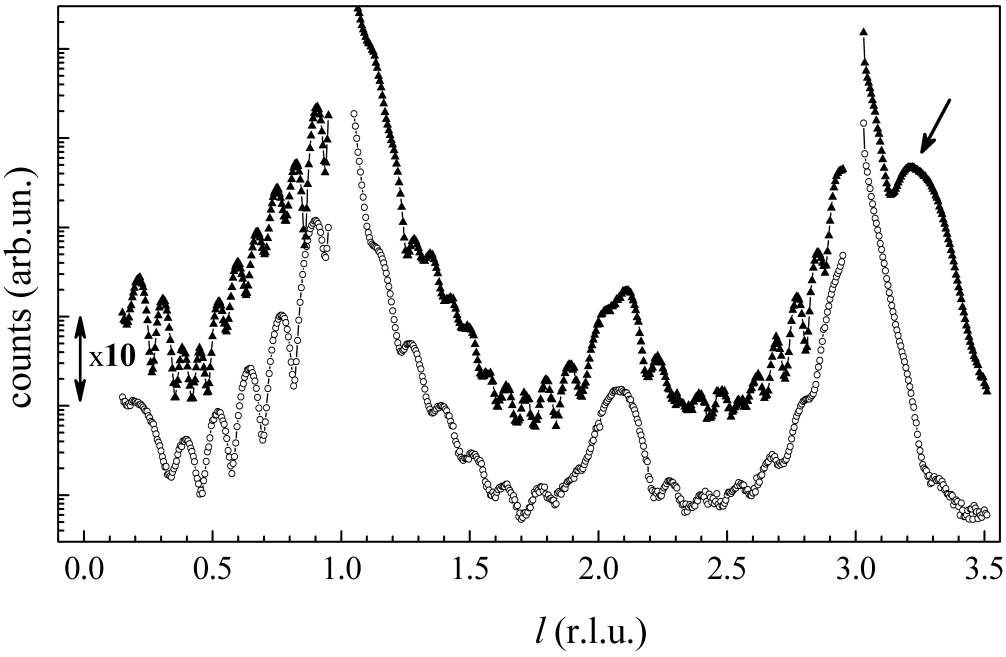

Figure 5.11: Comparison of the (0 1) l-scan before and after (shifted by x10 factor) FePt deposition. The arrow highlights the appearance of the FePt structure peak.

Before going on the quantitative analysis of the *in situ* measurements, we take a look at the *ex situ* GIXRD measurements, where high-order specular reflections were probed. To allow *ex situ* measurements, the sample was protected by a 8 ML Pt cap-layer. Figure 5.12 shows the (0 0) CTR around $l = 6$ to 8, with the structure peak of FePt well separated from the Pt-bulk one. Extracting a linear background and fitting a Gaussian (inset), we get a peak position of $l = 6.55 \pm 0.01$, with a FWHM corresponding to perpendicular correlation length of 9 to 10 MLs. The apparent double peak observed indeed is coming from a MnPt Kiessig oscillation that overlaps the FePt structure

peak. We determine the ratio between the FePt and Pt OP-lattice parameters to be $c_{FePt}/a^{OP} = \left(\frac{6.55}{6}\right)^{-1} = 0.916 \pm 0.002$ and $c_{FePt} = 3.595\,\text{Å}$. This value corresponds, within the error bar, to the expected value for a pseudomorphic $L1_0$ FePt alloy on Pt(001) with constant unit cell volume ($V_{FePt} = 55.32\,\text{Å}^3$ [97]). The tetragonality (c/a), however, is significantly changed compared to the bulk value ($a = 3.860\,\text{Å}$, $c = 3.713\,\text{Å}$ and $c/a = 0.962$ [97]). This tetragonality is discussed in more detail for the next sample, where FePt is directly deposited on the Pt substrate.

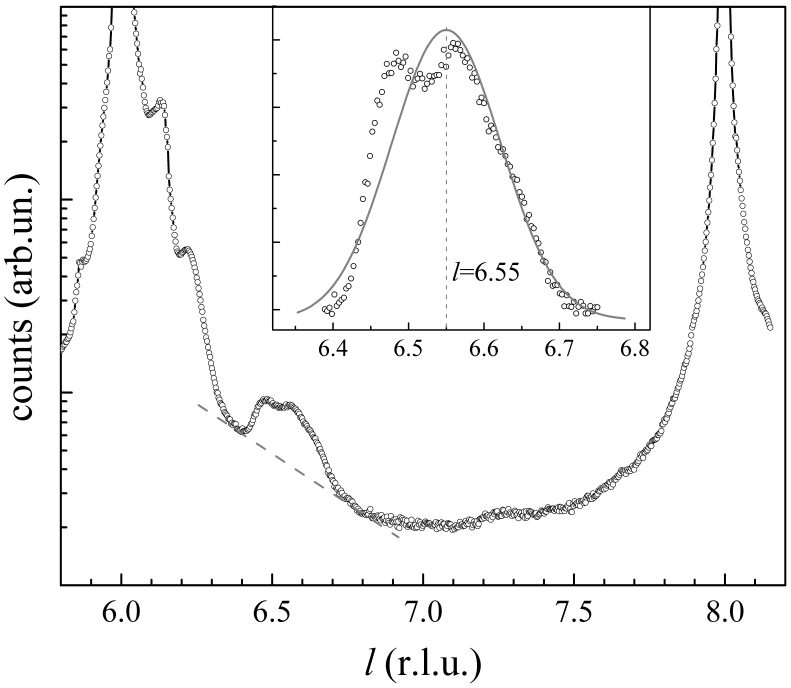

Figure 5.12: Specular CTR measurement around the (006) structure peak of FePt.

5.1.4 Modeling the $Pt_2/(PtFe)_4/(MnPt)_8/Pt(001)$ structure

For modeling and fitting the complete $Pt_2/(PtFe)_4/(MnPt)_8/Pt(001)$ film, we use the $|F_{hkl}|$ obtained from l-scans of 9 CTRs, being 5 nonequivalents. In the fitting process, the MnPt layer and the scale factor are kept the same as the previous fit. We use the FePt inter-layer distance measured *ex situ* as a fixed input to the fit. The only fitting parameters are the number of FePt layers and the amount of Pt in the cover layer. We consider an equiatomic stoichiometry, based on knowledge of the unit cell volume. The model that best fits the thickness oscillations is composed by 4 FePt BLs covered by 3 to 4 Pt MLs, including some roughness. The Pt layer in the interface FePt/Pt contains some Fe. To calculate the order parameter, we use a set of $\left|F_{hkl}^{order}\right|$ derived from rocking curves along the (0 1 2) order peak. In the higher l positions, corresponding to the FePt layer, the peak is larger, giving a lateral correlation length for the ordered domains of $L_{\parallel}^{FePt} = 4.3 \pm 0.8\,\text{nm}$, with the structural correlation always about two orders of magnitude higher ($\sim 500\,\text{nm}$). The experimental chemical order peak is compared to the simulation in figure 5.13, were the ordering is imposed to both the MnPt and FePt layers, so as to fit the experimental curve in the l position

corresponding to its lattice parameter. The OP order parameter calculated for FePt in this simulation is: $S_{FePt} = 0.7 \pm 0.2$. In the experimental curve the two peaks are not well separated due to the small domain size in all three directions, which tends to spread the peaks and screen the interference effects. The interference between the scattering coming from the bulk and from the layer leads to shifts in the peak position comparable to the expected value from the inter-layer distance. This contributes to the uncertainty in the order parameter determination.

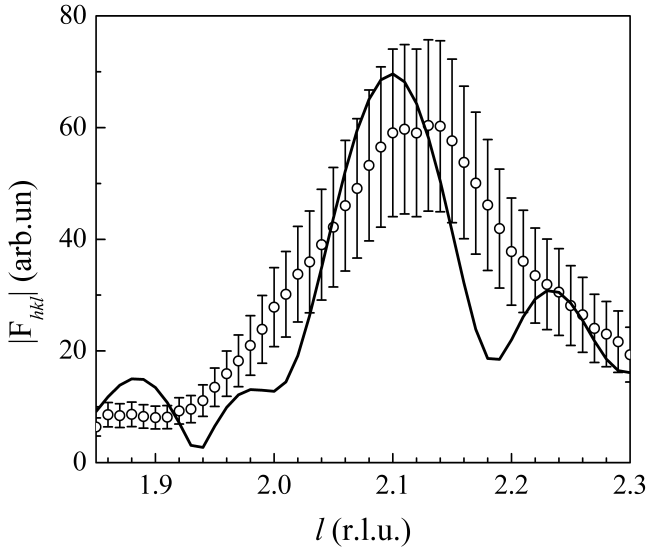

Figure 5.13: Experimental and simulated $|F_{hkl}|$ around the (0 1 2) order peak for the ordered FePt/MnPt/Pt(001) film.

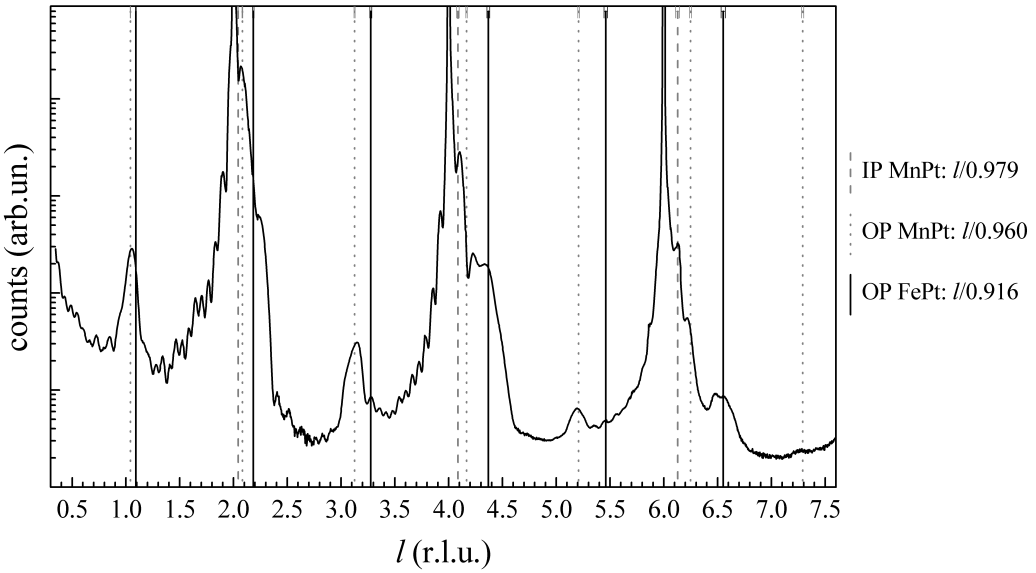

Figure 5.14: *Ex situ* measurement of the specular CTR for sample S4.

The specular CTR of the sample S4 is presented in figure 5.14 up to $l = 7.5$. In this picture the calculated l position for the $(00l)$ order and structure peaks are represented by vertical lines for the three kind of domains composing the sample, namely, OP-FePt

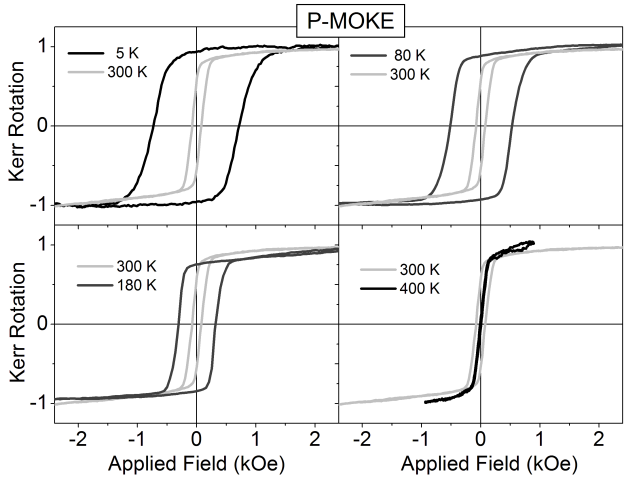

Figure 5.15: Hysteresis loops for $Pt_8/(PtFe)_4/(MnPt)_8/Pt(001)$ at a few selected temperatures 5, 80, 180 and 400 K, compared to 300 K.

(solid line), OP-MnPt (dot) and IP-MnPt (dashed line, only to structure peaks). The FePt order peaks are barely seen due to the small correlation length of these domains. However, the structure peak is clearly separated from both MnPt and bulk Pt peak for high order reflections. No peaks are observed between the FePt and MnPt, indicating that inter-mixing at the interface is limited.

5.1.5 Magnetic studies by MOKE

The magnetic measurements on the $Pt_8/(PtFe)_4/(MnPt)_8/Pt(001)$ film (sample S4) were performed using the MOKE facilities installed in the ultra-high vacuum (UHV) multi-chamber system at the Max Plank Institut of Halle, Germany. As we were interested in perpendicular exchange coupling properties, the measurements were done only in polar MOKE geometry (with an incidence angle of 69° to the sample normal). A laser diode of wavelength 670 nm with a beam diameter of about 200 μm were used as probe. The sample was mounted in the cold-finger holder of a cryostat, between the poles of an electromagnet whose field was reversing from -3000 to 3000 Oe.

Data reported here comes from two experiments. In the first one, we started by cooling S4 at an applied field of +3000 Oe perpendicular to the surface from RT down to 5 K. Then, we measured the hysteresis loops, looking for exchange bias and the training effects. The loops presented here are normalized to the maximum rotation. Before normalization, the maximum Kerr rotation was typically 0.4 mrad at 5 K and 0.6 mrad at RT. Fluctuations in the absolute Kerr rotation were coming from instabilities in the optical alignment. In figure 5.15 we present the loops at different temperatures compared to the one at 300 K. The increase in the coercive field, by one order of magnitude compared to RT, is largely coming from exchange coupling between FePt and MnPt, showing that MnPt is indeed AFM. In a second round the conditions were similar but the field cooling was initiated at 400 K, going down to 5 K. No remarkable differences were observed among the two rounds.

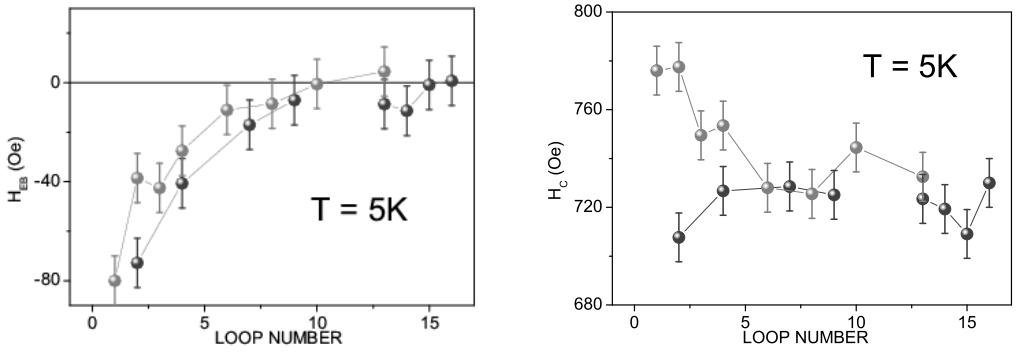

(a) (b)

Figure 5.16: Training effect after field cooling for $Pt_8/(PtFe)_4/(MnPt)_8/Pt(001)$: (a) exchange bias shift and (b) coercivity as function of the number of loops.

After field cooling, we could clearly observe an exchange bias shift of $H_{EB} \approx -80\,Oe$. This corresponds to an additional interface energy of $\Delta\sigma \approx 0.015\,erg/cm^2$, with $M_s = 1140\,emu/cm^3$ and $t_{FM} = 1.6nm$ for the FePt layer (see eq. 1.8). However, the exchange bias was not stable and vanished after a few loops (figure 5.16-a). This training effect is not unexpected since in this system the interfacial AFM spins are, *a priori*, all compensated. The pinning centers induced during the field cooling are out of equilibrium or frustrated, and relaxes to a more thermodynamically stable situation. The coercivity, on the other hand, remained rather stable, within ±20 Oe, around $H_C \approx 720\,Oe$ (figure 5.16-b).

After training loops at 5 K, the temperature was raised up to 400 K, in a time interval of 16 hours. During this interval, hysteresis loops were collected after temperature stabilization at different values. A few loops are shown in figure 5.15. The coercive field as function of temperature shows the typical behavior of an exchange coupled system (figure 5.17): below the ordering temperature of the AFM material, $T_N \approx 310\,K$, the AFM/FM coupling is more and more stable while temperature decreases, giving rise to an increase in the coercive field. The reversing field has to overcome the additional energy coming from the exchange coupling; above T_N, the coercivity has a weaker dependence on temperature. The intersection of the two straight lines yields an estimation of the Néel temperature. We should point out that this is a clear demonstration that the Néel temperature is around RT for a such thin layer, $t_{MnPt} \approx 3\,nm$. As far as we know, this is the thinnest MnPt film leading to AFM order at RT. We conclude that chemical order, in our case very close to one ($S \sim 1$), is the key parameter controlling the AFM order.

5.1.6 Magnetic studies by XMCD

To study the element specific magnetic moments of Mn and Fe on the $Pt_8/(PtFe)_4/(MnPt)_8/Pt(001)$ film (sample S4), we carried out XMCD measurements at the Mn and Fe $L_{3,2}$ edges. The XAS/XMCD experiments were performed on the ID08 beamline at ESRF, with ≈ 100% linear or circular polarizations. All scans were recorded simultaneously in both

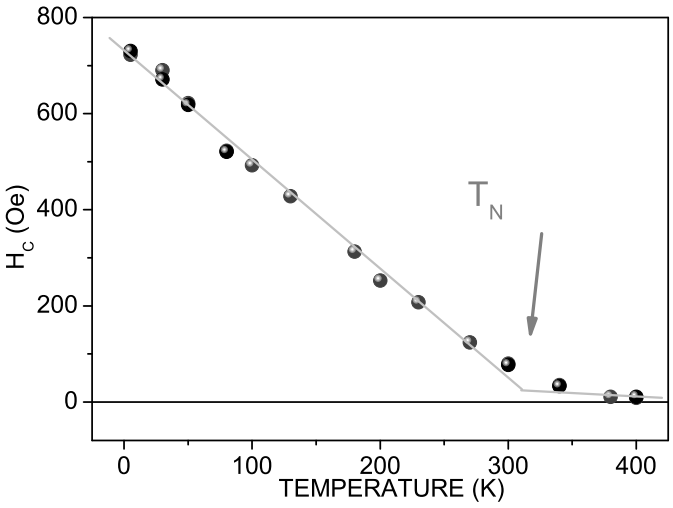

Figure 5.17: Coercivity for raising the temperature for $Pt_8/(PtFe)_4/(MnPt)_8/Pt(001)$ after field cooling and training. An estimation of the Néel temperature is given by the intersection of the two straight lines.

total electron yield (TEY) and total fluorescence yield (TFY) modes. The sample was aligned with the surface normal to the incident beam in order to have the magnetic field perpendicular to the surface. The maximum magnetic field was $\pm 5\,T$ generated by a split coil superconducting magnet. Here, $\mu^+(\mu^-)$ refers to the absorption coefficient for the photon helicity parallel (antiparallel) to the Fe 3d majority spin direction.

Figure 5.18 shows the raw data XAS spectra (μ^+ and μ^-) collected in TEY mode by flipping the circularly polarized light in the photon energy region of the Mn and Fe $L_{3,2}$ absorption. The sample temperature was set 10 K after field cooling under the applied field $+3000\,Oe$. The difference $\Delta\mu = (\mu^+ - \mu^-)$ associated to the XMCD is also presented. At the Mn region, the XMCD is multiplied by 10, to be discernible.

The amount of Mn is two times that of Fe and the transition strength is almost the same for both elements, however, the intensity measured at the Fe absorption edges is much higher. This is a consequence of the attenuation of the X-ray beam - less photons arrive at the buried MnPt layer - and of the limited escape depth of the electrons produced after the decay process. We are not concerned by absolute comparison of spectra and we simply normalize each spectrum to unit above the edges.

The XMCD signal at the Fe L_3 edge is, as expected, very large: the relative difference $\frac{\Delta\mu}{\mu} = \frac{(\mu^+ - \mu^-)}{(\mu^+ + \mu^-)}$ amounts to 40% at 10 K and $+3000\,Oe$. The important point to note here is that there is a XMCD signal at Mn L edges. The relative difference is only 1.2% but shows up clearly. To ensure that the difference is not coming from artifacts, the measurement was done also with the applied field in the opposite direction $-3000\,Oe$; both differences are shown in the inset of figure 5.18, where one can remark the very good reproducibility in amplitude and shape. Such an XMCD signal implies that some amount of uncompensated Mn spins are present. Moreover, the Mn XMCD signal is opposite to Fe, indicating that the Fe and Mn spins are aligned antiparallel to each other.

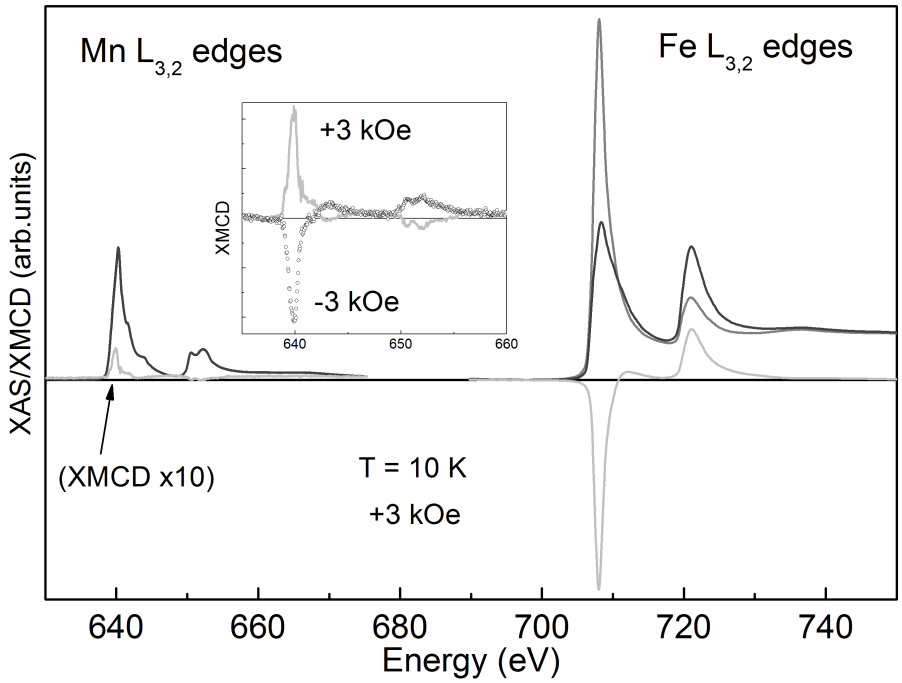

Figure 5.18: Mn and Fe $L_{3,2}$ XAS spectra (μ^+ and μ^-) of the $Pt_8/(FePt)_4/(MnPt)_8/Pt(001)$ sample collected in TEY mode by flipping the circularly polarized light at an applied magnetic field of +3 kOe and at 10 K.

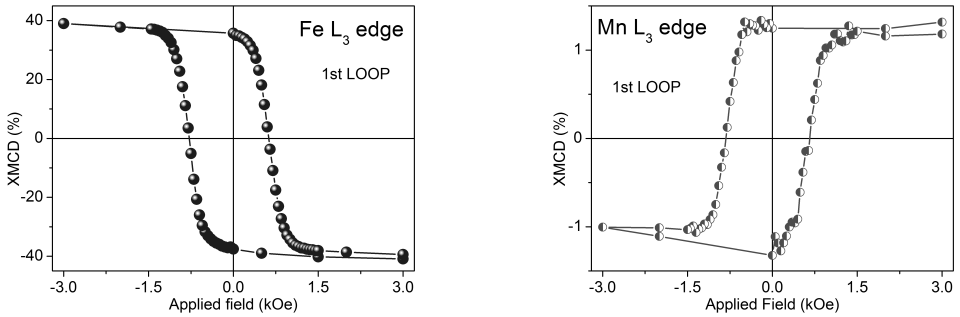

(a) (b)

Figure 5.19: Element selective hysteresis loops: (a) Fe and (b) Mn L_3 edges.

Another important outcome that can be remarked (inset fig.5.18) is that, when the magnetic field is reversed, the Mn XMCD is almost completely reversed, meaning that uncompensated Mn moments are following the Fe ones, so are not pinned (or frozen) by the AFM layer. The coupling between uncompensated interfacial Mn spins is stronger with the FM layer than with the AFM one. Element selective hysteresis loops measured at the maximum of each XMCD signals confirms such an almost completely reversible behavior (figure 5.19). One notes the mirror figures among the two selective loops. Even the small exchange bias shift ($H_{EB} \approx -90\,Oe$) can be observed in both curves. However, if the Fe behavior is completely symmetric by reversal of the applied field (figure 5.19-a), at the Mn edge one can remark that the XMCD amplitude is not completely reversed after the first half loop (figure 5.19-b); this vertical shift is small, about 10%, compared to the noise but, it could be associated to the amount of pinned Mn spins that are not rotating when Fe spins rotate. These pinned Mn spins, about 10% of the uncompensated spins, are giving rise to the exchange bias shift. This figure is comparable to that measured at the $Co/Ir_{0.8}Mn_{0.2}$ interface by Ohldag et al. [24].

The additional interface energy of $\Delta\sigma \approx 0.015\,erg/cm^3$, calculated in the previous section, assumes that the whole interface is contributing to the exchange bias shift. However, if one supposes that only uncompensated pinned Mn spins are contributing, the exchange coupling strength at the MnPt/FePt would be much higher. This is probably one of the main reasons giving rise to discrepancies when model calculations are performed.

5.2 $Pt_6/(PtMn)_8/(PtFe)_6/Pt(001)$ (Sample S3)

The FePt alloy in the $L1_0$ phase has one of the strongest magnetic anisotropies (see section 1.3.2). It has been shown by Imada et al. [157] that down to the thinnest limit, i.e. one Fe ML sandwiched by Pt, the perpendicular magnetic anisotropy persists below $\sim 160\,K$. Since ferromagnetism is a collective phenomenon, one can expect that the Curie temperature (T_C) of a material is lower in the ultra-thin regime than in the bulk. These authors found, for FePt prepared by alternate deposition at 503 K, that T_C is above RT for only two BLs and there is a remanent magnetization at RT from three BLs on. The order parameter, measured for the 10-BLs film, was reported to be $S = 0.6 \pm 0.1$ and assumed to be similar for the thinner layers. In section 3.1.5, we discussed the Fe on *Pt-hex* at different deposition and annealing temperatures and observed that an atomic site exchange process takes place among Fe (higher surface energy) and Pt substrate atoms. A STM study [51] showed that up to 1.2 MLs of Fe deposition on *Pt-hex*, no evidences of Fe atoms on the surface is found.

5.2.1 FePt deposition at 570 K on Pt(001)

We have prepared a 2 nm-FePt layer by alternate Fe and Pt thermal deposition[48, 157]. The *Pt(001)-hex* substrate was kept at 570 K and a sample with an excess in Fe, consisting of $[Fe(2\,ML)/Pt(1\,ML)]_3$, was deposited. The growth at 570 K was shown to reinforce the atom exchange process, so that the excess of Fe is expected to be

compensated by Pt atoms segregating to the surface during growth. The sample was kept at 570 K during 2 hours after deposition to improve ordering.

The *in situ* GIXRD measurements presented in this section were performed with a 20 keV beam under a grazing incidence angle of 0.6°, about 2.5 times the critical angle for total reflection of Pt at this energy ($\alpha_c = 0.24°$)[2]. Calibration with a quartz crystal micro-balance, cross-checked by the anti-phase scattering intensity oscillations, gives a deposition rate of 0.30 and 0.04 ML/min for Fe and Pt, respectively.

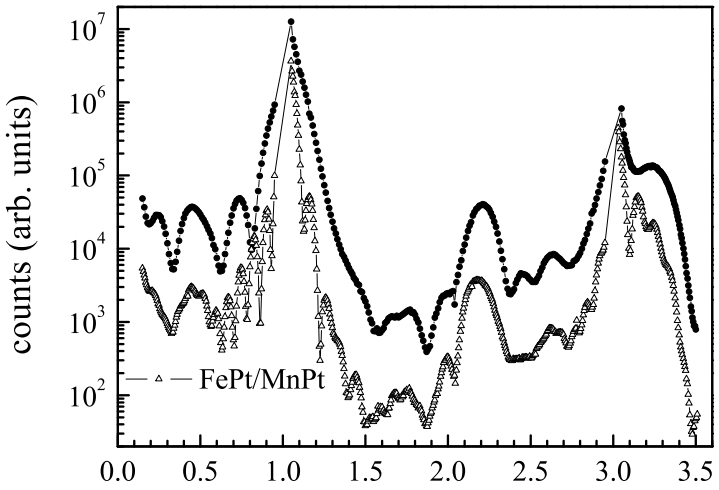

Figure 5.20: X-ray scattering along the (1 0) CTR for the FePt(2 nm) layer before (upper solid circles) and after (bottom open triangles) being covered by MnPt(3 nm).

After cooling down to RT the 2 nm-FePt layer, a set with the following non-specular CTRs were measured, (1 0), (0 1), (1 1), ($\bar{1}$ 1) and (2 0). Figure 5.20 shows the X-ray scattering along the (1 0 l) CTR (upper curve). The oscillations are preserved up to high l values. Moreover, no evidence of in-plane relaxation was observed by radial-scans. Both outcomes confirm a pseudomorphic growth of the layer. The FePt layer adopts the in-plane lattice parameter of Pt substrate, $a_{\mathrm{Pt}} = 3.924$ Å. The strong peak around $l = 2.2$ (fig. 5.20) arises from the OP chemically ordered $L1_0$ FePt layer. No traces of $L1_2$ or IP $L1_0$ phases were found. The tetragonality of the epitaxial FePt layer is $c/a = 0.907 \pm 0.002$, averaged from the whole set of CTRs (8 peaks in total, with positions fitted with Gaussian function), giving a value of $c_{\mathrm{FePt}} = 3.56$ Å. Such strong structural anisotropy has never been reported before for epitaxial $L1_0$ FePt thin films. One should note that FePt $L1_0$ alloy has lattice parameters of $a = 3.860$ Å and $c = 3.713$ Å ($c/a = 0.96$) [97]. This pseudomorphic FePt layer has a tensile strain of 1.7%. The rocking scan along the order peak has the same width as other parts of the CTR and no broad peak was observed, a behavior distinct of what happens to MnPt on Pt(001), presented in sections 4.2 and 5.1.1. The FePt surface has terraces estimated to be larger than 400 nm.

Quantitative analysis of the GIXRD data is done by simulating and fitting the experimental CTRs. The extraction of the structure factor amplitudes from the l-scans

[2]Estimated with the X-Ray Database calculation tools of www.cxro.lbl.gov.

follows the procedure described above (section 4.1). Once FePt domains have the same lateral correlation length as the surface, the rocking scans integration gives the same $|F_{hkl}|$ as obtained by the corrected l-scans. No specific integration of the rocking scan around the order peak is needed to extrapolate the order and the fitting gives directly the occupancies from where we calculate the order parameter. As a initial step, the number of layers are fitted so as to reproduce the thickness oscillations. Here, we keep fixed the inter-layer distance to the value corresponding to the tetragonality shown above, and the fit gives 12 to 13 MLs.

layers (n)	θ(Pt/Fe)	d(Å)	DW(Pt/Fe)
12	0.27/0	1.75	2.5/3.3
11	0.01/0.81	1.75	
10	0.55/0.45	1.82	
9	0.20/0.80	1.76	1.46/0.39
8	0.54/0.46	1.79	
[2, 4, 6]	0.76/0.24	1.78 (fix)	
[1, 3, 5, 7]	0.14/0.86	1.78 (fix)	
0	0.96/0.04	1.94	
Bulk	1/0	1.96	0.31/–
χ^2	11.4		

Table 5.2: Fitting results for the 2 nm-FePt layer.

The best fitting model consists of 13 FePt ML (2.1 nm) and is summarized in table 5.2. The first ML ($n = 0$) represents the Fe inter-diffusion and have a fitted occupancy of 0.04 and an inter-layer distance slightly smaller than the bulk Pt. Then, 7 ordered FePt MLs are considered with the inter-layer distance fixed to the tetragonality value shown above. The fitting procedure does not allow a precise determination of the layer stoichiometry. Possible values for the Fe concentration range from 0.5 to 0.65. However, the sample stoichiometry can be more precisely determined from the unit cell volume $V = 54.802\,\text{Å}^3$, calculated from the c_{FePt} and a_{Pt} given above. This value is in excellent agreement with that of ordered $Fe_{55}Pt_{45}$ nano-crystalline alloy [97] $V_{0.55} = 54.807\,\text{Å}^3$. This stoichiometry was used as input parameter for this 7 MLs region ($n = 1\,\text{to}\,7$). From $n = 8$ up to $n = 12$ all occupancy and inter-layer distance parameters are let free and the fit result gives a smaller degree of order. In this upper region, the Fe concentration is even higher, indicating that the intermediary ordered layer prevents the migration of Pt atoms to the surface or diffusion of Fe atoms in to the bulk. This effect is coherent with the transmission electron microscopy observation that bulk diffusion through the $L1_0$ ordered phase is activated only at elevated temperatures [146]. Two regions with different Debye-Waller parameters are considered, from $n = 0\,\text{to}\,9$ and the last 3 MLs. They are let free to vary and the reasonably high values obtained point to some structural disorder. However, we must be careful on interpreting this outcome, once the DW is very dependent on data correction mistakes or misalignment during measurements. The comparison of the fitted curve with the experimental data is presented in figure 5.21. The order parameter averaged for the whole layer thickness

is of $S_{\mathrm{FePt}} = 0.54 \pm 0.05$. Just in the region from $n = 1$ to 7 this order parameter is of 0.62.

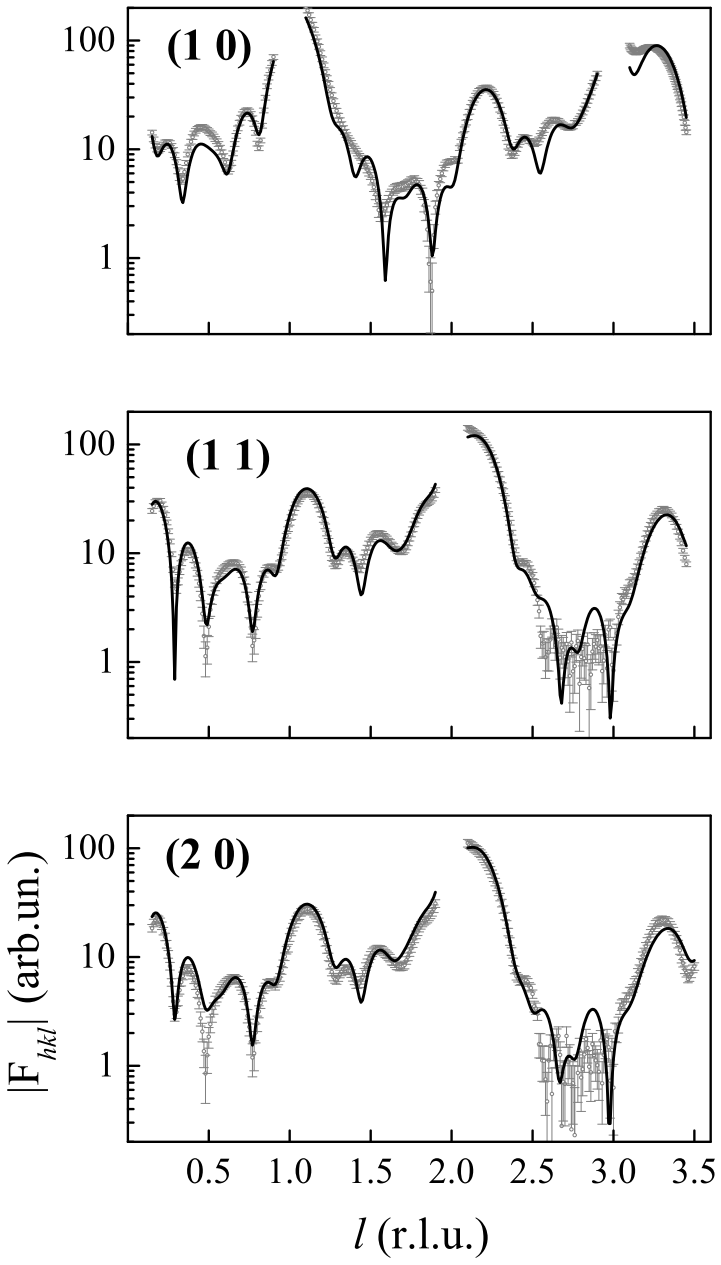

Figure 5.21: Fitted curve (black) compared to the experimental structure factors (gray) for [Fe(2 ML)/Pt(1 ML)]$_3$ deposited at 570 K.

5.2.2 MnPt deposition at 550 K on (FePt)$_6$/Pt(001)

As a second step of sample deposition, the (FePt)$_6$/Pt(001) film was covered, at 550 K, by a 3.0 nm-MnPt (8 MnPt BLs) layer. The (1 0) CTR is presented in bottom curve of in figure 5.20. After deposition of these 8 MnPt BLs, similar features as those reported in the previous section are observed. c(2x2) order peaks appears in the half-integer positions, corresponding to small in-plane $L1_0$ domains ($L_{\parallel}^{IP} \sim 2.8$ nm and thickness close to the total MnPt layer). Shifted l-scans draw out the presence of broad peaks

coming from small MnPt OP ordered domains. The tetragonality of these domains is measured to be $c/a^{OP} = 0.95 \pm 0.01$. The radial scan along the (1 1 1.07) position evidences the presence of the large peak superposed to the intense narrow peak (fig. 5.22). From the fitted peak positions we conclude that, if some relaxation exists for MnPt OP domains, it is smaller than 0.25%.

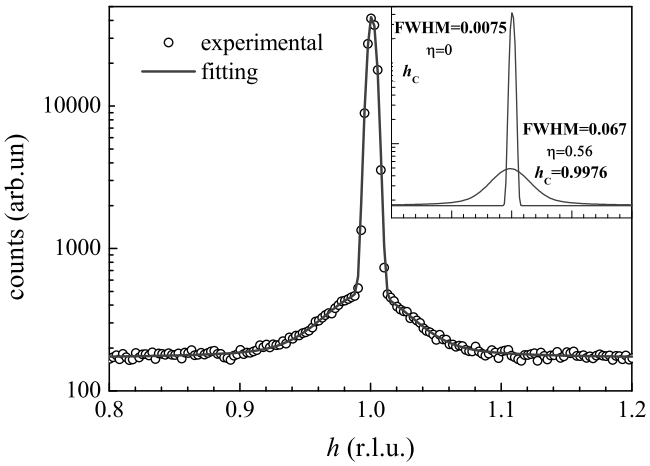

Figure 5.22: Radial scan along the reciprocal space position (1 1 1.07), the maximum of the order peak. If there is some relaxation in the FePt or MnPt layers it is smaller them 0.25%, as shown by the center position of each peak.

As a final step, the MnPt layer is covered with 6 MLs of Pt at 550 K to protect against oxidation in further *ex situ* studies. This Pt deposition favors the OP MnPt order, while IP domain intensity remains unchanged. Owing to the high complexity of the system, we do no attempt to quantitatively treat the order parameter of the MnPt layer. Figure 5.23 gives only a comparison in linear scale of the order peak close to the (1 1 1) before and after $Pt_6/(PtMn)_8$ deposition, showing that this peak increases by about 20%. We estimate that the order parameter of this layer is smaller than what we have obtained for the MnPt deposition directly on Pt(001) substrate at 570 K.

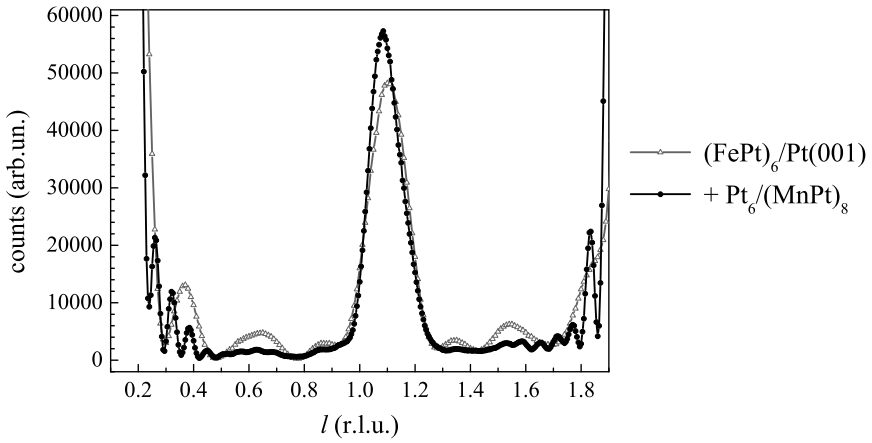

Figure 5.23: Comparison of the order peak close to (111) before and after the deposition of $Pt_6/(PtMn)_8$. The increase in maximum intensity is of about 20%.

5.2.3 X-ray Absorption Spectroscopy

We present here the results of hard X-ray absorption spectroscopy concerning the FePt layer. Local anisotropy is clearly observed in XAS measurements at the Fe K edge. In the XANES spectra of metallic compounds, the double resonance (A and B in fig. 5.24) just above the absorption edge is an experimental signature of the structures *fcc* or $L1_0$ and small differences in the relative height of these peaks are associated to variations in the local chemical order [158, 159].

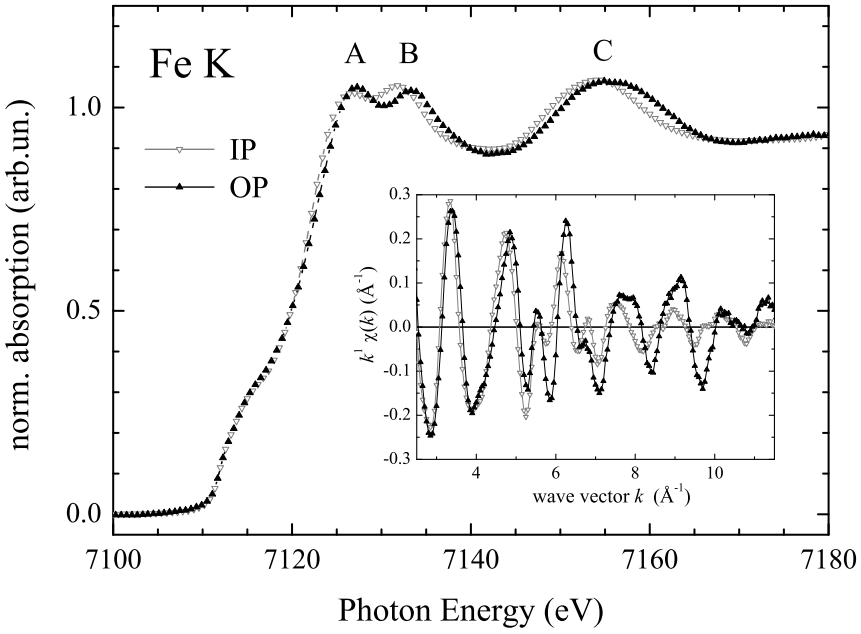

Figure 5.24: Polarization dependent XANES at the Fe K edge for X-ray beam polarization along the surface plane (IP) and out-of-plane (OP). Inset: structural anisotropy seen in the EXAFS oscillations.

The significant difference in these amplitudes for in-plane and out-of-plane XANES (fig. 5.24) reveal the anisotropy in the local order. In addition the position of the first EXAFS oscillation (C), around 7145 eV, is slightly shifted toward higher energies for the IP spectra with respect to the OP one. This shift corresponds to a shortening of the distance to the first neighbors in the [001] direction. The analysis of the EXAFS signal (inset in fig. 5.24) gives access to local structural anisotropy. The distance to the first neighbors is 2.635 ± 0.005Å in the film plane and 2.745 ± 0.005Å along the [001] direction, giving a c/a ratio value of 0.915 ± 0.005, in full agreement with the *in situ* GIXRD results. Mn K-edge spectra measured at the same conditions showed no evidences of anisotropy.

5.2.4 Magnetic studies by MOKE

The magnetic measurements on the $Pt_6/(MnPt)_8/(FePt)_6/Pt(001)$ film (sample S3) were performed using the MOKE facilities installed in the multi-chamber system at the Max Plank Institut of Halle, Germany. The experimental conditions were similar to

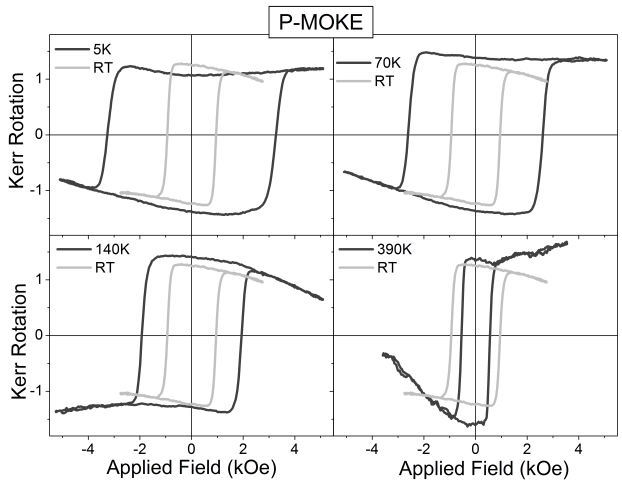

Figure 5.25: Hysteresis loops for $Pt_6/(MnPt)_8/(FePt)_6/Pt(001)$ at a few selected temperatures 5, 70, 140 and 390 K, compared to RT.

those reported for sample S4. For this sample coercivity was much stronger and the field was reversing from -5500 to 5500 Oe.

Data reported here comes also from two magnetic field cooling experiments. The first one at an applied field of$+3000\,Oe$ perpendicular to the surface from RT down to 5 K and the second one at $+5500\,Oe$ from 400 K down to 5 K. Both experiments gave the same features. The maximum Kerr rotation was typically 0.2 mrad to 0.4 mrad, however, the loop amplitudes presented here are given in arbitrary units: due to leaks in the magnetic field, the optics were affected, generating instabilities and deforming the loops, so that amplitude values were not reliable.

In figure 5.25 we present a few loops at different temperatures, compared to the one at RT. As for the sample S4, the increase in the coercive field at low temperatures, when compared to RT, is coming from the exchange coupling between FePt and MnPt. However, sample S3 displays a much larger coercive field, e.g. $H_C \approx 920\,Oe$ at RT, compared to the sample S4 (figure 5.17. At the lowest temperature, the coercive field increases to $H_C \approx 3300\,Oe$. We also observe a bias shift ($H_{EB} \approx 85\,Oe$) followed by a training effect. But, in this case, after the first loop the system seems to be already completely relaxed and there is no longer a bias shift (figure 5.26-a). A possible explanation for these peculiarities may come from the more disordered MnPt AFM layer and chemical roughness at the interface FM/AFM. Exchange coupling is known to be enhanced by interface roughness. The FePt layer is thicker in this case (6 BLs), compared to the previous one (4 BLs), but we do not think that this could be the source of such an increase in coercivity.

The coercive field as function of temperature is shown in figure 5.27. One can note that above $T_N \approx 195\,K$ data can be satisfactorily fitted to a straight line; below that temperature, the coercivity is increasing faster as temperature decreases. However, the ordering temperature is less clearly defined. The situation looks as a gradual increase of the coupling over a large range, which would be more compatible with a distribution of T_N. In this sense, this sample looks more like the sample S0, where the AFM layer

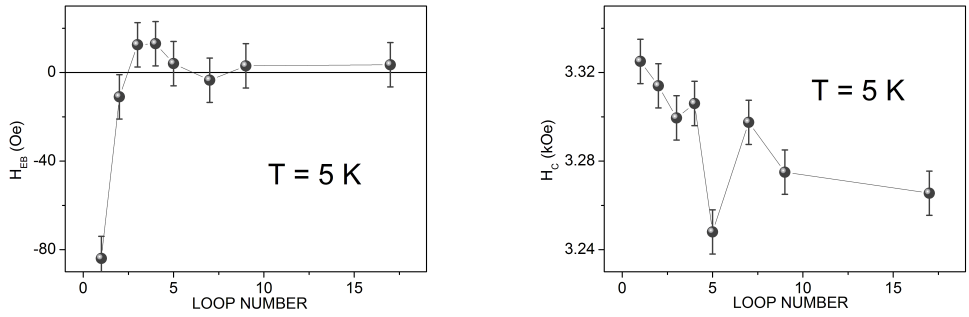

(a) (b)

Figure 5.26: Training effect after perpendicular magnetic field cooling for $Pt_6/(MnPt)_8/(FePt)_6/Pt(001)$: (a) exchange bias shift and (b) coercivity as function of the number of loops.

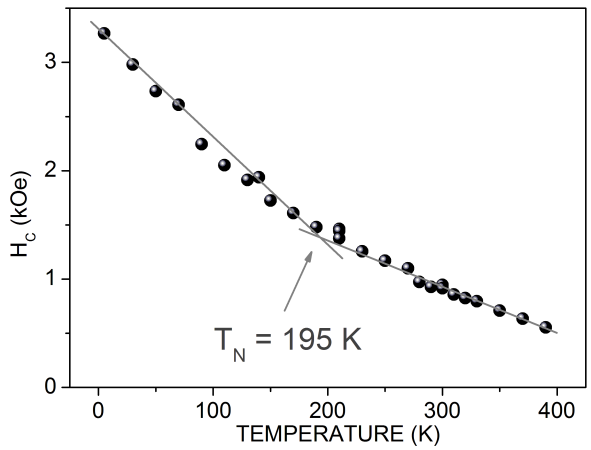

Figure 5.27: Coercivity as function of temperature for the $Pt_6/(MnPt)_8/(FePt)_6/Pt(001)$ sample.

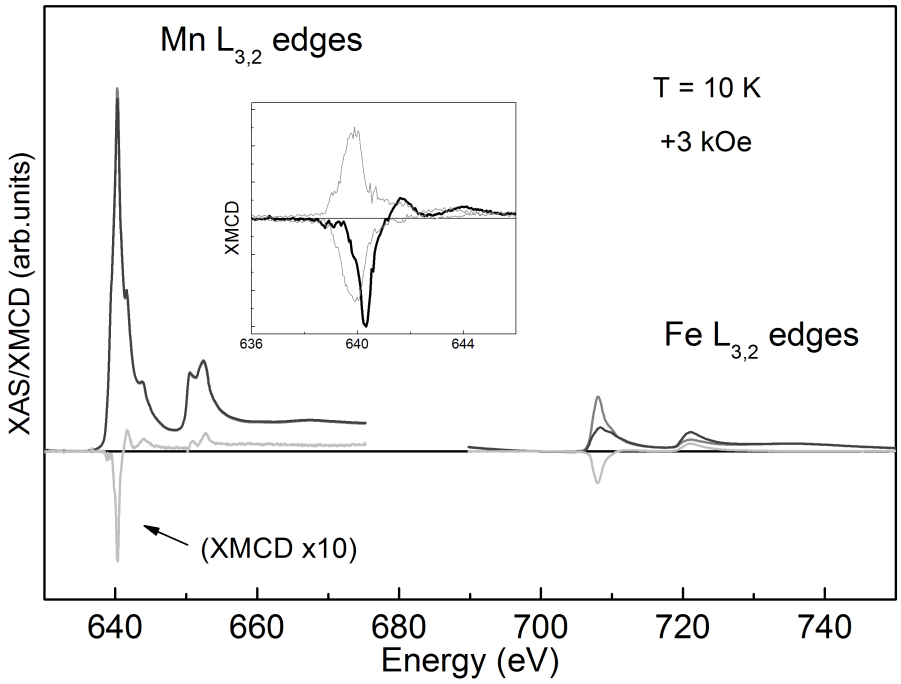

Figure 5.28: Mn and Fe $L_{3,2}$ XAS spectra (μ^+ and μ^-) of the $Pt_6/(MnPt)_8/(FePt)_6/Pt(001)$ sample by flipping the circularly polarized light at an applied magnetic field of 3 kOe and at 10 K.

was composed by a distribution of nanometric small domains with different ordering temperature.

5.2.5 Magnetic studies by XMCD

XAS and XMCD experiments were performed on the $Pt_6/(MnPt)_8/(FePt)_6/Pt(001)$ sample using the ID08 beamline at the ESRF, at the same experimental conditions as described for the previous sample.

Figure 5.28 shows the raw data XAS spectra (μ^+ and μ^-) collected in TEY mode by flipping the circularly polarized light in the photon energy region of the Mn and Fe $L_{3,2}$ absorption. The sample temperature was set to 10 K after field cooling under the applied field $+3000\,Oe$. The difference $\Delta\mu = (\mu^+ - \mu^-)$ associated to the XMCD is presented as well. At the Mn region, the XMCD is multiplied by 10, to be discernible.

In this sample, the Mn signal is stronger than for Fe, contrary to the sample S4, because Fe atoms are buried under the MnPt layer. The relative dichroic signal $\frac{\Delta\mu}{\mu} = \frac{(\mu^+ - \mu^-)}{(\mu^+ + \mu^-)}$ is still larger at the Fe edge. The XMCD signal amounts to 38.6% at the Fe L_3 edge, while it is only 2.3% at the Mn edge. On the Fe edge the signal is the same as for sample S4, while on the Mn edge it is a bit larger.

Nevertheless, the two most remarkable differences when comparing the two samples are the spectral shape and the signal. In the sample S3, the Mn XMCD has the same sign as that of Fe, which means that they are aligning parallel. Moreover, the spectral shape (inset figure 5.28) looks quite different from the previous situation. We also noted

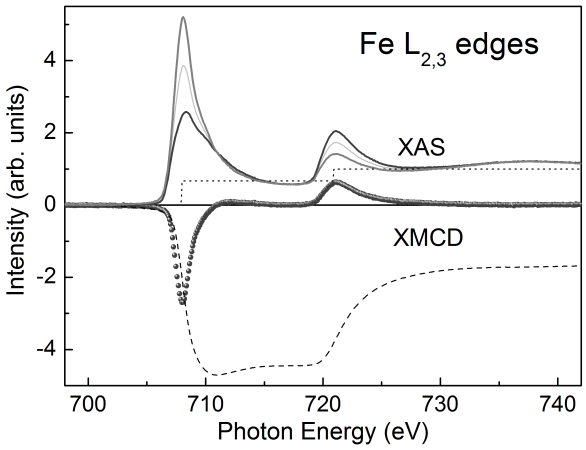

Figure 5.29: Normalized XAS (closed circles) and XMCD (open circles) spectra at the Fe $L_{2,3}$ edge of the sample. The integrated XMCD signal is shown by the dashed line.

that the signal at the Mn edge showed no remanence. Our interpretation for all these differences is that the Mn XMCD signal is not coming from the FePt/MnPt interface but, probably, from a ferromagnetic phase formed at the upper interface with Pt, e.g., Pt_3Mn that is ferromagnetic at low temperatures. By the way, the Mn XMCD signal vanishes at room temperature. We think that, if some uncompensated spins exist at the FePt/MnPt interface, they are hidden by that ferromagnetic contribution.

The spin and orbital contributions to the total moment of Fe in the FePt layer were investigated at RT, where the MnPt layer is above its Néel temperature. Figure 5.29 shows the normalized XAS and XMCD spectra at the $L_{2,3}$ edges. In this experiment, an applied magnetic field of 1 Tesla ensures nearly 100% saturation of Fe moments.

According to the sum rules, the effective spin (m_s^{eff}) and orbital (m_l) magnetic moments can be obtained by performing adequate integrals of the spectra [116]. The ratio m_l/m_s^{eff} is proportional to the deviation from zero of the integral of the XMCD signal (dashed line in fig. 5.29). To obtain absolute values for m_l and m_s^{eff} the excitations to $3d$ states must be separated from those to the continuum. A two-step function (dotted line in fig. 5.29) is usually subtracted from the XAS spectrum. The broad feature at 736 eV corresponds to a resonance of the $Pt\,4\,s$ electron excitation to the continuum of states ($Pt\,N_1$ edge). This excitation does not contribute to the XMCD signal, but affects the normalization and, consequently, the absolute values for m_l and m_s^{eff}.

We performed here a similar analysis as presented in the literature for FePt systems [160, 161]. We subtracted a two-step function, took the normalization energy around 730 eV and integrated the $3d$ states up to that energy. The additional contribution of the $Pt\,N_1$ edge has also been simulated. The experimental data reduction (background and normalization) yields an estimated error bar around 15% on m_l and m_s^{eff} and smaller than 10% for the ratio. Taking the theoretical number of d holes, $n_d = 3.705$ [162], we have found $m_l = 0.29(4)\,\mu_B$ and $m_s^{eff} = 2.6(4)\,\mu_B$. The values given by band structure calculations are $m_l = 0.072\,\mu_B$ and $m_s^{eff} = 2.87\,\mu_B$ [162]. Antoniak et al. [160] found an enhanced orbital magnetism in 6 nm FePt nano-particles when chemical order

is improved by annealing ($m_l/m_s^{eff} = 0.093$, $m_l = 0.24\,\mu_B$ and $m_s^{eff} = 2.59\,\mu_B$). In the case of thin films, the largest orbital contribution is reported for films grown on a MgO(001) substrate at 620 K ($m_l/m_s^{eff} = 0.099$, $m_l = 0.24\,\mu_B$ and $m_s^{eff} = 2.45\,\mu_B$) [161]. These films presented the $L1_0$ chemical order with lattice parameters of $a = 3.870\,\text{Å}$ and $c = 3.714\,\text{Å}$ ($c/a = 0.96$), very close to the bulk FePt values. Our pseudomorphic film, with a larger tetragonal distortion ($c/a = 0.91$), shows an even larger orbital contribution, $m_l/m_s^{eff} = 0.116 \pm 0.012$. This is the largest experimental orbital to spin moments ratio found in FePt ordered alloys. We interpret that as coming from the high degree of chemical order and from the enhanced tetragonal distortion.

5.3 Summary

We presented in this chapter the results on the synthesis of well-ordered MnPt/FePt heterostructures, with good quality in terms of chemical ordering and presenting interesting magnetic behavior. The synthesis was followed *in situ* by GIXRD throughout the different stages of growth and special care has be taken in a deep structural analysis.

We found that when the substrate is at 570 K, Pt grows layer-by-layer, while Mn has negligible diffusion into bulk. This particular temperature yields ultra-thin layers with $L1_0$ domains. These domains have the c-axis either out-of-plane (majority) and in-plane (minority and twinned). Subsequently, a tetragonally distorted PtFe layer with c-axis mostly perpendicular to the surface was grown on that PtMn layer. This bilayer system provided a well-suited system for perpendicular exchange coupling studies.

The magnetic properties of this sample were studied *ex situ* by polar MOKE. After field cooling, increased coercivity and exchange bias were observed. XMCD at the Mn and Fe $L_{2,3}$-edges show a coupling perpendicular to the surface between Fe and Mn magnetic moments and a large amount of uncompensated Mn spins at interface, the majority of them being rotatable.

We also demonstrated that a highly ordered $L1_0$ FePt may be obtained by co-deposition of Fe in excess over Pt, as far as the substrate is kept at 570 K. This highly ordered FePt was studied by XAS and XMCD. Sum rules were applied to these XMCD results and we interpret the enhanced orbital magnetism observed in our film as the result of the increased tetragonal distortion and the high degree of chemical order.

Chapter 6

CoO/Fe exchange bias system grown on Ag(001)

6.1 Introduction

The CoO/Fe bilayer is a widely studied exchange bias system. Many authors used this system to investigate the behavior of the antiferromagnetic CoO layer, in particular as function of the thickness. Among many other properties, the decreasing of the Néel temperature as thickness decreases, the robustness of the coupling, the amount of pinned and unpinned spins contributing to the bias shift, have been specially studied. However, in all studies of the CoO interface the Fe layer has the in-plane anisotropy, the Fe layer is always in the "thick" regime, larger than 6 MLs. Our aim here is to investigate the CoO/Fe exchange coupling in two different situations: in-plane and out-of-plane anisotropy of the Fe layer. The choice of the Ag(001) substrate relies on the fact that in the Fe/Ag(001) a spin reorientation transition occurs at about 6 MLs of Fe. In a wedge sample with Fe thickness varying from 1 ML to 10 MLs or more, one can obtain in-plane (thicker part) and out-of-plane (thinner part) anisotropy at the same sample.

The growth of CoO/Fe-wedge/Ag(001), called sample S6, and the MOKE experiments were performed using the facilities installed in the UHV multi-chamber system at the Max Plank Institut of Halle, Germany, in collaboration with the group of Dr. Marek Przybylski. The multi-chamber system is equipped with many instruments for surface physics experiments: ion gun sputtering, LEED, RHEED, AES, STM and synthesis by MBE and PLD (pulsed layer deposition). Two different chambers are equipped with effusion cells for metallic deposition; in one of them, Fe and Co targets are installed, with a precisely calibrated deposition rate, while in the other, it is possible to deposit the same metals under oxygen atmosphere. The MOKE apparatus is connected to these synthesis chambers through an UHV transfer line. Two different MOKE geometries are possible, with an incidence angle of 21° for longitudinal MOKE (L-MOKE) and with an incidence angle of 69° to the sample normal for polar MOKE (P-MOKE). *Ex situ* X-ray diffraction and absorption studies were conducted at the French CRG BM32 and FAME beamlines at the ESRF. X-ray reflectivity measurements were performed using the X-ray facilities at the Institut Néel, CNRS, Grenoble.

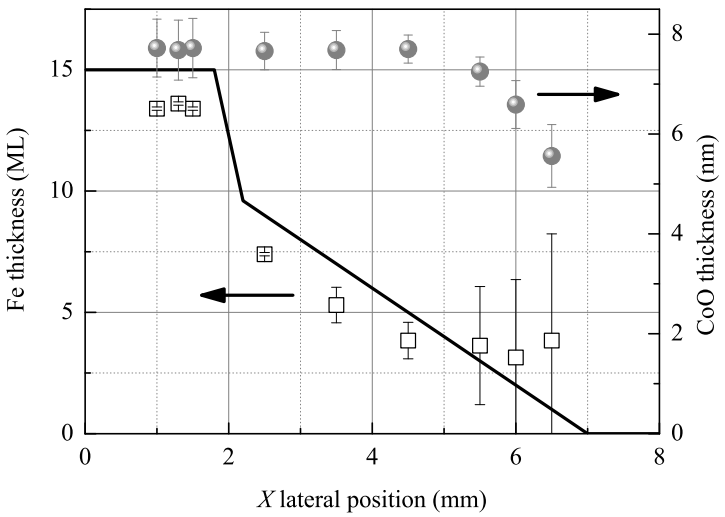

Figure 6.1: Nominal Fe thickness versus lateral X-position (mm) along the 8-mm diameter Ag(001) crystal (line); the total Fe deposition span over about 7 mm. Fe (squares) and CoO (circles) thickness for the CoO/Fe-wedge/Ag(001) sample obtained from X-ray reflectivity measurements.

6.2 Fe wedge on Ag(001) covered by a Co oxide

The nominal Fe-wedge thickness is shown schematically in figure 6.1 as function of the position along the [110] direction of the Ag(001) substrate of 8 mm in diameter, i.e. along the [100] direction of the Fe film. A plateau of a nominal thickness of 15 MLs was deposited in the first two millimeters. The wedge shape starts with a nominal thickness of 10 MLs and has a slope of 2 MLs/mm along the [110] direction of the Ag(001) substrate. The nominal Fe thickness in monolayers (MLs) and/or the lateral X-position (mm) will be used to label all measurements, even after Co deposition and oxidation. In MOKE measurements the edge is determined with the laser spot with an accuracy of ± 0.2 mm.

6.2.1 Growth

The Fe-wedge sample was deposited on a clean Ag(100) substrate and then covered by a cobalt oxide. The Ag(001) substrate was prepared using sputtering-annealing cycles. The bombarding energy was 800 eV, in a typical pressure of 5.10^{-6} mbar of Ar, generating a current of 10 μA for 30 min or more. The annealing temperature was set to 820 K for 30 min. The quality of the substrate was checked by AES and by LEED.

Both Fe and Co layers were deposited at RT by MBE using two effusion cells in the ultrahigh vacuum chamber with a base pressure better than 5.10^{-11} mbar and less than 2.10^{-10} mbar during deposition. The deposition rate for Fe was 1 ML in 2.4 minutes (0.41 MLs/min), so that the total deposition time for the plateau was 36 min.

The Fe wedge sample was measured at RT in the MOKE chamber, first in the longitudinal then in the polar geometry. After those MOKE measurements the sample was annealed in UHV for 5 minutes at 423 K, then checked again by LEED. After

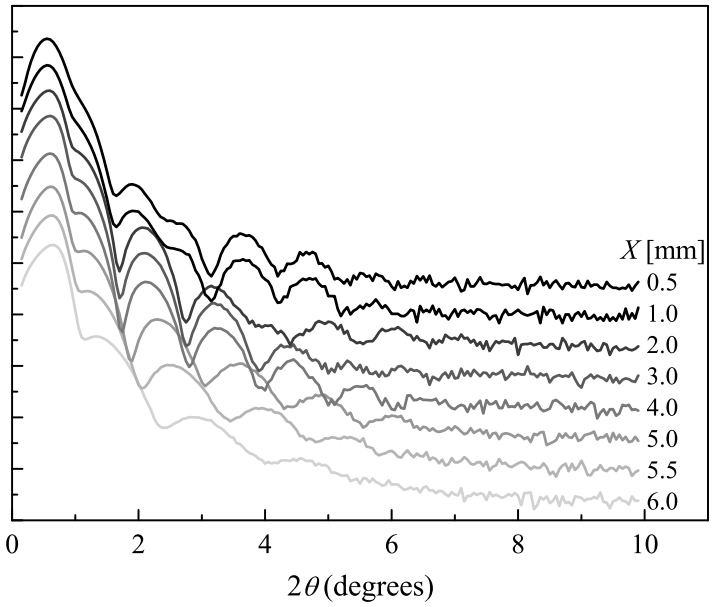

Figure 6.2: X-ray reflectivity at different positions along the sample wedge. From the top curve to the bottom one, we pass from the plateau of 15 MLs to the thinnest part.

this mild annealing the LEED spots and the polar MOKE measurements showed no changes.

After these measurements, one monolayer of Co was deposited at the same UHV conditions as for Fe. The Co deposition rate was 1 ML in 2.2 minutes (0.45 MLs/min). Then, in the chamber adapted for reactive deposition under oxygen atmosphere, the oxide was grown. During this growth, the substrate was kept at 340 K in an O_2 atmosphere of 5×10^{-7} mbar. RHEED spots were qualitatively observed: before oxidation the spots were sharp; after oxidation they became elongated and blurred. About 6 nm of Co oxide was deposited in a time interval of 25 minutes. Auger lines from Fe and Ag were no longer visible and LEED showed a square pattern with larger spots a the same position as before.

After deposition of the CoO layer, the sample was installed again in the MOKE chamber for detailed *in situ* magnetic characterization. These experiments are described in detail at section 6.4. The final CoO/Fe-wedge/Ag(001) sample was then removed from the multi-chamber in order to perform additional *ex situ* studies.

6.2.2 X-ray reflectivity and diffraction

X-ray reflectivity measurements were done on the CoO/Fe-wedge sample using Cu K_α radiation from a sealed X-ray tube. In figure 6.2 we display the reflectivity curves at different positions along the wedge (with a vertical shift for clarity). After the fitting procedure, the Fe and CoO thickness were obtained. The results are included in figure 6.1. The nominal Fe-wedge profile is represented by a continuous line. From the reflectivity analysis, one can see that the fitted Fe layer is reduced by about 2 MLs compared to the nominal film. Above the lateral position of 5 mm (below 4 MLs), it is difficult to define the metallic Fe layer and the results yield a large dispersion.

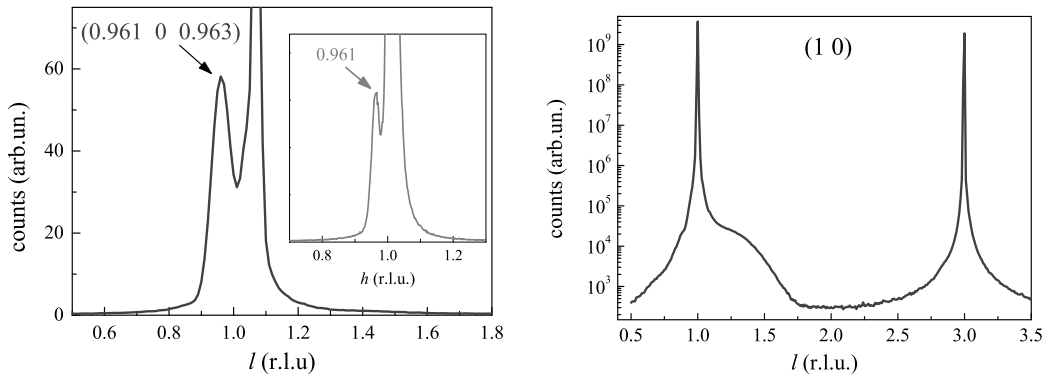

(a) (b)

Figure 6.3: (a) l-scan along (0.961 0 l) showing the relaxed CoO diffraction peak. The inset presents the radial scan along (h 0 0.96). (b) l-scan along the (1 0) CTR, sensible to the pseudomorphic Fe layer on Ag(001), buried under the CoO film.

These results can be explained with the oxidation of 2 to 3 MLs of Fe in contact with the CoO film. This Fe oxide contribution cannot be distinguished from the CoO due to their similar densities; its contribution to the reflectivity is included in what we call (CoO+FeO_x) layer. This (CoO+FeO_x) layer is about 7.7 nm-thick over almost all lateral positions, which is larger by about 1.2 nm compared to the nominal thickness of the deposited CoO. This could be explained by a deviation in calibration of the Co source but it may also come from the additional contribution of a few Fe oxide layers. For $X > 5$ mm, error bars became larger than the expected thickness for Fe, due to the rough oxide surface. One can also remark that the CoO thickness decreases from 7.7 nm down to about 5.5 nm at the border of the sample ($X = 6.5$ mm). This reduced deposited layer could be explained by a geometrical effect related to the sample mounting in the oxidation chamber. The range below 5 MLs ($X < 4.5$ mm) is better characterized by X-ray absorption spectroscopy in fluorescence mode, as shown in the next section.

To verify the epitaxy of the CoO on the Fe-wedge, GIXRD measurements were performed at the GMT instrument of the French CRG BM32 beamline at the ESRF. The energy of 25 keV ($\lambda = 0.4959$ Å) was used at a grazing incidence of 1°. hkl scans in the reciprocal space were done to investigate the lattice parameter within the plane (radial scans) and perpendicular (l-scans) to the sample surface. We observed that the symmetry and lattice parameters correspond to the growth of a Co oxide with NaCl structure and CoO stoichiometry. The CoO film grows epitaxially on Fe/Ag(001), but is not pseudomorphic, as seen by the relaxed peak of figure 6.3-a: its out-of-plane lattice parameter is $c = 4.242$ Å, while the in-plane one is $a = 4.251$ Å (or 3.006 Å in the surface lattice), i.e., larger than the Ag lattice parameter by $\approx 4\%$. This unambiguously shows that the CoO oxide layer is largely relaxed - but not completely ($a_{\mathrm{CoO}}^{bulk} = 4.260$ Å) - to the bulk structure and slightly distorted ($c/a \approx 0.998$). Such an anisotropy also manifests itself in the X-ray absorption spectra and will be discussed further in the next section. We also observed the peak corresponding to the epitaxial Fe layer buried under

the CoO. The position of the peak in the reciprocal space (fig. 6.3-b) is compatible with a pseudomorphic Fe layer.

6.3 X-ray absorption spectroscopy studies

Grazing incidence X-ray absorption spectroscopy (XAS) was performed at the Co and Fe K edges (Fe 7112 eV and Co 7709 eV) for the in-plane and out-of-plane geometries, at the French CRG FAME beamline at ESRF. The angle of incidence was set to about 5° for both geometries. The fluorescence photons were collected using a 30-element Ge-detector aligned perpendicular to the photon beam direction.

Above the Fe K edge the intensity of Fe K_α fluorescence line is proportional to the total Fe content in the sample. The Fe profile is obtained directly from fluorescence counts - selecting the Fe K_α fluorescence with the Ge solid state detector - as a function of the X lateral position for a given energy above the absorption threshold (black dots in fig. 6.4). To avoid possible effects of the local environment on fluorescence counts, the profile is checked from the amplitude of the edge jump in background subtracted XAS spectra collected for different X (open squares in fig. 6.4). The Fe profile is in good agreement with the nominal one. This experimental profile was used to set up the origin of the X scale in the XAS experiments. Contrary to XRR measurements, that are sensitive to contrasts in the total electronic density, XAS is element selective (only Fe atoms contribute to the selected energy) but probes all Fe atoms, independent on the oxidation state and on the local density. This explains the differences between figure 6.1 and figure 6.4.

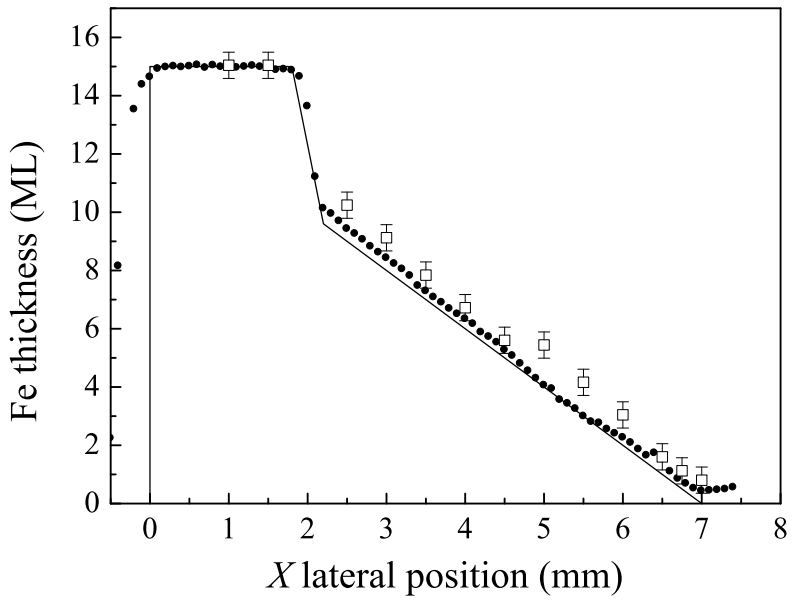

Figure 6.4: Iron profile in the sample obtained from the fluorescence count at 7500 eV (dots). The big open square correspond to the values obtained from the edge jump for the collected XANES spectra, in the IP geometry. Both measurements have been normalized to 15 on the plateau, in order to be comparable with the nominal profile (line).

6.3.1 Fe K-edge

Figure 6.5 displays the normalized Fe XAS spectra, in the XANES range, collected at different lateral positions. The XANES for the two positions on the 15 MLs plateau ($X = 1$ and $X = 1.5$) are identical and show the main features of a metallic Fe spectrum: marked shoulder just above the threshold, reduced main line at the edge, and smooth features up to 7200 eV. For $2 < X < 5$ the XANES features are progressively modified. The shoulder at the threshold vanishes, giving way to a small well structured pre-edge. At the same time the main line shifts towards higher energies and increases strongly, and sharper structures rise above edge. These features characterize an oxidized Fe state. For $X > 5.5$ mm (thickness smaller than 4 MLs), the XANES features keep almost unchanged.

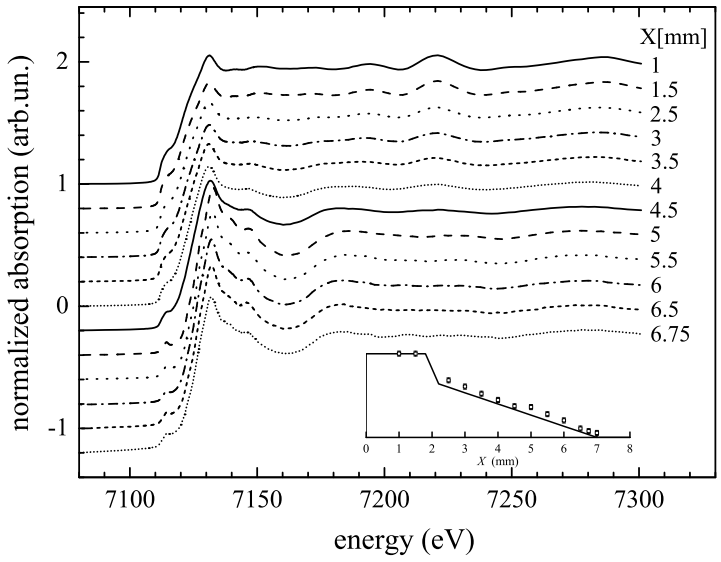

Figure 6.5: Normalized Fe K edge XANES spectra along the iron wedge (in-plane geometry). Spectra of different X are vertically shifted and the correspondence is indicated.

As the total iron thickness still progressively decreases with X, we can assume that above $X = 5$ (< 4 MLs), all iron atoms present in the sample are under an oxidized form. To confirm this point and identify the oxidation form, we compare the XANES at $X = 5.5$ ($\approx$3 MLs) to the XANES of reference spectra, for the three main bulk iron oxides FeO, αFe_2O_3 and Fe_3O_4 (fig. 6.6). FeO crystallize in the rock-salt structure ($Fm\overline{3}m$), the same as CoO. The ions Fe^{2+} have a symmetric octahedral environment of 6 oxygen at a distance of 2.155 Å. αFe_2O_3 crystallize in the rhombohedral $R\overline{3}c$ structure. The coordination shell of the Fe^{3+} ions is split into 3 oxygen at 1.944 Å and 3 at 2.115 Å. Fe_3O_4 crystallize in the spinel structure ($Fd\overline{3}m$), one third of the iron atoms are on the form Fe^{3+} in tetragonal sites with 4 oxygen neighbors at 1.876 Å, the two other thirds are split on the forms Fe^{3+} and Fe^{2+} in regular octahedral sites with 6 oxygen neighbors at 2.066 Å. Once the XANES of the reference spectra were not collected in the same experiments as the XANES of our sample, we do not discard the possibility of a shift in the energy calibration among them. We adopt then a relative energy scale

(fig. 6.6) where, for each spectrum, the origin is set at the maximum of the main line at the threshold (zero of the derivative).

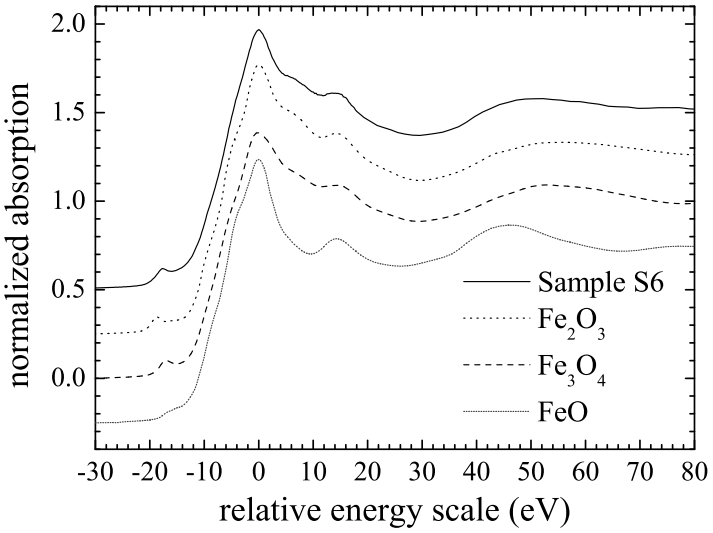

Figure 6.6: Comparison of the XANES at $X = 5.5$ (≈3 MLs) to the reference spectra for the three main bulk iron oxides FeO, αFe_2O_3 and Fe_3O_4.

The features of the XANES in the film clearly differ form those of FeO. It does not show the large dump around 9 eV and it has a higher and more structured pre-edge than the FeO one (fig. 6.6). The maximum of the first EXAFS oscillation is found at around 50 eV in the sample and around 45 eV in FeO, what suggests that the average distance is larger in FeO than in S6. The XANES features can be seen as intermediate between those of αFe_2O_3 (similar shoulder around 7 eV) and Fe_3O_4 (similar pre-edge). Actually, the best fit of the XANES as linear combination of the two references gives about $\frac{2}{3}\alpha Fe_2O_3 + \frac{1}{3}Fe_3O_4$. This result cannot be taken straightforwardly: the local environment of iron in an ultra-thin film (for less than 4 MLs) is not supposed to be identical to that in bulk iron oxide. The comparative study only deals with a qualitative description. This analysis of the XANES features indicate that the iron in the oxide is not in a FeO-like symmetric environment, and has smaller Fe-O distances. This is confirmed by the EXAFS range.

Figure 6.7 shows the EXAFS signal (a) and the moduli of the Fourier Transform (FT) of the k^2-weighted experimental spectra (b) for the sample and the three references. The EXAFS analysis is restricted to $k_{max} = 11\,\text{Å}^{-1}$ due to the low signal/noise ratio for the sample at higher k. The Fourier transform of the EXAFS signal gives a pseudo-radial partial distribution function around the absorbing atom. The height of peaks depends on the amplitude parameters of the EXAFS equation, while their position depends on phase parameters. The position of a peak is related to the distance between absorber and scatterer. Due to the phase function that depends on k always with a negative slope, the peaks are shifted to lower R values. On the FT we easily identify in the reference oxides the peak of the coordination shell (Fe-O) and the peak corresponding to the second neighboring shell of iron atoms (Fe-Fe), as indicated in figure 6.7-b. The relative amplitude of these two peaks are opposite in Fe_2O_3 and

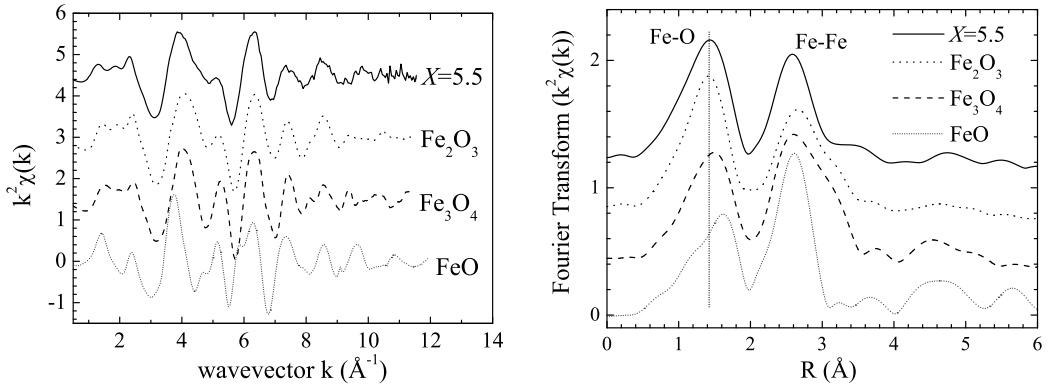

(a) (b)

Figure 6.7: Comparison of the (a) EXAFS and (b) FT data at $X = 5.5$ (≈3 MLs) to the reference for the three main bulk iron oxides FeO, αFe_2O_3 and Fe_3O_4 (in-plane geometry).

Fe_3O_4. In both cases, the local environment is distorted and the distribution of the iron neighbor distances is large. In FeO, where the second shell (Fe-Fe) is very symmetric, the corresponding amplitude is much higher. We can confirm in the sample a distorted local environment of iron oxide.

The evolution of the EXAFS spectra and their associated FT with increasing X are similar in the in-plane (fig. 6.8) and the out-of-plane (fig. 6.9) geometries and confirm the progressive oxidation of the iron layer.

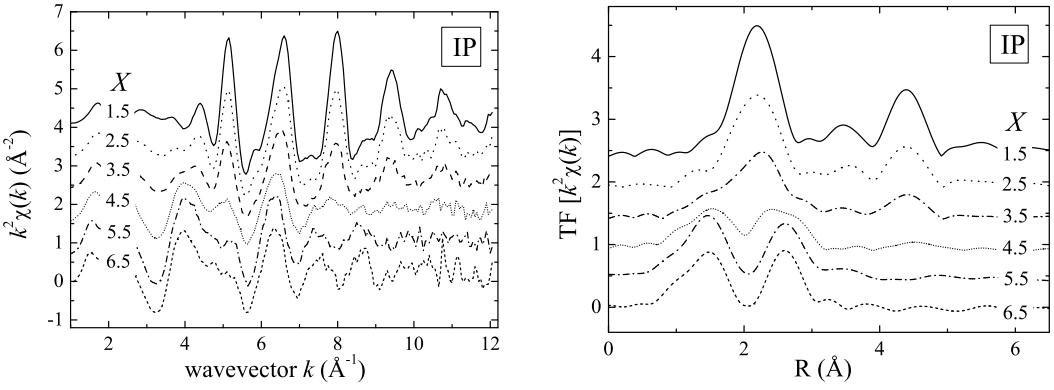

(a) (b)

Figure 6.8: Evolution of the EXAFS spectra (a) and their associated Fourier Transform (b) with increasing X for in-plane geometry.

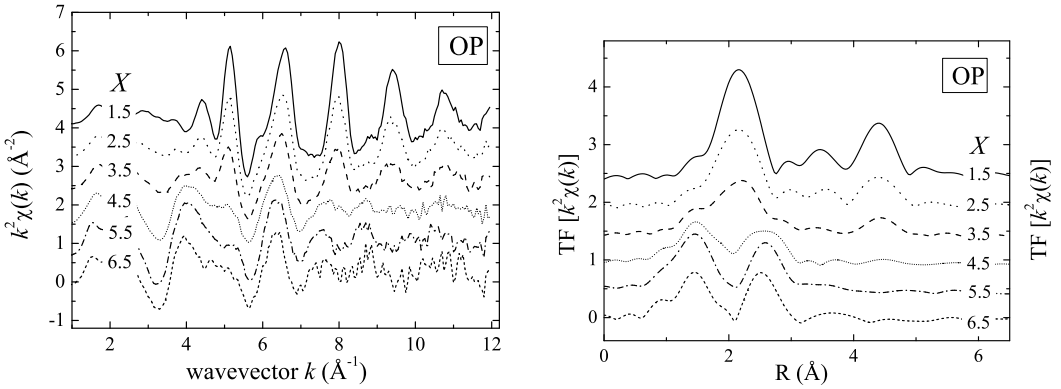

(a) (b)

Figure 6.9: Evolution of the EXAFS spectra (a) and their associated Fourier Transform (b) with increasing X for out-of-plane geometry.

We should specially highlight the case of OP measurements with $X > 5\,\text{mm}$, corresponding to nominal thicknesses lower than 4 MLs. As guessed from the XANES spectra, the FT peaks corresponding to the oxygen and iron nearest neighbors keep almost unchanged for $X > 5\,\text{mm}$ (fig. 6.10). From $X = 5.5$ ($\approx$3 MLs nominal) to $X = 6.5$ ($\approx$1 ML nominal) the decrease of about 15% in the amplitude of the oxygen peak can be associated to an increase in the disorder, as confirmed by the progressive splitting of this peak. However at the same time the iron peak keeps almost constant amplitude. These features are not compatible with a growth layer by layer, where the number of iron neighbors should progressively increase with the iron coverage. On the contrary, these results suggest the presence of isolated islands of iron oxide. In addition the progressive distortion of the coordination shell may be associated to a progressive increase of iron atoms at the surface of these islands, and then that their size decrease as X decreases.

On the plateau (15 ML of Fe), the XANES spectra have the main features of the *bcc* iron (fig. 6.11). However, we observe a reduction in the shoulder before the edge, the distortion of the structures close to the edge and important flattening around 7160 eV. This indicates the presence of oxidized iron also for this position. The oxide content is evaluated by a simple linear combination between the XANES spectra of bulk *bcc* iron and iron oxide film ($X \geqq 5.5$), that gives around 15% of iron under an oxidized form on the plateau. This corresponds to 2 ML of iron oxide covering 13 ML of metal iron.

Similar linear combinations of the XANES spectra are used to describe the iron oxide profile on the sample. This profile is given in figure 6.12. It shows that the oxide layer is not constant with X: it increases as the coverage decreases. For a nominal iron thickness of 4 ML, the iron is completely oxidized.

Aiming to quantify the short-range order and its eventual anisotropy in the metal iron layer, we made a quantitative analysis of the EXAFS measurements with in-plane and out-of-plane polarizations. We restrict this quantitative EXAFS analysis to the spectra collected on the 15 ML plateau. For these spectra, the oxide content is about 15%. The amplitude of the back-scattering function has a larger extension in wavevector for iron neighbors than for oxygen neighbors (fig. 6.13). In an analysis with a

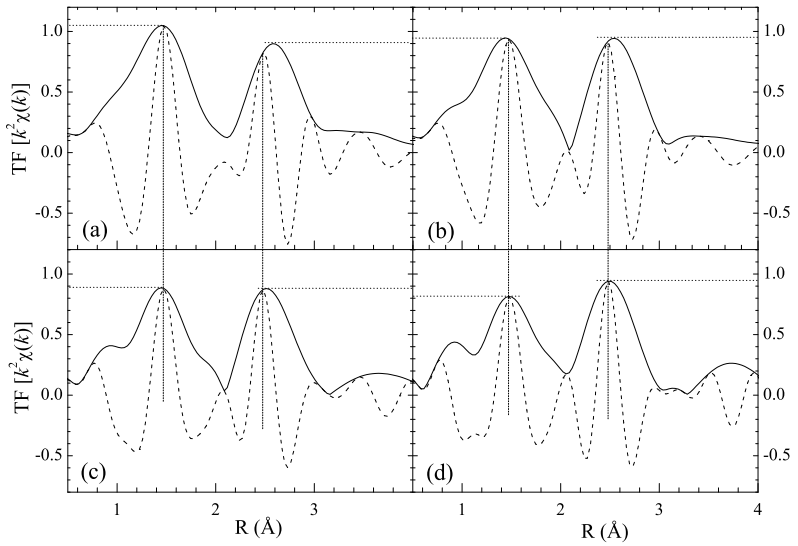

Figure 6.10: FT peaks corresponding to the oxygen and iron nearest neighbors for: (a) X=5.0 mm (≈4 ML), (b) X=5.5 mm (≈3 ML), (c) X=6.0 mm(≈2 ML) and (d) X=6.5 mm (≈1 ML). Solid lines give the moduli, while dashed lines give the real part of the FT.

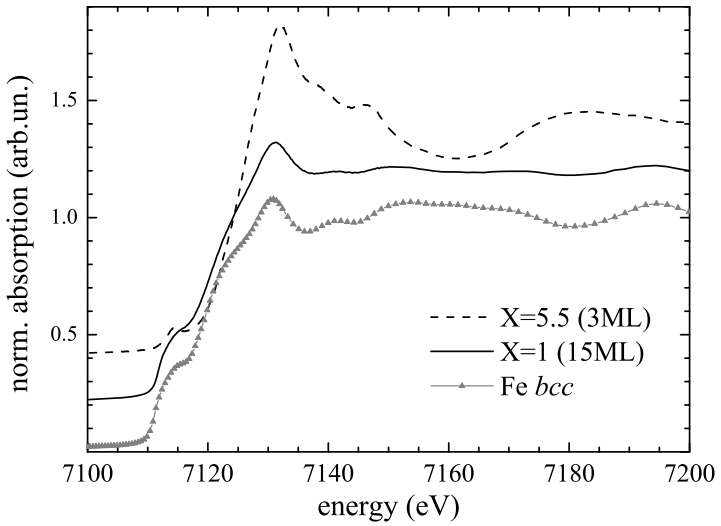

Figure 6.11: Fe K edge XANES on the plateau - 15 ML Fe nominal - (solid line) compared to a reference spectrum of bulk Fe *bcc* (gray triangles). Even if the main features are close, there are some differences, specially a flattening in the zone around 7160 eV, that indicates a contribution of iron oxide, where a large droop is observed in this zone (dashed line).

k^0 or k^1 weighing, in the k range $3-12\,\text{Å}^{-1}$, the signal due to the oxygen neighbors is expected to contribute by less than 5% to the total EXAFS signal. We can reasonably analyze the EXAFS signal assuming only metallic iron.

In metallic *bcc* iron ($a=b=c$) the coordination shell is made of two sub-shells : 8 Fe at $R_1 = a\frac{\sqrt{3}}{2}$ and 6 Fe at $R_1' = a$. In an expected body-centered tetragonal (*bct*) structure this coordination shell will be further split ($c<a$) and three sub-shells should be considered : 8 Fe at $R_1 = \frac{\sqrt{2a^2+c^2}}{2}$, 2 Fe at $R_1' = c$, and 4 Fe at $R_1'' = a$ (tab. 6.14).

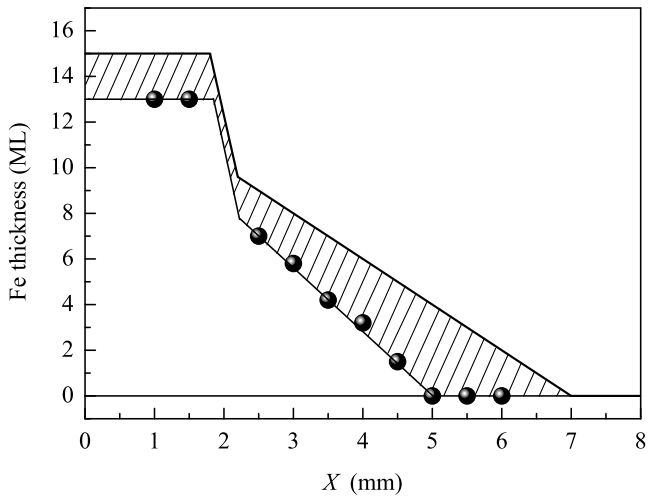

Figure 6.12: The spheres give the amount of *bcc* iron found after the linear combination, while the hatched area corresponds to iron oxide layer. This oxide layer is about 2 ML up to $X = 3$ (nominal iron coverage 7 ML) and increases up to 4 ML for $X = 5$ (nominal iron coverage 4 ML). Above this X value the whole iron layer is found to be oxidized.

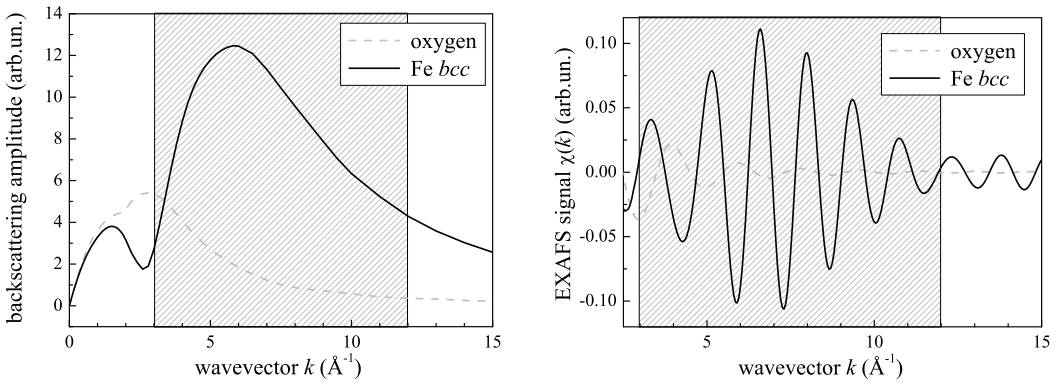

(a) (b)

Figure 6.13: (a) Calculated backscattering amplitudes for an oxide-like coordination shell formed by 6 oxygen atoms (dashed gray line) and by a *bcc* like coordination shell formed by 14 iron atoms (solid line). The hatched area corresponds to the EXAFS analysis domain (b) Calculated EXAFS signal for the contributions of these shells weighted by 0.15 for the oxide (dashed gray line) and 0.85 for the metal (solid line).

Assuming perfectly in-plane or out-of-plane polarization of the incident beam and grazing incidence ($\alpha_i = 0$), the apparent number of neighbors N_i for the ith shell is given by the expression $N_i = 3\sum_j cos^2\theta_{ij}$, where θ_{ij} is the angle between the absorber-scatterer axis and the polarization direction. For a *bct* iron structure, the expected values of N_1, at the first neighboring shells, are given in table 6.1. If $c = a$ one should find $R_1^{'} = R_1^{"}$. If $c < a$ the anisotropy ratio c/a will be given by the ratio $R_1^{'}/R_1^{"}$. Note that the anisotropic signal (Fe neighbors at distances $R_1^{'}$ and $R_1^{"}$) is superimposed with the contribution of the 8 Fe neighbors at $R_1 = \frac{\sqrt{2a^2+c^2}}{2}$.

The EXAFS signal on the plateau (15 ML nominal), are given in figure 6.15-a for the in-plane and out-of-plane geometries, together with the corresponding k^1-weighted FT

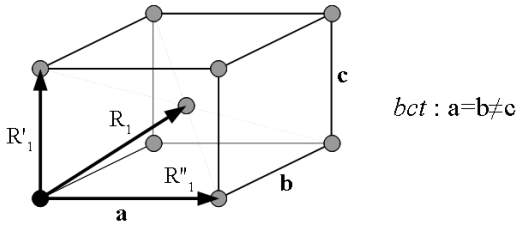

Figure 6.14: Schema showing the three different distances in the coordination shell of the *bct* structure.

Subshell	In-plane ($\varepsilon \parallel c$)	Out-of-plane ($\varepsilon \perp c$)
1: ($R_1 = \frac{\sqrt{2a^2+c^2}}{2}$)	8	8
1': ($R_1^{'} = c$)	0	6
1": ($R_1^{"} = a$)	6	0

Table 6.1: Apparent number of neighbors, for in-plane and out-of-plane measurements in each sub-shell of the first coordination shell.

(fig. 6.15-b). The three peaks observed show nonnegligible anisotropy. This anisotropy is clearly observed from the moduli of the FT, but the real part of the FT cross the zero at the same position in R. This indicates that the corresponding EXAFS contributions should be well matched in phase. The anisotropy observed in the modulus of the FT is then guessed as essentially due to amplitude terms: lower average number of neighbors and/or higher disorder in the out of plane measurements. This is not surprising due to the lower size of the sample in the direction perpendicular to the films.

The quantitative analysis of the coordination shell confirm this outcome (table 6.2). Within the error bars the cell appears to be cubic, with $c = a = 2.87 \pm 0.02$ Å. A decrease by about 20% of the number of neighbors strictly out-of-plane (along c) with respect to those in the (a,b) plane accounts for the reduced thickness of the film.

6.3.2 Co K edge

At the Co K edge, we observe that XAS spectra show a decrease in the amplitude of the edge jump for the $X > 5$ mm values (fig. 6.16). This indicates that the CoO layer

subshell	R (Å)	N	σ^2(Å^2)
1	2.46 ± 0.02	7.6 ± 0.5 (expected 8)	0.005 ± 0.002
1' (OP)	2.87 ± 0.02	5.7 ± 0.5 (expected 6)	
1" (IP)	2.86 ± 0.02	4.5 ± 0.5 (expected 6)	

Table 6.2: Fitting results for the 15 MLs Fe layer. The analysis of the in-plane (out-of-plane) spectrum gives the structural parameters for 1 and 1" (1 and 1'). The spectra of both geometries have been fitted together to straighten the robustness of the results. k range: [4.1-12.1]. R range for first peak selection: [1.85-3.0]. In order to limit the number of free parameters the disorder factor σ have been imposed identical for the 3 subshells. The amplitude factor, S_0^2, has been taken as 0.75, value found from the analysis of the Fe *bcc* reference.

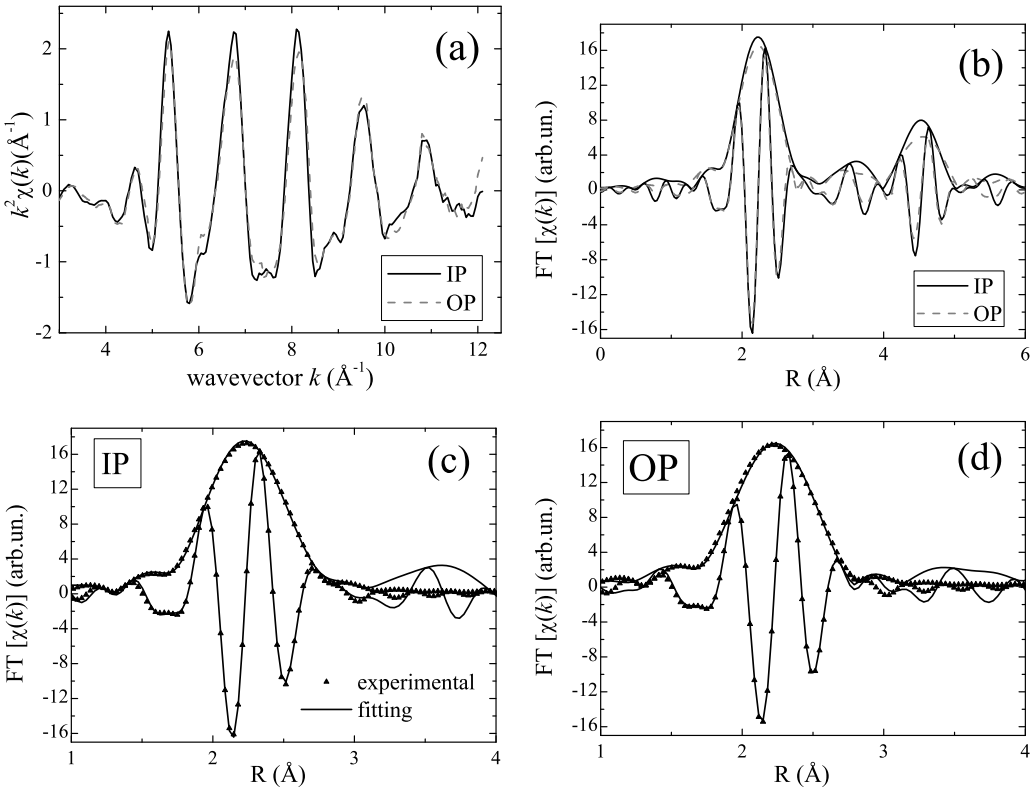

Figure 6.15: IP-OP anisotropy for 15 MLs nominal Fe: (a) EXAFS signal IP and OP; (b) FT (amplitude and real part) of IP and OP; experimental and fitting FT for IP (c), and for OP (d).

is reduced at the thin end of the wedge, as suggested by the XRR measurements. It confirms a shielding effect during the growth of the CoO layer.

The XAS spectra collected at the Co edge show the typical feature of CoO bulk oxide. The XANES spectra does not show significant evolution with X. We observe a damping of the EXAFS signal with increasing X, well evidenced by an overall damping of the moduli of the FT, both for IP and OP geometries (fig. 6.17). This damping reveals an increase of the average disorder with increasing X and may be correlated to a growth by islands in the earliest steps of the CoO layer.

For a given X, the XAS spectra shows small but significant anisotropy. The first EXAFS oscillation is shifted towards lower energies for the OP geometry, indicating a shorter distance in IP measurements. The quantitative EXAFS analysis confirms this shortening but the results have a limited precision. The difference found for the IP and OP cell parameters is about 0.02 Å, just about the error bars. The most striking difference between IP and OP XANES spectra lies in the pre-edge range (fig. 6.18). This anisotropy exist for all lateral positions, with an excellent reproducibility.

CoO the pre-edge is assigned to the dipolar transition from Co $1s$ levels to $4p$ empty levels. $4p - 3d$ hybridization for orbitals of the same Co atom is forbidden due to the centro-symmetry of the Co sites. However the $4p$ orbitals, having a large extension, hybridize with $3d$ orbitals of the Co neighboring atoms. The structures at the pre-edge reflect then the $3d$ partial density of states. To investigate the origin of the anisotropy in these electronic states, we performed *ab initio* simulations, using the FDMNES code.

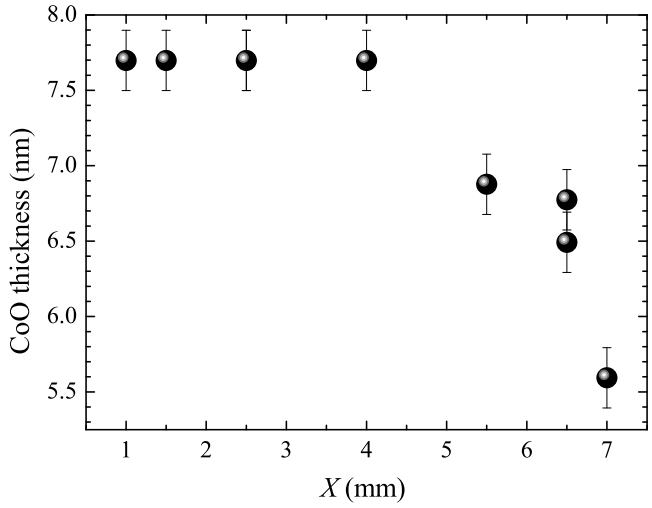

Figure 6.16: Co profile obtained from the amplitude of the edge jump in background subtracted XAS spectra collected for different X positions.

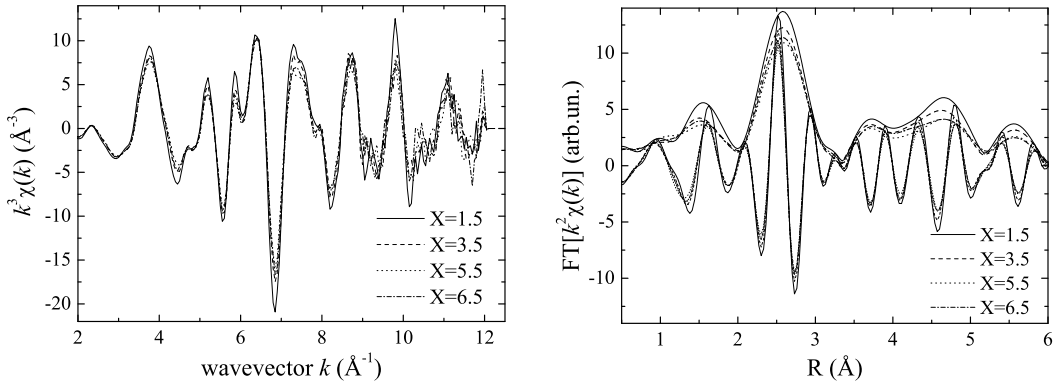

(a) (b)

Figure 6.17: (a) Co K-edge EXAFS and (b) FT (moduli and real part) for different X positions.

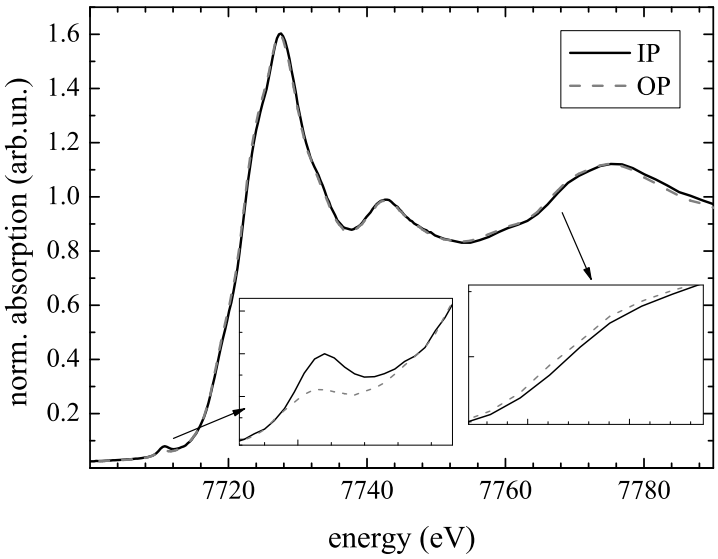

Figure 6.18: Co K-edge XANES for IP (solid line) and OP (dashed line) geometry ($X = 3.5$). The insets highlight the main differences between the geometries.

This code uses a mono-electronic approach, perfectly justified for delocalized probed states with minor interaction between the core-hole. This is the case for the metal K-edge. Calculations are performed inside a cluster centered around the absorbing atom. From these atomic positions the code calculates the electronic structure around the absorbing atoms using the Local Spin Density Approximation. The electronic structure is solved using the multiple scattering theory within the muffin-tin approximation for the potential shape. The absorption cross section is then calculated using the polarization conditions: $\epsilon \| [001]$ and $\epsilon \| [100]$ to simulate respectively OP and IP experiments. This absorption is then convoluted to a Lorentzian with an energy-dependent width, to take into account the core and final state lifetimes.

A cluster with CoO structure is build from crystallographic data in the cubic rock-salt structure (space group $Fm\overline{3}m$): $a = 4.2667\,\text{Å}$. Once the structure is cubic, there is no anisotropy in the calculated spectra. The calculated XANES spectrum reproduces well the experimental features (fig. 6.19-a). The position of the pre-edge peak is slightly shifted, but its shape and amplitude are very close to that of the IP XANES.

Calculations are then performed with a tetragonal model for CoO, with $a = b = 4.2667\,\text{Å}$ and $c = 4.1867\,\text{Å}$ ($c/a = 0.98$). The calculations with $\epsilon \| [100]$ (IP) and $\epsilon \| [001]$ (OP) present an anisotropy due to the tetragonal distortion (fig. 6.19-b). However, this anisotropy, even if larger than the actual one (GIXRD gives $c/a = 0.998$) has only a very small effect on the pre-edge structure. The origin of the anisotropy in the electronic states is not linked to the tetragonal distortion.

We then performed preliminary simulations taking magnetism into account (including spin states). We use a very simplified spin distribution: the spin direction is taken along [100] and the spin orientations alternate antiferromagnetically between planes $z = 0$ and $z = 1/2$. The spin distribution breaks the symmetry of the structure. The calculated pre-edge show notable anisotropy for $\epsilon \| [001]$ and $\epsilon \| [100]$ (figure 6.20) However the proposed simplified spin distribution gives an anisotropy contrary to the

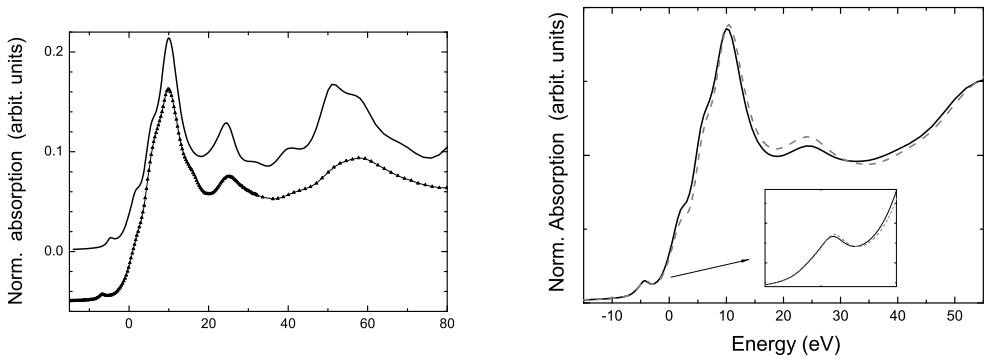

(a) (b)

Figure 6.19: (a) Calculated (solid line) and experimental XANES (line+symbols) for CoO in the rock-salt structure. (b) Calculated spectra for CoO with tetragonal distortion, IP (solid line) and OP (dashed line) cases.

experiments. These preliminary calculations suggest that the anisotropy experimentally observed in the pre-edge is connected with the magnetic properties of the film, but the real spin direction and orientations should be taken into account to properly simulate this effect.

6.4 Magnetic studies by MOKE

The magnetic measurements on the CoO/Fe-wedge/Ag(001) sample were performed using the MOKE facilities installed in the ultra-high vacuum (UHV) multi-chamber system at the Max Plank Institut of Halle, Germany. We recall that the wedge shape has a slope of 2 ML/mm along the [110] direction of the Ag(001) substrate, i.e. along the [100] direction of the Fe film (fig. 6.1). Longitudinal (with an incidence angle of 21°) and polar (with an incidence angle of 69° to the sample normal) MOKE geometries were applied to probe the anisotropy and exchange bias characteristics of the sample. A laser diode of wavelength 670 nm with a beam diameter of about 200 μm was used as probe.

6.4.1 *In situ* MOKE

The magnetic properties were measured *in situ* after each step of the sample preparation. The *in situ* MOKE measurement involves just a transfer of the sample under UHV from the preparation chamber to the MOKE chamber. As discussed previously, Fe films deposited on Ag(001) displays perpendicular magnetic anisotropy and a spin reorientation transition at RT at a critical film thickness of about 5 to 6 MLs [70]. Above that critical thickness, Fe films show an in-plane fourfold anisotropy, with easy axis along the [100] or [010] crystallographic directions related to the Fe (or [110] and [1$\bar{1}$0] along Ag substrate). The Ag substrate used in this experiment is perfectly flat.

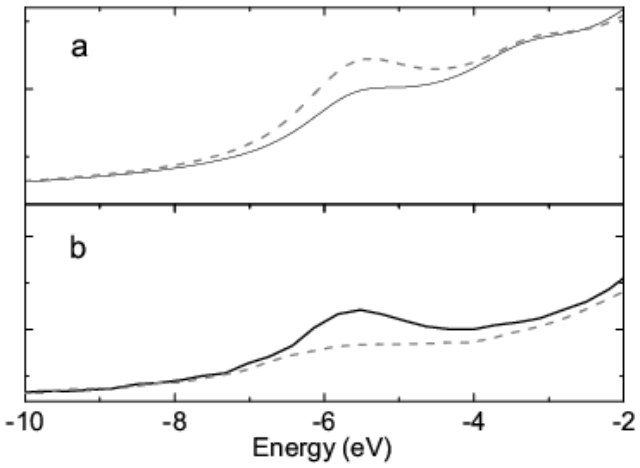

Figure 6.20: (a) Calculated anisotropy pre-edge including magnetism - simplified model. (b) Experimental pre-edge. The energy scale has been shifted to align the edge structures. Plain lines: IP, dashed lines: OP.

room temperature measurements on Fe-wedge/Ag(001)

We present here the sequence of longitudinal, along the easy axis of Fe, and polar MOKE measurements at RT as function of the Fe thickness for the uncovered sample.

The *in situ* longitudinal MOKE (L-MOKE) data (fig. 6.21-a) yields the expected linear decrease in the saturation (M_S) magnetization as function of Fe thickness. Moreover, the ratio of remanence (M_R) over the saturation magnetization (M_S), M_R/M_S, which gives the squareness of the hysteresis loop, is about one, down to 6 MLs. The coercive field (H_C) in the plateau of 15 MLs is 17 Oe and within the 6 to 9 MLs range is 9 Oe. At 5 MLs and below, one can observe that there is no longer an open loop, the coercivity goes to zero. A few selected *in situ* polar MOKE (P-MOKE) loops is shown in figure 6.21-b. One can remark that from 3 to 6 MLs the saturation M_S is almost reached at relatively low applied magnetic fields. In addition, a linear behavior of the M_S as function of the Fe thickness is observed, while coercivity is zero. This behavior looks like that of an ensemble of uncoupled superparamagnetic particles being aligned under an applied field. At 6 MLs and above, a small projection of the applied field in the plane of the sample gives rise to an open loop. This is coming from the in-plane magnetization that can be easily rotated at relatively very small fields. From these outcomes, it seems clear that the SRT at RT is taking place within 5 to 6 MLs in our sample.

The remanence M_R and saturation M_S magnetization from L-MOKE measurements as function of thickness are presented in figure 6.22. M_S is fitted to a straight line in the range 6 to 9 MLs and extrapolated for the whole range: M_S crosses the zero at about 1 ML meaning that there is one magnetically dead layer of Fe on Ag(001). M_R gives the same figure. The existence and the origin of that dead layer has never been reported in literature. MOKE measurements alone cannot tell if this dead layer is coming from the interface with Ag or from the free surface.

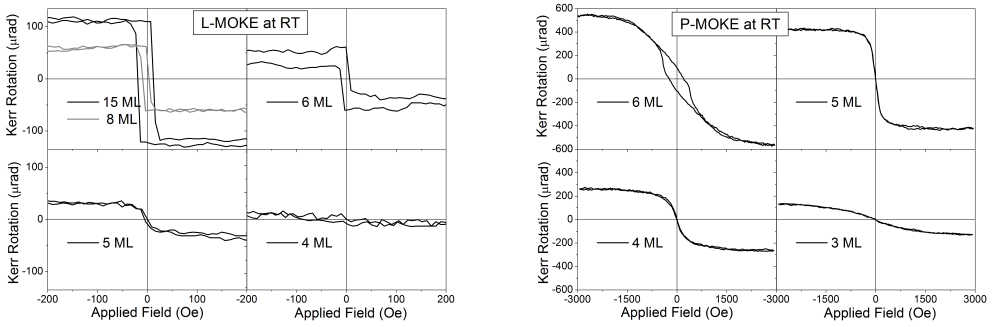

(a) (b)

Figure 6.21: (a) Representative L-MOKE hysteresis loops for the uncovered Fe-wedge at RT. (b) idem for P-MOKE hysteresis loops: from 3 to 6 MLs, one observe a linear behavior of the saturation magnetization as function of the thickness; at 6 MLs, one can still observe the projection of the open loop coming from the in plane magnetization.

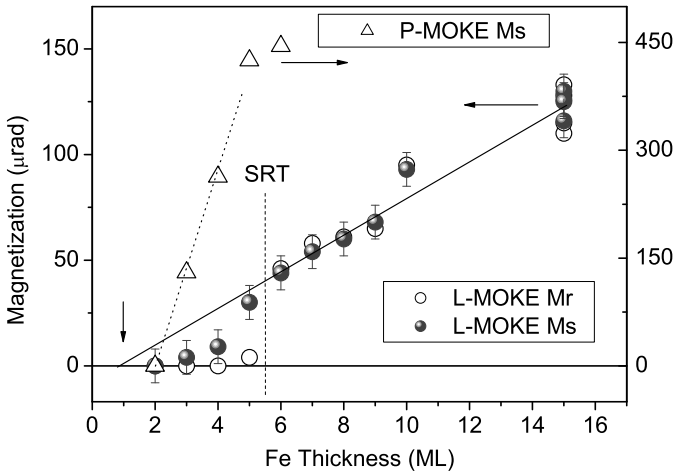

Figure 6.22: Remanence (open circles) and saturation (closed circles) magnetization from L-MOKE measurements at RT as function of the Fe thickness. A straight line is fitted from 6 to 9 MLs and extrapolated to zero yields one dead layer. Magnetization at maximum applied field (open triangles) from P-MOKE measurements at RT as function of the Fe thickness.

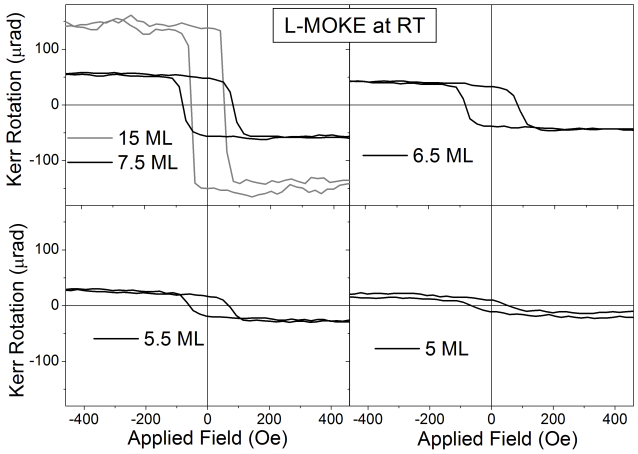

Figure 6.23: Room temperature L-MOKE loops for the Fe wedge covered by a Co oxide layer.

The magnetization (or Kerr rotation) at the maximum applied field (3000 Oe) for P-MOKE in the range of perpendicular anisotropy (up to 5 MLs) as function of the thickness shows a linear increase (fig. 6.22). The magnetization goes to zero close to 2 MLs, but we cannot argue about dead layers in the P-MOKE geometry because there is not enough magnetic field to saturate magnetic moments for the thinnest layers.

After the above experiments, the sample was annealed to 423 K for 5 min. to improve surface quality. The observed LEED spots were strictly the same and the P-MOKE measurements were checked and showed no changes. Then, the Co oxide layer was deposited on the Fe-wedge and *in situ* MOKE measurements were performed again on the covered sample.

room temperature measurements on CoO/Fe-wedge/Ag(001)

In figure 6.23, we present the sequence of L-MOKE hysteresis loop measurements at RT as function of the Fe thickness for the CoO-covered sample, just after oxide deposition. One can observe a similar linear decrease in the saturation magnetization but with a much larger coercivity (by a factor of ≈10) at all positions when compared to the uncovered sample (fig. 6.21). The SRT is less marked, as can be noted at 5 MLs by a still remaining magnetization for zero applied field. In addition, the squareness (M_R/M_S) is no longer equal to one at all positions.

The magnetization (M_R and M_S) from these L-MOKE loops as function of the thickness are shown in figure 6.24. After oxide deposition, the straight line extrapolation for the saturation goes to zero close to 2.3 MLs, instead of 1 ML, showing that the dead layer has increased after oxidation. One can also remark that the loops are less squared and remanence decreases more quickly as function of thickness. If one extrapolates M_R, the straight line crosses zero at about 4 MLs. It looks like the oxide layer is increasing as going to the thinnest Fe-wedge side. P-MOKE measurements were tried at RT but the applied magnetic field was not sufficient to yield any reliable signal.

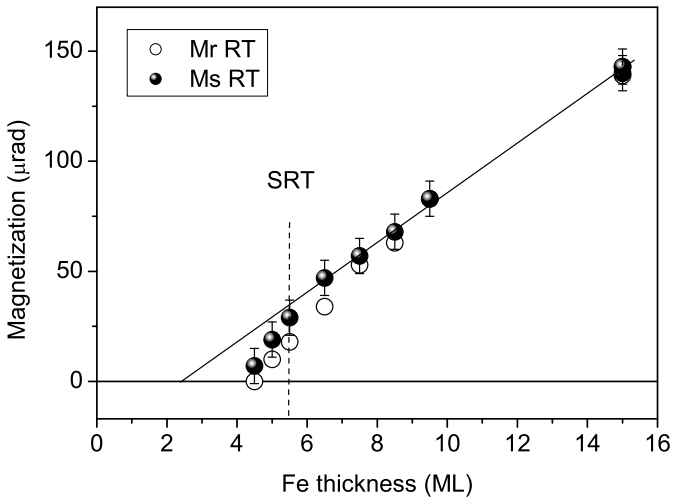

Figure 6.24: Remanence (open circles) and saturation (closed circles) magnetization from L-MOKE data as function of the thickness for the CoO/Fe-wedge/Ag(001) sample.

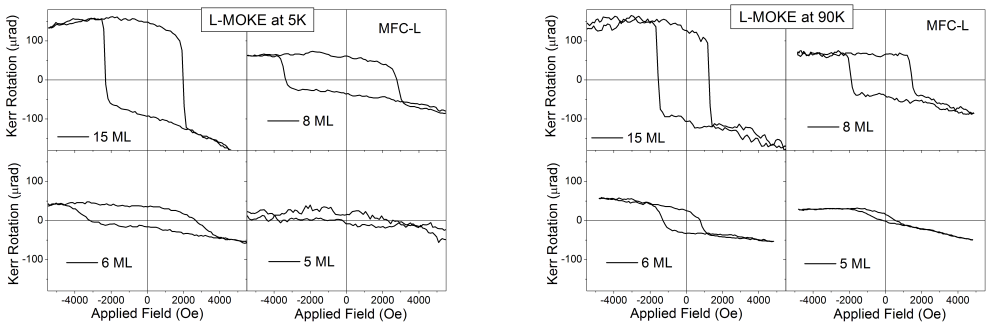

(a) (b)

Figure 6.25: L-MOKE hysteresis loops measured at (a) 5 K and at (b) 90 K after magnetic field cooling along the in-plane Fe easy axis (MFC-L) at 0.55 Tesla.

magnetic field cooling and low temperature measurements on CoO/Fe-wedge/Ag(001)

After RT measurements, we proceeded to magnetic field cooling (MFC) studies at different temperatures. L-MOKE and P-MOKE hysteresis loops were measured at 5 K and at 90 K after field cooling under an applied magnetic field of 0.55 Tesla. The cooling field was applied in-plane along the [100] easy axis of Fe (MFC-L) or perpendicular to the surface (MFC-P). The L-MOKE measurements are shown in figures 6.25 and 6.26 for the MFC-L and MFC-P, respectively. For the P-MOKE configuration it was not possible to saturate the sample and the coercivity values were above the maximum available field. The P-MOKE results will be briefly discussed at the end of this section.

When the magnetic field cooling is applied along the Fe easy axis (MFC-L) all Fe spins are saturated along this direction. One expects that the Co spins are exchange-coupled with Fe spins, which should give rise to an increase in coercivity and an

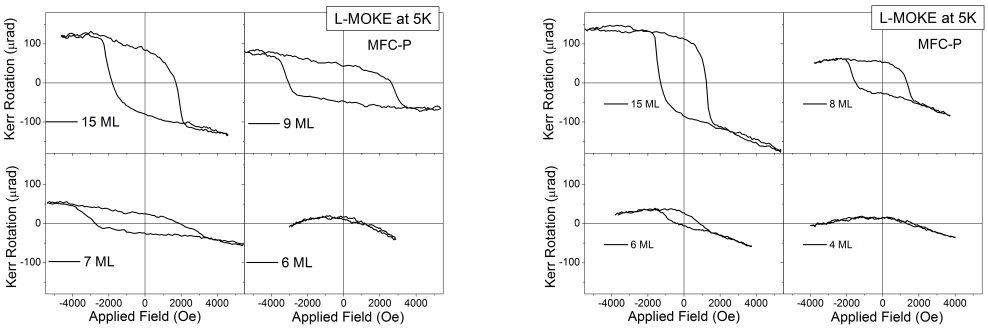

Figure 6.26: L-MOKE hysteresis loops measured at (a) 5 K and at (b) 90 K after magnetic field cooling perpendicular to the surface (MFC-P) at 0.55 Tesla.

exchange-bias shift. Both effects are clearly observed for L-MOKE loops (fig. 6.25-a) measured at 5 K after the MFC-L at 0.55 Tesla. One can observe the huge increase in coercivity. For thickness smaller than 6 MLs, the applied magnetic field is not enough to give any measurable rotation at 5 K. The L-MOKE measurements at 90 K (fig. 6.25-b) were done after measurements at 5 K, without any other magnetic field cooling. One can see that the coercivity is still much larger than at RT. Nevertheless, contrary to the 5 K results, there is an open loop for the thickness of 5 MLs. The 4 MLs measurement yield just a monotonous variation, which has been used as background, to estimate the saturation. Obviously, using this procedure, the error bar for saturation magnetization must be quite large. Nevertheless, one note (fig. 6.27-a, square and triangle) that the overall behavior of M_S is quite similar to the one at RT: linear decrease following the "two dead layers" straight line and rapid decrease around 5 MLs. M_R gives, within the error bars, a similar behavior (fig. 6.27-b). This is not surprising: the magnetization of the Fe film is preserved, even if more difficult to reverse, when the cooling field is imposed along one of the easy axis. A contribution to the total magnetization coming from uncompensated Co spins may exist but would be within our error bars.

Interesting results come out when the cooling field is applied perpendicular to the surface: MFC-P at 0.55 Tesla (fig. 6.26). Compared to what happens for the MFC-L at the same conditions, 5 K or 90 K, one can note that there is still a huge increase in coercivity but the loops are less squared, with reduced magnetization at remanence. Moreover, at the 6 MLs position, the magnetic field is no longer enough to produce any detectable rotation. These results are summarized in figure 6.27, where M_S and M_R measured by L-MOKE after MFC-L (square and triangle) and MFC-P (stars) are compared. Data are also compared to behavior at RT (circles). M_S and M_R are in good agreement when low-temperature (LT) data for MFC-L is compared to RT data. However, when the applied field cooling is perpendicular to the surface (MFC-P), M_R is reduced everywhere. One can even note, as for M_S, that the SRT seems to be shifted to higher thickness, as shown by the zero magnetization for 6 MLs. Our interpretation is that the MFC-P pin a large amount of Co interfacial spins perpendicular to the interface

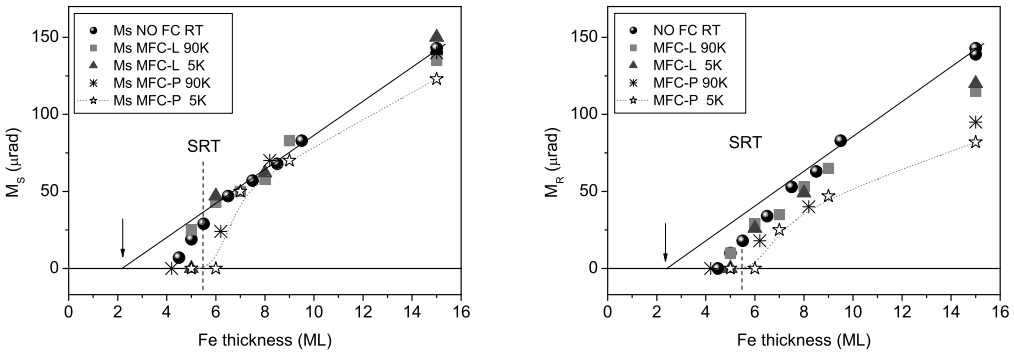

(a) (b)

Figure 6.27: (a) Saturation and (b) remanent magnetization at low temperatures from L-MOKE measurements after MFC-L (squares, triangles) and after MFC-P (stars). Data are compared to behavior at RT (circles).

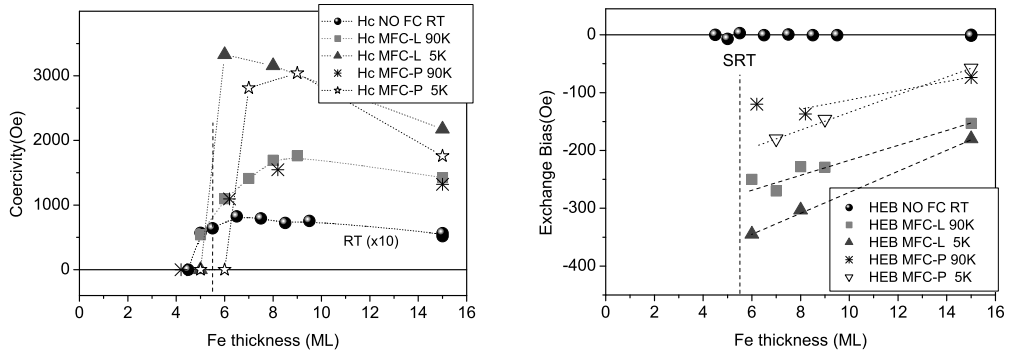

(a) (b)

Figure 6.28: (a) Coercivity and (b) exchange bias shift for the CoO/Fe-wedge sample for different temperatures after magnetic field cooling from 315 K to 5 K under 0.55 Tesla.

and those spins, which are exchange coupled to the Fe spins, causes a decrease in the remanence and shifts onset for spin reorientation transition to higher thickness.

We turn now to the coercivity and exchange bias results coming out from these *in situ* MOKE experiments. In figure 6.28, we shown a comparison among all results for the CoO/Fe-wedge/Ag(001) sample. As discussed above, from the free Fe surface to the Co oxide covered one, the coercivity values had increased by a factor of 10 ($H_c \approx 80$ Oe). At 5 K, after field cooling, we observe that the coercivity has increased by an additional factor of 40, reaching $H_c \approx 3000$ Oe in the range of 6 to 9 MLs and $H_c \approx 2000$ Oe for the 15 MLs. One can remark that the coercivity is larger for smaller thickness, which is consistent with the fact that the increase is coming from the interface exchange coupling, and suddenly vanishes at the critical thickness for spin reorientation. The exchange bias field also displays the expected behavior, increasing as the thickness decreases, at least for the condition where the field cooling is applied in-plane. At 5 K, it reaches the largest value of -380 Oe for the 6 MLs position.

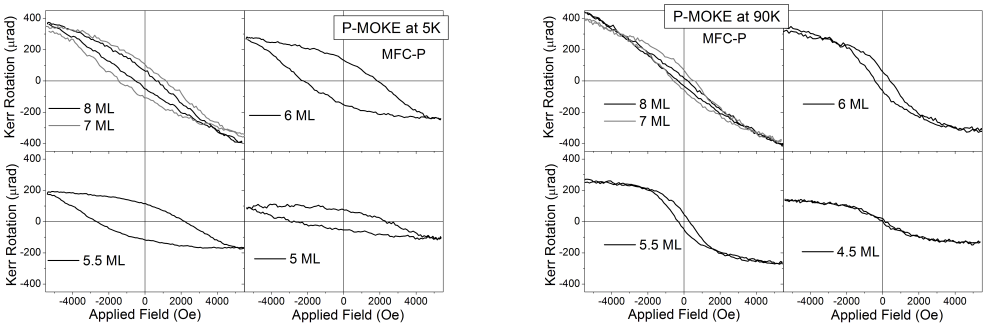

(a) (b)

Figure 6.29: P-MOKE hysteresis loops measured at (a) 5 K and at (b) 90 K after MFC-P at 0.55 Tesla.

Polar MOKE at 5 K and 90 K after magnetic field cooling

P-MOKE hysteresis loops were measured at 5 K and at 90 K after field cooling under an applied magnetic field of 0.55 Tesla. Some selected loops are shown in figure 6.29. At 5 K one can clearly see the limitation imposed by the applied magnetic field: it was not possible to saturate the sample and the coercivity values were above the maximum available field. At 90 K, the situation is better, one can observe that the magnetization raises as function of thickness from 4 to 6 MLs and that some remanence shows up. Nevertheless, even if a small exchange bias may be present, about -250 Oe at 5 K and -50 Oe at 90 K, this could come from artifacts, as for instance, a projection from the in-plane magnetization behavior. The experiment for the perpendicular coupling should be re conducted under better conditions with higher applied magnetic fields.

6.4.2 *Ex situ* MOKE

Once all measurements discussed above were performed, the sample was taken out from the chamber and exposed to the atmosphere. During about five months it was studied by different X-ray techniques - reflectivity, diffraction, absorption - whose results are presented in the previous section concerned by structural characterization. After all these studies, the sample was back to the MOKE apparatus at Halle for additional magnetic studies. One of the main goals of these new experiments were checking the condition of the sample and verifying possible aging effects. We report in this section these results.

In a first experiment, the sample was field cooled from 315 K to 5 K under a magnetic field of 5.5 kOe applied along the easy axis ([100]) of Fe. In a second experiment, the sample was simply cooled without any applied field, i.e., a ZFC study. The L-MOKE hysteresis loops in both experiments were measured after warming the sample at 100 and 200 K. The magnetic field was flipped along the [100] easy axis.

In figure 6.30, we present the remanence for these *ex situ* measurements compared to the results for the *in situ* MFC-L at 90 K. One can see that there is no significant difference among the *in situ* 90 K data and those for the *ex situ* at 100 and 200 K

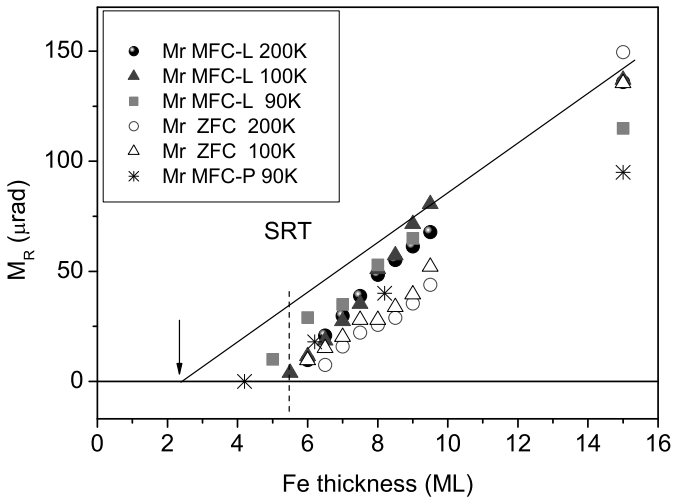

Figure 6.30: Remanence as function of thickness from the *ex situ* L-MOKE data at 100 and 200 K compared to the *in situ* data at 90 K.

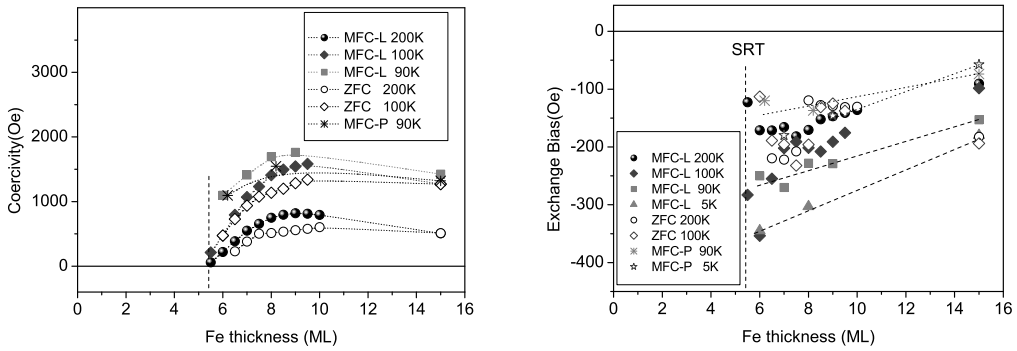

(a) (b)

Figure 6.31: (a) coercivity and (b) exchange bias shift as function of thickness from the *ex situ* L-MOKE data at 100 and 200 K compared to the *in situ* data at 90 K. The guide for the eyes is kept as in figure 6.28 for the *in situ* data.

after MFC-L. A straight line extrapolation of the remanence shows that about 5 MLs are not contributing to remanent magnetization. On the other hand, one can clearly observe that the remanent magnetization is smaller for the ZFC data when compared to the others. This is expected because for MFC-L the applied field along the easy axis stabilizes not only the Fe moments along that direction but also some Co moments, that remain pinned. In the case of the ZFC experiment, interfacial spins are most likely frozen in a disordered state. The ZFC experiment is similar, in that sense, to the MFC-P experiment that pinned some Fe and Co moments away from the easy axis of Fe.

In figure 6.31 we compare the coercivity and exchange bias shift for the *ex situ* and *in situ* measurements. The results at 100 and 200 K are very consistent with those of the *in situ* 90 K experiment in a fresh sample. The coercivity increases as thickness decreases

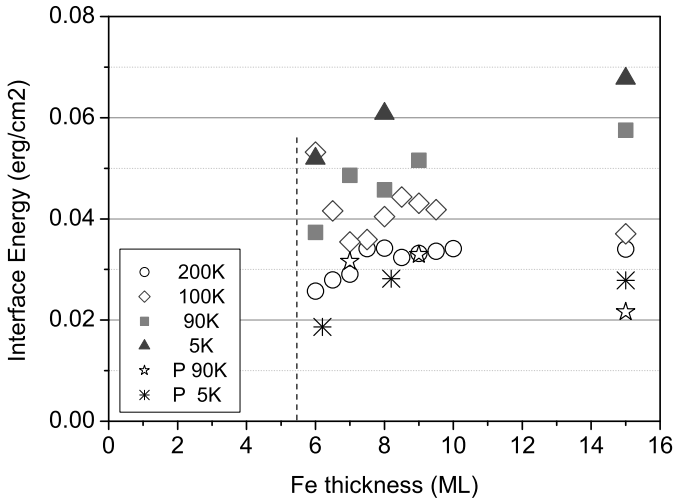

Figure 6.32: Interface energy density as function of thickness from the *in situ* and *ex situ* L-MOKE at different temperatures, and for in-plane and out-of-plane field cooling.

and has a maximum around 8 to 9 MLs. At the same temperature, one notes that the coercivity for the ZFC is smaller, showing that the coupling is less effective to generate an additional coercivity. The observed exchange bias shift displays a similar behavior, slightly increasing as thickness decreases. The density of interface energy associated to the exchange coupling is shown in figure 6.32. The relation $H_{EB} = \Delta\sigma/(M_{FM} \times t_{FM})$ converts exchange bias field H_{EB} to additional interface energy $\Delta\sigma$, where the Fe nominal thickness and $M_{FM} = 1750\,\mathrm{emu/cm^3}$ for Fe is used.

6.5 Summary

An Fe-wedge sample covered by a Co oxide was successfully synthesized and characterized. The *in situ* studies revealed many interesting properties. Before covering the Fe-wedge with CoO, we observed that the spin reorientation transition takes place between 5 to 6 MLs at RT, as often reported in the literature. In our uncovered sample, both remanence and saturation magnetization straight line extrapolation points to one dead layer of Fe. After CoO deposition, sample presents a larger number of dead layers, 2.3 MLs when one extrapolates the saturation magnetization and about 4 MLs when one extrapolates the remanence. This is a consequence of the formation of an Fe oxide at the interface with the CoO.

X-ray reflectivity yields a reduced Fe layer, by about 2 MLs, and a thicker CoO layer compared to the nominal coverages.

X-ray absorption spectroscopy reveals the presence of such an oxide and yields a detailed description, discarding the existence of the FeO phase, which is antiferromagnetic at low temperature. A mixture of $\alpha - Fe_2O_3$ and Fe_3O_4 simulates quite well the spectra. In fact, the most reasonable situation is a decreasing gradient of oxygen into the Fe layer. At RT, this thin FeO_x layer is probably not contributing to remanent magnetization but can easily respond to an applied magnetic field. This explains why

one measures about 4 dead MLs at remanence and only 2.3 at saturation. XAS and MOKE results are entirely compatible in this regard, in particular in the wedge portion with less than 4 deposited MLs of Fe.

After CoO deposition, the coercive field H_C has increased by a factor of 10 at RT. For the CoO thickness deposited, of about 7 nm, the Néel temperature is around 250 K. As expected, after magnetic field cooling, a huge increase in the coercivity is observed as a consequence of the exchange coupling of the Fe layer with the oxide CoO. In addition, one also observes a shift in the hysteresis loop, whose dependence was studied as function of a few different parameters, as temperature and applied field cooling orientation. An almost linear dependence of the shift as the thickness decreases was observed, compatible with an effect that is taking place in the interface.

Chapter 7

Conclusions and prospects

Our motivation was, in this thesis work, to understand the mechanism of exchange coupling at the interface of some AFM/FM bilayer systems. We aimed at a fine control of the structure and end up with optimized model systems. To synthesize model samples, our approach was to exploit the ability to grow ultra-thin epitaxial films and multilayers by molecular beam epitaxy, combined with structural probes available in synchrotron light sources. The French CRG BM32 beamline at ESRF for *in situ* grazing incidence X-ray diffraction (GIXRD) was an invaluable tool for the accomplishment of our aim. In addition, investigations, on the same samples, of the short-range-order arrangement and of the local magnetic moments and anisotropy of selected atomic species, using X-ray absorption spectroscopy (XAS) and Magnetic Circular Dichroism (XMCD), allowed us to go deeper into the understanding of the combined layers.

We were especially interested in thin ferromagnetic films with perpendicular magnetic anisotropy. Many steps were needed, starting by the comprehension of the earliest steps of growth of the different atomic species on selected surfaces, before the achievement of model systems. The study of the earliest stages of the metal (Mn, Fe and Pt) growth on Pt(001) and on Ag(001) single-crystals led to important outcomes for the elaboration of ordered $L1_0$ alloys.

The growth on *Pt(001)-hex* is strongly affected by the hexagonal reconstruction, which is lifted locally through metal deposition. When Mn is deposited, we found that lifting the reconstruction results in an excess of Pt atoms in the first layer of the film, yielding a surface alloy with local $c(2 \times 2)$ arrangement. Lifting the reconstruction previous to Mn deposition inhibits such alloying. Such deconstruction process was achieved by depositing Pt at an elevated temperature. The growth of Pt on Pt(001) or Pt on Mn/Pt(001) at RT resulted in quite a rough surface. On the contrary, an almost layer-by-layer Pt growth is achieved by deposition at about 600 K. At this temperature, there is no significant Mn diffusion into the Pt bulk. Deposition of Fe on *Pt-hex* at 600 K results directly in an out-of-plane ordered $L1_0$ phase.

For the Ag(001) substrate, we observed that Fe grows pseudomorphically up to 14 MLs. The spin reorientation transition, taking place at 6 MLs, seems to be related to a change in the unit cell volume, rather than to a relaxation of the in-plane lattice parameter. For Pt deposition, Ag segregates to the surface. Alternated Pt and Mn deposition at 570 K, favored by the large Ag lattice constant, and possibly by

the surfactant effect, yields an $L1_0$ ordered alloy with out-of-plane orientation. Future investigation of such MnPt/Ag(001) layer coupled with a perpendicular magnetic anisotropy layer, like FePt, sounds interesting.

In terms of data analysis, we developed and validated a procedure for quantifying the order parameter of pseudomorphic alloys from GIXRD measurements. The faster acquisition mode based on stationary scan was used to study thick films. A new area detector, that has just become available at the BM32 beamline, should make this acquisition mode a standard, once the entire diffraction signal, including background, may be collected in a single exposure.

Based on the knowledge of the earliest stages of growth, we studied the growth of MnPt and FePt ordered alloys on Pt(001). For MnPt, RT growth leads to a rough and disordered layer that, when annealed at 770 K, becomes smooth and presents small $L1_0$ ordered domains with the *c*-axis oriented either in-plane and out-of-plane. The best out-of-plane $L1_0$ MnPt film, with coexisting in-plane minority domains, was obtained for deposition at 570 K. A tetragonally distorted FePt layer with *c*-axis perpendicular to the surface was grown on that MnPt layer (still at 570 K). *Ex situ* polar MOKE showed that, after field cooling, the coercive field increases and exchange bias shows up. XMCD at the Mn and Fe $L_{2,3}$-edges revealed a coupling perpendicular to the surface between Fe and Mn magnetic moments and a large amount of uncompensated Mn spins at interface, the majority of them being rotatable.

For this same substrate temperature, we also demonstrated that a highly ordered $L1_0$ FePt may be obtained by a Fe-rich alternate deposition on a clean substrate. This highly ordered FePt film was studied by XAS and XMCD. Sum rules were applied to the XMCD results and we interpret the enhanced orbital magnetism observed in our film as the result of the increased tetragonal distortion and the high degree of chemical order.

An Fe-wedge sample (0-10 ML) grown on Ag(001) and covered by a Co oxide was successfully synthesized and characterized. The *in situ* MOKE investigation on the uncovered sample revealed that the spin reorientation transition takes place between 5 to 6 MLs at RT and there is one dead layer of Fe. After CoO deposition, the number of dead layers increases as a consequence of Fe oxidation at the interface with the CoO. X-ray absorption spectroscopy reveals the characteristics of such oxide, excluding the presence of antiferromagnetic FeO. At RT, this thin FeO_x layer is probably not contributing to remanent magnetization but can easily respond to an applied magnetic field. After magnetic field cooling, a huge increase in the coercivity and exchange bias are observed at low temperatures, as a consequence of the $CoO/FeO_x/Fe$ exchange coupling.

Prospects

- The best out-of-plane $L1_0$ MnPt film was obtained for deposition at 570 K. Ordered domains with in-plane *c*-axis orientations (twinned) also coexists, even if the out-of-plane domains are majority and wider. Lifting the *Pt-hex* reconstruction previous to Mn deposition, for instance by exposure to hydrogen, and deposi-

tion at even higher (∼650 K) temperature would probably further improve the out-of-plane order.

- Synthesizing $L1_0$ ordered alloys of MnPt and FePt on Ag(001) substrate has been seldom exploited. Our very first experiment on the MnPt on this substrate indicates that this is a promising way to follow.

- The CoO/Fe and CoO/FePt bilayer systems were not deeply investigated during this thesis work and deserve more attention. In particular, the CoO epitaxy depends a lot on the mismatch and on the reactive growth conditions and this way should be explored to produce oxides with different out-of-plane orientations. For the CoO/Ag(001), our XAS investigation points to a distorted rocksalt structure and to an anisotropy in the electronic structure. Nevertheless, when CoO is deposited on Pt(001) our preliminary results indicate a (111) texture with a in-plane and out-of-plane distorted unit cell. This will be explored in the future.

- All models developed up to now to describe exchange-bias are based on the implicit assumption that the AFM magnetic moment arrangement at the interface is not significantly altered by AFM/FM interface exchange coupling. This means that all uncompensated AFM spins should be pinned by the AFM layer and participating in the exchange bias field. However, when the AFM/FM interface exchange is strong enough, some of the interface AFM moments rotate together with the FM ones, under the external applied field. This effect was observed by XMCD in one of our samples. It seems of crucial importance for the exchange bias coupling to investigate the spin configuration at the interface with element selectivity and atomic layer depth sensitivity.

Résumé de la thèse en français

Ce travail de thèse se situe dans un contexte d'étude de l'effet du couplage d'échange dans les couches minces magnétiques avec anisotropie hors du plan. Il déploie un ensemble de techniques expérimentales qui utilisent le rayonnement synchrotron, pour étudier l'interaction, au niveau de l'interface, entre un matériau antiferromagnétique (AFM) et un ferromagnétique (FM), et la relation entre le couplage d'échange et la structure des couches.

Le premier chapitre introduit les motivations fondamentales et technologiques des études sur les systèmes magnétiques à couplage d'échange. Sont mis en avant le rôle essentiel de la qualité des couches et des interfaces et la nécessité d'aller vers des dimensions de plus en plus réduites. Chacun des systèmes étudiés, avec ses problématiques et intérêts spécifiques, est ensuite décrit. Le chapitre se termine par une présentation de l'approche fondamentale de la physique de surface.

Le deuxième chapitre présente les différentes techniques expérimentales mises en oeuvre lors de la synthèse et la caractérisation des surfaces et couches minces. Pour chacune de ces techniques sont décrits les principes de base et méthodologies d'analyse qui serviront de support à la présentation des résultats. Un développement tout particulier est donné à la diffraction de surface, technique centrale dans ce travail de thèse, et au paramètre d'ordre S qui défini l'ordre chimique dans les alliages bimétalliques.

Le troisième chapitre est consacré à l'étude structurale des premières étapes de la croissance des différents métaux et alliages utilisés dans les couches et bicouches réalisées sur deux substrats différents, Pt(001) et Ag(001). Le faible désaccord paramétrique entre la maille *fcc* du platine et la base de maille quadratique de la phase $L1_0$ de l'alliage bimétallique (MnPt, FePt) favorise la croissance de ces alliages selon leur axe c et permet d'obtenir ainsi une orientation des moments magnétiques perpendiculaires à la surface. Cependant la surface propre Pt(001) présente une reconstruction hexagonale du dernier plan de surface susceptible d'affecter les premières étapes de la croissance des couches d'alliage. Afin d'optimiser le démarrage de cette croissance, il a été étudié le processus de déconstruction de la surface pour les différents éléments chimiques en jeu. La température du substrat s'avère un paramètre crucial pour l'obtention d'un bon ordre chimique. La croissance sur le substrat Ag(001) qui ne présente pas de reconstruction s'avère plus simple, mis à part un effet surfactant observé pour tous les systèmes étudiés. Cet effet peut favoriser une bonne croissance couche-par-couche mais aussi modifier les propriétés magnétiques du système.

Le quatrième chapitre décrit une méthode de détermination du paramètre d'ordre chimique de la phase $L1_0$ à partir des données de diffraction de surface. Dans le cas de

couches “épaisses” composées de plus d'une dizaine de monocouches, la stratégie de la mesure consiste à utiliser des “l-scans” pour décrire les tiges de troncature (CTR) plutôt que l'approche classique d'une succession de “rocking-scans” aux différentes valeurs de l. Cette méthodologie réduit le temps d'acquisition de façon très conséquente et s'avère la seule façon de mesurer les tiges avec une bonne résolution dans des temps raisonnables. L'information sur la contribution de la diffusion diffuse liée entre autre aux processus thermiques et au désordre chimique sont pris en compte par des balayages décalés par rapport aux crêtes des tiges et quelques “rocking-scans” bien choisis. La croissance des couches MnPt en vue de l'obtention de l'ordre chimique avec l'axe perpendiculaire à la surface est étudiée dans le cas des dépôts à température ambiante et à 500 K suivi d'un recuit. Les paramètres d'ordre pour des domaines dans le plan et hors du plan sont obtenus de façon quantitative.

Le cinquième chapitre présente l'étude détaillée de bicouches MnPt/FePt couplées par échange. La croissance a été optimisé afin d'obtenir l'ordre chimique $L1_0$ avec l'axe perpendiculaire à la surface. Les conditions optimales, à la fois pour la couche MnPt et pour celle de FePt, sont obtenues pour un dépôt alterné associé une température aux alentours de 570 K. Dans ces condition l'ordre chimique dans les couches bimétalliques approche l'unité. Les études magnétiques réalisées sur ces systèmes mettent en évidence l'existence d'un couplage d'échange à l'interface, qui se traduit par un décalage du cycle d'hystérésis et par une forte augmentation du champ coercitif. Les mesures de dichroïsme magnétique montrent aussi clairement le couplage entre les spins du Mn et du Fe.

Le sixième chapitre décrit l'étude d'un autre système à couplage d'échange, la bicouche CoO/Fe déposée sur Ag(001). Les propriétés magnétiques sont étudiées d'abord sur la couche de Fe/Ag(001) et ensuite après dépôt de l'oxyde de cobalt. Une transition de spin en fonction de l'épaisseur de la couche est observée autour de 5 à 6 MLs. Après dépôt du CoO, une couche d'oxyde de fer est formée, ce qui entraine une diminution de l'aimantation du système. L'augmentation du champ coercitif et l'apparition d'un décalage d'échange montrent que le système est bien couplé par échange à l'interface.

Le dernier chapitre rappelle les résultats les plus importants de ce travail de thèse et donne les principales perspectives pour les travaux à venir. A travers le contrôle d'un certain nombre de paramètres, comme la structure de la surface, la propreté, le taux et la température de déposition, nous avons acquis une connaissance approfondie du processus de croissance dans les systèmes MnPt et FePt sur Pt(001) et Pt, MnPt et Fe sur Ag(001). Ces systèmes ont été étudiés *in situ* (et *ex situ*) par la diffraction de surfaces et *ex situ* par MOKE, réflectivité et spectroscopie d'absorption de rayons X. La relation entre le couplage d'échange et la structure des couches est discutée pour les interfaces MnPt/FePt et CoO/Fe.

Bibliography

[1] R. P. Feynman, "Plenty of room at the bottom." `http://www.its.caltech.edu/~feynman/plenty.html`.

[2] S. N. Piramanayagam, "Perpendicular recording media for hard disk drives," *Journal of Applied Physics*, 102 (1), 011301, 2007.

[3] M. N. Baibich, J. M. Broto, A. Fert, F. N. Van Dau, F. Petroff, P. Etienne, G. Creuzet, A. Friederich, and J. Chazelas, "Giant magnetoresistance of (001)Fe/(001)Cr magnetic superlattices," *Physical Review Letters*, 61 (21), 2472–2475, 1988.

[4] W. H. Meiklejohn and C. P. Bean, "New magnetic anisotropy," *Physical Review*, 105 (3), 904–913, 1957.

[5] S. S. P. Parkin, K. P. Roche, M. G. Samant, P. M. Rice, R. B. Beyers, R. E. Scheuerlein, E. J. O'Sullivan, S. L. Brown, J. Bucchigano, D. W. Abraham, Y. Lu, M. Rooks, P. L. Trouilloud, R. A. Wanner, and W. J. Gallagher, "Exchange-biased magnetic tunnel junctions and application to nonvolatile magnetic random access memory," *Journal of Applied Physics*, 85 (8), 5828–5833, 1999.

[6] C. A. F. Vaz, J. A. C. Bland, and G. Lauhoff, "Magnetism in ultrathin film structures," *Reports on Progress in Physics*, 71 (5), 056501, 2008.

[7] D. P. Pappas, C. R. Brundle, and H. Hopster, "Reduction of macroscopic moment in ultrathin Fe films as the magnetic orientation changes," *Physical Review B*, 45 (14), 8169–8172, 1992.

[8] F. Yildiz, F. Luo, C. Tieg, R. M. Abrudan, X. L. Fu, A. Winkelmann, M. Przybylski, and J. Kirschner, "Strongly enhanced orbital moment by reduced lattice symmetry and varying composition of $Fe_{1-x}Co_x$ alloy films," *Physical Review Letters*, 100 (3), 2008.

[9] J. Als-Nielsen and D. McMorrow, "Elements of modern x-ray physics,". John Wiley and Sons, 2001.

[10] J. Stohr and H. C. Siegmann, "Magnetism: From fundamentals to nanoscale dynamics,". Berlin: Springer, 2006.

[11] A. Aharoni, "Introduction to the theory of ferromagnetism,". Oxford: University Press, 1998.

[12] A. P. Guimarães, "Magnetism and magnetic resonance in solids,". New York: John Wiley and Sons, 1998.

[13] J. Nogues and I. K. Schuller, "Exchange bias," *Journal of Magnetism and Magnetic Materials*, 192 (2), 203–232, 1999.

[14] A. E. Berkowitz and K. Takano, "Exchange anisotropy – a review," *Journal of Magnetism and Magnetic Materials*, 200 (1-3), 552–570, 1999.

[15] F. Radu and H. Zabel, "Exchange bias effect of ferro-/antiferromagnetic heterostructures," in *Magnetic Heterostructures* (H. Zabel and S. Bader, eds.), vol. 227 of *Springer Tracts in Modern Physics*, pages 97–184, Springer Berlin / Heidelberg, 2008.

[16] A. P. Malozemoff, "Random-field model of exchange anisotropy at rough ferromagnetic-antiferromagnetic interfaces," *Physical Review B*, 35 (7), 3679–3682, 1987.

[17] D. Mauri, H. Siegmann, P. Bagus, and E. Kay, "Simple model for thin ferromagnetic films exchange coupled to an antiferromagnetic substrate," *Journal of Applied Physics*, 62 (7), 3047–3049, 1987.

[18] N. C. Koon, "Calculations of exchange bias in thin films with ferromagnetic/antiferromagnetic interfaces," *Physical Review Letters*, 78 (25), 4865–4868, 1997.

[19] M. D. Stiles and R. D. McMichael, "Model for exchange bias in polycrystalline ferromagnet-antiferromagnet bilayers," *Physical Review B*, 59 (5), 3722–3733, 1999.

[20] U. Nowak, K. D. Usadel, J. Keller, P. Miltényi, B. Beschoten, and G. Güntherodt, "Domain state model for exchange bias. I. Theory," *Physical Review B*, 66 (1), 014430, 2002.

[21] K. Lee, Y. Yu, and S. Kim, "An interface proximit model," *Applied Physics Letters*, 86, 192512, 2005.

[22] J. Kortright, D. Awschalom, J. Stohr, S. Bader, Y. Idzerda, S. Parkin, I. Schuller, and H. Siegmann, "Research frontiers in magnetic materials at soft X-ray synchrotron radiation facilities," *Journal of Magnetism and Magnetic Materials*, 207, 7–44, 1999.

[23] H. Ohldag, T. J. Regan, J. Stöhr, A. Scholl, F. Nolting, J. Lüning, C. Stamm, S. Anders, and R. L. White, "Spectroscopic identification and direct imaging of interfacial magnetic spins," *Physical Review Letters*, 87 (24), 247201, 2001.

[24] H. Ohldag, A. Scholl, F. Nolting, E. Arenholz, S. Maat, A. T. Young, M. Carey, and J. Stöhr, "Correlation between exchange bias and pinned interfacial spins," *Physical Review Letters*, 91 (1), 017203, 2003.

[25] C. Binek, S. Polisetty, X. He, and A. Berger, "Exchange bias training effect in coupled all ferromagnetic bilayer structures," *Physical Review Letters*, 96 (6), 067201, 2006.

[26] B. Kagerer, C. Binek, and W. Kleemann, "Freezing field dependence of the exchange bias in uniaxial FeF2-CoPt heterosystems with perpendicular anisotropy," *Journal of Magnetism and Magnetic Materials*, 217 (1), 139–, 2000.

[27] S. Maat, K. Takano, S. S. P. Parkin, and E. E. Fullerton, "Perpendicular exchange bias of Co/Pt multilayers," *Physical Review Letters*, 87 (8), 087202, 2001.

[28] J. Sort, V. Baltz, F. Garcia, B. Rodmacq, and B. Dieny, "Tailoring perpendicular exchange bias in [Pt/Co]-IrMn multilayers," *Physical Review B (Condensed Matter and Materials Physics)*, 71 (5), 054411, 2005.

[29] S. M. Zhou, L. Sun, P. C. Searson, and C. L. Chien, "Perpendicular exchange bias and magnetic anisotropy in CoO/permalloy multilayers," *Physical Review B*, 69 (2), 024408, 2004.

[30] A. Baruth, D. J. Keavney, J. D. Burton, K. Janicka, E. Y. Tsymbal, L. Yuan, S. H. Liou, and S. Adenwalla, "Origin of the interlayer exchange coupling in [Co/Pt]/NiO/[Co/Pt] multilayers studied with XAS, XMCD, and micromagnetic modeling," *Physical Review B*, 74 (5), 054419, 2006.

[31] S. Bader, "SMOKE," *Journal of Magnetism and Magnetic Materials*, 100 (1-3), 440 – 454, 1991.

[32] Z. Qiu and S. Bader, "Surface MOKE," *Journal of Magnetism and Magnetic Materials*, 200, 664–678, 1999.

[33] T. Shima, K. Takanashi, Y. K. Takahashi, and K. Hono, "Coercivity exceeding 100 kOe in epitaxially grown FePt sputtered films," *Applied Physics Letters*, 85 (13), 2571–2573, 2004.

[34] D. Weller, A. Moser, L. Folks, M. Best, W. Lee, M. Toney, M. Schwickert, J. Thiele, and M. Doerner, "High K-u materials approach to 100 Gbits/in^2," *IEEE Transactions on Magnetics*, 36 (1), 10–15, 2000.

[35] T. Klemmer, D. Hoydick, H. Okumura, B. Zhang, and W. A. Soffa, "Magnetic hardening and coercivity mechanisms in L10 ordered FePd ferromagnets," *Scripta Metallurgica et Materialia*, 33 (10-11), 1793 – 1805, 1995.

[36] T. Shima, M. Okamura, S. Mitani, and K. Takanashi, "Structure and magnetic properties for L10-ordered FeNi films prepared by alternate monatomic layer deposition," *Journal of Magnetism and Magnetic Materials*, 310 (2, Part 3), 2213 – 2214, 2007.

[37] J. P. Nozieres, S. Jaren, Y. B. Zhang, A. Zeltser, K. Pentek, and V. S. Speriosu, "Blocking temperature distribution and long-term stability of spin-valve

structures with Mn-based antiferromagnets," *Journal of Applied Physics*, 87 (8), 3920–3925, 2000.

[38] S. Sun, C. B. Murray, D. Weller, L. Folks, and A. Moser, "Monodisperse FePt nanoparticles and ferromagnetic FePt nanocrystal superlattices," *Science*, 287 (5460), 1989–1992, 2000.

[39] P. Bayliss, "Revised unit-cell dimensions, space group, and chemical formula of some metallic minerals," *Canadian Mineralogist*, 28 (4), 751–755, 1990.

[40] Y. Nosé, A. Kushida, T. Ikeda, H. Nakajima, K. Tanaka, and H. Numakura, "Re-examination of phase diagram of Fe-Pt system," *Materials Transactions*, 44 (12), 2723–2731, 2003.

[41] P. Villars and L. D. Calvert, "Pearson's handbook of crystallographic data for intermetallic phases,". American Society for Metals, Metals Park, OH, 1985.

[42] J. Lyubina, I. Opahle, M. Richter, O. Gutfleisch, K.-H. Muller, L. Schultz, and O. Isnard, "Influence of composition and order on the magnetism of Fe-Pt alloys: Neutron powder diffraction and theory," *Applied Physics Letters*, 89 (3), 032506, 2006.

[43] A. Sakuma, "1^{st} principle calculation of the magnetocrystalline anisotropy energy of FePt and CoPt ordered alloys," *Journal of the Physical Society of Japan*, 63 (8), 3053–3058, 1994.

[44] R. F. C. Farrow, D. Weller, R. F. Marks, M. F. Toney, A. Cebollada, and G. R. Harp, "Control of the axis of chemical ordering and magnetic anisotropy in epitaxial FePt films," *Journal of Applied Physics*, 79 (8, Part 2B), 5967–5969, 1996.

[45] R. Farrow, D. Weller, R. Marks, M. Toney, S. Horn, G. Harp, and A. Cebollada, "Growth temperature dependence of long-range alloy order and magnetic properties of epitaxial FexPt1-x (x similar or equal to 0.5) films," *Applied Physics Letters*, 69 (8), 1166–1168, 1996.

[46] S. Okamoto, N. Kikuchi, O. Kitakami, T. Miyazaki, Y. Shimada, and K. Fukamichi, "Chemical-order-dependent magnetic anisotropy and exchange stiffness constant of FePt (001) epitaxial films," *Physical Review B*, 66 (2), 024413, 2002.

[47] A. Cebollada, D. Weller, J. Sticht, G. R. Harp, R. F. C. Farrow, R. F. Marks, R. Savoy, and J. C. Scott, "Enhanced magneto-optical Kerr effect in spontaneously ordered FePt alloys: Quantitative agreement between theory and experiment," *Physical Review B*, 50 (5), 3419–3422, 1994.

[48] T. Shima, T. Moriguchi, S. Mitani, and K. Takanashi, "Low-temperature fabrication of L10 ordered FePt alloy by alternate monatomic layer deposition," *Applied Physics Letters*, 80 (2), 288–290, 2002.

[49] Y. F. Ding, J. S. Chen, E. Liu, C. J. Sun, and G. M. Chow, "Effect of lattice mismatch on chemical ordering of epitaxial $L1_0$ FePt films," *Journal of Applied Physics*, 97 (10), 10H303, 2005.

[50] Z. Lu, R. V. Chepulskii, and W. H. Butler, "First-principles study of magnetic properties of $L1_0$-ordered MnPt and FePt alloys," *Physical Review B*, 81 (9), 094437, 2010.

[51] K. He, L. J. Zhang, X. C. Ma, J. F. Jia, Q. K. Xue, and Z. Q. Qiu, "Growth and magnetism of ultrathin Fe films on Pt(100)," *Physical Review B*, 72 (15), 155432, 2005.

[52] E. Krén, G. Kádár, L. Pál, J. Sólyom, P. Szabó, and T. Tarnóczi, "Magnetic structures and exchange interactions in the Mn-Pt system," *Physical Review*, 171 (2), 574–585, 1968.

[53] H. Hama, R. Motomura, T. Shinozaki, and Y. Tsunoda, "Spin-flip transition of $L1_0$-type MnPt alloy single crystal studied by neutron scattering," *Journal of Physics: Condensed Matter*, 19 (17), 176228, 2007.

[54] J. Borme, *Alliage antiferromagnétique MnPt: croissance, propriétés magnétiques et structurales*. PhD thesis, Université Joseph Fourier, 2006.

[55] A. Sakuma, "First-principles study on the non-collinear magnetic structures of disordered alloys," *Journal of the Physical Society of Japan*, 69 (9), 3072–3083, 2000.

[56] B. Dieny and O. Redon, "DISPOSITIF MAGNETIQUE A JONCTION TUNNEL MAGNETIQUE, MEMOIRE ET PROCEDES D'ECRITURE ET DE LECTURE UTILISANT CE DISPOSITIF," *Organisation Mondiale de la Propriete Intellectuelle*, 2003.

[57] K. Nishioka, S. Shigematsu, T. Imagawa, and S. Narishige, "Thickness effect on ferro/antiferromagnetic coupling of Co/CrMnPt systems," *Journal of Applied Physics*, 83 (6), 3233–3238, 1998.

[58] M. Rickart, A. Guedes, J. Ventura, J. B. Sousa, and P. P. Freitas, "Blocking temperature in exchange coupled MnPt/CoFe bilayers and synthetic antiferromagnets," *Journal of Applied Physics*, 97 (10), 10K110, 2005.

[59] M. F. Toney, M. G. Samant, T. Lin, and D. Mauri, "Thickness dependence of exchange bias and structure in MnPt and MnNi spin valves," *Applied Physics Letters*, 81 (24), 4565–4567, 2002.

[60] T. Sato, M. Tsunoda, and M. Takahashi, "Correlation between the exchange bias and the degree of ordering of antiferromagnetic layer in PtMn/Co-Fe bilayers," *Journal of Magnetism and Magnetic Materials*, 240 (1-3), 277 – 279, 2002.

[61] H. Xi, R. M. White, Z. Gao, and S. Mao, "Antiferromagnetic thickness dependence of blocking temperature in exchange coupled polycrystalline ferromagnet/antiferromagnet bilayers," *Journal of Applied Physics*, 92 (8), 4828–4830, 2002.

[62] T. Ambrose and C. L. Chien, "Dependence of exchange coupling on antiferromagnetic layer thickness in NiFe/CoO bilayers," *Journal of Applied Physics*, 83 (11), 6822–6824, 1998.

[63] P. J. van der Zaag, Y. Ijiri, J. A. Borchers, L. F. Feiner, R. M. Wolf, J. M. Gaines, R. W. Erwin, and M. A. Verheijen, "Difference between blocking and Néel temperatures in the exchange biased Fe_3O_4/CoO system," *Physical Review Letters*, 84 (26), 6102–6105, 2000.

[64] Y. S. Choi, A. K. Petford-Long, R. C. C. Ward, R. Fan, J. P. Goff, and T. P. A. Hase, "Molecular beam epitaxy growth of exchange-biased PtMn/NiFe bilayers with a spontaneously ordered PtMn layer," *Journal of Applied Physics*, 99 (8), 083903, 2006.

[65] A. Mougin, J. Borme, R. L. Stamps, A. Marty, P. Bayle-Guillemaud, Y. Samson, and J. Ferré, "Antiferromagnetic relaxation and induced anisotropy in Fe-twinned/PtMn bilayers," *Physical Review B*, 73 (2), 024401, 2006.

[66] Y. Choi, A. K. Petford-Long, and R. C. C. Ward, "Epitaxial PtMn/NiFe exchange-biased bilayers containing directly deposited ordered PtMn," *Journal of Applied Physics*, 97 (10), 10C512, 2005.

[67] S. I. Csiszar, M. W. Haverkort, Z. Hu, A. Tanaka, H. H. Hsieh, H.-J. Lin, C. T. Chen, T. Hibma, and L. H. Tjeng, "Controlling orbital moment and spin orientation in CoO layers by strain," *Physical Review Letters*, 95 (18), 187205, 2005.

[68] R. Abrudan, J. Miguel, M. Bernien, C. Tieg, M. Piantek, J. Kirschner, and W. Kuch, "Structural and magnetic properties of epitaxial Fe/CoO bilayers on Ag(001)," *Physical Review B*, 77 (1), 014411, 2008.

[69] J. Wu, J. S. Park, W. Kim, E. Arenholz, M. Liberati, A. Scholl, Y. Z. Wu, C. Hwang, and Z. Q. Qiu, "Direct measurement of rotatable and frozen CoO spins in exchange bias system of CoO/Fe/Ag(001)," *Physical Review Letters*, 104 (21), 217204, 2010.

[70] Z. Q. Qiu, J. Pearson, and S. D. Bader, "Asymmetry of the spin reorientation transition in ultrathin Fe films and wedges grown on Ag(100)," *Physical Review Letters*, 70 (7), 1006–1009, 1993.

[71] W. Kuch, L. I. Chelaru, F. Offi, J. Wang, M. Kotsugi, and J. Kirschner, "Tuning the magnetic coupling across ultrathin antiferromagnetic films by controlling atomic-scale roughness," *Nature Materials*, 5 (2), 128–133, 2006.

[72] H. Ibach, "Physics of surfaces and interfaces,". Berlin: Springer, 2006.

[73] S. Andrieu and P. Muller, "Les surfaces solides: concepts et methodes,". EDP Sciences, CNRS Editions - Paris, 2005.

[74] M. V. Hove, R. Koestner, P. Stair, J. Biberian, L. Kesmodel, I. Bartos, and G. Somorjai, "The surface reconstructions of the (100) crystal faces of iridium, platinum and gold: I. Experimental observations and possible structural models," *Surface Science*, 103 (1), 189–217, 1981.

[75] S. Hagstrom, H. B. Lyon, and G. A. Somorjai, "Surface structures on the clean platinum (100) surface," *Physical Review Letters*, 15 (11), 491–493, 1965.

[76] J. A. Venables, G. D. T. Spiller, and M. Hanbucken, "Nucleation and growth of thin films," *Reports on Progress in Physics*, 47 (4), 399, 1984.

[77] P. Gambardella, A. Dallmeyer, K. Maiti, M. Malagoli, W. Eberhardt, K. Kern, and C. Carbone, "Ferromagnetism in one-dimensional monatomic metal chains," *Nature*, 416 (6878), 301–304, 2002.

[78] A. Buchsbaum, M. De Santis, H. C. N. Tolentino, M. Schmid, and P. Varga, "Highly ordered Pd, Fe, and Co clusters on alumina on $Ni_3Al(111)$," *Physical Review B*, 81 (11), 115420, 2010.

[79] R. Kunkel, B. Poelsema, L. K. Verheij, and G. Comsa, "Reentrant layer-by-layer growth during molecular-beam epitaxy of metal-on-metal substrates," *Physical Review Letters*, 65 (6), 733–736, 1990.

[80] E. Weschke, C. Schüßler-Langeheine, R. Meier, G. Kaindl, C. Sutter, D. Abernathy, and G. Grübel, "q dependence of the growth-oscillation period of x-ray reflectivity in heteroepitaxy: Ho/W(110)," *Physical Review Letters*, 79 (20), 3954–3957, 1997.

[81] B. E. Warren, "X-ray diffraction,". New York: Dover, 1969.

[82] I. K. Robinson, "Handbook of synchrotron radiation,", vol. 3. North Holland - Amsterdam, 1991.

[83] I. K. Robinson and D. J. Tweet, "Surface x-ray diffraction," *Reports on Progress in Physics*, 55 (5), 599, 1992.

[84] R. Feidenhans'l, "Surface structure determination by x-ray diffraction," *Surface Science Reports*, 10 (3), 105–188, 1989.

[85] C. M. Schlepütz, *Systematic structure investigation of YBCO thin films with direct methods and surface X-ray diffraction.* PhD thesis, Universität Zürich, 2009.

[86] P. Eisenberger and W. C. Marra, "X-ray diffraction study of the Ge(001) reconstructed surface," *Physical Review Letters*, 46 (16), 1081–1084, 1981.

[87] A. Munkholm and S. Brennan, "Influence of miscut on crystal truncation rod scattering," *Journal of Applied Crystallography*, 32 (2), 143–153, 1999.

[88] I. K. Robinson, "Crystal truncation rods and surface roughness," *Physical Review B*, 33 (6), 3830–3836, 1986.

[89] E. Vlieg, "X-ray diffraction from rough, relaxed and reconstructed surfaces," *Surface Science*, 210, 301–321, 1989.

[90] E. Vlieg, "Rod: a program for surface crystallography," *Journal of Applied Crystallography*, 33, 401–405, 2000.

[91] E. Vlieg, O. Svensson, and R. Wilke, "ANA-ROD project." `http://www.esrf.eu/computing/scientific/joint_projects/ANA-ROD/index.htm`.

[92] E. Vlieg, "Integrated intensities using a six-circle surface x-ray diffractometer," *Journal of Applied Crystallography*, (30), 532–543, 1997.

[93] I. K. Robinson and P. J. Eng, "Near-surface and bulk short-range order in Cu_3Au," *Physical Review B*, 52 (14), 9955–9963, 1995.

[94] L. Barbier, S. Goapper, B. Salanon, R. Caudron, A. Loiseau, J. Alvarez, S. Ferrer, and X. Torrelles, "X-ray observation of a chemical order driven morphological transition on the surface of an A_3B type alloy," *Physical Review Letters*, 78 (15), 3003–3006, 1997.

[95] H. Reichert, P. J. Eng, H. Dosch, and I. K. Robinson, "Thermodynamics of surface segregation profiles at $Cu_3Au(001)$ resolved by x-ray scattering," *Physical Review Letters*, 74 (11), 2006–2009, 1995.

[96] S. Krimmel, W. Donner, B. Nickel, H. Dosch, C. Sutter, and G. Grübel, "Surface segregation-induced critical phenomena at FeCo(001) surfaces," *Physical Review Letters*, 78 (20), 3880–3883, 1997.

[97] J. Lyubina, O. Isnard, O. Gutfleisch, K.-H. Müller, and L. Schultz, "Ordering of nanocrystalline Fe-Pt alloys studied by *in situ* neutron powder diffraction," *Journal of Applied Physics*, 100 (9), 094308, 2006.

[98] M. R. Visokay and R. Sinclair, "Direct formation of ordered CoPt and FePt compound thin films by sputtering," *Applied Physics Letters*, 66 (13), 1692–1694, 1995.

[99] R. Baudoing-Savois, M. D. Santis, M. C. Saint-Lager, P. Dolle, O. Geaymond, P. Taunier, P. Jeantet, J. P. Roux, G. Renaud, A. Barbier, O. Robach, O. Ulrich, A. Mougin, and G. Bérard, "A new UHV diffractometer for surface structure and real time molecular beam deposition studies with synchrotron radiations at ESRF," *Nuclear Instruments and Methods in Physics Research Section B: Beam Interactions with Materials and Atoms*, 149 (1-2), 213 – 227, 1999.

[100] J. Daillant and A. Gibaud, "X-ray and neutron reflectivity: Principles and applications,". New York: Springer, 1999.

[101] H. Kiessig, "Investigations into the total reflexion of roetgen rays," *Annalen der Physik*, 10 (6), 715–768, 1931.

[102] H. Kiessig, "Interference of X-rays in thick layers," *Annalen der Physik*, 10, 769–788, 1931.

[103] L. G. Parrat, "Surface studies of solids by total reflection of x-rays," *Physical Review*, 95, 359–369, 1954.

[104] A. Ulyanenkov, "Novel methods and universal software for HRXRD, XRR and GISAXS data interpretation," *Applied Surface Science*, 253 (1), 106 – 111, 2006.

[105] A. Bianconi, "Xanes spectroscopy," in *X-ray absorption: principles, applications, techniques of EXAFS, SEXAFS and XANES* (D. C. Koningsberger and R. Prins, eds.), vol. 92 of *Chemical Analysis*, John Wiley and Sons, 1988.

[106] B. K. Teo, "EXAFS: Basic principles and data analysis,". Springer-Verlag, 1986.

[107] Y. Joly, "X-ray absorption near edge structure calculations beyond the muffin-tin approximation," *Physical Review B*, 63, 125120, 2001.

[108] J. J. Rehr and R. C. Albers, "Theoretical approaches to x-ray absorption fine structure," *Reviews of Modern Physics*, 72, 621–654, 2000.

[109] O. Proux, X. Biquard, E. Lahera, J. J. Menthonnex, A. Prat, O. Ulrich, Y. Soldo, P. Trevisson, G. Kapoujyan, G. Perroux, P. Taunier, D. Grand, P. Jeantet, M. Deleglise, J.-P. Roux, and J.-L. Hazemann, "FAME: A new beamline for X-ray absorption investigations of very-diluted systems of environmental, material and biological interests," *Physica Scripta*, T115, 970–973, 2005.

[110] O. Proux, V. Nassif, A. Prat, O. Ulrich, E. Lahera, X. Biquard, J. Menthonnex, and J. Hazemann, "Feedback system of a liquid-nitrogen-cooled double-crystal monochromator: design and performances," *Journal of Synchrotron Radiation*, 13, 59–68, 2006.

[111] B. Ravel and M. Newville, "ATHENA, ARTEMIS, HEPHAESTUS: data analysis for X-ray absorption spectroscopy using IFEFFIT," *Journal of Synchrotron Radiation*, 12, 537–541, 2005.

[112] S. Zabinsky, J. J. Rehr, A. Ankudinov, R. Albers, and M. J. Eller, "Multiple-scattering calculations of x-ray-absorption spectra," *Physical Review B*, 52 (4), 2995–3009, 1995.

[113] G. Schutz, W. Wagner, W. Wilhelm, P. Kienle, R. Zeller, R. Frahm, and G. Materlik, "Absorption of circularly polarized x-rays in iron," *Physical Review Letters*, 58 (7), 737–740, 1987.

[114] B. T. Thole, P. Carra, F. Sette, and G. van der Laan, "X-ray circular dichroism as a probe of orbital magnetization," *Physical Review Letters*, 68 (12), 1943–1946, 1992.

[115] P. Carra, B. T. Thole, M. Altarelli, and X. Wang, "X-ray circular dichroism and local magnetic fields," *Physical Review Letters*, 70 (5), 694–697, 1993.

[116] C. T. Chen, Y. U. Idzerda, H.-J. Lin, N. V. Smith, G. Meigs, E. Chaban, G. H. Ho, E. Pellegrin, and F. Sette, "Experimental confirmation of the x-ray magnetic circular dichroism sum rules for iron and cobalt," *Physical Review Letters*, 75 (1), 152–155, 1995.

[117] R. Wu and A. J. Freeman, "Limitation of the magnetic-circular-dichroism spin sum rule for transition metals and importance of the magnetic dipole term," *Physical Review Letters*, 73 (14), 1994–1997, 1994.

[118] C. Piamonteze, P. Miedema, and F. M. F. de Groot, "Accuracy of the spin sum rule in XMCD for the transition-metal L edges from manganese to copper," *Physical Review B*, 80 (18), 184410, 2009.

[119] W. Grange, M. Maret, J. Kappler, J. Vogel, A. Fontaine, F. Petroff, G. Krill, A. Rogalev, J. Goulon, M. Finazzi, and N. Brookes, "Magnetocrystalline anisotropy in (111) $CoPt_3$ thin films probed by x-ray magnetic circular dichroism," *Physical Review B*, 58 (10), 6298–6304, 1998.

[120] W. Grange, I. Galanakis, M. Alouani, M. Maret, J. Kappler, and A. Rogalev, "Experimental and theoretical x-ray magnetic-circular-dichroism study of the magnetic properties of $Co_{50}Pt_{50}$ thin films," *Physical Review B*, 62 (2), 1157–1166, 2000.

[121] I. Galanakis, M. Alouani, and H. Dreyssé, "Calculated magnetic properties of low-dimensional systems: the AuCu- and $AuCu_3$-type ferromagnets," *Journal of Magnetism and Magnetic Materials*, 242-245, 27 – 32, 2002.

[122] Z. Q. Qiu and S. D. Bader, "Surface magneto-optic Kerr effect," *Review of Scientific Instruments*, 71 (3), 1243–1255, 2000.

[123] M. Przybylski, L. Yan, J. Żukrowski, M. Nyvlt, Y. Shi, A. Winkelmann, J. Barthel, M. Waśniowska, and J. Kirschner, "Topology-dependent interface contribution to magneto-optical response from ultrathin Co films grown on the (001), (110), and (111) surfaces of Pd," *Physical Review B*, 73 (8), 085413, 2006.

[124] S. Bedanta, T. Eimüller, W. Kleemann, J. Rhensius, F. Stromberg, E. Amaladass, S. Cardoso, and P. P. Freitas, "Overcoming the dipolar disorder in dense CoFe nanoparticle ensembles: Superferromagnetism," *Physical Review Letters*, 98 (17), 176601, 2007.

[125] S. Boukari, J. Balay, E. Beaurepaire, G. Biechel, B. Carriere, J. Deville, B. Muller, and F. Scheurer, "Four pole electromagnet for in situ magneto-optical measurements," *Vacuum*, 52 (3), 327–331, 1999.

[126] H. Bergh, B. Gergen, H. Nienhaus, A. Majumdar, W. Weinberg, and E. McFarland, "An ultrahigh vacuum system for the fabrication and characterization

of ultrathin metal-semiconductor films and sensors," *Review of Scientific Instruments*, 70 (4), 2087–2094, 1999.

[127] J. Zak, E. R. Moog, C. Liu, and S. D. Bader, "Magneto-optics of multilayers with arbitrary magnetization directions," *Physical Review B*, 43 (8), 6423–6429, 1991.

[128] C. Kittel, "Optical rotation by ferromagnetic substances," *Physical Review*, 83 (1), 208, 1951.

[129] G. Ritz, M. Schmid, P. Varga, A. Borg, and M. Rønning, "Pt(100) quasihexagonal reconstruction: A comparison between scanning tunneling microscopy data and effective medium theory simulation calculations," *Physical Review B*, 56 (16), 10518–10525, 1997.

[130] A. Borg, A.-M. Hilmen, and E. Bergene, "STM studies of clean, CO- and O2-exposed Pt(100)-hex-R0.7," *Surface Science*, 306 (1-2), 10–20, 1994.

[131] E. Ritter, R. Behm, and G. P "Direct observation of a nucleation and growth process on an atomic scale," *Surface Science*, 181 (1-2), 403–411, 1987.

[132] B. Schaefer, M. Nohlen, and K. Wandelt, "Growth of copper on reconstructed Pt(100)," *The Journal of Physical Chemistry B*, 108 (38), 14663–14670, 2004.

[133] P. Havu, V. Blum, V. Havu, P. Rinke, and M. Scheffler, "Large-scale surface reconstruction energetics of Pt(100) and Au(100) by all-electron density functional theory," *Physical Review B*, 82 (16), 161418, 2010.

[134] P. van Beurden and G. J. Kramer, "Atomistic mechanisms for the (1 x 1)⇌hex surface phase transformations of Pt(100)," *The Journal of Chemical Physics*, 121 (5), 2317–2325, 2004.

[135] D. L. Abernathy, S. G. J. Mochrie, D. M. Zehner, G. Grübel, and D. Gibbs, "Orientational epitaxy and lateral structure of the hexagonally reconstructed Pt(001) and Au(001) surfaces," *Physical Review B*, 45 (16), 9272–9291, 1992.

[136] M. Yoon, S. G. J. Mochrie, D. M. Zehner, G. M. Watson, and D. Gibbs, "Faceting and the orientational phase diagram of stepped Pt(001) surfaces," *Physical Review B*, 49 (23), 16702–16720, 1994.

[137] M. Batzill and B. E. Koel, "Deposition of silver on the Pt(1 0 0)-hex surface: kinetic control of alloy formation and composition by surface reconstruction," *Surface Science*, 498 (1-2), L85 – L90, 2002.

[138] W. Kim, S. C. Hong, J. Seo, S.-J. Oh, H. G. Min, and J.-S. Kim, "Surface effect on the magnetism of a $MnPt_3$-type ordered surface alloy on Pt(001)," *Physical Review B*, 70 (17), 174453, 2004.

[139] S. M. Valvidares, T. Schroeder, O. Robach, C. Quirós, T.-L. Lee, and S. Ferrer, "Structural and magnetic properties of bcc Co films on Pt(001) studied by magnetic resonant surface x-ray diffraction, STM, and magneto-optical Kerr effect," *Physical Review B*, 70 (22), 224413, 2004.

[140] C. H. Macqillavry, G. D. Rieck, and K. Lonsdale, "International tables for x-ray crystallography,", vol. III. Kynoch Press - Birmingham, 2nd ed. ed., 1968.

[141] T. Yamada, M. Bischoff, T. Mizoguchi, and H. van Kempen, "STM and STS study of ultrathin Mn layers on Fe(001)," *Surface Science*, 516 (1-2), 179–190, 2002.

[142] T. R. Linderoth, J. J. Mortensen, K. W. Jacobsen, E. Lægsgaard, I. Stensgaard, and F. Besenbacher, "Homoepitaxial growth of Pt on Pt(100)-hex: Effects of strongly anisotropic diffusion and finite island sizes," *Physical Review Letters*, 77 (1), 87–90, 1996.

[143] G. Kellogg, "Temperature dependence of surface self-diffusion on Pt(001)," *Surface Science*, 246 (1-3), 31 – 36, 1991.

[144] R. J. Behm, "Topography modification and microscopic motion on metal surfaces," in *Diffusion at Interfaces: Microscopic Concepts* (M. Grunze, H. Kreuzer, and J. Weimer, eds.), vol. 12 of *Springer Series in Surface Science*, pages 92–101, Springer Berlin, 1988.

[145] T. B. Massalski, "Binary alloy phase diagrams,". Ohio: ASM, 1990.

[146] T. Kaiser, W. Sigle, D. Goll, N. H. Goo, V. Srot, P. A. van Aken, E. Detemple, and W. Jäger, "Transmission electron microscopy study of the intermixing of Fe-Pt multilayers," *Journal of Applied Physics*, 103 (6), 063913, 2008.

[147] S.-L. Chang, J.-M. Wen, P. A. Thiel, S. Günther, J. A. Meyer, and R. J. Behm, "Initial stages of metal encapsulation during epitaxial growth studied by STM: Rh/Ag(100)," *Physical Review B*, 53 (20), 13747–13752, 1996.

[148] R. J. Hicken, S. J. Gray, A. Ercole, C. Daboo, D. J. Freeland, E. Gu, E. Ahmad, and J. A. C. Bland, "Magnetic anistropy in ultrathin epitaxial Fe/Ag(100) films with overlayers," *Physical Review B*, 55 (9), 5898–5907, 1997.

[149] P. Schieffer, C. Krembel, M.-C. Hanf, G. Gewinner, and Y. Gauthier, "Atomic structure of the Ag(001) c(2×2) Mn surface alloy," *Physical Review B*, 65 (23), 235427, 2002.

[150] P. Schieffer, C. Krembel, M. C. Hanf, and G. Gewinner, "Room-temperature instability of the Mn/Ag(100) interface in the monolayer range," *Physical Review B*, 55 (20), 13884–13893, 1997.

[151] D. M. Schaller, D. E. Bürgler, C. M. Schmidt, F. Meisinger, and H.-J. Güntherodt, "Spin reorientations induced by morphology changes in Fe/Ag(001)," *Physical Review B*, 59 (22), 14516–14519, 1999.

[152] D. Lerch, A. Klein, A. Schmidt, S. Müller, L. Hammer, K. Heinz, and M. Weinert, "Unusual adsorption site of hydrogen on the unreconstructed Ir(100) surface," *Physical Review B*, 73 (7), 075430, 2006.

[153] E. D. Specht and F. J. Walker, "A method for the accurate determination of crystal truncation rod intensities by X-ray diffraction," *Journal of Applied Crystallography*, 26 (2), 166–171, 1993.

[154] X. Torrelles and J. Rius, "Faster acquisition of structure-factor amplitudes in surface X-ray diffraction experiments," *Journal of Applied Crystallography*, 37 (3), 395–398, 2004.

[155] J. Fujii, F. Borgatti, G. Panaccione, M. Hochstrasser, F. Maccherozzi, G. Rossi, and G. van der Laan, "Evidence for in-plane spin-flop orientation at the MnPt/Fe(100) interface revealed by x-ray magnetic linear dichroism," *Physical Review B*, 73 (21), 214444, 2006.

[156] J. Fujii, F. Borgatti, G. Panaccione, M. Hochstrasser, F. Maccherozzi, and G. Rossi, "Magnetic properties of epitaxial Fe films on MnPt/Fe(1 0 0)," *Surface Science*, 601 (18), 4288 – 4291, 2007.

[157] S. Imada, A. Yamasaki, S. Suga, T. Shima, and K. Takanashi, "Perpendicular magnetization of $L1_0$-ordered FePt films in the thinnest limit," *Applied Physics Letters*, 90 (13), 132507, 2007.

[158] N. M. Souza-Neto, A. Y. Ramos, H. C. N. Tolentino, A. Martins, and A. D. Santos, "Depth-dependent chemical and magnetic local orders in thin magnetic films," *Applied Physics Letters*, 89, 111910, 2006.

[159] A. Martins, N. Souza-Neto, M. Fantini, A. Santos, R. Prado, and A. Ramos, "X-ray absorption spectroscopy study of FePt thin films," *Journal of Applied Physics*, 100 (1), 013905, 2006.

[160] C. Antoniak, J. Lindner, M. Spasova, D. Sudfeld, M. Acet, M. Farle, K. Fauth, U. Wiedwald, H.-G. Boyen, P. Ziemann, F. Wilhelm, A. Rogalev, and S. Sun, "Enhanced orbital magnetism in $Fe_{50}Pt_{50}$ nanoparticles," *Physical Review Letters*, 97 (11), 117201, 2006.

[161] C. J. Sun, G. M. Chow, G. H. Fecher, J. S. Chen, H.-J. Lin, and Y. Hwu, "Spin and orbital magnetic moments of FePt thin films," *Japanese Journal of Applied Physics*, 45 (1), 2539, 2002.

[162] I. Galanakis, M. Alouani, and H. Dreyssé, "Perpendicular magnetic anisotropy of binary alloys: A total-energy calculation," *Physical Review B*, 62 (10), 6475–6484, 2000.

Résumé

Nous nous proposons d'étudier l'interaction au niveau de l'interface entre un matériau antiferromagnétique et un ferromagnétique par un ensemble de techniques expérimentales qui utilisent le rayonnement synchrotron. Nous nous sommes particulièrement intéressés par l'effet de couplage d'échange dans les couches minces magnétiques avec anisotropie hors du plan. Les systèmes que nous avons étudiés sont les couches ordonnées chimiquement, FePt et MnPt sur Pt(001), et Fe/Ag(001), éventuellement couplée à CoO. Notre approche consiste à trouver des surfaces adaptées et à étudier, pour chaque bicouche, la croissance individuelle de chaque élément, alliage ou oxyde. A travers le contrôle d'un certain nombre des paramètres, comme la structure de la surface, la propreté, le taux et la température de déposition, nous avons obtenus une bonne connaissance du processus de croissance. Les systèmes obtenus ont été étudiés *in situ* par la diffraction de surfaces et *ex situ* par l'effet Kerr magnéto-optique, le dichroïsme circulaire magnétique de rayons X et la spectroscopie d'absorption de rayons X. La relation entre le couplage d'échange, qui se manifeste par l'augmentation de la coercivité et par un champ de décalage, et la structure des couches est discutée pour les interfaces MnPt/FePt and CoO/Fe.
Mots clef: décalage d'échange, alliage ordonnée, MnPt, FePt, Fe/Ag(001), diffraction de rayon X de surface, absorption de rayon X, MOKE, synchrotron.

Abstract

Our aim is to study the interaction of antiferromagnetic and ferromagnetic materials with well-defined interface by combining structural, electronic and magnetic techniques using synchrotron light. Our interest is guided by the exchange bias effect in thin ferromagnetic films with perpendicular magnetic anisotropy. The main systems studied in this work were ultra-thin layers of chemically-ordered alloys of FePt and MnPt on Pt(001) and of Fe/Ag(001), eventually coupled to CoO. Our strategy was to find an appropriate surface and, for each coupled bilayer, study the individual growth of each element, alloy or oxide. By controlling a variety of parameters, such as surface structure, cleanliness, deposition rate and temperature, we have got a good understanding of the growth process. The coupled systems obtained were studied *in situ* by grazing incidence X-ray diffraction and *ex situ* by magneto-optic Kerr effect, X-ray magnetic circular dichroism and X-ray absorption spectroscopy. The relation between the exchange coupling, which manifests itself by an increase in coercivity and a bias field, and the structural characteristics was discussed for the MnPt/FePt and CoO/Fe interfaces.
Keywords: exchange bias, ordered alloys, MnPt, FePt, Fe/Ag(001), surface X-ray diffraction, X-ray absorption, MOKE, synchrotron.